Influences of Crystalline Anisotropy, Doping, Porosity, and Connectivity on the Critical Current Densities of Superconducting Magnesium Diboride Bulks, Wires, and Thin Films

DISSERTATION

Presented in Partial Fulfillment of the Requirements for the Degree Doctor of Philosophy in the Graduate School of The Ohio State University

By

Michael Adam Susner

Graduate Program in Materials Science and Engineering

The Ohio State University

2012

Dissertation Committee:

Prof. Michael D. Sumption, Advisor

Prof. Edward W. Collings

Prof. Suliman A. Dregia

Prof. Wolfgang E. Windl

“Those who have handled sciences have been either men of experiment or men of dogmas. The men of experiment are like the ant, they only collect and use; the reasoners resemble spiders, who make cobwebs out of their own substance. But the bee takes a middle course: it gathers its material from the flowers of the garden and of the field, but transforms and digests it by a power of its own. Not unlike this is the true business of philosophy; for it neither relies solely or chiefly on the powers of the mind, nor does it take the matter which it gathers from natural history and mechanical experiments and lay it up in the memory whole, as it finds it, but lays it up in the understanding altered and digested. Therefore from a closer and purer league between these two faculties, the experimental and the rational (such as has never yet been made), much may be hoped.”

Sir Francis Bacon, 1st Viscount St. Alban

Novum Organum (1620), Aphorism 95

Abstract

Magnesium diboride (MgB_2) is a material with a superconducting transition temperature of 39 K. Discovered in 2001, the relatively large coherence length (and associated lack of weak links) together with its simple binary composition (making phase pure formation relatively easy) have made it a material of substantial interest. However, it has been difficult to assess in detail the relative importance of the roles of flux pinning, crystalline anisotropy, porosity, connectivity, doping, and doping homogeneity on the observed transport limitations of this conductor. This work focused on deconvoluting the most dominant of these effects.

First, the overall effects of electrical connectivity and crystalline anisotropy of critical current density (J_c) were investigated. In doing so the J_cs of dense, well-connected c-axis oriented films were compared with the relatively degraded J_cs of standard powder-in-tube MgB_2 wires. With the aid of a percolation model it was deduced that at 4.2 K, 10 T. about 60% of the degradation was due to MgB_2's crystalline anisotropy and the remaining 40% to porosity.

Second, chemical substitutions onto both the Mg and B sites were investigated in terms of effects on structure and superconducting properties. The homogeneity of C-substitution onto the B site was quantified in terms of the width of the superconducting specific heat transition. Analysis of the results led to optimization of methods for homogeneous doping of C into the B sublattice. Zr substituted onto the Mg sublattice was

investigated using samples prepared by pulsed laser deposition (PLD). Changes in magnetic, resistive, superconductive, chemical, and structural properties were studied over a wide range of Zr composition.

Dedication

This document is dedicated to my family and friends.

Acknowledgements

I would like to thank both Dr. Sumption and Dr. Collings for the guidance, enthusiasm, and support they have given me throughout the completion of my work. I would also like to thank the members of my dissertation committee, Dr. Dregia and Dr. Windl, for their support, advice, and constructive criticism. In addition, I would like to thank the co-workers and colleagues with whom I have worked while at The Ohio State University, including but not limited to Madhu Kongara, Scot Bohnenstiehl, Milan Majoros, Mohit Bhatia, Madhu Kongara, Rakesh Dhaka, Chris Kovacs, Tom Daniels, Logan Ward, Dan Owsley, Mohammed Mahmud, Yuan Yang, Cory Myers, Guangze Li, Hyun-Sung Kim, Yi Ding, and Xingchen Xu. I would also like to thank my collaborators at Hyper-Tech Research, Inc., including Matt Rindfleisch, Xuan Peng, Mike Tomsic, and Bob Boone. Furthermore, I would like to thank the staff of the Department of Materials Science and Engineering, particularly Ken Kushner, Ross Baldwin, Steve Bright, Mark Cooper, Mei Wang, and Lloyd Barnhart. Additionally, thanks need to be given to Henk Colijn, Cameron Begg, and Dan Huber of the Campus Electron Optics Facility for their help with XRD, TEM, SEM, and FIB training. I am also indebted to the United States Department of Energy, Office of High Energy Physics for their financial support under grant DE-FG02-95ER40900. Additionally, a portion of this work was performed at the National High Magnetic Field Laboratory, which is supported by National Science

Foundation Cooperative Agreement No. DMR-0654118, the State of Florida, and the U.S. Department of Energy. Finally, and most importantly, I would like to acknowledge the support of my loving family: my mother, Karen A. McGuire, my father Michael J. Susner, and my step-mother Caroline S. Susner. None of this work would be possible without their support.

Vita

May 8, 1983 .....Born in Joliet, IL

1997.....Ludwig Jr. High School District 92, Lockport, IL

2001.....Lockport High School District 205, Lockport, IL

2005.....B.S. Chemistry, Michigan State University

2009.....M.S. Materials Science and Engineering, The Ohio State University

2006 to present .....Graduate Research Associate, Department of Materials Science and Engineering, The Ohio State University

Publications

1. Collings E W, Sumption M D, Susner M A, Dietderich D R, and Nijhuis A, "Magnetic Measurement of Interstrand Contact Resistance and Persistent-Current Magnetization on Nb3Sn Rutherford Cables With Cores of MgO Tape and Woven S-Glass Ribbon." *AIP Conference Procedings* **1435**(1) 235.

2. Yang Y, Susner M A, Sumption M D, Rindfleisch M A, Tomsic, M J, and Collings E W (2012) "Influence of Strand Design, Boron Type, and Carbon Doping Method on the Transport Properties of Powder-in-Tube $MgB_{2-x}C_x$ Strands." *IEEE Trans. Appl. Supercond.* **22**(2) 6200110/1-10.

3. Hauser A J, Soliz J R, Dixit M, Williams R E A, Susner M A, Peters B, Mier L M, Gustafson T L, Sumption M D, Fraser H L, Woodward P M, and Yang F Y (2012) “Fully Ordered Sr_2CrReO_6 Epitaxial Films: A High Temperature Ferrimagnetic Semiconductor.” *Phys. Rev. B* **85** 161201(R)/1-4.

4. Susner M A, Daniels T W, Sumption M D, Rindfleisch M A, Thong C J, and Collings E W (2012) “Drawing Induced texture and the Evolution of Superconductive properties With Heat Treatment Time in Powder-in-Tube in-situ processed MgB_2 Strands.” *Supercond. Sci. Technol.* **25** 065002/1-13.

5. Li G Z, Yang Y, Susner M A, Sumption M D, and Collings E W (2012) “Critical Current Densities and n-values of MgB_2 Strands Over a Wide Range of Temperatures and Fields” *Supercond. Sci. Technol.* **25** 025001/1-10.

6. Ding Y, Sun Y, Zhuang J C, Cui L J, Shi Z X, Sumption M D, Majoros M, Susner M A, Kovacs C J, Li G Z, Collings E W, and Ren Z A (2011) “Density Effect on Critical Current Density and Flux Pinning Properties of Polycrystalline $SmFeAs_{1-x}F_x$ Superconductor.” *Supercond. Sci. Technol.* **24** 125012/1-7.

7. Susner M A, Yang Y, Sumption M D, Collings E W, Rindfleisch M A, Tomsic M J, and Marzik J V (2011) "Enhanced Critical Fields and Superconducting Properties of Pre-doped B Powder-Type MgB_2 Strands." *Supercond. Sci. Technol.* **24**(1) 012001/1-012001/5.

8. Shi Z X, Susner M A, Sumption M D, Collings E W, Peng X, Rindfleisch M A, and Tomsic M J (2011). "Doping Effect and Flux Pinning Mechanism of Nano-SiC Additions in MgB_2 Strands." *Supercond. Sci. Technol.* **24**(6) 065015/1-065015/7.

9. Myers C S, Susner M A, Motowidlo L, Distin J, Sumption M D, and Collings E W (2011). "Transport, Magnetic, and SEM Characterization of a Novel Design Bi-2212 strand." *IEEE Trans. Appl. Supercond.* **21**(3, Pt. 3) 2804-2807.

10. Mentink M G T, Anders A, Dhallé M M J, Dietderich D R, Godeke A, Goldacker W, Hellman F, ten Kate H H J, Putnam D, Slack J L, Sumption M D, and Susner M A (2011). "Analysis of Bulk and Thin Film Model Samples Intended for Investigating the Strain Sensitivity of Niobium-Tin." *IEEE Trans. Appl. Supercond.* **21**(3, Pt. 3) 2550-2553.

11. Majoros M, Sumption M D, Susner M A, Collings E W, Souc J, Gomory F, Vojenciak M, Fisher L M, Kalinov A V, and Voloshin I F (2011). "AC Magnetization Loss of a YBCO Coated Conductor Measured Using Three Different Techniques." *IEEE Trans. Appl. Supercond.* **21**(3, Pt. 3) 3293-3296.

12. Majoros M, Kunuchova M, Susner M A, Sumption M D, Myers C S, Bohnenstiehl S D, and Collings E W (2011). "Effects of Heat Treatments on the Properties of $SmFeAsO_{1-x}F_x$ oxypnictide bulks prepared via a single-step route." *IEEE Trans. Appl. Supercond.* **21**(3, Pt. 3) 2853-2857.

13. Collings E W, Sumption M D, Susner M A, Ditderich D R, and Nijhuis A (2011). "Coupling Loss, Interstrand Contact Resistance, and Magnetization of Nb_3Sn Rutherford Cables With Cores of MgO Tape and S-glass Ribbon." *IEEE Trans. Appl. Supercond.* **21**(3, Pt. 2) 2367-2371.

14. Collings E W, Sumption M D, Susner M A, Barzi E, Turrioni, D, Yamada R, Zlobin A V, and Nijhuis (2010). "Coupling- and persistent-current magnetizations of Nb_3Sn Rutherford cables." *IEEE Trans. Appl. Supercond.* **20**(3) 1387-1390.

15. Bohnenstiehl S D, Susner M A, Yang Y, Collings E W, Sumption M D, Rindfleisch M A, and Boone R (2011) "Carbon doping of MgB2 by toluene and malic-acid-in-toluene" *Physica C* **471** 108-111.

16. Varanasi C V, Reichart J, Burke J, Wang H, Susner M A, Sumption M D, Barnes P N (2010). "Second Phase ($BaGeO_3$, $BaSiO_3$) Nanocolumns in $YBa_2Cu_3O_{7-x}$ Films." *Advances in Cryo. Eng.* **1219** 362-369.

17. Sumption M D, Majoros M, Susner M A, Lyons D, Peng X, Clark C F, Lawless W N, and Collings E W (2010). "Thermal Diffusion and Quench Propagation in YBCO Pancake Coils Wound With ZnO and Mylar Insulations." *Supercond. Sci. Technol.* **23**(7) 075004/1-075004/16.

18. Shi Z X, Susner M A, Majoros M, Sumption M D, Peng X, Rindfleisch M A, Tomsic M J, and Collings E W (2010). "Anisotropic Connectivity and Its Influence on Critical Current Densities, Irreversibility Fields, and Flux Creep In in-situ Processed MgB_2 Strands." *Supercond. Sci. Technol.* **23**(4) 045018/1-045018/10.

19. Majoros M, Sumption, M D, Susner M A, Bhartiya S, Mahmud M, Collings E W, Tomsic M J, Rindfleish M A Phillips J, Lyons D, and Yue J (2010). "A Nb_3Sn-Based, Model Superconducting Helical Undulator Fabricated Using a Wind and React Process." *IEEE Trans. Appl. Supercond.* **20**(3) 270-273.

20. Collings E W, Sumption M D, Susner M A, Dietderich D R, Barzi E, Zlobin A V, and Nijhuis A (2010). "Coupling-Current and Persistent-Current Magnetizations in Nb_3Sn Rutherford Cables and Strands." *Adv. Cryo. Eng.* **1219** 191-198.

21. Bohnenstiehl S D, Susner M A, Yang Y, Collings E W, Sumption M D, Rindfleisch M A, and Boone R (2010). "Carbon Doping of MgB_2 by Toluene and Malic-Acid-in-Toluene." *Physica C* **471**(3-4) 108-111.

22. Susner M A, Bhatia M, Sumption M D, and Collings E W (2009). "Electrical resistivity, Debye Temperature, and Connectivity in Heavily Doped Bulk MgB_2 Superconductors." *J. Appl. Phys.* **105**(10) 103916/1-103916/7.

23. Sumption M D, Susner M A, Collings E W, Dietderich D R, Barzi E, Turrioni D, Yamada R, and Zlobin A V (2009). "Effect of Cable Edge Deformation on RRR and Magnetization of Strands Extracted from Nb_3Sn Rutherford-Type Cables." *IEEE Trans. Appl. Supercond.* **19**(3, Pt. 2) 2481-2485.

24. Majoros M, Sumption M D, Susner M A, Tomsic M J, Rindfleisch M A, and Collings E W (2009). "AC Losses in MgB_2 Multifilamentary Strands With Magnetic and Non-Magnetic Sheath Materials." *IEEE Trans. Appl. Supercond.* **19**(3, Pt. 3) 3106-3109.

25. Majoros M, Sumption M D, Susner M A, Bhartiya S, Bohnenstiehl S D, Collings E W, Tomsic M J, Rindfleisch M A, Phillips J, Lyons D, and Yue J (2009). "A Model Superconducting Helical Undulator Wound Using a Wind and React MgB_2 Multifilamentary Wire." *IEEE Trans. Appl. Supercond.* **19**(3, Pt. 2) 1376-1379.

26. Mahmud M A A, Susner M A, Sumption M D, Rindfleisch M A, Tomsic M J, Yue J, and Collings E W (2009). "Comparison of Critical Current Density in MgB_2 with Different Boron Sources and Nano-Particle Dopant Additions." *IEEE Trans. Appl. Supercond.* **19**(3, Pt. 3) 2756-2759.

27. Susner M A, Sumption M D, Bhatia M, Tomsic M J, Rindfleisch M A, and Collings E W (2008). "Changes in Microstructure and Transport Properties of Magnesium Diboride Strands Through Hot Uniaxial Pressing." *Adv. Cryo Eng.* **986** 375-381.

28. Collings E W, Sumption M D, Susner M A, Dietderich D R, Barzi E, Zlobin A V, Ilyin Y, and Nijhuis A (2008). "Influence of a Stainless Steel Core on Coupling Loss, Interstrand Contact Resistance, and Magnetization of an Nb_3Sn Rutherford Cable." *IEEE Trans. Appl. Supercond.* **18**(2) 1301-1304.

29. Collings E W, Sumption M D, Bhatia M, Susner M A, and Bohnenstiehl S D (2008). "Prospects for Improving the Intrinsic and Extrinsic Properties of Magnesium Diboride Superconducting Strands." *Supercond. Sci. Technol.* **21**(10) 103001/1-103001/14.

30. Susner M A, Sumption M D, Bhatia M, Peng X, Tomsic M J, Rindfleisch M A, and Collings E W (2007). "Influence of Mg/B Ratio and SiC Doping on Microstructure and High Field Transport J_c in MgB_2 Strands." *Physica C* **456**(1-2) 180-187.

31. Sumption M D, Susner M A, Bhatia M, Rindfleisch M A, Tomsic M J, McFadden K J, and Collings E W (2007). "High Critical Current Density Multifilamentary MgB_2 Strands." *IEEE Trans. Appl. Supercond.* **17**(2, Pt. 3) 2838-2841.

32. Chen K, Susner M A, and Vyazovkin S (2005). "Effect of the Brush Structure on the Degradation Mechanism of Polystyrene-Clay nanocomposites." *Macromol. Rapid Commun.* **26**(9) 690-695.

Fields of Study

Major Field: Materials Science and Engineering

Table of Contents

List of Tables

List of Figures

Chapter 1: Introduction to MgB_2- History and Materials Properties

Magnesium diboride (MgB_2) offers a unique opportunity to develop a superconductor that is inexpensive and able to carry current at temperatures achievable through modern refrigeration techniques. Although it was first characterized as early as 1953 [1], its superconducting qualities were not discovered until 2001 [2]. MgB_2 is a superconductor that, among the many that follow the conventional phonon-mediated mechanism described by the BCS theory, exhibits the highest superconducting critical temperature, T_c (~39 K) [3]. In addition, its superconducting properties are more similar to the more well-established intermetallics Nb_3Sn and Nb_3Ge with regards to bulk pinning force behavior [4]. Nevertheless, many have noted [5] that there exist three properties to be considered during the development of MgB_2 for applications: i) electrical connectivity, ii) sample homogeneity (specifically in terms of the superconducting critical fields), and iii) flux pinning.

1.1 History of Magnesium Diboride

MgB_2 was first seen in the literature in 1881 as a product of the reduction of B_2O_3 or BCl_3 with Mg [6]; however, at the time it was identified as Mg_3B_2. The process

whereby B_2O_3 is reduced by Mg was later investigated in more detail by Moissan [7] (for whom the most widely used process to synthesize commercial amorphous B is named), who again asserted that Mg_3B_2 as well as other borides were present as reaction products.

Ray [8], in 1914, used acid digestion to confirm the absence of borides other than the previously identified Mg_3B_2; he found no other boride phase. Finally, Russell *et al.* [1], followed by Jones and Marsh [9], used X-ray diffraction (XRD) to determine the lattice parameters of MgB_2, thereby fixing the composition at MgB_2 for the lowest boride phase based on geometric constraints. Russell *et al.* [1], in contrast to the work of Ray [8], were also the first to note the presence of the higher boride phase MgB_4, although it and the other commonly identifiable boride phase, MgB_7, were not fully characterized until later [10],[11].

In 1957 Swift and White [12] used MgB_2, because of its layered hexagonal crystal structure, as an analog for graphite to determine if the heat capacity of MgB_2 had a T^2 or T^3 low temperature dependence. The low temperature data were displayed only in tabular form, and as a result the authors missed the low-T heat capacity transition characteristic of a superconductor. These data are plotted in Figure 1 as C/T vs. T. At the time, the T_c of 39 K would have been more than twice that of the next highest superconductor in the literature, Nb_3Sn, which was shown to have a T_c of ~18 K in 1954 [13]. Unfortunately, this discovery was overlooked for the next 47 years. During this period, MgB_2 was seen as little more than a curious impurity phase in the reaction of B_2O_3 with Mg [14], as a possible precursor for the synthesis of cubic boron nitride [15], or as a diaphragm material for a honeycomb speaker [16].

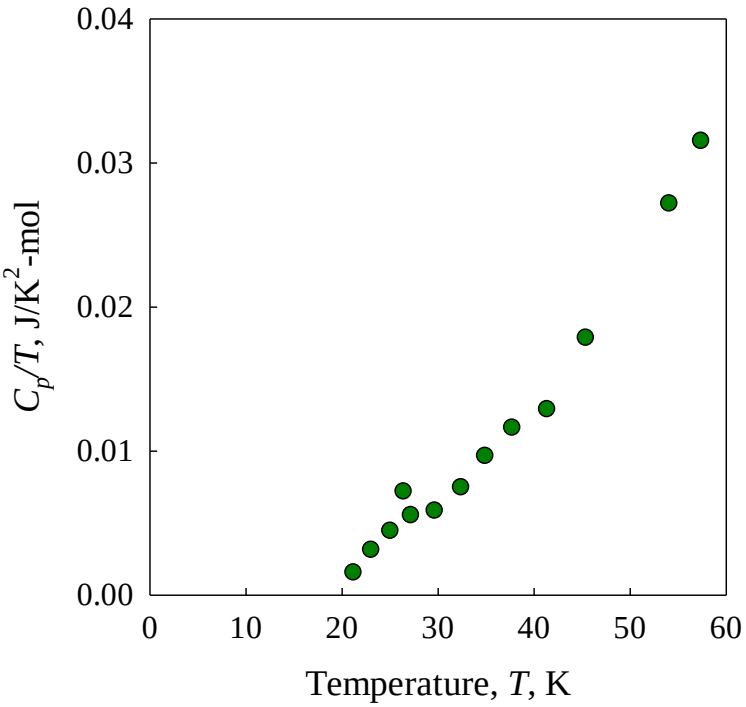

Figure 1. C_p/T vs. T plotted from tabular data in [12] (with permission from ACS publications).

Previous research into the superconductivity of metal diborides (MB_2) had been performed by Cooper *et al.* [17] and Leyarovska and Leyarovski [18] where M is Y, Nb, Mo, Ti, Hf, V, Ta, and Cr. Among these only the compound NbB_2 was found to be superconducting with a T_c of ~6.4 K. However, other ternary M_2B_5 phases were found with higher T_cs, with $Mo_{1.69}Zr_{0.31}B_5$ exhibiting a T_c of 11.2 K [17]. In the late 1990's and early 2000's, Akimitsu and his students were systematically investigating the Mg-Ti-B ternary system for other possible superconducting compounds [2], [19]. This system was chosen to reduce the mass of the elements present and to increase the density of itinerant electron states, both effects serving to increase T_c according to conventional BCS

superconductivity [20]. Serendipitously, the simple binary control sample MgB_2 exhibited the high T_c of ~39 K [2] and spurred over a decade of research into this superconducting compound.

Although its T_c of ~39 K is not as high as seen in "high-temperature superconductors" like YBCO (93 K) [21] or Bi-2212 (95 K) [22],[23], MgB_2's T_c is high enough that cryocoolers can be used to cool down devices and magnets made with this material without the use of liquid helium [24]. This is an important advantage given the current depletion of world helium reserves [25]. Although MgB_2's critical current density (J_c) and upper critical field (B_{c2}) have little margin over the same properties for NbTi or Nb_3Sn at 4.2 K, the higher temperatures at which MgB_2 can operate allows for a niche application, as is shown in Figure 2. One driving force for MgB_2 research has been for the eventual goal of relatively low-cost, conduction-cooled magnetic resonance imaging instruments (MRIs) [26] and research magnets [27],[28] which would allow for more availability of these systems for various important scientific investigations [29],[30]. Additionally, the costs of the constituent materials necessary to manufacture MgB_2 are relatively low, especially compared to the relatively expensive Nb and Ti needed for the more traditional NbTi and Nb_3Sn conductors [31] as well as the Ag needed as stabilizers or sheath materials for high-temperature superconductors (HTS).

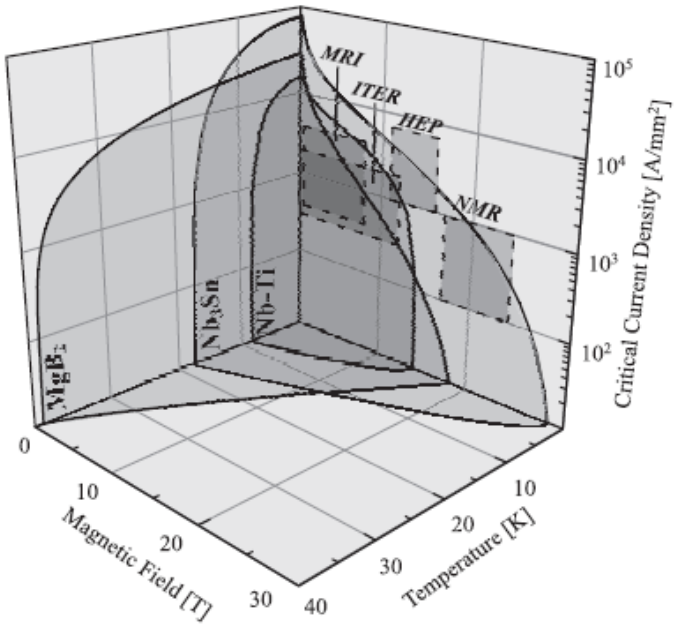

Figure 2. Superconducting phase diagram for MgB_2 as compared to NbTi and Nb_3Sn, from [31].

1.2 MgB_2 Crystal Structure and Bonding

As previously mentioned, the correct stoichiometry and crystal structure of MgB_2 were not identified until 1953-1954 [1],[9] , at which point MgB_2 was recognized as having a *P6/mmm* space group with lattice parameters of a = 3.0849 Å and c = 3.5187 Å. The spacegroup *P6/mmm* common to all diborides excepting those formed by Mo, Os, Re, Ru, and Tc. MgB_2 is isomorphous with the prototype AlB_2 crystal structure [32].

Figures 3a-3c show a representation of the MgB_2 structure, created with the software Mercury. The MgB_2 unit cell is traced in red and can be described with the Mg

at (0,0,0) and the B at (⅓, ⅔, ½) and (⅔, ⅓, ½). Figure 4a shows the view down the c-axis, highlighting the hexagonal B structure. Figure 4b shows the view down the a-axis, showing the stacking of the B planes. Finally, Figure 4c shows the view from an arbitrary point. In essence, the structure is that of a series of 2-D B honeycombs, similar to graphene, stacked in registry with no displacement [33]; the Mg atoms (6 x larger than the B atoms) are situated at the center of the honeycombs and act to stabilize the structure through the donation of charge.

Together three bonding types are present in MgB_2: B-B, Mg-B, and Mg-Mg. Ivanovskii [34] used *ab initio* modeling to conclude that the cohesion energies for the aforementioned bonding types contribute 68%, 23%, and 9%, respectively, to the cohesion energy of the bulk. The different bonding types present give rise to the two-band nature of MgB_2. The in-plane B-B bonds are sp^2 hybridized, leading to covalent bonding similar to that of graphite; these bonds give rise to the σ band. The out-of-plane p_z orbitals of the B planes create π bonding, also similar to graphite. This type of bonding results in the π band [19]. The Mg-B bonds are essentially ionic [35],[36]. Kortus *et al.* [33] calculated that the Fermi surface of the material is derived mainly from the B electron orbitals: the four B p_{xy} orbitals that constitute the σ band and the B p_z orbitals that constitute the π band. It is therefore from this anisotropic bonding that the different charge densities are derived and hence the two superconducting energy gaps.

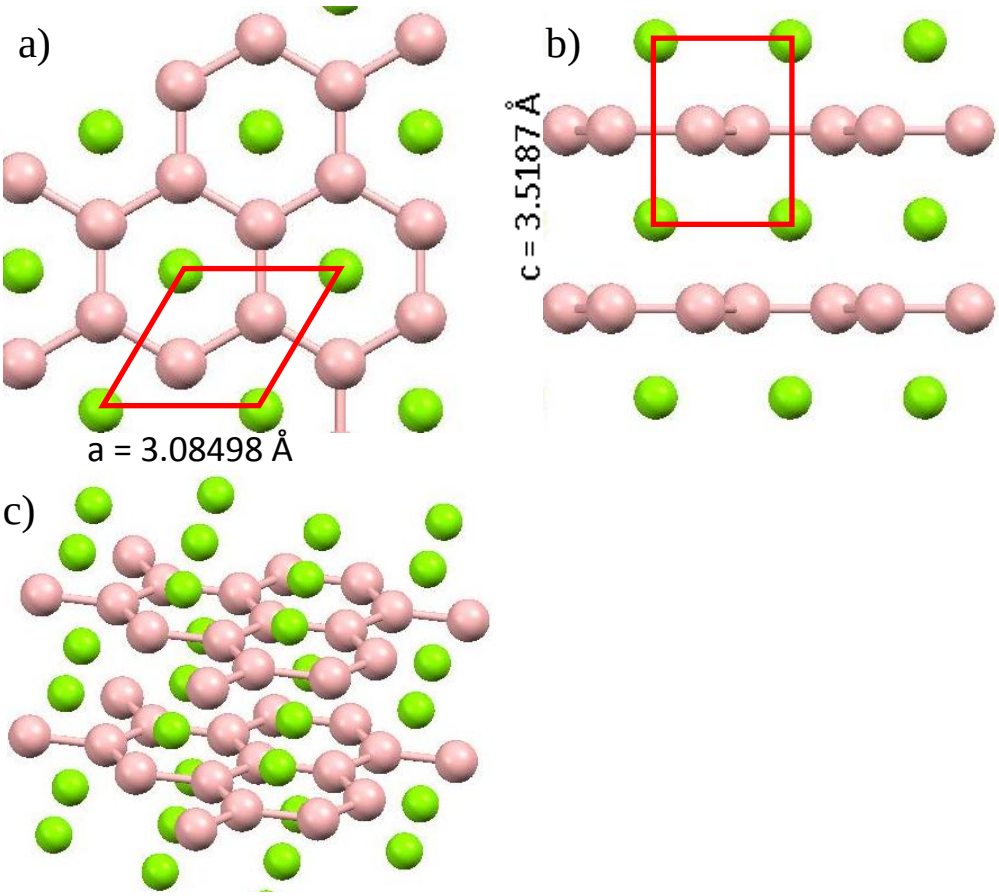

Figure 3. a) MgB_2 structure looking down the *c*-axis; b) MgB_2 structure looking down the *a*-axis; and c) MgB_2 viewed from an arbitrary point.

1.3 BCS Superconductivity in MgB_2

MgB_2 is unique due to its high T_c for a BCS superconductor (that is, a superconductor following the phonon-mediated mechanism outlined by Bardeen, Cooper, and Schrieffer [37]). In this respect, MgB_2 is not a member of the family of HTS superconductors since i) its T_c is intermediate, hot high and ii) the HTS superconductors

do not share the BCS mechanism. According to the BCS theory, for a 1-gap superconductor

$$k_B T_c = 1.13\hbar\omega_D \exp\left(\frac{-1}{VN(E_F)}\right) \quad (1)$$

where k_B represents Boltzmann's constant, $\hbar$ represents the reduced Planck constant, V is the phonon-moderated electron-electron interaction, $N(E_F)$ is the density of itinerant electron states, and T_c is the superconducting transition temperature. The Debye frequency, represented by ω_D in Equation 1, can be represented by the expression $(k/m)^{½}$ (in the simplest possible model and illustration of the effect [38]) where k is the spring constant and m represents the mass of the atoms in the lattice. Therefore, $T_c \propto \omega_D \propto m^{-½}$. Other more physically correct descriptions of the phonon-electron coupling for more complicated systems exist in the literature (see [39] for a review) but are not necessary to describe the so-called "isotope effect" for the purpose of this document.

After measuring MgB_2 specimens formed with the isotopes ^{10}B and ^{11}B, various groups [3], [38], [40–43] showed that MgB_2 does indeed obey the principles set described above, implying that phonon-electron coupling is present. The lighter ^{10}B containing sample yielded a T_c of 40 K while the heavier ^{11}B sample yielded a T_c of 39 K. Naturally occurring B has a composition of ~81% ^{11}B and ~19% ^{10}B, resulting in a T_c that is smeared from 39-40 K and weighted toward the lower end of this range. Isotope-effect investigations based on Mg using isotopically pure ^{24}Mg and ^{26}Mg showed a "small but measurable" effect [38] on the T_c, with a ~0.1 K drop in T_c induced by the higher mass isotope.

The electron-phonon mode of most concern to MgB_2 is the Raman mode centered at ~580 cm^{-1} that represents the in-plane displacement of B atoms [44]. This phonon mode, called the E_{2g}, is the one from which superconductivity in MgB_2 is thought to be derived based on its strong coupling with the B σ orbitals (in which the charge carriers are electron holes) [44],[45].

One of its most interesting properties is that MgB_2 exhibits two superconducting energy gaps. The first of these has a 0 K energy of ~5-8 meV [46] and results from the strong E_{2g} electron-phonon coupling. The second energy gap, with a 0 K value of ~1.8-3.0 meV [46], results from weak phonon coupling to the π-band [47]. Because of these differing energy gaps and the hexagonal structure several superconductive properties are anisotropic in MgB_2. For example, the coherence length ξ, or distance between coupled electrons forming a Cooper pair, varies as $\xi_{ab(0K)}$= 3.7-12 nm and $\xi_{c(0K)}$ = 1.6-3.6 nm [46]. The magnetic penetration depth λ, or the distance a magnetic field penetrates into a superconductor, varies from λ_{ab}(0K)=110-120 nm and λ_c(0K)=220-280 nm [48]. The upper critical magnetic field B_{c2}, also exhibits a large degree of anisotropy, with $B_{c2//c(0\ K)}$ = 2-24 T and $B_{c2\perp c(0\ K)}$ = 14-60 T [46],[49] (that is, with the magnetic field applied parallel or perpendicular to the c-axis, respectively). If just a single gap was present, the anisotropies in B_{c2}, λ, and ξ (γ_{Bc2}, γ_λ, and γ_ξ, respectively) would be equal to each other at all temperatures [50]. However, it is seen for MgB_2 that $\gamma_{Bc2}=B_{c2\perp c}/B_{c2//c}$ is 6-8 at low T but decreases to ~2.5 as T approaches T_c. The values of γ_ξ follow a very similar pattern [51]. γ_λ, on the other hand however, is ~1 at low temperatures and increases to ~2.5 on

approaching T_c. These anisotropies have significant effects on the properties dependent on these variables, including but not limited to flux pinning and critical current density.

For the majority of investigations, MgB_2 characterization is performed on bulk samples composed of a large number of small (almost always < 1μm), randomly oriented grains. Only in thin film or single crystal studies are the anisotropic superconducting properties able to be carefully measured and quantified. The large variation reported for values for ξ, λ, and B_{c2} are likely the result of measurements made indiscriminately on bulk samples. Bulk samples, then, represent an amalgam of grains that are in both preferential and non-preferential orientations with respect to their important properties. Several models have been put forth in the literature which account for the effect of the two-gap nature of MgB_2 polycrystalline bulk samples. For instance, Eisterer [52] has advanced a percolation model which can quantify the effect of grain orientations on the J_c of MgB_2 samples. In effect, his model utilizes a "percolation threshold" based on a distribution of grain orientations with respect to the applied magnetic field, determining when a path is no longer capable of carrying supercurrent.

1.4 MgB_2 Phase Diagram and Reaction Formation

A widely cited representation of the standard pressure (0.1 MPa) Mg-B phase diagram is presented in Figure 3. This diagram was calculated by Kim *et al.* [53] using *ab initio* calculations (employing density functional theory) to compute the enthalpies of the phases present. Additive entropy formation was used to calculate the entropies and

thus also the heat capacities. The software package PANDAT [54] was used together with the CALPHAD [55] method to calculate the theoretical phase diagram presented in Figure 3. The authors of this work forewent attempting to construct an experimental phase diagram due to the volatility and high vapor pressure of the Mg.

Several important features of this system should be noted. First, there is little solubility for Mg in B or B in Mg at standard pressure (0.1 MPa). Specifically, the solubility for B in Mg is ~1.17 at% at 1100^{o}C (the boiling point of Mg). The solubility of Mg in B is ~0.004 at% at 2092^{o}C (the melting point of B). The lack of solubility makes it difficult to homogeneously melt Mg and B to form a homogeneous compound and to introduce dopants in a homogeneous manner [56].

Second, all boride phases are line compounds and, as a result, are practically impossible to obtain in a single phase. The boride phases are MgB_2 [1],[9], MgB_4 [10], and MgB_7 (often referred to as Mg_2B_{14} in the literature) [11]. Other boride phases have been noted in the literature, including but certainly not limited to MgB_{12} [57], $MgB_{17.4}$ [58], and MgB_{20} [57],[59]. These phases are generally not included in literature equilibrium phase diagrams and have little bearing on the present work. The MgB_2 phase, as will be discussed in detail in the next section, has a space group of *P6/mmm* with lattice parameters of a = 3.0849 Å and c = 3.5187 Å [1],[9]. MgB_4 is orthorhombic (space group *Pnam*) and has lattice parameters of a = 5.464 Å, b = 7.472 Å and c = 4.428 Å [10]. MgB_7 is also orthorhombic (space group *Imam*) with lattice parameters a = 5.970 Å, b = 8.125 Å and c = 10.480 Å [11].

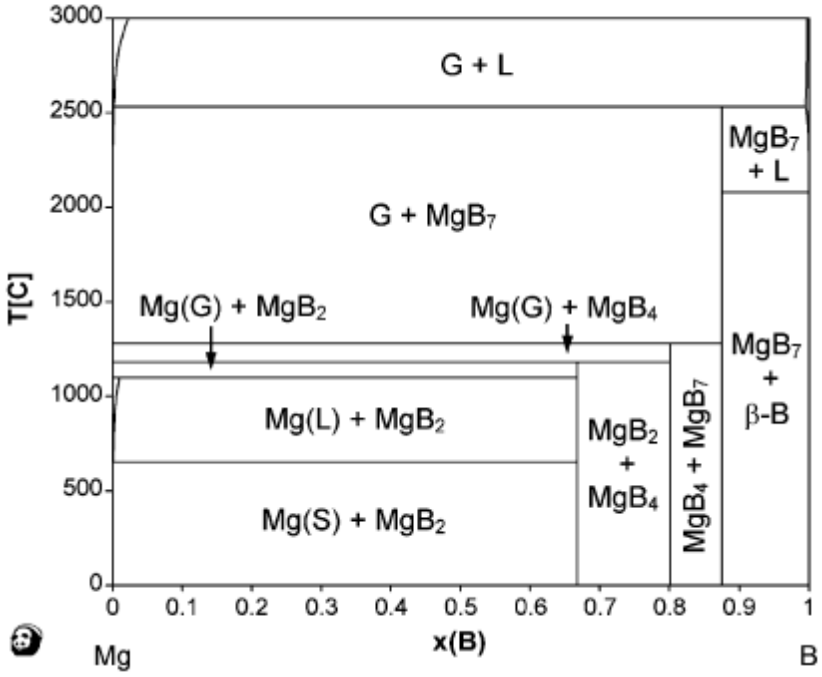

Figure 4. 0.1 MPa Mg-B phase diagram, after [53] (with permission from Elsevier).

Due to the volatility of Mg, most groups, like Kim *et al.* [53] have relied on theoretical phase diagrams based on either *ab initio* calculations or extrapolations of thermodynamic data (which can vary widely [60–63], likely due to differences in the purity of the initial B and Mg precursors [56]). It follows, then, that most of the phase diagrams in the literature can also vary. Recently, Bohnenstiehl [56] experimentally investigated the peritectic (asymmetric) phase transition at high pressures (10 MPa) so that the value of this peritectic transition temperature between MgB_2(s) and MgB_4(s)+Mg(g) could be investigated without Mg vapor loss. It was found [56] that (at

10 MPa) the peritectic transition temperature was 1430-1500^{o}C, depending on the purity of the B used (C was found to be the largest impurity).

The reaction mechanism of MgB_2 from its constituents Mg and B has been well-investigated. By embedding in a Mg matrix B fibers grown via a CVD process on a WB core (where the B was essentially amorphous), DeFouw and Dunand [64],[65] essentially created a circular diffusion couple for the investigation of the kinetics of the Mg-B phase diagram, as represented in Figure 5. The B filaments were 100-200 μm in diameter and 99.999% pure. A series of optical micrographs of the reacted fiber is presented in Figure 4. These were reacted at 1000^{o}C for: a) 1 min., b) 2 min., c) 3 min., and d) 5 min.

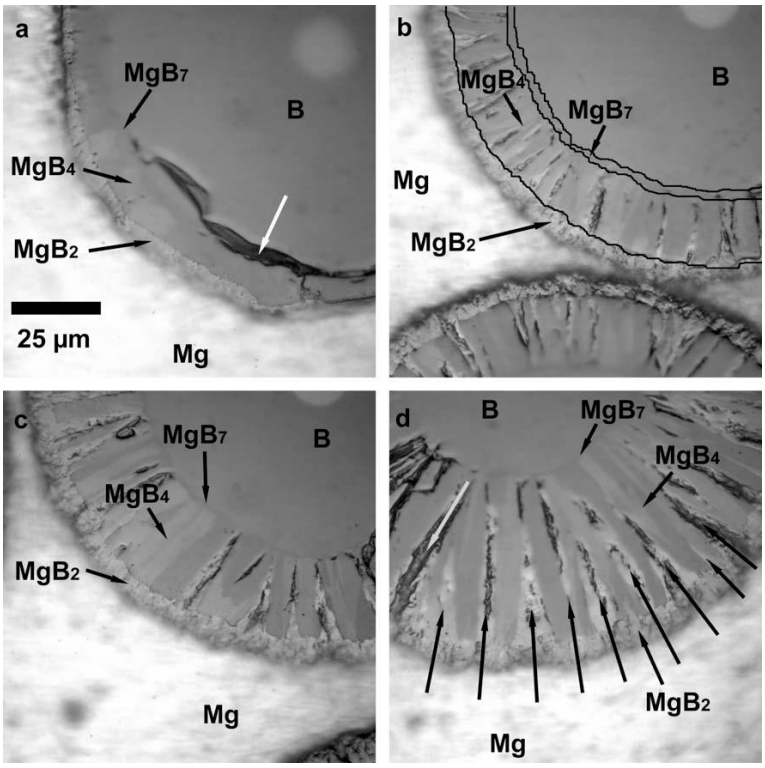

Figure 5. B fiber reacted in Mg showing shrinking core reaction of MgB_7 to MgB_4 to MgB_2. These fibers were reacted at 1000°C for: a) 1 min., b) 2 min., c) 3 min., and d) 5 min., after [65] (with permission from Elsevier).

One obvious feature of this reaction is the lack of boride phases other than MgB_7, MgB_4, and MgB_2; MgB_{20} is not observed, a result which has been ascribed to a lack of compositional contrast between this phase and B [65], the phase being too thin to observe, or that MgB_{20} might simply represent a solid solution of Mg in B [56]. The boride phases were identified via time-of-flight secondary ion mass spectroscopy. It is observed that MgB_2 formation follows a shrinking core type reaction model whereby MgB_7 forms on the outer shell of the B fiber, followed by MgB_4 and, finally, MgB_2. The reaction, assuming an unlimited source of Mg, proceeds as

$$B \xrightarrow{Mg} MgB_7 \xrightarrow{Mg} MgB_4 \xrightarrow{Mg} MgB_2$$
$$\Delta\text{Vol.} \quad +18\% \qquad +24\% \qquad +28\%$$

where the accompanying increase in molar volume is listed. This overall increase in molar volume of ~89% from B to MgB_2 is responsible for the cracking around the outer shell of Figure 5, which in turn allows for deeper penetration of the Mg into the core, circumventing the solid-state diffusion barrier that would otherwise slow the kinetics on the surface of the fiber.

The solid-state diffusion through the increasingly growing intermediate boride phases is a phenomenon that severely retards the reaction of MgB_2. Faced with this difficulty, researchers have either: i) increased the reaction temperatures to increase the diffusion and therefore decrease the amount of reaction time or ii) decreased the initial size of the B. The latter route is advantageous in terms of reducing the overall MgB_2 reaction time but is detrimental in that the increased surface area caused by the reduction in B size provides a greater opportunity for oxide formation when exposed to ambient atmosphere. The former option is problematic in that special equipment not necessarily compatible with efficient manufacturing techniques is required to react Mg and B into MgB_2 at high *T*; here high *P* techniques are essential to circumvent the volatility of Mg.

Because MgB_2 is a line compound it is difficult to obtain the exact stoichiometric composition, resulting in a mixture of either MgB_2 + Mg or MgB_2 + MgB_4 after reaction. With respect to compositional variation, some [66] have stated that up to 5% Mg vacancies can exist in MgB_2, resulting in strain that in turn results in a T_c which is lowered by ~2-3 K. However, no direct microstructural evidence was presented to prove

this thesis. Additionally, the presence of these vacancies was derived from strain seen in the XRD analysis; indeed, Mg vacancies are given as the only source of the lattice strain. Ribeiro *et al.* [67] investigated the crystallographic and superconducting properties of both Mg-rich and Mg-poor MgB_2 and found that MgB_4 is present in the XRD patterns of the Mg-deficient MgB_2 and Mg is present in the XRD patterns of the Mg-rich MgB_2, wholly consistent with MgB_2 existing as a line compound. However, the composition ranges investigated had step sizes of ~5%, leaving open the question of the possibility of non-stoichiometry being present, if only in small quantities. In contrast, Hinks *et al.* [68] showed that the Mg vacancy content in MgB_2 is ~1% and attributed changes in lattice constants as a result of composition to grain-interaction stresses. Nevertheless, if there is a possibility for non-stoichiometry in MgB_2 it is limited and is not supported by the equilibrium phase diagram. Also, the heat treatments in these samples were quite varied depending on the author, with Serquis *et al.* [66] performing relatively short heat-treatments of 1 h. at 900^{o}C, Ribeiro *et al.* [67] using heat-treatments of 3 h. at 950^{o}C, and Hinks *et al.* [68] using a heat-treatment of 2 h. at 850^{o}C. As a result, MgB_2 homogeneity could conceivably be different between the different sample sets. Also, starting B purity for the various studies differed.

1.5 Boron Powders: Effects of Structure and Purity

A non-trivial aspect to MgB_2 synthesis is the effects of the starting powder on both the final microstructure and the final electronic and superconductive properties. The

effects of the starting B powder can be separated into two broad categories: i) powder morphology and ii) powder purity. The former category is mainly dependent on the allotrope of B [69],[70] or the manufacturing process involved in creating the B. There exist five allotropes of B, including the amorphous phase: i) "amorphous" B, where B is arranged in randomly oriented B_{12} icosohedra with no long-range order present, ii) the α-rhombohedral phase, iii) the β-rhombohedral phase, iv) the γ-orthorhombic phase, and v) the tetragonal phase [70]. The β-rhombohedral and amorphous phases are both commercially available at purities ranging from very low for applications such as airbag inflation (<90% by trace metals analysis) to very high for the semiconductor industry (99.9999%). It is important to remember that often light elements such as C are not included in trace metals analysis and that, as a result, B powders with nominally high purities can contain a not-insignificant fraction of C [71]. In any case, MgB_2 is most often synthesized from either amorphous or β-rhombohedral starting powders. Generally speaking, the crystalline phases require higher reaction temperatures for MgB_2 formation, usually in the range of 800-1000^{o}C compared to the 600-700^{o}C typically used for the amorphous powders, although ball milling to smaller sizes can lower the reaction temperatures for the crystalline B, an effect ascribed to an increase in the surface area.

Boron is found naturally as B_2O_3. As stated previously, a relatively simple technique for isolating B is to use the Moissan process whereby B_2O_3 is reduced by Mg. However, unless substantial purification is performed, higher boride phases remain as impurities, as well as other elements that were in the starting B_2O_3. Higher purity (amorphous) B can be obtained by the thermal decomposition of diborane or pentaborane

gases; subsequent annealing will convert the amorphous phase into the β-rhombohedral phase. This process is rather expensive and requires the additional special safety precautions needed when working with borane gasses. Another method for producing (mostly) amorphous B powder is the plasma assisted reaction of BCl_3 with H_2, whereby HCl and partially crystalline B (β-rhombohedral, [72]) with particle sizes of 20-50 nm is produced.

Starting B purity has a substantial effect on the final electronic properties of MgB_2. Ribiero *et al.* [67] saw the residual resistivity ratio (RRR, a measure of the impurity scattering present in a material where a higher RRR indicates less impurity scattering) vary from 4-20 depending on the starting B purity. Others [72–77] noted significant changes in the critical current density, J_c, in response to variation of the initial B powder purity. Kim *et al.* [72] noted a large increase in J_c at high fields for MgB_2 made from the amorphous diborane-route B, an effect attributed to small grain size and thus large flux pinning force density, F_p[1]. Zhang *et al.* [76] saw large differences in T_c and J_c between MgB_2 samples made from high purity amorphous borane-route B and β-rhombohedral B, with the amorphous B resulting in a lower weight fraction of MgO in the final product. Zhang *et al.* attempted to scale the T_c with the lattice parameters and did in fact establish a fit (albeit with three data points). However, Zhang *et al.* created an argument that uses Mg vacancies, MgO impurity content, and strain to explain differences in the structural, electronic, and superconducting properties density of their

[1] The flux pinning force is defined as $-\vec{F}_p = \vec{J}_c \times \vec{B}$ and may be interpreted as the critical current J_c at a magnetic field B which allows the Lorentz force to be balanced by a pinning force (per unit volume), F_p [78]. This topic will be covered in more detail in a later section.

samples. These relationships are difficult to definitively establish with only three samples. Jiang *et al.* [75] showed that through reducing as-received B powder with 4% H_2 forming gas (and thereby removing B_2O_3 which can form on the powder surface upon exposure to air), the normal state resistivity decreased significantly and the RRR increased from ~5 to ~9. Scanning electron microscopy (SEM) that was also performed showed the presence of less MgO in the MgB_2 sample made from the purified B powder. Jiang *et al*. took the normal state resistivity data from their experiments (from 40-300 K) and, by comparing them to MgB_2 single crystal data, deduced the electrical connectivities of their samples [79]. They found that purified B led to an MgB_2 sample that was 48% connected in contrast to the unpurified B sample, which was only 25% electrically connected. Electrical connectivity in MgB_2 is discussed in detail in Chapters 3 and 5 of this document

Little research has been performed on the effect of the initial Mg purity on the final MgB_2 powder, excepting reports by [60] and [80] where MgH_2, rather than Mg with an MgO or $Mg(OH)_2$ layer is used as a precursor for MgB_2. Bohnenstiehl *et al.* [60] used MgH_2 to investigate the reaction kinetics of MgB_2 formation, finding that Mg with the $MgO/Mg(OH)_2$ layer exhibited an exothermic event at ~450^oC, possibly initiating a low *T* reaction of MgB_2; MgB_2 made from MgH_2 did not show these exothermic events. Fujii *et al.* [80] fabricated and compared Fe-clad MgB_2 wires made from MgH_2 and Mg and found that the T_c was relatively unaffected by the Mg type used. Changes in J_c were attributed to the lack of the formation of a reaction layer with the Fe outer sheath using the MgH_2 route.

1.6 MgB_2 Synthesis Techniques: Bulks and Wires

Powder synthesis is used for the majority of research present in the literature. Here, the term powder synthesis can encompass two complementary techniques: i) *in-situ synthesis*, where an Mg+B powder mixture is heated (typically from ~600^{o}C up to 1000^{o}C) and reacted to form MgB_2, and 2) the *ex-situ* technique, where pre-reacted MgB_2 powder is ground, shaped into a pellet or wire, and sintered (typically at above 800^{o}C). Both techniques are performed in an inert environment such as Ar so as to prevent any oxygen contamination (MgO is extremely stable, requiring a P_{O2} of < ~10^{-23} MPa at 1000^{o}C to prevent its formation). The *ex-situ* technique can sometimes be disadvantageous in that, if exposed to oxygen, MgB_2 is rather difficult to "sinter" (if indeed it does at all, e.g. [81]) and no real grain growth occurs. The *in-situ* technique is disadvantageous in that the combined molar volume of an Mg and B powder admixture (23.0 cm^3/mol assuming no porosity is present) is less than that of the final MgB_2 molar volume (17.21 cm^3/mol). Figure 6 shows the relationship between initial packing density of the Mg+B mixture and the resulting MgB_2 packing factor assuming equi-sized Mg and B (curve 1) and large Mg with small B particles (curve 2). This phenomenon has an important implication in synthesis of MgB_2 in that a significant degree of porosity is present after the reaction is complete, the pores coinciding with the location of the prior Mg. Figure 7, transverse (7a) and longitudinal (7b) cross-sections of an MgB_2 powder-in-tube (PIT) wire made by Hyper Tech Research, Inc. (HTR) [82], highlights this effect.

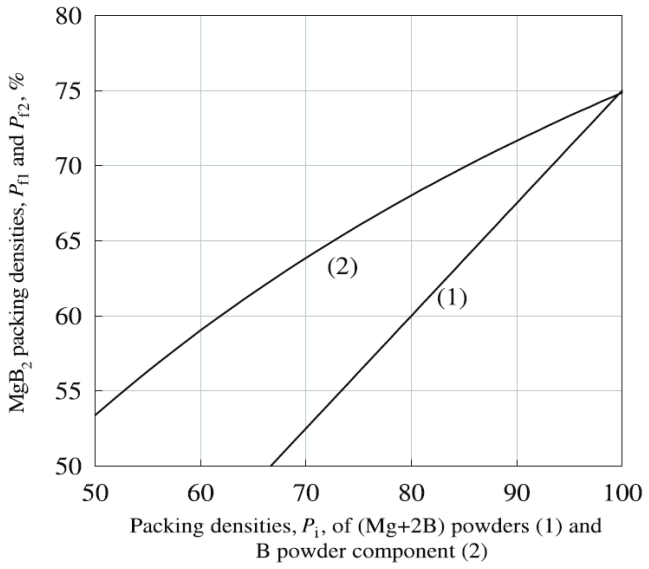

Figure 6. Packing density of MgB_2 formed from equi-sized Mg and B particles (1) and formed from large Mg particles imbedded in fine B powder (2), after [5] (with permission from IOP publishing).

MgB_2 superconducting wires can be produced via several different methods. For the sake of brevity only two will be mentioned here: powder-in-tube (PIT) and internal magnesium diffusion (IMD). Either *in-situ* or *ex-situ* powders can be used with the former method. Powders are packed into a tube that is non-reactive with MgB_2, Mg, or B; Nb and Fe constitute the majority of materials chosen in the literature, although Fe has been seen to form a reaction layer after HT [83]. This Mg + B or MgB_2-filled tube is then either i) drawn to a smaller diameter such that an array of these powder-filled tubes can be stacked in an electrically conductive (for stability purposes) outer tube, typically Monel or another Cu alloy, and then drawn to a final wire diameter; or ii) directly placed in the Monel or Cu tube and then drawn to a final diameter. The resulting monofilament wire is low cost and useful for experimentation. A variant of the PIT process is HTR's

continuous tube forming and filling (CTFF) Process, where powder is poured from a hopper onto a Nb or Fe strip which is then folded into a tube. In any variant of the PIT process, the final wire is shaped or wound to a form suitable for its final application. The wire is heat treated to form the MgB_2 core either before winding (as in "react-and-wind") or after winding (as in "wind-and-react") [27], [84].

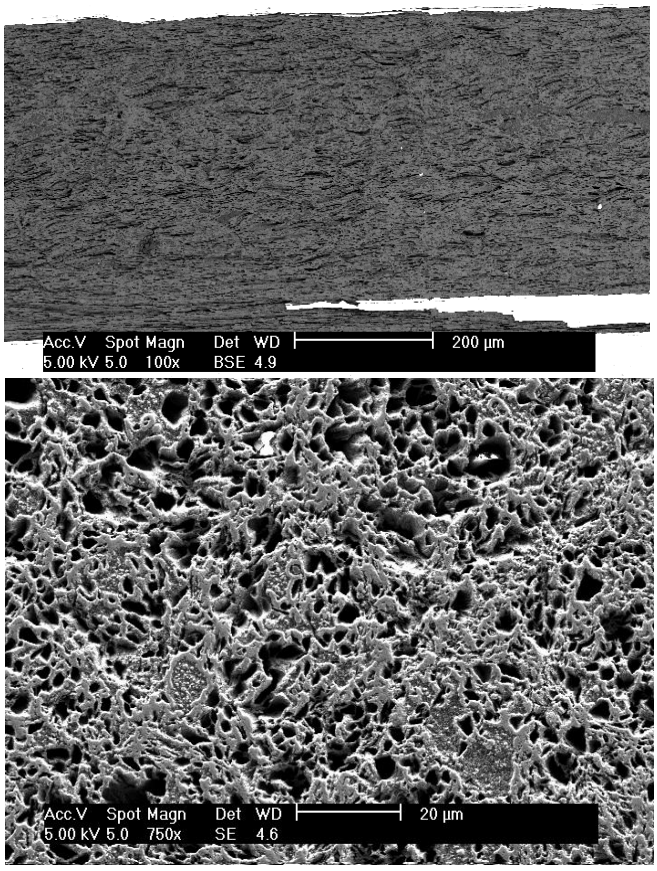

Figure 7. a) longitudinal cross-section of an MgB_2 wire (BSE SEM, Exp. 1391 HT 700°C 6 hrs.); b) transverse cross-section of the same MgB_2 wire (SE SEM). Both micrographs show a significant quantity of porosity in the prior Mg particle locations.

The IMD process, on the other hand, is not based on either *ex-situ* MgB_2 or *in-situ* Mg+B powders; instead an Mg rod is inserted into a pack of B powder in a Nb or Fe tube. This Mg rod/ B powder assembly is then drawn down to wire and heat-treated at temperatures ranging from 600°C to 900°C, leaving a dense MgB_2 ring surrounding a large cylindrical void where the Mg rod was previously located. A disadvantage of this technique is that by eliminating most of the porosity in the MgB_2, strain tolerance is severely reduced, making handling of the reacted wire difficult. Figure 8 shows a reacted IMD monofilamentary MgB_2 wire with a dense MgB_2 reaction layer and the central large void.

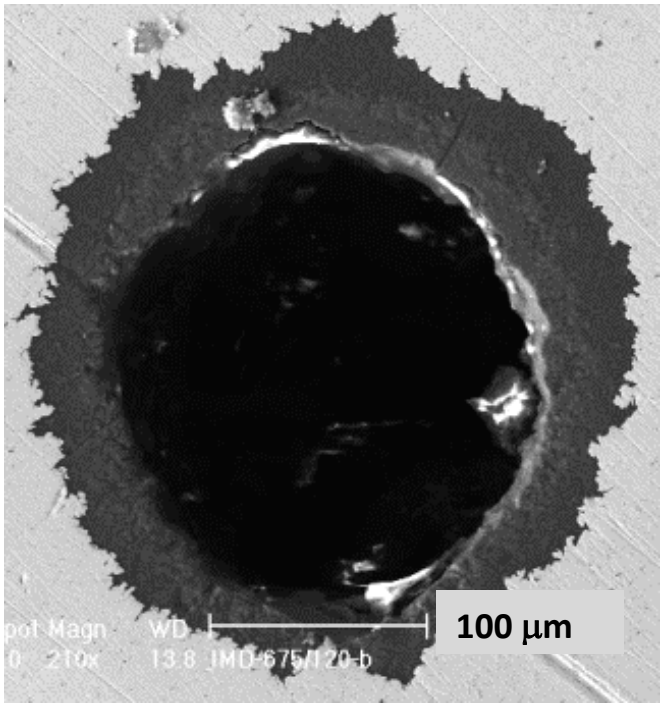

Figure 8. Reacted monofilamentary internal Mg diffusion (IMD) MgB_2 wire showing dense MgB_2 reaction layer and large void where the Mg rod was located before heat-treatment[2].

[2] This image was taken by Guangze Li

When reacting Mg+B powders or PIT wires, the formation of MgB_2 is largely dependent on the initial powder size. Smaller powders, particularly the large surface area-to-volume amorphous B powders, are usually preferred because their relatively open structure allows for easy Mg transport, allowing MgB_2 to form below the melting point of Mg (650^{o}C) [60], presumably facilitated by the high vapor pressure of Mg (21 Pa at 527^{o}C, 1430 Pa at 727^{o}C, and 54 kPa at 1027^{o}C) [85] . Indeed, it has been shown that the reaction to MgB_2 using amorphous B as a precursor powder is nearly complete by 650^{o}C [60]. However, the large surface area of these fine powders also increases the likelihood of oxide formation on exposed surfaces when exposed to air.

1.7 MgB_2 Synthesis Techniques: Thin Films

MgB_2 thin films can be produced using a variety of techniques; however, most reports use some variation of one of three techniques: i) Hybrid Physical Chemical Vapor Deposition (HPCVD), ii) reactive evaporation, or iii) Pulsed Laser Deposition (PLD). In general, MgB_2 thin film growth is made difficult by the divergent melting points and vapor pressures of Mg and B, necessitating novel techniques and approaches [86].

HPCVD is a technique that uses H_2 and B_2H_6 gas together with a substrate (most often 4H- or 6H-SiC) heated to ~700-800^{o}C [86–88]. The Mg-rich atmosphere is created by the physical melting of high purity Mg metal using an induction coil. The films produced via this method are limited in size only by the dimensions of the thermal hot

zone. These ~100- 800 nm films are epitaxial with respect to the substrate (with an orientation relationship of $(0001)\left[11\bar{2}0\right]_{MgB_2} \| (0001)\left[11\bar{2}0\right]_{SiC}$), and T_cs ~41 K (the increase above 40 K is likely an effect of tension induced from the ~0.2% lattice mismatch between SiC and MgB_2) [88]. Unfortunately this technique does not easily lend itself to adding artificial flux pinning centers or dopants, although metalorganic magnesium precursors such as bis(methylcyclopentadienyl)magnesium can be added to the carrier gas for C-doping [49]. 4.2 K transport J_c is typically ~10^6-10^7 A/cm^2 at 0 T and, with C-addition, 10^5 A/cm^2 at 9 T.

Reactive evaporation, developed by Moeckly *et al.* [89], involves e-beam evaporation of B onto a heated substrate (typically Al_2O_3). The substrate platform is rotated at several hundred rpm through a semi-sealed heated chamber containing Mg. These c-axis oriented ~100-500 nm films are extremely smooth with RMS surface roughness values of 1-5 nm and grains of ~100-200 nm [89]. Values of T_c are ~39 K. Again, although this process is ideal for producing homogeneous MgB_2 films, any chemical modification would have to be made to the starting B target or the Mg vapor. However, increased flux pinning (as investigated through microwave radiation) has been introduced to these films via ion-radiation induced defects [90].

Pulsed laser deposition, or PLD, has been used by numerous groups to make MgB_2 thin films. PLD is advantageous in that pinning centers or dopants can be easily added to the film through either modification of the target or sequential ablation of multiple targets of different materials, as is common with the synthesis of HTS YBCO thin films [91]. However, PLD-fabricated MgB_2 thin films invariably require post-

annealing in a Mg-rich environment, either by i) applying a Mg cap layer and annealing *in-situ* in the PLD chamber or ii) applying a protective cap layer (usually Mg), removing the sample from the chamber, sealing it in a vessel with Mg, and then annealing it. PLD thin films also vary in composition, microstructure, and superconducting properties based on the type of target used. For even deposition with a minimum of splashing of large particles from the target surface, a dense MgB_2 target is required. The composition of these targets has varied from pure B [92], sintered commercially available MgB_2 powder, and MgB_2 bulks prepared via a variety of techniques. Additionally, MgB_2 films have been prepared off-axis [93] (that is, where the surface normal is perpendicular to the plasma plume so as to provide for smoother films by reducing the likelihood of impacts from large particulates ejected from the target surface). Superconducting properties from these films vary widely in the literature. *In-situ* annealing provides for the least chance of contamination as the sample is never exposed to O_2 or H_2O through opening the chamber. Nevertheless, the highest T_c seen in the literature for *in-situ* processed MgB_2 thin films is ~35 K. The reasons for this degradation are not entirely clear, though oxygen contamination and the small grain size seen in these films have been cited as contributing factors [94]. The latter process, whereby the thin film in annealed *ex-situ*, produces MgB_2 with a T_c ~39 K. However, the *ex-situ* method also produces a distribution of grains that are randomly oriented compared to the smaller, more rounded, and c-axis oriented grains seen in the *in-situ* HT [95]. Also, the increased grain boundary area in the *in-situ* annealed samples serves to increase the flux pinning density, allowing the J_c to exceed 10^6 A/cm^2 at 6 T.

1.8 Inter-Grain Elecrtrical Connectivity in MgB_2

Soon after the discovery of superconductivity in MgB_2, Klie *et al.* [96] produced bulk samples using the *in-situ* method (solid state reaction between Mg and B) and were one of the first groups to try to determine structure-property relationships in MgB_2 based on the effects of second phases. Electron energy loss spectroscopy (EELS) was used to map the composition of the small grained MgB_2. Klie *et al.* noted that two types of oxides were present, the first being a BO_x phase on the order of ~2 nm that appeared to be present at every grain boundary. The second was an insulating MgO phase on the order of ~10 nm sometimes present between the BO_x phases. The BO_x phase has a width much smaller than the coherence length of MgB_2 ($\xi_{ab}(0)$=3.7-12 nm [46]), suggesting that the BO_x second phase is transparent to current. The addition of the MgO phase, however, creates an insulating layer that blocks current. Within the grains no oxygen was found to be present. It is assumed that the oxide phases were formed during synthesis.

Later work by Birajdar *et al.* [97] noted that both the J_cs and resistivities of MgB_2 samples in the literature varied by orders of magnitude after having been prepared by ostensibly the same methods. An attempt was made to extract such parameters as grain size, colony (dense arrangement of grains) size, oxygen at%, and overall fraction of B-rich secondary phases in a series of MgB_2 samples. Both *in-situ* and *ex-situ* tape, wire, and bulk specimens were analyzed using a variety of quantitative electron microscopy techniques, including, but not limited to, STEM-EDS and ESI chemical mapping. In the

in-situ specimens the presence of non superconducting B-rich phases (MgB_4, MgB_7) was noted at the center of the grains, as was the presence of MgO at grain boundaries, voids, and cracks. However, the initial Mg and B ratio was set to be 1:2. With the vapor pressure of Mg being so high, most experimenters choose to add a slight excess quantity of Mg to make up for any deficiency that may result from reacting at higher *T*. The lack of this precaution could explain why B-rich phases are present in these samples. Curiously, even though both Klie *et al.* [96] and Birajdar *et al.* [97] used the same techniques on the same types of samples to obtain their respective images, Birajdar noted no BO_x compounds in his analysis. It has been suggested by Jiang *et al.* [75] that the starting purity of the B powder, particularly the presence of B_2O_3, may have an effect on the final oxide content of the bulk.

Using XRD analysis on a series of thin film specimens, Yates *et al.* [98] found that MgO was present after initial MgB_2 formation. After annealing the samples at 400°C for various times, Yates found evidence for MgO and $Mg_3(BO_3)_2$ or $Mg_2(B_2O_5)$; the latter two products eventually degrading into MgO and B_2O_3 after a period of several days. Unfortunately, no microscopy was performed to determine the size and location of these precipitates; however resistivity measurements showed that longer annealing times (and coinciding higher oxide contents) yielded larger resistivities.

Rowell [79][99] has noted that specimens with a higher oxide content also exhibit higher normal-state resistivities. He hypothesized that if the high resistivities seen in MgB_2 are a result of a lack of connectivity between MgB_2 grains (whether as a result of insulating oxide layers or porosity), then this reduction in effective cross-sectional area

should also be reflected in J_cs obtained from the specimens. To this end he established the relationship:

$$\rho_m(T) = F[\rho_0 + \rho_i(T)] \tag{2}$$

where the left-hand term represents the measured resistivity and ρ_0 and $\rho_i(T)$ represent the residual and phononic resistivities, respectively. F^{-1} represents the relative cross-sectional area for current transport and would be equal to unity for an ideal single crystal. Taking the ratio of the published data from Eltsev [100] to that of a series of data from the literature, Rowell obtained the general expression:

$$F = \frac{\Delta\rho_m\left(300K - 50K\right)}{4.3} \tag{3}$$

in which the value 4.3 represents the $\Delta\rho$ from 300 K to 50 K (in μΩ-cm, thus preserving the unitlessness of F) for an average of three of Eltsev's undoped crystals. Figure 9, taken from Matsushita's [101] use of Rowell's analysis on a series of undoped bulk samples prepared with different heat treatments and packing densities, correlates the values of connectivity with the J_cs those samples achieved (at 0T, 20 K). As can be discerned, the overall connectivity plays a very large role in the final transport properties of the material. Implicit in any analysis using Equation 3 is the assumption that the value 4.3 is a constant for all MgB_2 samples. However, the same group that published the data for the undoped single crystal [100] also published results [102] that show this value can be in excess of 11 μΩ-cm for heavily C-doped single crystals.

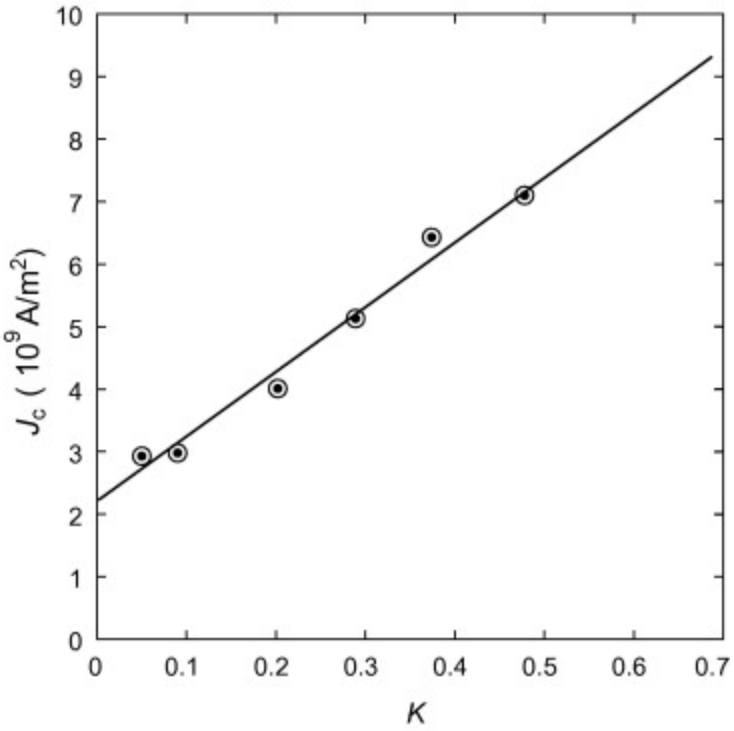

Figure 9. 20 K, 0 T J_c as a function of connectivity, after [101] (with permission from Elsevier).

It has been shown [103] that the insulating oxide layers located on the outside of grains or grain clusters can serve to reduce the super-current carrying ability of MgB_2 wires. As a result of the wire drawing process the well-connected regions were heavily aspected. This geometrical anisotropy was credited with causing connectivity anisotropy, in essence creating two different types of current paths: well connected paths along the length of the wire and poorly connected paths across itse. This topic will be covered in more detail in Chapter 3.

1.9 Doping in MgB_2

One of the most important functions of a superconducting material is an ability to remain in the superconducting state in the presence of high magnetic fields. In other words, it must have a high upper critical fields, B_{c2}. With its two superconducting bands, MgB_2 presentes an opportunity for tuning each band to control the B_{c2}. In the so-called "dirty limit" where $B_{c2}(0\ \mathrm{K})=3.06\rho_0\gamma_v T_c$ [104] (in which T_c is the critical transition temperature, γ_v is the electronic specific heat coefficient per unit volume, and ρ_0 is the residual resistivity) as the value of ρ_0 is increased, the charge-carrier scattering is also increased, thereby reducing the coherence length and increasing the total amount of flux that may be present in the mixed state [105]. According to Gurevich [106], it is seen that near T_c,

$$B_{c2 near T_c} \propto \frac{1}{\lambda_{ep,1} D_\sigma + \lambda_{ep,2} D_\pi} \tag{4}$$

where λ_{ep} represents the appropriate respective intraband electron-phonon coupling constant and the Ds represents the charge-carrier diffusivites ($1/\rho_0=e^2 N_F D$) of both the σ and π bands. At low T, it is seen that

$$B_{c2}(0K) \propto \frac{1}{\sqrt{D_\sigma D_\pi}} \tag{5}$$

Simply interpreted, Equations 4 and 5 indicate that in order to increase B_{c2} near T_c to any significant degree, it is necessary to induce scattering in both bands. However, at

low *T*, one only needs to induce scattering in one or the other of the two bands to increase B_{c2}.

Substitution of an element onto the B site (such as C [107]) or a Mg site (Na [108], Zr [109],[110], Al [111], Ca [112], Mn [113], and Pb [114]) brings about changes in the electronic structure of the material and also produces lattice distortions. The result is an increase in ρ_0 and, as a consequence, B_{irr} and B_{c2}. However, some of the recently reported results are contradictory and ambiguous. For example, Bhatia *et al.* [109] reported, with a 7.5 mol% addition of ZrB_2, a noticeable shift in both *a* and *c* lattice parameters that was concomitant with an increase of 4.2 K B_{c2} of ~8 T. However, Zhang *et al.* [110] saw no such shift and no real evidence of improved B_{c2} with ~10 mol% ZrB_2 addition. A significant increase in high-field F_p is noted, especially at higher *T* (20 K), implying that the ZrB_2 acts not as a vector for Zr substitution but as a pinning center. The discrepancy between these two reports highlights the question of how ZrB_2 additions affect the properties of MgB_2: specifically, does Zr substitute for Mg and provide uniform strain or does ZrB_2 act as a pinning center? It should be noted that samples were heat treated differently, with Zhang *et al*. heat treating their sample at 800^{o}C for 1 hr. and Bhatia *et al.* heat treating their sample at 700^{o}C for 30 mins. Additionally, the size and purity of the starting ZrB_2 powder is never mentioned by Bhatia *et al.*, leaving open the possibility that the differences between the two experimental results could be due to kinetics as a result of initial powder size.

Although substitution on both the Mg and B sites is possible, it has been suggested that scattering may be induced in *both* bands by substitution of C into the B

site [5]. Therefore, C-substitution has been the most efficient and most widely researched method of increasing the critical fields in MgB_2. However, given the small amount of dopant introduced, assuring uniformity and homogeneity of C-substitution is difficult.

In work by Birajdar *et al.* [97], energy-loss spectroscopy imaging was used to identify the composition of second phases in undoped MgB_2. In addition to these undoped samples, additional samples were investigated using SiC as a vector for C-substitution and as a method of adding additional pinning centers. Energy-loss spectroscopy images showed an inhomogeneous distribution of C and O throughout the sample, with O seeming to accumulate at the grain boundaries and C randomly distributed. Additionally, the presence of MgB_4 and MgB_7 second phases likely serve to skew the composition profile.

S. Lee *et al.* [102] produced a series of C-doped single crystal MgB_2 specimens, showing a monotonic decrease in T_c with C addition. If one assumes that the C distribution in C-substituted MgB_2 is concentrated around the presence of prior SiC particles (or for that matter, any C-source) and is therefore not entirely homogeneous, one can also assume that T_c also varies throughout the sample. This variation in T_c can be used to estimate the overall homogeneity of the superconductor in question.

1.10 Specific Heat to Determine Doping Homogeneity

In the solid state at low temperatures the specific heat, *C*, at constant pressure is

equal to the specific heat at constant volume; it can be expressed in terms of entropy, *S*, as [115]:

$$C = T\left(\frac{\partial S}{\partial T}\right) \tag{6}$$

Because superconductivity is an ordered state that experiences a decrease in entropy in the superconducting regime, in a normal state/superconducting transition the specific heat experiences a jump, referred to as the specific heat anomaly, at T_c. The specific heat measurement is ideal for investigating the homogeneity of a superconducting specimen because it is a measurement over the entirety of the sample. Magnetic and resistive techniques may only probe parts of the sample; the latter measurement, for example, follows only a "path of least resistance" [116].

To study a similar phenomenon in superconducting Ti alloys, Bucher *et al.* [117] and later Junod *et al.* [118] studied a variety of A15 superconducting compounds and measured their heat capacities to distinguish between homogeneous and non homogeneous transitions. When approaching T_c, although the specimens exhibited a complete diamagnetic transition, a reduced calorimetric anomaly, $C_{es,r}$ was observed. This "transition smearing" was discussed in terms of a distribution ideal specific heat transitions, C_{es}, each with its own value of T_c:

$$C_{es,r} = \int_{T}^{T_{c,\max}} C_{es}(T, T_c)\, f(T_c)\, dT_c \tag{7}$$

where $f(T_c)$ represents the fraction of the superconductor having a specific value of T_c. Normalization requires the integral of the distribution function over all T_c to be unity. The

lattice specific heat was eliminated by subtracting the high-field normal state specific heat measurement from the zero-field value. The ideal form of the superconducting specific heat anomaly, C_{es}, can be quantified by the Gorter-Casimer two-fluid model [119]:

$$C_{es}(T,T_c) = \frac{3\gamma_e T^3}{T_c^2} \tag{8}$$

where γ_e represents the Sommerfeld constant, or electronic specific heat coefficient, of the material in question [120]. Since at low temperatures ($T < \sim\theta_D/12$ [116]) the total specific heat can be modeled as $C = \gamma_e T + \beta_3 T^3$, where the first term on the right hand side of the equation represents the electronic component of the specific heat and the second term represents the lattice (phononic) component (where β_3 is the lattice specific heat coefficient). The terms γ_e and β_3 can be solved through analysis of the plot T^2 vs. C/T, where they can be elucidated by the intercept and slope, respectively [121].

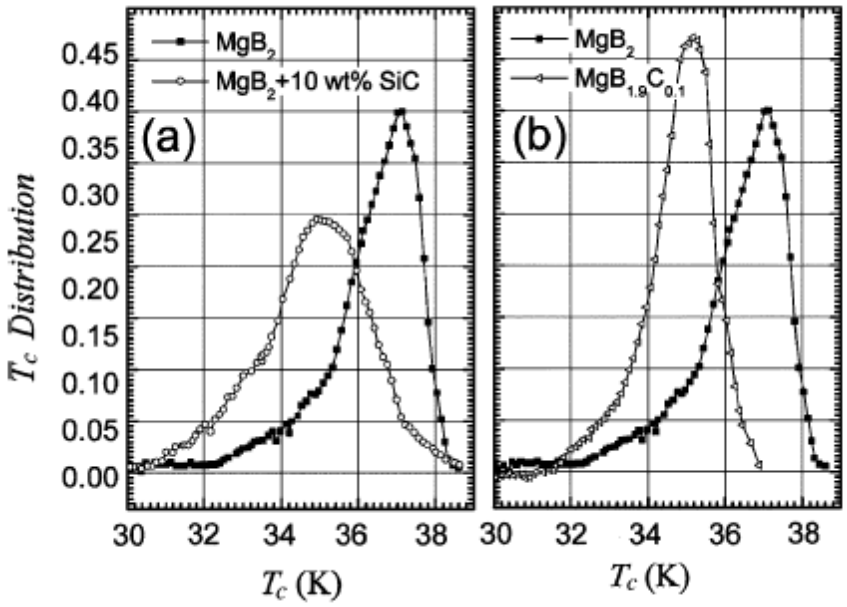

Figure 10. T_c distribution in C-doped MgB_2 samples, after [122] (with permission from IEEE publishing).

Wang *et al.* [123], followed by Senatore *et al.* [122],[124] used a similar approach to determine the T_c distribution of Nb_3Sn and MgB_2 wires. The results for Senatore's analysis [122] of MgB_2 T_c distribution are given in Figure 10. These C-doped MgB_2 samples were sintered at 800°C for 30 minutes. The most interesting result is the comparison between different methods of C-doping where the addition of SiC as a source of C yields a much wider distribution than nano-C powder. Presumably this increase in inhomogeneity is a result of either Mg_2Si left behind from the Mg+SiC reaction [5] or as a result of a more uniform dispersion of C, as has been reported in other sources [125]. Senatore and Flükiger later [126] noted that at lower sintering temperatures and times, the distribution of T_c was much wider (with T_cs as low as ~10 K included in the distribution)

which they attributed to strain effects causing increased scattering. However, whether the increase in the distribution of T_c is a result of lattice strain or is a function of inhomogeneous C substitution is an open question. In addition, Senatore's method forces a modification to the Gorter-Casimir model such that the temperature exponent "3" in the numerator is altered so that the distribution is forced to unity. The physical interpretation of this variation is left unanswered.

Surprisingly, with the plethora of published studies in the literature on doping MgB_2, there is a dearth of information on the effects of these additions on the T_c, in terms of optimizing the HT schedules for the most homogeneous properties. Instead, most literature has focused on investigations into changes in the transport J_c, F_p, and T_c measured through magnetic or resistive techniques (where only the best current paths are probed). Sometimes, the changes in lattice parameter through XRD analyses are also reported.

1.11 Flux Pinning in MgB_2

One of the most important properties of a Type II superconductor[3] is the ability to pin fluxons in the mixed state. In a Type II superconductor when a magnetic field of a certain strength is applied full flux exclusion from the bulk ceases and it becomes more

[3] A Type I superconductor is defined as a material that cannot be penetrated by a magnetic field until the point where a field B_c is applid such that superconductivity is no longer present. In a Type II superconductor, it is energetically favorable to maximize the superconducting-normal state boundary, leading to the presence of flux vortices (each with a value of $\phi_0=h/2e$) arranged in a hexagonal lattice (called the Abrisokov lattice) above a lower critical field B_{c1}. This is referred to as the Shubnikov or mixed state. At higher magnetic fields the vortex spacing d decreses as $d(\text{nm}) = 1.072\text{x}10^9\ (\phi_0/\text{B})^{½}$. Superconductivity ceases to exist at the upper critical field B_{c2} [127].

energetically favourable to maximize the normal-superconducting interface area. It is from this condition that the we get a mixed state containing individual fluxons, each with the value of 2.068 x 10^{-15} Wb (ϕ_0) and a normal core of radius ξ, the coherence length. A repulsive interaction exists between these fluxons, which is supported by the circulating supercurrent that is required to produce a magnetic flux equal to ϕ_0.

The flux pinning force is defined as $-\vec{F}_p = \vec{J}_c \times \vec{B}$ and may be interpreted as the critical current J_c at a magnetic field B which allows the Lorentz force to be balanced by a pinning force (per unit volume) F_p [78]. Without the presence of flux pinning, the Lorentz force acting upon a fluxon would cause it move, inducing a Bardeen-Stephen flux flow resistance [128].

In a superconductor, the volumetric magnetic free energy is lowered when in an applied magnetic field by $-\frac{1}{2}\mu_0 H^2$ [129]. Taking a small spherical normal state precipitate of diameter d, the overall energy of the system is increased by $(4/3\ \pi\ (d/2)^3)(\frac{1}{2}\mu_0 H^2)$. If, however, the fluxon (whose normal state core has radius ξ) were to be superimposed on the normal precipitate, then the total energy of the system would be lowered by $\sim(\pi\xi^2 d)(\frac{1}{2}\mu_0 H^2)$. This reduction of energy is the essence of flux pinning. The pinning force then is the spatial derivitive of the potential well formed by this interaction [130] and is overcome when it is surpassed by the Lorentz force produced by a certain current at a certain magnetic field. The pinning interaction may therefore be caused by any non-superconducting region of the specimen, including normal-state precipitates, voids, and grain boundaries. This is what is conventionally referred to as normal pinning.

Another type of pinning mechanism, $\Delta\kappa$ pinning, occurs when two separate

superconducting regions are present in the same specimen. One can imagine this situation occurring in a superconducting alloy where variations in composition yield variations in κ. Regions with smaller values of κ will then have a higher value of ξ; hence the fluxons will be attracted to these regions such that the volumetric free energy og the system be be lowered[4]. $\Delta\kappa$ pinning has been seen to occur in superconducting materials exhibiting variations in normal state resistivity due to changes in composition or the presence of a non-uniform distribution of dislocations [78], [132], [133].

Fluxon spacing goes as $d(\text{nm}) = 1.072\text{x}10^9 (\phi_0/B)^{½}$ [134]. At magnetic fields just above the lower critical field, B_{c1}, their spacing and quantity is such that repulsions between them are considered to be very small. As a result one can assume, as Campbell and Evetts did [135], that the fluxons will all interact with pinning centers until the number of fluxons equals the number of pinning centers. The total pinning force of the sample is then the sum of the individual pinning forces. This model is known as direct summation and is noted by a linear relationship between B and F_p.

The summation of the pinning energy is complicated at higher magnetic fields, where the number of fluxons has increased and the effect of their mutual repulsion must now be considered. The literature provides two models, of which the most applicable will be considered: the flux line shear model.

The flux line shear model, first proposed by Labusch [136], assumes that the mutual repulsion between fluxons which result in the Abrikosov lattice can be modeled as a rigid 2-D elastic solid, where the competing forces are the Lorentz force supplied by

[4] κ being defined as $0.957\lambda/\xi$ in the "clean limit" and $0.72\ l/\xi$ in the so-called "dirty limit" (where l is the electronic mean free path , λ is the magnetic penetration depth, and ξ is the coherence length) [131].

the current and the pinning force supplied by the pinning centers. As the current (and hence the Lorentz force) is increased, the Abrikosov lattice elasically distorts until either the lattice as a whole breaks free and starts to move or the interfluxon forces are overcome in such a way that the lattice fragments [130].

Approximating the flux line lattice as a 2-D crystal (here the reference frame is set so that the z-axis coincides with the length of the fluxon), the relevent stiffness matrix can be expressed as [137]:

$$\begin{bmatrix} \sigma_{xx} \\ \sigma_{yy} \\ \sigma_{yz} \\ \sigma_{xz} \\ \sigma_{xy} \end{bmatrix} = \begin{bmatrix} C_{11} & C_{12} & 0 & 0 & 0 \\ C_{12} & C_{11} & 0 & 0 & 0 \\ 0 & 0 & C_{44} & 0 & 0 \\ 0 & 0 & 0 & C_{44} & 0 \\ 0 & 0 & 0 & 0 & C_{66} \end{bmatrix} \begin{bmatrix} \varepsilon_{xx} \\ \varepsilon_{yy} \\ \varepsilon_{yz} \\ \varepsilon_{xz} \\ \varepsilon_{xy} \end{bmatrix} \tag{9}$$

Considering displacements in the z-direction yields the conclusion that these forces cannot depend on the ε_{zz} term since line tension is independent of length. Therefore the third column and third row of c_{ij} is zero [135]. Here $C_{12}=C_{11}-2C_{66}$, leaving three independent terms:

$$C_{11} \approx C_{44} \approx \frac{H^2}{4\pi} \tag{10}$$

$$C_{66} \propto \left(1-\frac{H}{H_{c2}}\right)^2 \tag{11}$$

where C_{11} is the elastic modulus in the plane normal to the flux line axes (a measure of the stiffness of the fluxon lattice due to fluxoid repulsion), C_{44} is the elastic tilt modulus

(describing the bending of flux lines along along their axes), and C_{66} is the shear modulus (describing the resistance of the fluxon lattice to the shear of fluxoids past each other) [130]. Since the assumption is made that there are more fluxons than pinning centers, the overall picture for the flux shear model holds that some flux lines are strongly held in place by strong pinning centers; the reminder are held in place by the mutual repulsion between fluxons. As can probably be surmised from the name of the model, the flux line shear model assumes that at a large enough current density, the Lorentz force is larger than what can be supported by the shear modulus, meaning that fluxons flow; hence critical current density is determined by the C_{66} term [138]. As can be ascertained from Equations 12 and 13, as the value of the magnetic field increases, the stiffness in bending and compression also increases, whereas the value of the C_{66} term steadily decreases.

The original flux line shear model proposed by Labusch [136] and later Fietz and Webb [139] assumed that pinning centers were smaller than the fluxon lattice spacing in every dimension. Later, Campbell and Evetts [135] and Kramer [140] extended the treatment to 2-D phenomena such as dislocations and grain boundaries. Finally, Dew-Hughes [78] further extended the theory to cover every possible size scenario by assuming that the pinning center could be larger larger than the fluxon lattice spacing in every dimension. Dew-Hughes [78] summarizes all of the preceding conditions, where he characterizes the pinning interactions in terms of: i) type of pinning mechanism, $\Delta\kappa$ or normal; ii) the size of the pinning center compared to the fluxon lattice spacing; and iii) the stiffness of the fluxon lattice. The important bulk pinning force functions from the Dew-Hughes model (at least as they apply to MgB_2) are:

$$F_p \propto b^{1/2}(1-b)^2 \qquad \text{Surface (grain boundary) pinning, normal} \quad (12)$$

$$F_p \propto b(1-b)^2 \qquad \text{Point pinning, normal} \quad (13)$$

To qualify as surface pinning the pinning center is smaller than *d*, the fluxon lattice spacing in 2 dimensions (as with grain boundaries); point pinning meets this criterion for 3 dimensions. The term b[5] is simply equal to B/B_{c2}[6]. The plots of the normalized functional forms of all six pinning mechanisms proposed by Dew-Hughes are presented in Figure 11.

As pointed out in later works by Brandt [143] and Dew-Hughes himself [144], the C_{66} stiffness term is only really valid at high fields (i.e, as $b \rightarrow 1$). Nevertheless, numerous authors [145–147] have shown that experimental data (e.g. from intermetallic Nb_3Sn) fit this model well over a wide field range

The grain boundary pinning model derived by Kramer and Dew-Hughes more or less fits the experimental F_p vs. B data for MgB_2, as has been repeatedly demonstrated in the literature [4],[103]. However, important features seemingly unique to MgB_2 are noted; on a plot of F_p vs. b (or, more often, $F_p/F_{p,max}$ vs. b) as $b \rightarrow 1$ the flux pinning curve smears out or has a "tail." Figure 12 represents one of the earliest works to point out this phenomenon [4]. Here, Figure 12a shows what is commonly referred to as a "Kramer

[5] Technically speaking, these equations were developed for NbTi and Nb_3Sn superconductors where no real difference is exhibited between B_{irr} (the magnetic field at which J_c is 0) and B_{c2} (the magnetic field at which superconductivity is no longer present and the coherence length ξ goes to infinity). In MgB_2 there is a quantifiable difference between these two values [141]. As a result, it would be more correct to use B_{irr} in the normalization for B ($b=B/B_{irr}$) for the term inside the parentheses of Equations 12 and 13. The normalization outside the parentheses is based on thermodynamic considerations from the original Dew-Hughes derivation [78] and thus should always be normalized by B_{c2}.

[6] Henceforth B will describe the magnetic field and will be referred to as "magnetic field" rather than "magnetic flux density" for the sake of simplicity. Since the magnetic fields of interest (both within and outside the superconducting material) are generated by macroscopic currents, there is no need to distinguish between H and B [142].

Plot" which is simply a geometric re-interpretation of the grain boundary pinning function where the ordinate is $J_c^{0.5}B^{0.25}$ and the abscissa is B. A linear $J_c^{0.5}B^{0.25}$ implies grain boundary pinning. The x-intercept is usually taken as the irreversability field, B_{irr} (denoted B_{Kramer} or B_K). While Figure 12a indeed shows a linear region, using the x-intercept of this region to determine B_{irr} causes a large underestimateion of the value of this important material parameter. This discrepancy manifests itself in two ways: i) in Figure 12a $J_c^{0.5}B^{0.25}$ is present at fields higher than B_K- an unphysical result; ii) for the same reason, in Figure 12b F_p remains non-zero for some range of $b>1$. Additionally, the Kramer plots in Figure 12a show the beginnings of a "hook" at low fields, another deviation from linearity. Larbalestier *et al.* (the authors of the figure) make no attempt to explain this phenomenon.

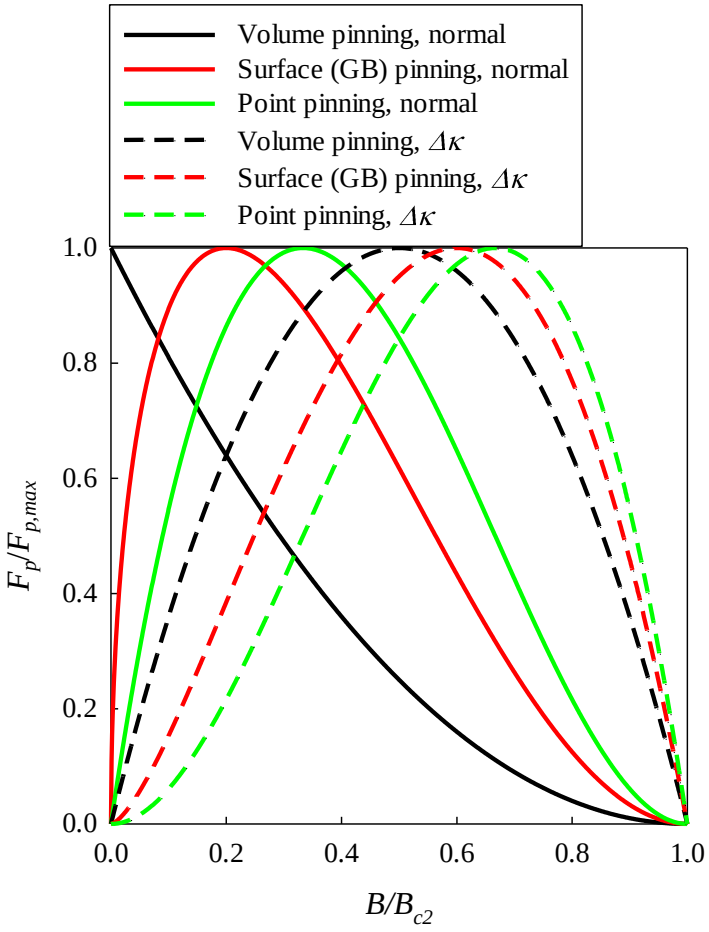

Figure 11. Normalized F_p vs. b for various pinning types (volume, surface, and point) for normal and $\Delta\kappa$ pinning.

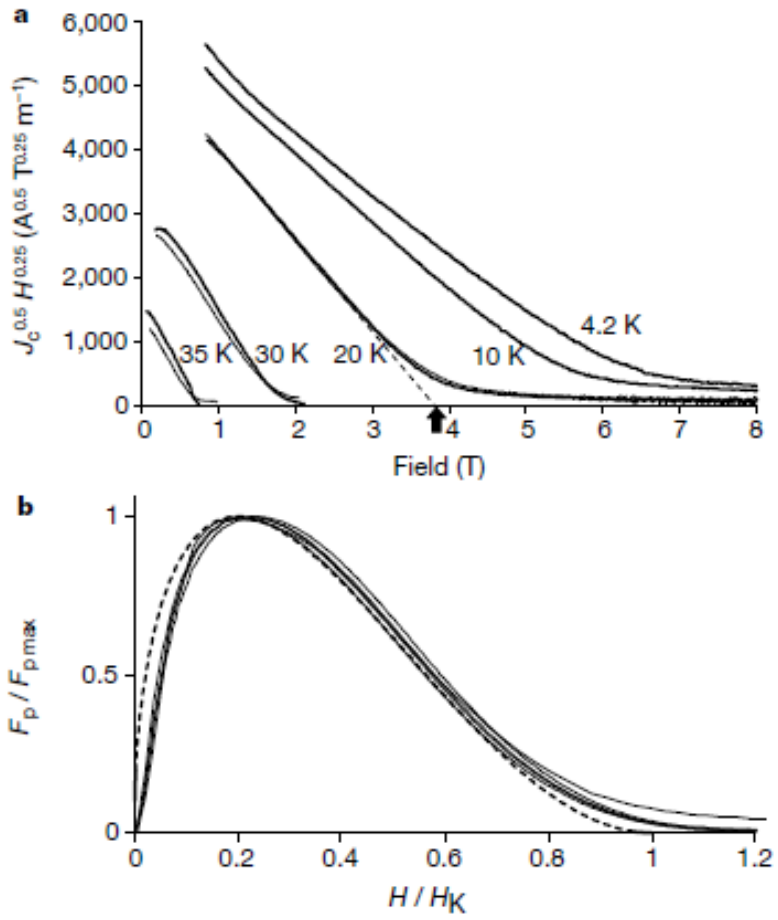

Figure 12. a) Kramer plot showing "tail" at high fields and "hook" at low fields (for higher T data; b) $F_p/F_{p,max}$ vs. B/B_{Kramer} showing deviation from Kramer function at high fields, after [4] (with permission from Nature Publishing).

Differing interpretations of the deviations from Kramer have been made in the literature. Larbalestier *et al.* [4] initially suggested that the tail of the Kramer plot could be due to a second low-J_c phase (e.g. an inhomogeneity). Bhatia [148] suggested that the effect is due to the additive effects of two different pinning functions- grain boundary and volume pinning (the latter a result of large normal state regions that were present). The

likeliest scenario requires inspection of the physics underlying the grain boundary pinning mechanism. The mechanisms described by Equations 12 and 13 assume an isotropic homogeneous superconducting material. Given that MgB_2 is anisotropic, the model is likely to be inadequate. Eisterer *et al.* [52], using percolation theory, showed that the high field tail is a result of the anisotropic nature of MgB_2.

1.12 Summary of Chapter 1

MgB_2 is a heavily studied material, responsible for more than 5000 papers published in the past decade. However, despite the large research effort, several important questions are still actively debated. First, the exact nature of this material's flux pinning is still often called into question. The irregularities in the Kramer plot are often attributed to effects that are unrealistic rather than simply re-evaluating the underlying fundamentals of the grain boundary pinning model in terms of the anisotropic nature of MgB_2. Moreover, there are still vociferous debates about the relative influences of porosity and anisotropy on the critical current density of the material. Finally, the detailed effect of doping in MgB_2 is unresolved. Some authors have added every conceivable C-containing compound (e.g. [72], [149]) without fully investigating why these compounds alter the superconducting properties of MgB_2. Most C-containing organics are used to simply "coat" the B powder particles and are subsequently pyrolized such that only C remains after treatment; these coated powders are then mixed together with Mg and reacted to form C-doped MgB_2. Most other C-containing compounds simply decompose

or react with Mg at the reaction temperatures of MgB_2. In either case, only C is capable of chemically altering MgB_2. With this in mind, it is important to carefully assess the effects of C by adding it to MgB_2 as homogeneously as possible. Also, the substitution of Zr for Mg (specifically, whether or not it does indeed chemically substitute) is an unresolved issue and has yet to be studied in a systematic manner.

The aim of this work is then two-fold. First, to deconvolute the effects of anisotropy and porosity on the superconducting properties of MgB_2, with a specific emphasis on wires (the form of MgB_2 used for applications). Second, to determine the way in which certain dopants substitute into the Mg and B sites.

Chapter 2: Experimental Methods

The experimental techniques used for the characterization of samples included: X-ray diffraction (XRD), scanning electron microscopy (SEM), transmission electron microscopy (TEM), vibrating sample magnetometry (VSM), A.C. susceptibility, specific heat measurements, and electrical transport measurements of normal state resistivity and critical current density. The basics of the pulsed laser deposition technique will be discussed in this chapter. However, Chapter 4 will detail specifics as they relate to MgB_2 synthesis

2.1 X-Ray Diffraction

X-ray diffraction (XRD) is a versatile experimental technique that can be used for phase identification, determination of crystallographic orientation, or the determination of the lattice parameters of a material, among other applications. The underlying principle of XRD starts with a coherent X-ray beam (most often Cu K_α wavelength λ = 1.5408 A) striking a sample where it is diffracted when Bragg's Law ($n\lambda=2d\sin\theta$) for coherent scattering is satisfied. Here λ is the wavelength of the incident radiation, n is an integer, d is the interplanar spacing of a crystal, and θ is the angle of diffraction, Figure 13a.

Coherent scattering occurs when the path length ACB is an integer of the incoming wavelength.

Experiments were performed on a Rigaku SmartLab diffractometer with grazing incident diffraction (GID) in-plane and out-of-plane capability, Figure 13b. This system utilizes a Cu K_α X-ray sources (λ = 1.5406 Å) operating at a power of 2.2 kW. This instrument was located at the Rigaku Americas facility and was used for two primary reasons: i) the current lack of grazing incident diffraction capabilities at Ohio State, especially for in-plane analysis; and ii) scans of MgB_2 films using the present facilities at Ohio State (utilizing the standard Bragg-Brentano diffractometers available) were unable to be made in a timely manner before the films degraded as an effect of moisture. Rigaku's applications scientists Jianhua Li and Aya Takase assisted in data collection of the thin films.

For phase identification and the comparison of sample lattice parameters with that of the literature, the ICDD Powder Diffraction File (PDF2) data base was employed.

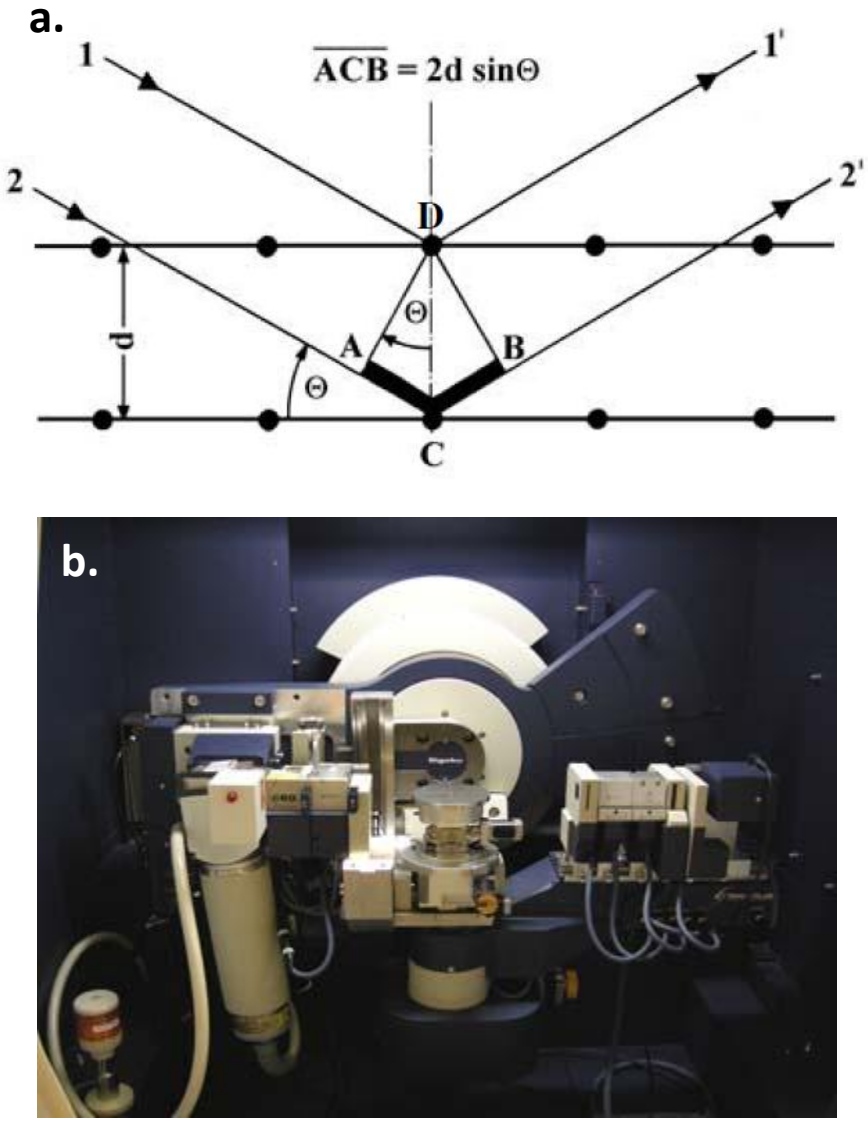

Figure 13. a) Schematic of Bragg's Law, after [150]; b) Rigaku SmartLab X-Ray Diffractometer.

2.2 Scanning Electron Microscopy

Scanning electron microscopy (SEM) is an experimental technique whereby a solid's surface is scan by a rastered beam of high energy electrons [151]. Both backscattered (BSE) and secondary (SE) electrons can be used for imaging, each technique yielding different information. X-ray emissions from interactions between the e-beam and the material can also be used for local (on the ~10 μm scale) elemental characterization in a given sample. Figure 14 gives a schematic for a typical SEM (with the exception that most CRT displays have been replaced by newer LCD technology).

Electrons are emitted from a W-filament via Schottky- type thermionic emission or field emission. The electron beam is then focused with a series of magnetic lenses. Upon interacting with the specimen, either BSE or SE electrons can be used for imaging. Secondary electrons are created by the interaction of the e-beam with electrons in the *K* orbital of the sample. These *K* orbital electrons are ejected and detected via a scintillation detector. Since SE electrons are only produced from a depth of 5-50 nm, they are primarily used for imaging surface features. BSE electrons are high energy electrons from the e-beam that are reflected via interactions with sample atoms. Heavier elements, having a higher atomic number (and hence a larger cross-section) are more likely to reflect electrons; thus, BSE electrons are more useful for imaging compositional differences (elemental *Z*-contrast) given a flat surface.

X-ray emissions produced by the interaction of the e-beam with the sample can also produce characteristic X-rays, enabling compositional analysis of the sample. The e-

beam ejects an inner-shell electron; when a higher-energy outer-shell electron fills the electron hole, X-rays are emitted from the specimen with a wavelength equivalent to the energy difference between the shells (via the relation $E=hc/\lambda$). This technique is known as energy dispersive X-ray spectroscopy (EDS). Unfortunately, this technique is not particularly useful for the study of MgB_2 itself due to: i) the low fluorescence yield of B [152]; and ii) the low value of the *K*-absorption energy of B (0.188 keV) which makes it all but (quantitatively) undetectable unless using a windowless detector [153]. However, EDS can be used for the quantitative detection and analysis of Mg, Zr, or other heavier elements.

For use in this document, both SE and BSE micrographs were taken with either a Philips (FEI) Sirion field emission source SEM or a Philips (FEI) ESEM field emission SEM. Typically, accelerating voltages of 5-30 kV were used depending on the application.

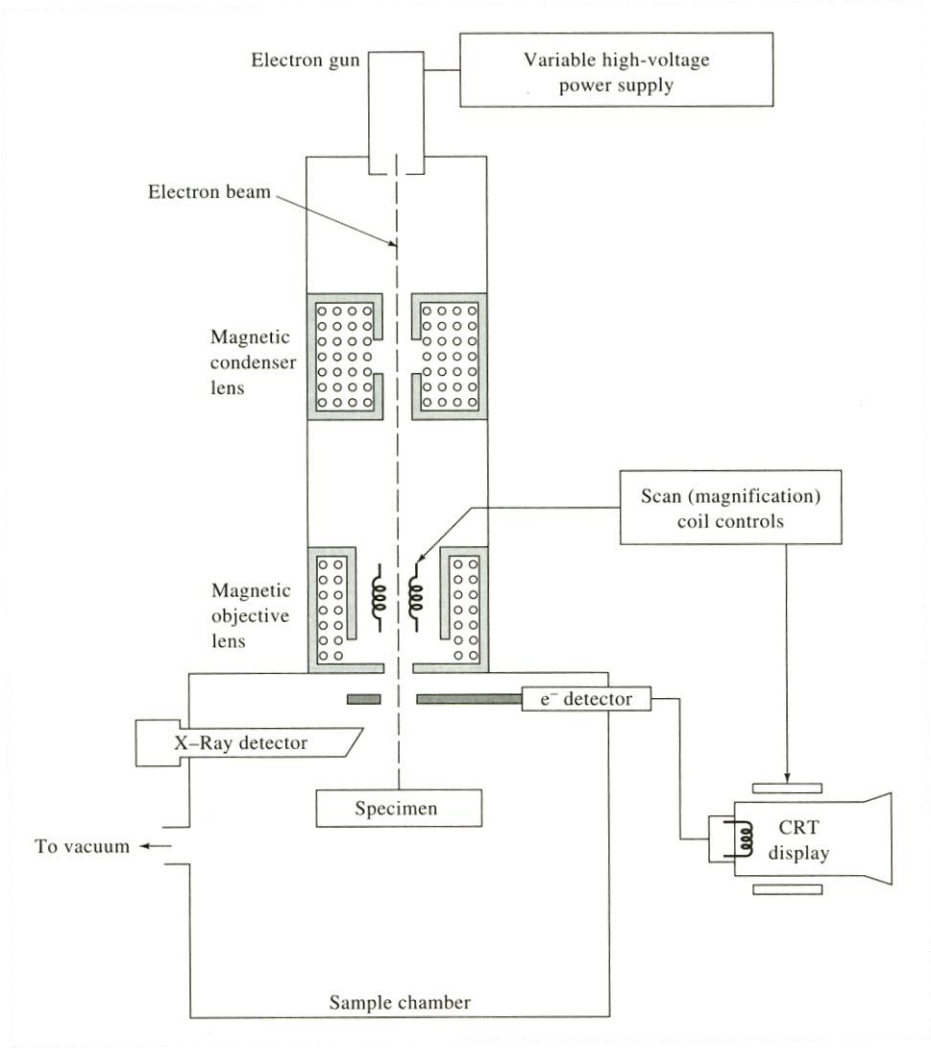

Figure 14. Schematic of typical SEM set-up, after [151] (with permission from Brooks Cole publishing).

2.3 Transmission Electron Microscopy

Transmission electron microscopy (TEM) operates on much the same principle as SEM, in that an e-beam is used to image a sample and the interaction of the e-beam with

the sample can yield important chemical information. However, in TEM much higher accelerating voltages are used (>100 kV) and the e-beam is transmitted through the sample. Multiple types of information can be extracted by performing from a TEM on a sample, including but not limited to morphology (from the sample image), structure (from the diffraction pattern obtained from diffracted electrons) and composition (from EDS detection of X-rays produced by the e-beam interacting with inner-shell electrons of the sample).

Figure 15 is a schematic diagram of a TEM. As with the SEM, the e-beam is focused with magnetic lenses. After the e-beam is transmitted through the sample both diffracted electrons and transmitted electrons are present. Depending on the type of information one wants to obtain from a TEM experiment, one selects different apertures to screen out either the diffracted or transmitted electrons, allowing for imaging of the sample or a selected area diffraction pattern from it, respectively.

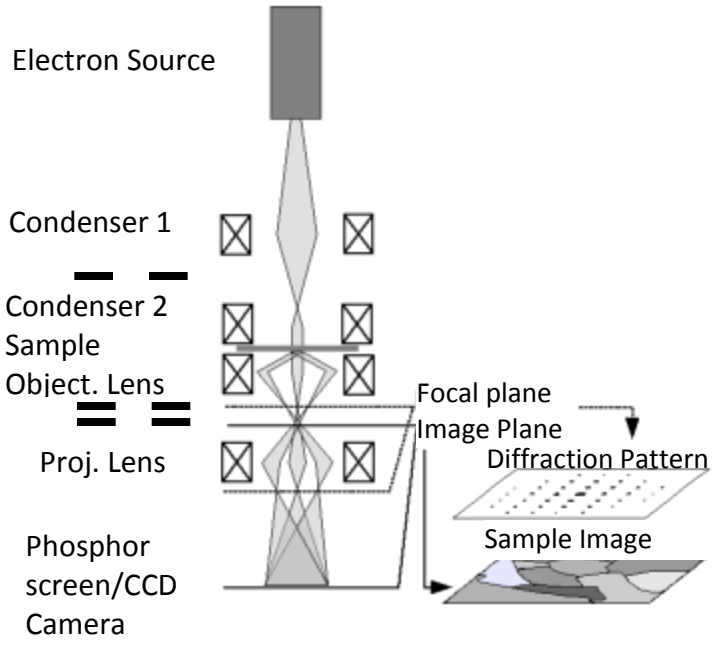

Figure 15. Schematic of typical TEM set-up, after [154].

For the present work, a Philips (FEI) CM 200 was the primary instrument used for characterizing MgB_2 samples, although an FEI Technai was used for scanning transmission electron microscopy (STEM) in which the e-beam is focused into a narrow spot and rastered across the sample for detailed EDS analysis of small areas. The former instrument uses a LaB_6 electron source while the latter instrument uses a field emission source. Samples were prepared via traditional ion-milling techniques using an FEI Helios 600 dual-beam focused ion beam (FIB) or a Nova 600 dual-beam FIB. A Pt strip, produced by Ga^+ focused ion beam decomposition of an organometallic precursor, is deposited across a ~20 μm length on the sample surface. Ga+ ions are then used to cut

trenches into the sample surface such that only a small isthmus of sample, protected by Pt, remains. The TEM "foil" is extracted with the Omniprobe micro-tool and secured to a special Cu grid with more Pt. Finally, the sample is thinned with grazing incident Ga^+ ions at lower energies, as the MgB_2 is easily amorphized by the Ga^+ ions.

2.4 Vibrating Sample Magnetometry and A.C. Susceptibility

A vibrating sample magnetometer (VSM) was used to determine the magnetization of the samples. From the magnetization, important superconducting properties such as T_c and a "magnetic J_c" can be deduced.

The VSM works under the principle that a magnetized vibrating a sample will induce a voltage in a pick-up coil according to an expansion of the Maxwell-Faraday equation:

$$\begin{aligned} V_{coil} &= \frac{d\phi}{dt} \\ V_{coil} &= \left(\frac{d\phi}{dz}\right)\left(\frac{dz}{dt}\right) \\ V_{coil} &= 2\pi\, fCmA\sin(2\pi\, ft) \end{aligned} \tag{14}$$

Here the sample is oscillated at a fixed frequency f (40 Hz). The amplitude of oscillation is A, t represents time, ϕ represents magnetic flux, C is a coupling constant, and m is the magnetic moment of the magnetized sample. The VSM is calibrated with a Pd standard (262.7 mg) at 298 K and 2 T such that a voltage is related to a magnetic moment. The

magnetization can be then obtained by normalizing the moment to either the sample mass or the sample volume.

The type of VSM used in the present work is an accessory to a Model 6000 PPMS (serial number 497) made by Quantum Design, Inc. The limitations of the instrument are $1.8 < T < 400$ K and $-14\text{ T} < B < 14$ T. The minimum sensitivity is ~1×10^{-6} emu.

The superconducting critical transition temperature, T_c, can be measured via VSM. First, a "zero-field cool" (ZFC) sequence is used to clear the sample (and incidentally the superconducting magnet that is responsible for the magnetic field) of magnetic flux. This is accomplished by setting the magnetic field to 2 T while above the T_c and then oscillating the field around 0 T in successively decreasing amplitudes (70-80 % of the previous B). This procedure serves to reduce the residual field to < 1 mT. The temperature is then ramped to below T_c and a magnetic field (say B_a) is applied. While in the presence of this B_a, the T is scanned to above T_c and then back below T_c again ("field-cooled" or FC). Because the flux pinning in the superconductor is irreversible, the FC branch of the measurement has a much smaller value (in terms of magnitude of flux expulsion) than the ZFC branch. In this way both the temperatures at which this B_a represents B_{irr} and B_{c2}, respectively, can be determined (Figure 16). A new field is applied and the experiment repeated. The results of these experiments are usually plotted in the format B_{c2} & B_{irr} vs. T.

Of course, the DC susceptibility χ_{DC} may be calculated for a given material (assuming the geometry is known so that an appropriate demagnetizing factor α_d can be applied) using the relation $B=\mu_0 H(1+\chi_{DC})/(1+\alpha_d\chi_{DC})$; Schenck [155] gives a

comprehensive review of both DC susceptibility and the demagnetization factor as a function of geometry. For the present work, it is enough to know that α_d is 1/3 for a sphere, ½ for a cylinder where B_a is perpendicular to the cylinder axis, and 0 for a cylinder where B_a is parallel to the cylinder axis.

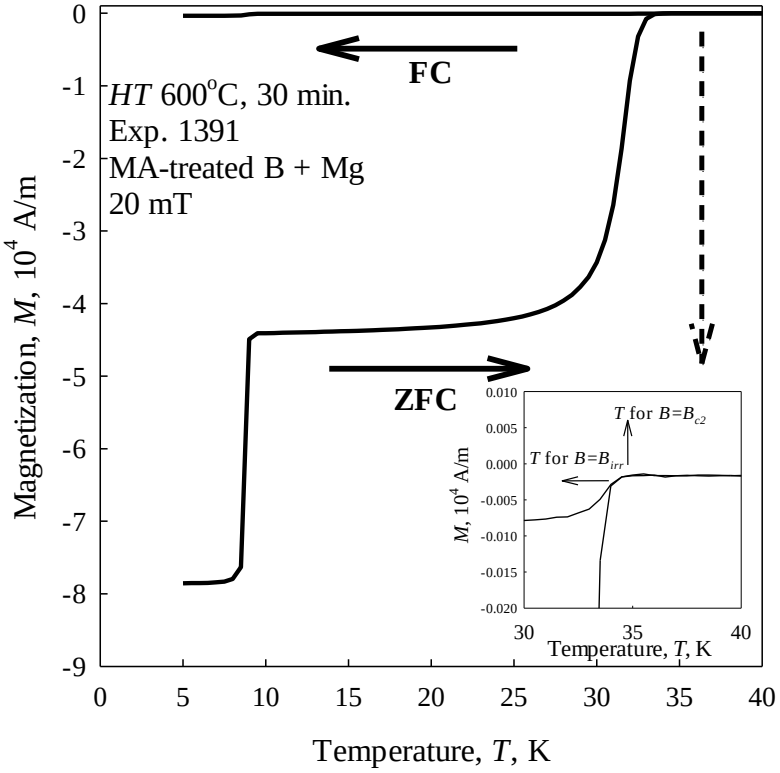

Figure 16. Magnetic T_c plot for an MgB_2 wire. The two transitions are due to the Nb (T_c~9 K) sheath surrounding the MgB_2.

The other important result that can be obtained from a VSM measurement of a superconductor is its *M*-*B* loop, where the magnetization is taken as a function of *B*. For a

superconductor, which is a perfect diamagnetic material at $B<B_{c1}$, gradually nucleates fluxons as B is increased until B_{c2} (or the limit of the magnetic field for the apparatus, whichever comes first) is reached. This branch of an *M-B* loop is referred to as the "flux shielding" branch. As B is decreased the amount of fluxons also decreases, leading to the "flux trapping" branch of the *M-B* loop. The shielding and trapping legs are repeated as the magnetic field is ramped in the negative direction, Figure 17.

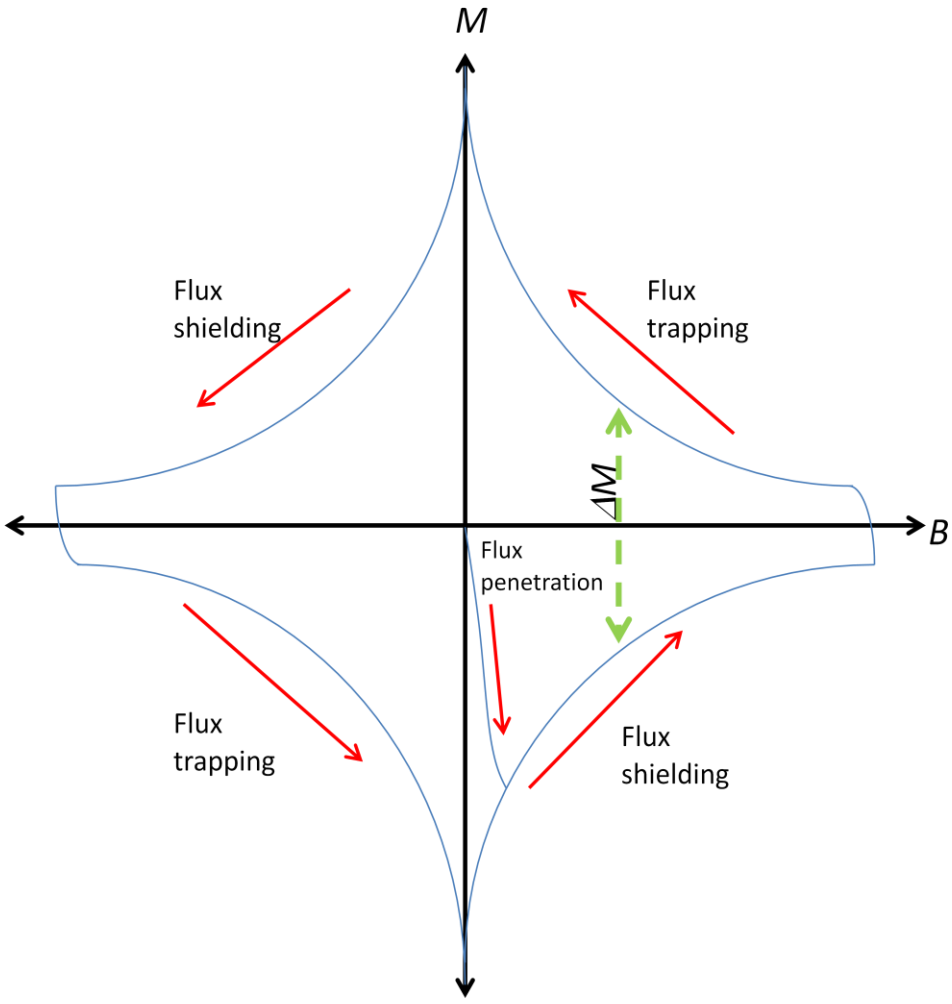

Figure 17. *M-B* loop for a type-II superconductor.

The magnetic critical current density, or J_{cm}, can be obtained from an *M-B* loop using the Bean model [156], [157] where $J_{cm} \propto \Delta M$ (ΔM being the width of the hysteresis loop at a given *B*). Of course, since the irreversible magnetization of a superconductor is dependent on geometry, the proportionality between J_{cm} and ΔM is also geometrically dependent. Figure 18 shows the geometries and resultant equations for various sample shapes and orientations [158].

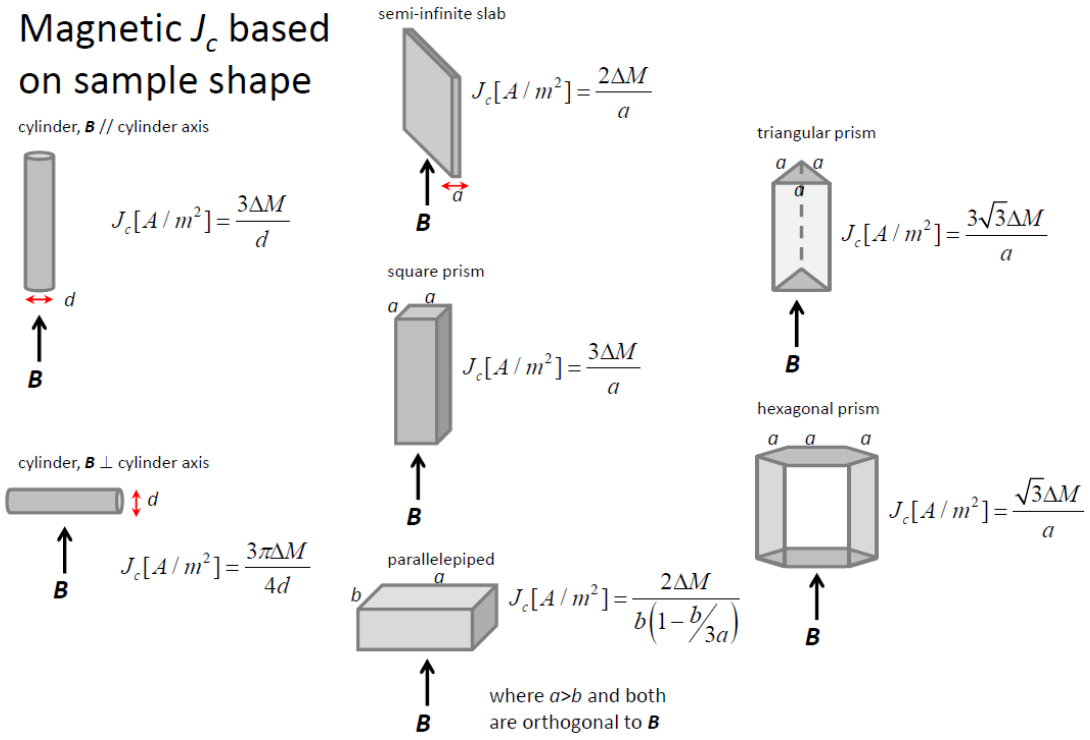

Figure 18. Magnetic J_c for various sample geometries and orientations, adapted from the equations in [158].

The so-called "ACMS" option on the Model 6000 can be used to measure either the DC magnetization or the AC susceptibility. The AC susceptibility, χ_{ac}, is equal to dM/dB and is thus a dynamic measurement. The susceptibility itself has two components $\chi_{AC} = \sqrt{\chi'^2 + \chi''^2}$ where χ' is the real (or in-phase) component and χ'' is the imaginary (out-of-phase) component. To measure χ_{ac} a mall AC magnetic field is applied (which can be in addition to a separate DC field); the magnetization induces a voltage in a pick-up coil which is calibrated to a magnetization using a Pd standard, as with the VSM. The AC magnetic field is set at +/- 10 Oe while the frequency can be varied from 10-10000 Hz. The ACMS is more sensitive than the VSM option (up to three orders of magnitude, depending on the sample).

2.5 Resistivity and I_c Measurements

Resistivity was measured on a variety of samples using the 4-point measurement technique, Figure 19. This is a technique whereby voltages from the voltmeter and the current contacts can be mitigated. For a sample wired similarly to the arrangement described in Figure 19,

$$\begin{aligned} V &= (I - \varepsilon)(R_{sample}) - \varepsilon(2r_{contact} + 2r_{lead}) \\ \varepsilon &<< I \\ V &\cong IR_{sample} \end{aligned} \tag{15}$$

where V is the voltage measured by the voltmeter, ε is the current through the voltmeter, I is the current from the current source, and R_{sample}, $r_{contact}$, and r_{lead} are the resistances from the sample, the voltage contacts, and the current leads, respectively. The advantage to using the 4-point technique to measure resistance (and hence resistivity) is that since $\varepsilon << I$, the effects of r_{lead} and $r_{contact}$ are minimized. For a 2-lead arrangement, the total resistance would represent the sum of all resistances present, meaning that $V \approx I(R_{sample}+2r_{contact}+2r_{lead})$ which would prevent an easy measurement of the sample resistance [159].

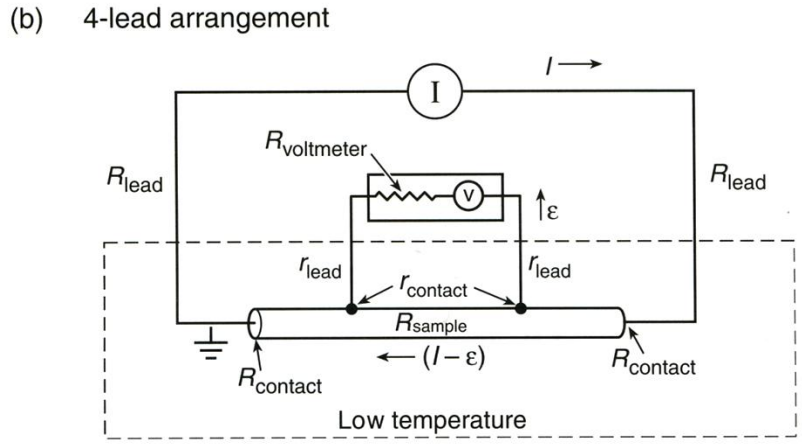

Figure 19. Schematic of the 4-point measurement technique, after [159] (with permission from Oxford University Press).

Resistivity measurements for smaller samples and thin films were taken with the Model 6000 PPMS's resistivity option. This system has a current limit of 5 mA (DC mode) and 2 A (AC mode) with resolution limits of 20 nV and 10 nA. Samples were mounted on the DC sample puck which can hold up to 3 samples at once. For the voltage

or current contacts either In (99.99%) or silver paint was used for the current leads/voltage taps. Generally speaking, the In contacts were used for thin films whilst the Ag paint was used for wire samples. The contact resistivity of both materials is ~10^{1}-10^{-2} Ωcm^{2}, with the In having a value slightly lower than Ag. Resistance vs. temperature (*R*-*T*) plots were taken with a temperature ramp rate of ~1 K/min. or less to ensure a homogeneous temperature distribution in the sample. The "standard" calibration mode was used where an *I*-*V* reading is calibrated against a known resistor. Furthermore, to reduce thermal emf and other *T*-related effects, "AC mode" was used in which the DC current is reversed in a square wave-type oscillation about 0; both the positive and negative voltages were used to calculate *R*.

The second type of measurement is termed an I_c measurement and was performed using an in-house set-up controlled by a Labview interface. These measurements investigated the superconducting current-voltage (*I*-*V*) transition in terms of *B* and *T*. A 1 μV/cm voltage criterion was used to determine I_c from a given *I*-*V* curve (i.e. I_c was determined by a 1 μV voltage drop across the length of the voltage taps). J_c was calculated by dividing the I_c by the superconducting area within the wire. These measurements may be divided into 3 categories:

i) For 4.2 K measurements of samples with an $I_c > 220$ A, ~ 3 m samples were submerged in a liquid He bath inside of an Oxford Instruments 15 T research magnet. Current was supplied with three HP 6681 current sources connected in series. Voltages were measured with a Keithley

182 nanovoltmeter. Current transfer length was ~ 1 m and voltage taps were separated by ~ 500 mm.

ii) For 4.2 K measurements of samples with an I_c < 220 A, 3 cm samples were submerged in a liquid He bath inside of an Oxford Instruments 15 T research magnet. Current was supplied with a HP 6671 current source. Voltages were measured with a Keithley 182 nanovoltmeter. The separation between voltage taps was ~5 mm. Current transfer length was also ~5 mm.

iii) For variable temperature measurements (10-40 K) of samples with an I_c < 220 A, 3 cm samples were mounted in an evacuable brass canister that was sealed with Wood's metal (a eutectic alloy of weight composition of 50% Bi, 26.7% Pb, 13.3% Sn, and 10% Cd). The voltage taps were fixed at a distance of 5 mm and attached with Pb-Sn solder. The current leads were attached to Cu blocks with Pb-Sn solder. A 50 Ω Kapton heater was laid across the Cu leads, as was a Cernox temperature sensor. Temperature control was accomplished through a Lakeshore Model 330 Temperature Controller; thermal conduction was through the current leads to the liquid helium bath. Current was supplied with a HP 6671 current source. Voltages were measured with a Keithley 182 nanovoltmeter.

2.6 Specific Heat

The heat capacity was measured via the Model 6000 PPMS heat capacity accessory. The heat capacity is measured using the "pulsed calorimetry" technique whereby a small amount of thermal energy is imparted to the sample and the temperature decay over a period of time is recorded. Hwang *et al.* [160] and Stewart [161] both provide excellent reviews, but the simplest description of the measurement technique can be summarized by:

$$C_{total}\frac{dT}{dt} = -K_w\left(T - T_b\right) + P(t) \tag{16}$$

where C_{total} is the total heat capacity (sample and sample platform), K_w is the thermal conductance of the support wires, T_b is the temperature of the chamber (and hence the sample holder), and $P(t)$ is the power applied by the heater (equal to P_0 during the heating portion of the measurement and equal to 0 afterward) [162].

The measurement limits are: sample size is limited between 1 and 200 mg and temperature constrained by the limits of the PPMS chamber itself ($1.8 < T < 400$ K). A heat capacity puck was carefully calibrated for magnetic fields between 0 and 14 T in 1 T increments. For a sample measurement, Apiezon N grease is applied to the sample platform and the heat capacity is measured as a function of T. These data are stored in an addenda file that is analogous to "taring" a scale. After the addenda measurement is taken, the sample is mounted on the grease (which is present to both secure the sample and provide for thermal conduction) and measured. As mentioned in the Introduction, the

T_c distribution of a superconducting sample may be extracted from a tightly spaced dataset of the heat capacity. The simplest method of applying this analysis is through the use of the expression:

$$\int_0^T f(T_c)dT_c = \frac{n(S_e)-(C_e)}{(n-1)\gamma_e T} \tag{17}$$

where C_e is the superconducting contribution to the electronic specific heat (obtained through the measurement of the heat capacity as a function of T at 0 T and subtracting the heat capacity at $B>B_{c2}$ or as high a field as can be applied), S_e is the entropy derived from the measured C_e, γ_e is the electronic specific heat coefficient, T is the temperature, f is the fraction of the sample with a T_c at T, and n is equal to 3 for the two-fluid Gorter-Casimir model [119]. The derivation of this expression is provided in the Appendix.

2.7 Pulsed Laser Deposition

Pulsed laser deposition (PLD) is a technique used to fabricate thin films. Additional details of this technique as applied to MgB_2 are presented in Chapter 4 of this work. Figure 20 is a schematic of a PLD device; it is a versatile physical evaporation instrument in which a pulsed laser is focused onto a target material. For a given energy density (which is entirely dependent on the material) the laser striking the sample surface creates a significant and rapid heating of the target material, causing a laser-induced plasma to form on the target surface. The plasma plume is ejected orthogonally to the

surface of the target and subsequently impinges on the substrate, depositing the species from the target onto the substrate [163].

As can be imagined, this process is non-equilibrium in nature and relies heavily on kinetics. A process gas (typically O_2 or Ar, depending on the material being deposited) can be used to control the kinetics (and thus the size) of the plasma as it is ejected from the target surface through attenuating the kinetic energy of the plasma through collisions. Depending on the mass and pressure of the process gas, these collisions can be used to tune the kinetic energy of the plasma from 0.1-100 eV [164].

For the vast majority of materials used in PLD synthesis, it has been shown that the stoichiometry of the target readily transfers to the manufactured film. However, in some cases where at least one component is volatile (say for example Mg) it is necessary to compensate for the loss of this element. For oxide phases, this task is accomplished through using O_2 as the process gas. For MgB_2 Mg loss can be compensated for by introducing Mg into the deposition process, either through increasing the Mg in the target and/or the addition of a Mg cap.

The PLD system used in this work was manufactured by Neocera, Inc. The laser is a Lambda-Physik KrF excimer laser with a maximum energy of ~400 mJ. The laser beam is reflected off of two lenses, each at a 45^o angle, into a focusing lens whose focal length is 540 mm. The energy of the incident 248 nm radiation is read via an Ophir Orion energy meter with a PE50BB-SH-V2 sensor. The energy loss of the laser beam passing through the lens and the window is purportedly <10% as stated by the manufacturer but was unable to be confirmed due to certain damage that the test would impart to the

expensive sensor (the focused beam having an increased energy density). The calibration for the energy meter was performed by Ophir and is NIST traceable. The size of the laser spot was measured by placing laser burn paper on top of the target and measuring the resulting burn spot with a travelling microscope. The need for high energy densities to create an MgB_2 plume necessitated an optimization procedure where the focusing lens position was changed and the resultant spot size was recorded. The tightest spot was then used for deposition. This spot was inhomogeneous in nature, with a lighter center (indicating a higher energy density). If the entire spot area was used, then the energy densities were ~6-8 J/cm^2. If, however, only the brightest area of the spot was used, the energy densities could be in excess of 15 J/cm^2. Due to the precise calibration of the width of the spot mentioned earlier, the energy densities were highly reproducible. The vacuum chamber itself is a 46 cm OD (50 L volume) chamber made by Kurt Lesker. A Pfeiffer T600 turbopump (1000 Hz rotation) with a dry backing pump was used to pump out the deposition chamber.

The process gas used in this work was high-purity Ar at 75-120 torr. The Ar was nominally 99.998% pure and was further filtered via a Centorr Ti getter furnace (set to 800^{o}C) and a Microtorr MC1-902F in-line filter. The pressures were read via an Instrutech CVG convection vacuum gauge for pressures of 1 mtorr to 760 torr and a Pfeiffer IKR 251 cold cathode gauge measured pressures of 10^{-3} torr to 10^{-8} torr.

A sample carousel (more precisely described as a planetary rotator) was capable of holding six 2.54 cm targets or three 5.08 cm targets. Targets were mounted to their respective platforms using Ag paint and inserted into the carousel slot. The post could be

moved up or down in the slot to adjust the target height. The maximum achievable target height (and hence minimum substrate-target distance) for the vacuum chamber in this work was 35 mm. The 2.54 cm targets were rastered about their center-point such that the laser scanned from edge to edge of the target (typically +/- 12-15^{o} at a rate of 5^{o}/s); rotation was also employed at the rate of 60^{o}/s).

The heater was a radiant heater manufactured by Neocera, Inc. capable of temperatures of 1050^{o}C as read by a Type-K thermocouple. Substrates were mounted onto an Inconel 400 substrate holder (5 cm diameter). The thermal conduction through the substrate holder was accounted for by welding a Type-K thermocouple to the holder and reading the resulting temperature. The T of the substrate holder T_{sub} (and hence the substrate) was found to be equal to 80% of the T as read by the Type-K thermocouple T_{set} (T_{sub}=0.8 x T_{set}). Control of the laser, the turbo, the target carousel and the heater was accomplished through a Labview-based program.

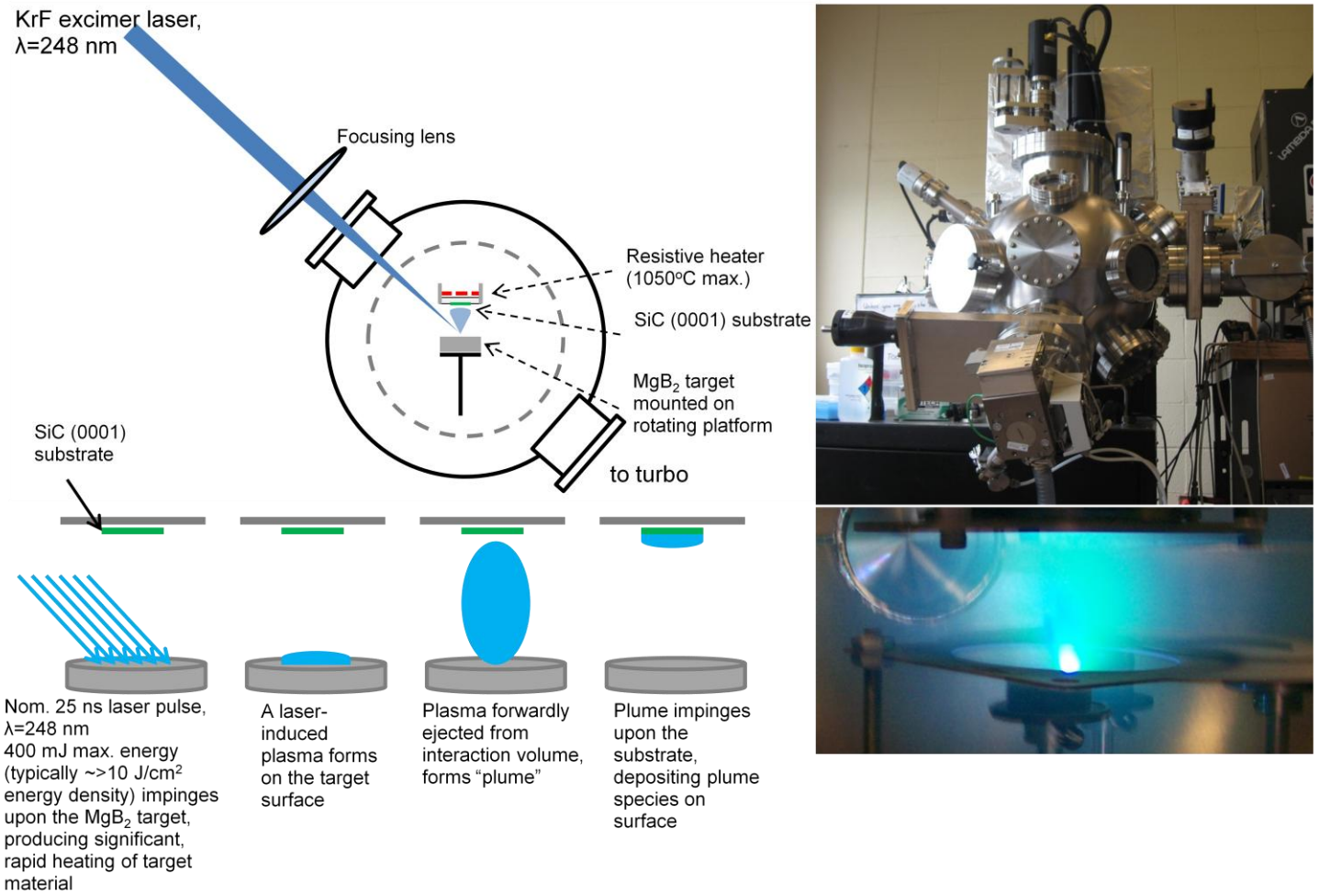

Figure 20. Schematic and picture of the PLD apparatus.

Chapter 3: Electrical Connectivity in MgB_2 Superconducting Wires

The electrical connectivities of MgB_2 samples made via different techniques (i.e., PIT and IMD) are compared. The microstructural evolution of C-doped MgB_2 PIT wires is investigated in detail in terms of drawing effects on the elongation of the Mg particles and on the resultant superconductive properties. The effect on the microstructure on the radial and longitudinal connectivity is quantified in terms of a simple model. Finally, these results are compared to IMD wires, which essentially can be considered as a limiting case of the PIT wire.

3.1 The Drawing-Induced Microstructure of PIT MgB_2 Wires: Unreacted Microstructural Features

For applications such as MRI and magnetic coils it is necessary to produce a superconducting material in the form of a wire or cable (which is essentially a bundle of wires). The most common method of manufacturing MgB_2 wire is the Powder-in-Tube (PIT) method. Please refer to Chapter 1 of this work for more information regarding wire preparation.

Although high values of transport J_c and flux pinning have been seen in MgB_2 thin films since the earliest publications on MgB_2 [165], translating these properties into

wires has been elusive. The 4.2 K, 0 T depairing critical current density, J_d (the current density that represents the thermodynamic depairing energy required to break apart the Cooper pairs in the superconductor), has been reported to be equal to ~7.7 x 10^7 A/cm^2 [166]. The highest 4.2 K self-field J_c reported for MgB_2 in films is 1.2 x 10^7 A/cm^2 [165], giving a J_c/J_d of 15.6%. For comparison, the J_c/J_d ratio of NbTi and Nb_3Sn superconductors are 0.3 and 6%, respectively. It is evident, then, that suitably formed MgB_2 has the ability to realize extremely high critical current densities in relation to the theoretical values. However, at 0 T and 4.2 K the highest J_c reported for a standard PIT wire was ~10^6 A/cm^2 [167]. It is therefore necessary to determine the cause of this discrepancy.

There exist several differences between the MgB_2 thin films and wires in terms of preparation and final microstructure. The thin films are usually epitaxial or at least c-axis oriented and also fairly homogenous. Additionally, thin film sample preparation uses highly pure target materials or gasses, helping to mitigate the effects of impurities on these materials. Wires, on the other hand, are made using solid state synthesis of Mg and B powders. The purity of the precursor powders, the wire drawing process, and the heat treatment procedure are all variables that have to be considered in attempting to explain the less than optimal superconducting properties exhibited in MgB_2 wires.

It is well known that Mg has limited ductility, with an elongation-to-fracture of ~7% under static strain. However, a Mg rod embedded in fine B powder (either amorphous or microcrystalline) can undergo ductile elongation when drawn through a series of dies. This phenomenon is well-known, having been performed by both Giunchi

et al. [168], [169] and Hur *et al.* [170] who described packing an axial rod of Mg into an experimental billet with B powder and drawing it to fine wire sizes (typically a ~90% area reduction). Likewise imbedded Mg particles also undergo elongation during drawing though dies as reported previously by Uchiyama *et al.* [171] and shown conceptually in Figure 21. The B powder, being composed of small, amorphous particles, does not deform during the drawing process; rather, the particles re-arrange to accommodate the deformed Mg .

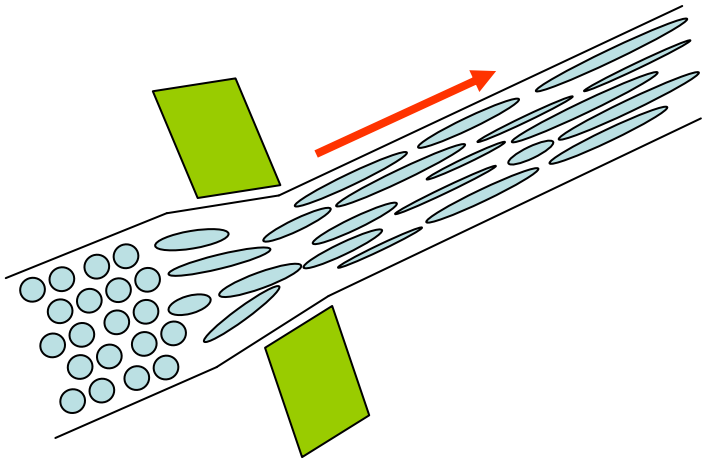

Figure 21. Conceptualization of Mg elongation during the wire drawing process.

In examining this effect, a section of MgB_2 wire was removed after each stage of the drawing process. These samples were then cut into smaller segments for metallographic analysis. Both longitudinal and transverse (with respect to the wire axis)

cross-sections were taken of the wires. Figures 22 and 23 show the BSE micrographs at various stages in the drawing process. The transverse cross sections, seen in Figures 22a-22d, show the effects of wire drawing in terms of the sizes of the Mg particles (white) whose cross-sections decrease in diameter as the wire is drawn. Figures 23a-23d, displaying the longitudinal cross-sections, show a more striking result. Here, the Mg is seen to "ribbonize" during the drawing process, proceeding from round particles to highly aspected stringers.

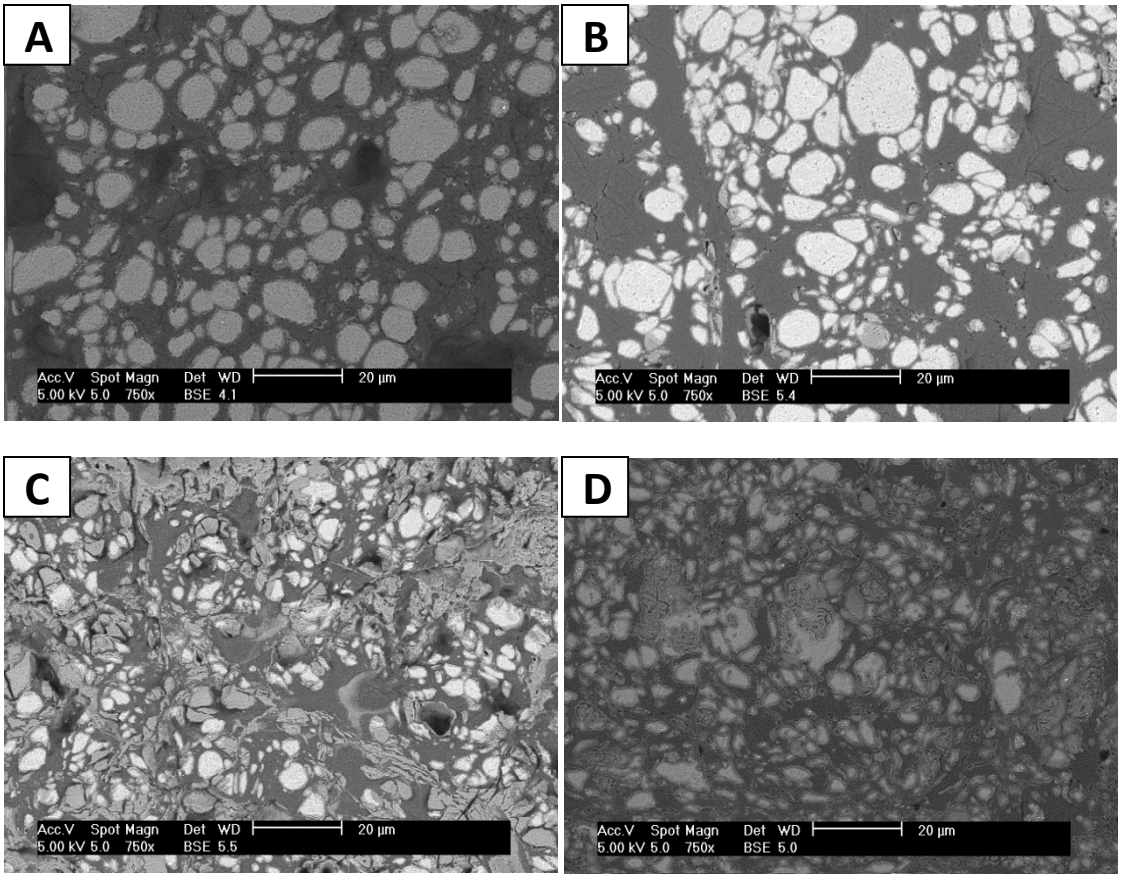

Figure 22. BSE SEM images of the transverse cross sections of an unreacted MgB_2 strand at various stages along the wire reduction process. The strand (starting OD of 9.53 mm) is shown at wire OD/area reduction values of (a) 4.08 mm /57% area reduction, (b) 2.41 mm/75% area reduction, (c) 1.42 mm/85% area reduction, and (d) 0.83 mm/91% area reduction.

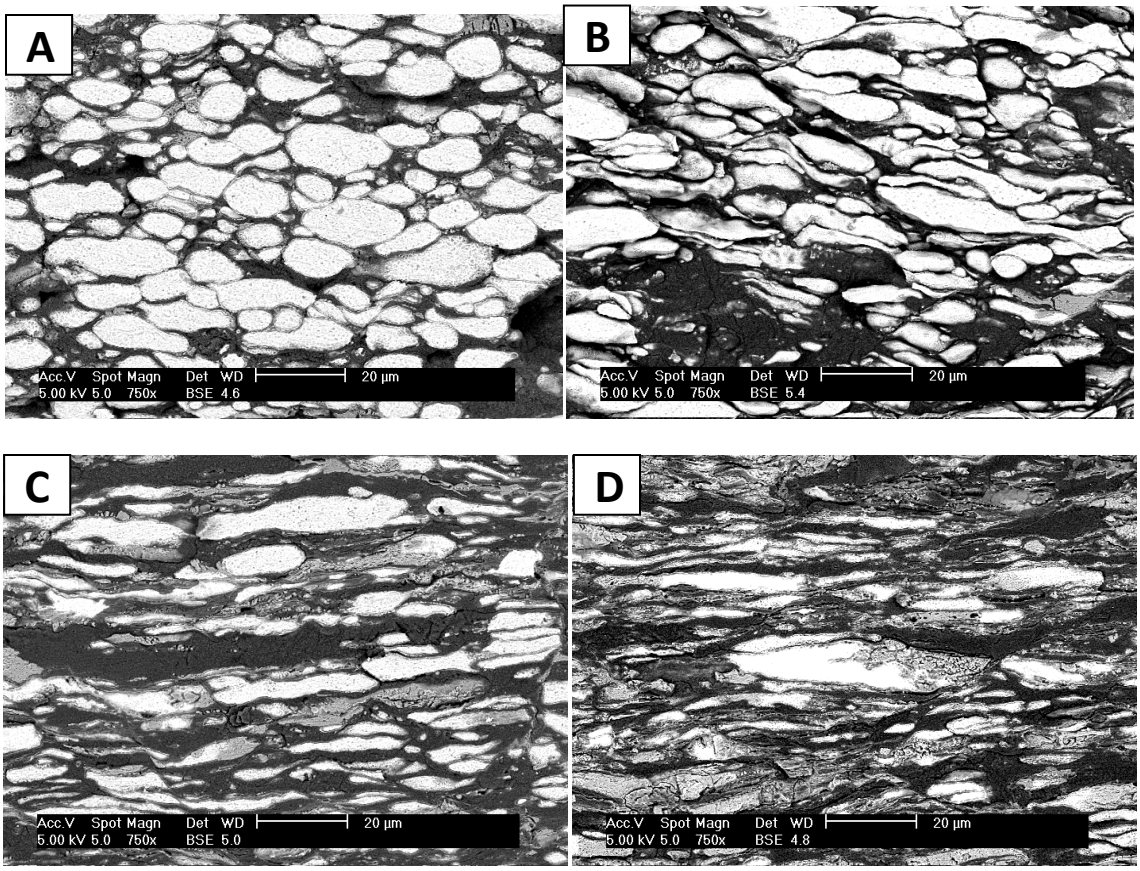

Figure 23. BSE SEM images of the longitudinal cross sections of an unreacted MgB_2 strand at various stages along the wire reduction path. Evident is the evolution of microstructure, in particular the "ribbonization" of the Mg. The strand (starting OD of 9.53 mm) is shown at wire OD/area reduction values of (a) 4.08 mm /57% area reduction, (b) 2.41 mm/75% area reduction, (c) 1.42 mm/85% area reduction, and (d) 0.83 mm/91% area reduction.

Figure 24 shows the aspect ratio of these Mg stringers as a function of cross-sectional area reduction of the MgB_2 wire. These data represent an average of at least 40 elongated particles. The graph shows a large increase in the aspect ratio of the Mg as the wire is drawn to its final diameter. As will be discussed in the following sections the

microstructure resulting from this Mg elongation leads to anisotropic superconducting properties.

As a final important point with regards to the unreacted wire, Figure 25 shows a detailed image of a Mg particle. An oxide layer surrounding the Mg is clearly visible around the particle's periphery. This feature expected given that Mg readily acquires an oxide layer when exposed to atmosphere, forming MgO or $Mg(OH)_2$ [172], depending on the moisture content of the oxygen containing environment to which it exposed . This feature will play a key role in the post-reacted MgB_2 in terms of electrical connectivity.

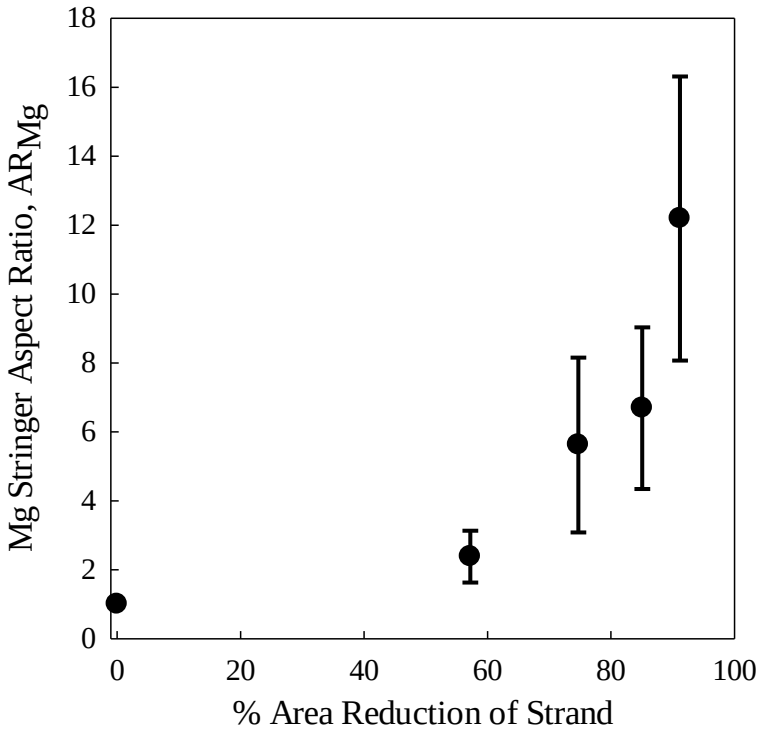

Figure 24. Aspect ratio of Mg stringers vs. % area reduction of the MgB_2 strand.

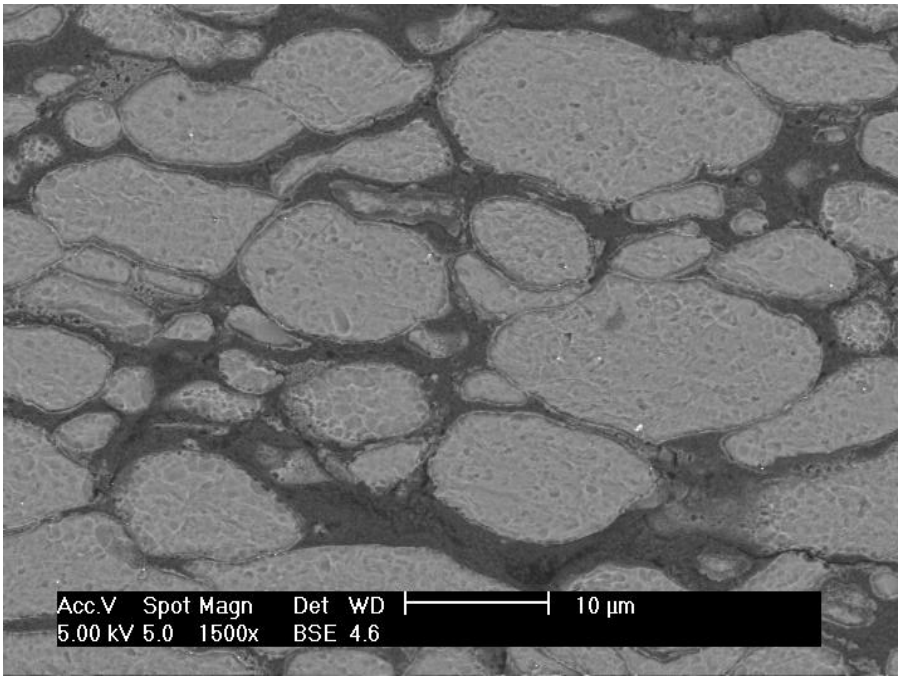

Figure 25. BSE SEM images of the longitudinal cross-section of a 4.08 mm /57% area reduction highlighting the MgO layer surrounding each prior Mg particle.

3.2 The Drawing-Induced Microstructure of PIT MgB_2 Wires: Reacted Microstructural Features

For a complete study of the connectivity of the MgB_2 wires, a series of heat-treatments was given to sections of unreacted MgB_2 strand. The microstructure was fully investigated and characterized to provide a strong foundation for correlating the microstructure, critical current density, and connectivity.

Monofilamentary powder-in-tube (PIT) strands with a Nb chemical barrier and an outer sheath of Monel 400® (a 70% nickel- 30% copper alloy henceforth referred to as

simply “monel”) were manufactured by Hyper-Tech Research Inc. The final strand had a cross-section which was (by area) 50% monel, 29% Nb barrier, with the remaining 21% allocated to the mixed-powder core. The basic powder components were commercial Mg powder (99%, < 44 μm particle size) and “amorphous grade” B from Alpha Aesar. Listed as 99% pure, and made from the thermal decomposition of diborane gas, this powder consists of submicrometer-size agglomerations of 30 -100 nm size particles. Also included in the starting powder as a C-contributing dopant was small fraction of malic acid. (Alfa Aesar, 99% purity) which was mixed with the B powder in the ratio of 98.3 at% B to 1.7 at% malic acid. After this, 60 mL of toluene was added to create a slurry which was subsequently high energy ball milled for 12 minutes. The slurry was then transferred to a Pyrex jar and vacuum-dried at 150^{o}C during which the malic acid melted and decomposed and, along with the toluene, contributed C to the powder mixture [71]. An appropriate amount of Mg powder was then was added to restore the Mg:B ratio to 1:2. The powders were planetary milled at 100 rpm for 10 minutes followed by additional planetary milling steps performed at 500 rpm for 12 mins. Bimetallic Nb/monel tubes were filled with this powder using HTR’s previously described CTFF process [173–175] in preparation for wire drawing to a diameter of 0.83 mm followed by *in-situ* heat treatment (HT).

Strand sections were sealed under Ar in quartz tubes; the Ar pressure at ambient *T* (~200 torr) was chosen such that the pressure at the furnace temperature would be ~600 torr to prevent overpressurization of the quartz tube according to the Gay-Lussac Law.

Temperatures were chosen to be 600°C and 700°C to bracket the melting point T_m of Mg (650°C). Temperatures were ramped at 6°/min. A type-K thermocouple was used with a Fuji Electric Model PXG-4 temperature controller. Heat-treatment hold times were varied from 0.5 to 71 hrs (specifically, 0.5, 1, 2, 4, 6, 8, and 71 hrs); after the HT time was reached the quartz tubes were quenched in an ice water bath and opened with a diamond cutter to extract the MgB_2 wire.

During HT a "shrinking-core reaction" $Mg+2B \rightarrow MgB_2$ takes place during which Mg liquid or vapor reactively diffuses into the B particles, forming MgB_7, MgB_4, and finally MgB_2 [65]. This is confirmed on the macroscopic scale by observations following the formation of MgB_2 in the "internal magnesium diffusion" (IMD) process [168], [169]; wherein a void replicates the space previously occupied by Mg. Powder-in-tube *in-situ* MgB_2 formation is analogous; its noted porosity is a direct result of the voids left behind after the prior Mg has reacted.

Figure 26 shows the microstructures of MgB_2 strands after HT 600°C and 700°C for some representative times. The most obvious feature of the microstructure is the fibrous nature of the MgB_2 carried forward from the as-drawn strands. These fibers, typically ~27 μm x ~2.5 μm, are composed of a dense arrangement of <100 nm sized, randomly oriented grains (Figure 27) and are located in the regions where the B veins were located in the unreacted samples. Also immediately obvious are an abundance of highly aspected pores aligned with the wire axis; these represent the location of the pre-reacted Mg stringers.

From Figure 26, it is immediately seen that the microstructure for the 700^{o}C HT is, for the most part, invariant with respect to HT time. This observation is fully consistent with the literature and the work of Bohnenstiehl *et al.* [60]. At 600^{o}C, the MgB_2 phase is seen to take longer to form completely. This result is also not surprising, considering that the work of Bhatia *et al.* [176] showed a similar incompleteness of reaction after 3 hrs. The work of Bohnenstiehl *et al*. [60] showed that for a moderate ramp rate of 10^{o}C/min. an MgH_2+B powder mixture had largely reacted by 600^{o}C. However, an Mg+B powder mixture (where the Mg had an $MgO/Mg(OH)_2$ layer) showed a slightly higher onset temperature for the formation of MgB_2, suggesting that these oxide layers serve to impede Mg vapor diffusion. Also, the powder used in the thermal analysis experiments in the same aforementioned work was a loose mixture. The denser B veins in the wire could also impede Mg diffusion. These two observations may explain the longer times needed to fully form the MgB_2 phase at 600^{o}C in MgB_2 wires.

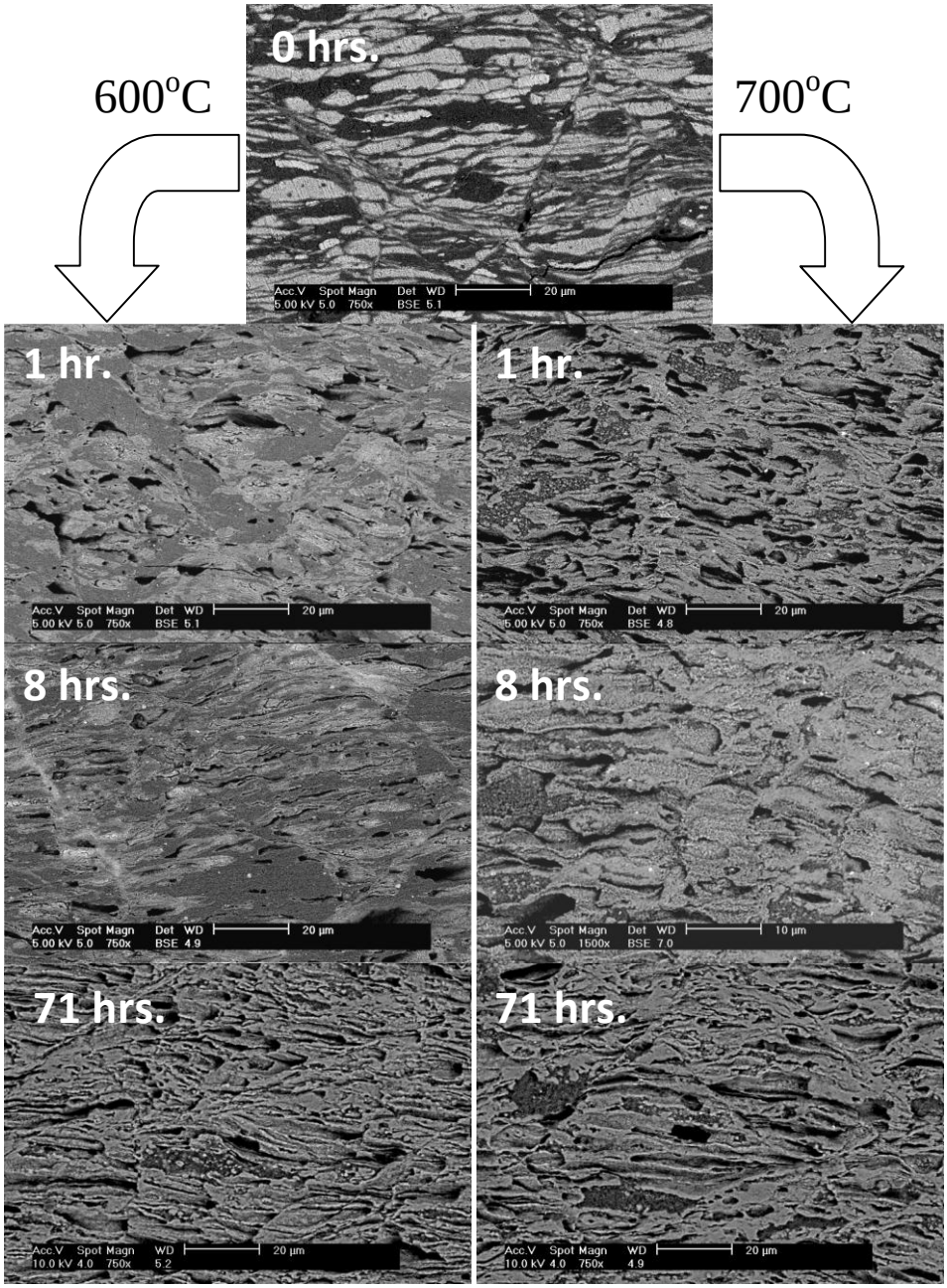

Figure 26. BSE SEM images of the longitudinal cross-section of a reacted MgB_2 wire at different parameters.

Figure 26 also shows large areas of a darker phase in the BSE micrographs. Quantitative EDS of B is not possible on the apparatus used. However, this phase is likely to be either MgB_4 or MgB_7 given the phase diagram of MgB_2 [53].

Even though the microstructure at the ~20 μm scale can be shown to be dependent on the HT parameters, the microstructure on a ~200 nm scale changes little. The average grain size increases only marginally with HT time, at 700°C HT growing from an initial average value of 37.4 ± 1.8 nm at 30 min. to 50.0 ± 3.2 nm after 8 hrs. Extended times of 71 hrs. showed a statistically meaningless increase to 53.2 ± 4.3 nm. The 600°C results showed similar behavior [177]. Figure 27 shows a fracture SEM of the MgB_2 grains resulting from the 700°C, 1 hr. HT and is fairly representative of the entire sample set.

Vignolo *et al.* [178] showed that grain growth in MgB_2 is more or less non-existent if the material is exposed to oxygen (where species transport inhibiting MgO layers are formed). In that study it was also found that MgB_2 that was never exposed to O_2 exhibited a significant degree of grain growth, with a wider particle distribution size. It is unsurprising then that the MgB_2 inside of a wire exhibits the same behavior as the MgO-coated MgB_2 considering that the B and Mg precursor powders were planetary milled and then placed in a powder hopper where the material flowed onto a Nb strip which was subsequently folded into a Nb tube. This full process is performed in air, allowing for ready oxygen contamination of the powder surfaces.

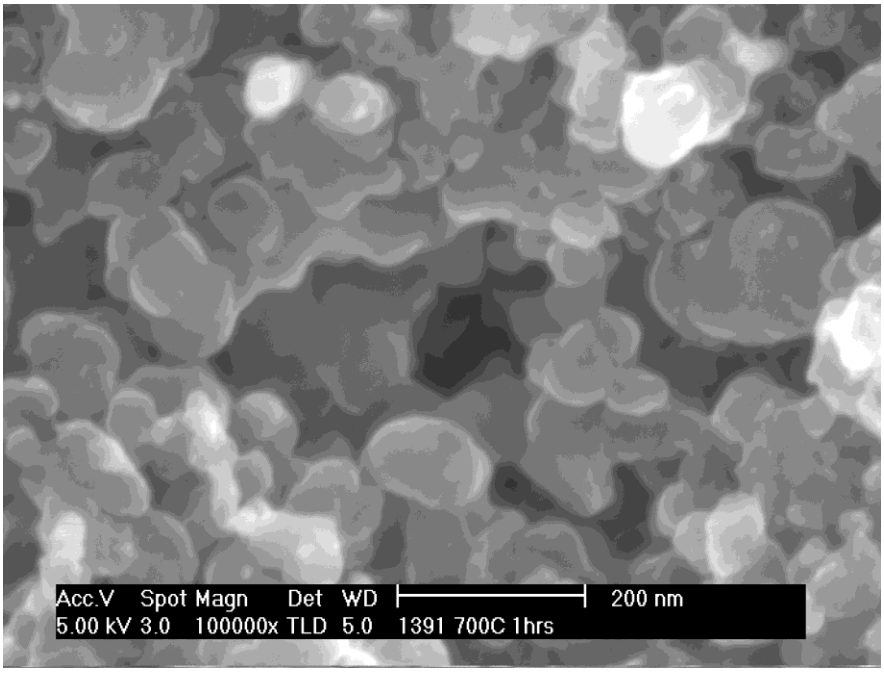

Figure 27. Fracture SE-SEM (using TLD) of MgB_2 grains for 700°C, 1 hr. HT.

Figure 28 displays the magnetic susceptibilities at different times for the two HT temperatures chosen in the study. The transition at ~9 K is due to the Nb sheath surrounding the MgB_2. The upper part of the figure shows the first derivative of the normalized susceptibility vs. T plot ($d(\chi/\chi_0)/dT$ vs. T) which is a measure of the sharpness of the T_c transition and, by extension, the homogeneity of the MgB_2. Here it is readily seen that the T_c does not change with HT time at 700°C, giving further evidence that the formation of the MgB_2 phase is largely complete after a short period of time. At 600°C, the T_c has a gradual increase in both value and sharpness with HT time until both the susceptibility and its derivative with respect to temperature are indistinguishable from the 700°C samples, mirroring the evolution of the microstructure presented in Figure 26.

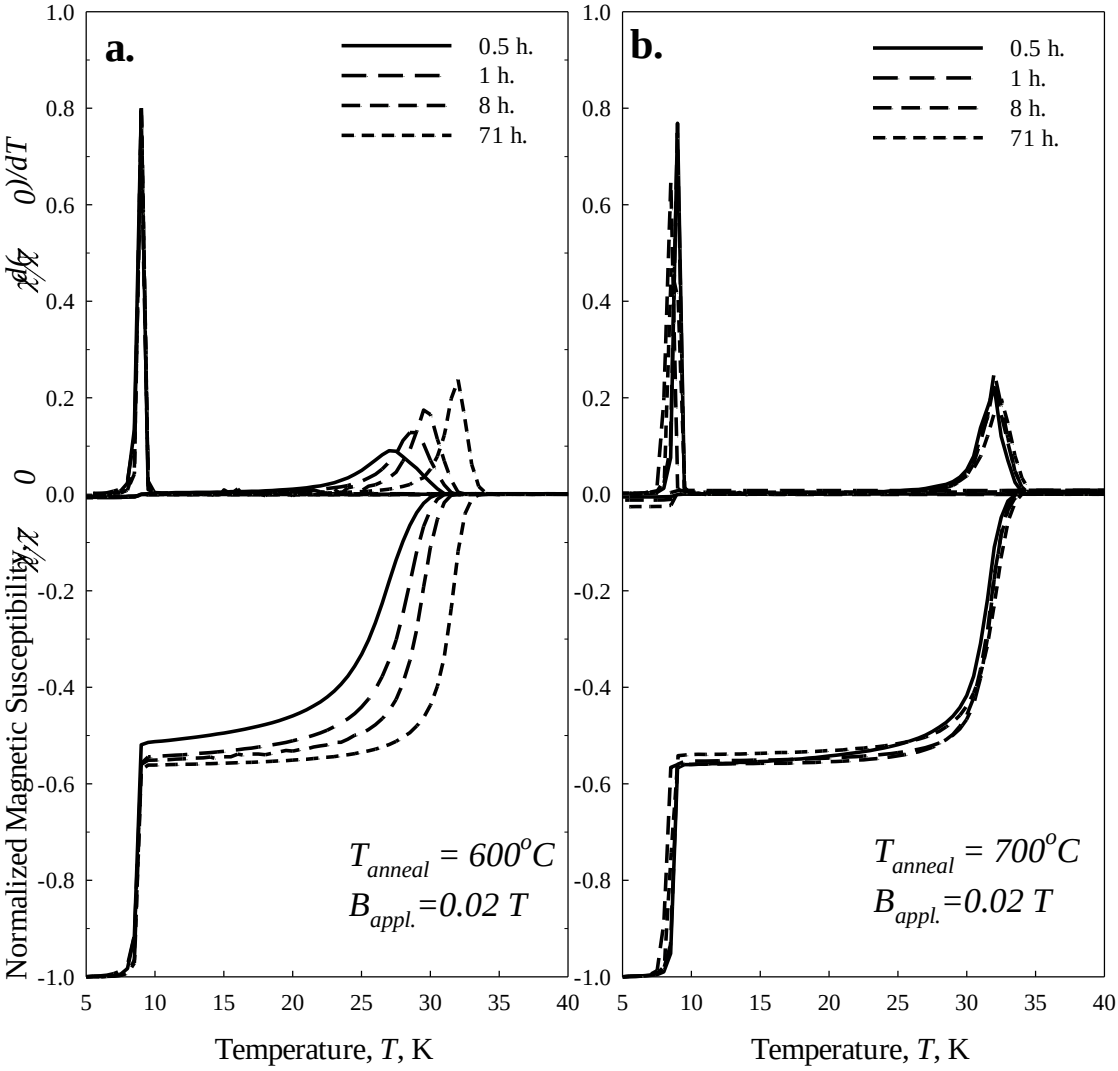

Figure 28. χ/χ_0 vs. T and d(χ/χ_0)/dT vs. T for four HT times at 600°C and 700°C.

In summary, description of the microstructure of an MgB_2 wire, its formation, and its evolution with HT time is a very complex topic. Parameters such as the drawing process and heat-treatment schedule affect the microstructural properties and in turn the

superconductive properties of the material. Most importantly, exposure to O_2, evident in the oxide layers surrounding the unreacted Mg particles, serves to inhibit grain growth of the MgB_2 which in turn limits the electrical connectivity of the MgB_2. The next section will detail how the drawing-induced microstructure leads to anisotropy in the critical current density.

3.3 Anisotropic Critical Current Density in PIT MgB_2 Wires

For an MgB_2 wire, one can consider connectivity manifesting itself at two levels: i) between the individual MgB_2 grains and ii) between aggregates of well-connected polycrystalline grains (i.e. the fibers). It has been shown qualitatively [103] that this fibrous microstructure begets an anisotropic connectivity.

Numerous authors have noted a difference between the transport measured J_{ct} and the magnetically measured J_{cm}s [103], [179], [180]. These differences have been quite dramatic, with $J_{cm}^{\perp}(B)$ trending to 0 at a much faster rate than $J_{ct}(B)$. Figure 29 compares these trends. In particular, a two order of magnitude difference between J_{ct} *and* $J_{cm}^{\perp}$ at 8 T.

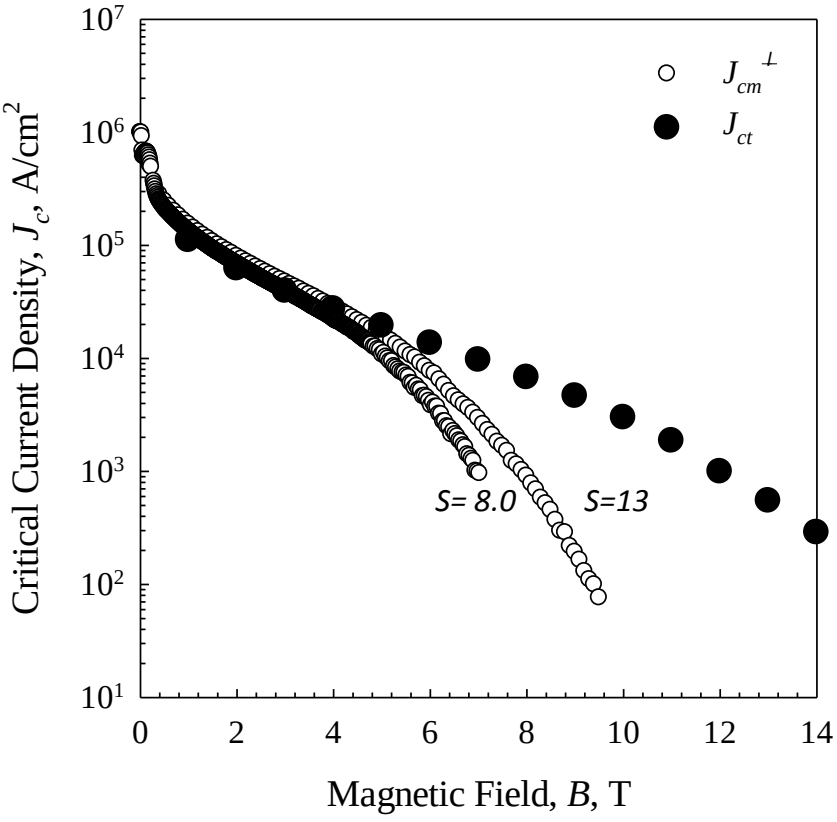

Figure 29. Measured J_{ct} together with measured $J_{cm}^{\perp}$ at aspect ratios of S=8 and S=13.

Other superconductors such as NbTi and Nb_3Sn exhibit little variation between the J_{ct} and $J_{cm}^{\perp}$ [181], excepting for when the aspect ratio of the sample $S=L/D$ is relatively small. Here L is the length of the wire and D is its diameter. Figure 30 displays a cartoon of the critical state models [103], showing that for a magnetic J_c measurement at low perpendicular B, longitudinal current paths are being probed; this configuration mimics the flow of supercurrent through a sample in a transport measurement. At higher

H, the transverse (or azimuthal in a cyndrilical sample, J_{cm}^{ϕ}) current paths dominate. As a result, if anisotropy in J_c is present higher *B* measurements will show a lower $J_{cm}^{\perp}$ than J_{ct}.

Some authors have misled themselves into thinking that these differences are due to defects [180] or current loops of different length scales caused by porosity [179]. This work offers an alternative model based on drawing-induced J_c anisotropy. Application of an anisotropic J_c model previously used for low temperature superconductors [182] is appropriate and explains the noted premature drop-off of $J_{cm}^{\perp}(B)$ with increasing field relative to $J_{ct}(B)$. For clarity of discussion, Table 1 displays a list of symbols representing all variants of the critical current density (CCD) to which this chapter refers.

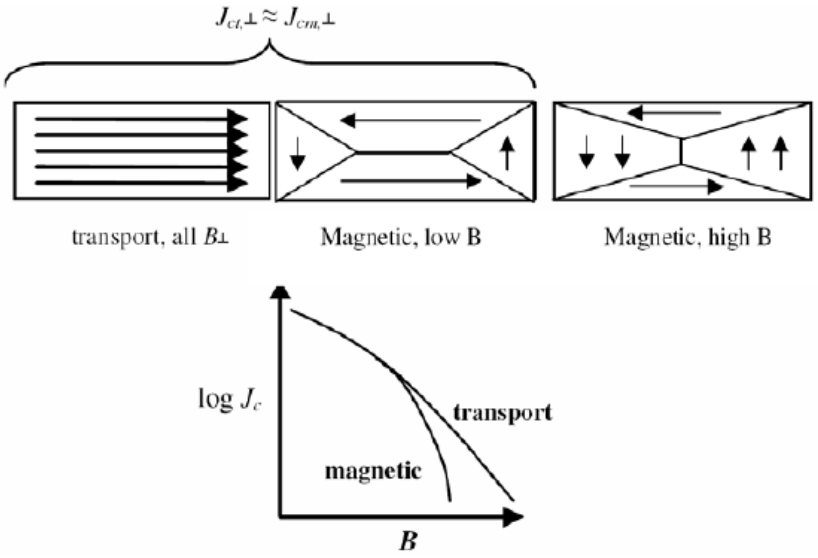

Figure 30. "Rooftop" critical state profiles and schematic field-perpendicular magnetic and transport J_cs, after [103].

Table 1. Definitions of Symbols for Critical Current Density, CCD.

Symbol	Definition
J_{ct}	Measured transport CCD
$J_{cm}^{\perp}$	Measured perpendicular field magnetic CCD
J_{cm}^{ϕ}	Measured parallel field magnetic CCD
$J_{cm,\ MOD}^{\perp}$	Model perpendicular field magnetic CCD, Eqn. (18)
J_3	Model strand-longitudinal CCD, Eqn. (1), = J_{ct}
J_2	Model strand-transverse CCD, Eqn. (1), = J_{cm}^{ϕ}

Comparisons were made of the transport and magnetic J_cs in perpendicular applied fields (J_{ct} and $J_{cm}^{\perp}$, respectively) of strands HT for 2 h. at 600°C. This HT was chosen since it enabled a direct overlap of J_{ct} and $J_{cm}^{\perp}$; the strand HT at 700°C would have had a low field critical current greater than the 220 A limit of the power supply. For the magnetic measurements the samples were cut to two lengths corresponding to aspect ratios (length/diameter, $L/D = S$) of 13 and 8. Associated with Figure 30, are several important observations: i) The transport J_{ct} extends well past the equipment limit of 14 T; ii) The magnetic $J_{cm}^{\perp}$ dies off "prematurely" at a rate that depends on S, indeed $J_{cm}^{\perp}$ plunges towards zero in fields of 7 – 11 T; and (3) The $J_{cm}^{\perp}$s of J_c-isotropic cylinders with S-values of 13 and 8 differ from J_{ct} by only about 2% and 4%, respectively (see Equation 18a below).

It is vital to note that the values of $J_{cm}^{\perp}$ and J_{ct} are affected by the selected electric field criterion due to flux creep effects. This dependence is very significant for J_{ct}, where critical current densities can have a large variance depending on the voltage criterion chosen (typically 0.1 or 1 μV cm^{-1}). For magnetic measurements (where the values of ΔM in M-B loop height at various magnetic fields are used to calculate $J_{cm}^{\perp}$), the voltage

criterion is dependent on the magnetic field sweep rate. For this sample, the sweep rate was 13 mT s^{-1}, corresponding to a voltage criterion of ~0.04 μV cm^{-1}. Applying this criterion to the J_{ct} results would yield a $J_{cm}^{\perp}$ only 11% reduced from J_{ct} at 9 T, which is too small to account for the observed values of $J_{cm}^{\perp}$. Indeed, one would have to reduce the voltage criterion to << 1 nV/cm to even begin to approach the values of the observed $J_{cm}^{\perp}$. Therefore, as pointed out in previous works [103], [183] the premature drop-off in $J_{cm}^{\perp}$ must result from a different phenomenon.

A relationship between the drop-off of $J_{cm}^{\perp}$, the *S*-dependence of that drop-off, and departure from J_c-isotropy (i.e. anisotropy) is discussed below with reference to the results of detailed SEM observations and critical state analysis. In short, two different J_cs are operative in the MgB_2 strand: i) the relatively strong J_c along an MgB_2 fiber which is largely representative of J_{ct} and ii) a degraded J_c in inter-fiber regions whose effect does not become readily apparent unless performing a magnetic J_c measurement.

In a perpendicular applied field the current loop supporting the magnetization consists of longitudinal currents of density, say J_3, (which can be identified with J_{ct}) in series with transverse currents of density, say J_2. According to Sumption's calculations [182] the "perpendicular field" magnetic critical current density, $J_{cm,\,MOD}^{\perp}$, is sample-aspect-ratio dependent and given by:

$$J_{cm,MOD}^{\perp} = J_{c3}\left[1-\frac{3\pi D}{32L}\left(\frac{J_{c3}}{J_{c2}}\right)\right] \qquad L_t < \frac{L}{2} \tag{18a}$$

$$J_{cm,MOD}^{\perp} = \frac{3\pi L}{8D} J_{c2}\left[1-\frac{4L}{3\pi D}\left(\frac{J_{c2}}{J_{c3}}\right)\right] \qquad L_t > \frac{L}{2} \tag{18b}$$

in which L_t represents a quantity which is analogous to the current transfer length of an anisotropic finite-slab model [182]. Associated with Figure 30 and Equations 18a and 18b are several important observations: i) The transport J_{ct} is 10^3 A/cm^2 at 12 T while the magnetic $J_{cm}^{\perp}$s drop off "prematurely" at a rate that depends on S and fall to 10^3 A/cm^2 at 7.9 T (S = 13) and 6.9 T (S = 8); ii) For long isotropic superconductors (L » D, J_{c3} = J_{c2}) Equation 18a shows that $J_{cm,}{}^{\perp}{}_{MOD} \approx J_{c3} \equiv J_{ct}$. Therefore, the observed J_{ct} - $J_{cm}^{\perp}$ bifurcation can be attributed to finite aspect ratio coupled with critical current anisotropy. The latter seems to be the driving mechanism since, according to Equation 18a, the $J_{cm,}{}^{\perp}{}_{MOD}$ s of isotropic cylinders with S-values of 13 and 8 differ from J_{ct} by only about 2% and 4%, respectively, scarcely the thickness of the lines in Figure 30.

The projected deviation between $J_{cm,}{}^{\perp}{}_{MOD}$ and J_{ct} becomes even stronger once field dependencies are introduced, however the modification of Equation 18 needed to include the field dependencies of J_3 and J_2 is beyond the scope of this work. Figure 30 compares the measured values J_{ct} and $J_{cm}^{\perp}$. Next, in order to compare J_{ct} with the model $J_{cm,}{}^{\perp}{}_{MOD}$ s predictions of Equation 18 it is necessary to find J_2. This is done by applying the field along the strand axis and from the resulting magnetization determine the circumferential critical current density, $J_{cm}^{\phi} = 30\Delta M/D$. The next step of identifying J_{cm}^{ϕ} with J_2 is taken since both currents pass transversely across the strand and encounter the same microstructural features. After inserting $J_{cm}^{\phi} \equiv J_2$ into Equation 18 and identifying J_3 with J_{ct} it is possible to calculate the model $J_{cm,}{}^{\perp}{}_{MOD}$ and compare it with the measured $J_{cm}^{\perp}$ as in Figure 31. Also included in that figure are i) the transport-measured $J_{ct} \equiv J_3$, ii) the magnetically-measured $J_{cm}^{\phi} \equiv J_2$, and iii) Kramer plots based on $J_{ct}(B)$ and $J_{cm}^{\varphi}(B)$.

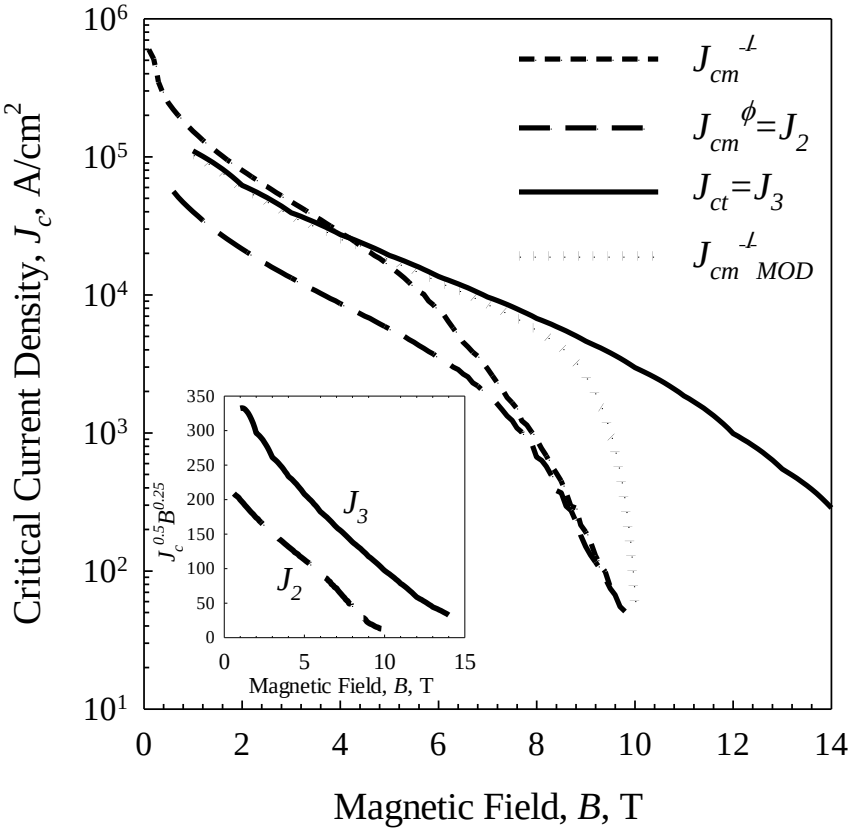

Figure 31. $J_{cm}^{\perp}{}_{MOD}$ (Equations 18a and 18b) as a function of B compared to J_{ct}, J_{cm}^{ϕ} and $J_{cm}^{\perp}$. The inset shows the Kramer plot of the same J_c-B curves to emphasize the different values of B_{irr} that can be measured depending on the technique.

In Figure 31, although $J_{cm,}^{\perp}{}_{MOD}$ *(B)* and $J_{cm}^{\perp}$ *(B)* do not track exactly, they both tend towards a common irreversibility field (B_{irr}, 10^2 A/cm^2 criterion) of about 10 T; the B_{irr} associated with J_{ct}*(B)* is projected to be about 16 T. Referring again to Figure 31 the differences between J_{ct}*(B)* and J_{cm}^{ϕ} *(B)* (i.e J_3 and J_2) and the differences between the corresponding B_{irr}s are clearly responsible for the bifurcation of the measured J_{ct}*(B)*and $J_{cm}^{\perp}$ *(B).*

It can then be inferred that the drop-off of $J_{cm}^{\perp}$ *(B)*, the *S*-dependence of that drop-off, and J_c- anisotropy are interrelated. Several authors have reported on the influence of sample size, at fixed *S* [184], [185], and fixed and variable *S* [186] on $J_{cm}^{\perp}$. Attention was directed primarily on measurements with the field applied parallel to the sample's long axis and various explanations for the size dependencies were offered. In a broad extension of the size-effect studies, Horvat *et al.* [179] compared the field dependencies of J_{ct} and $J_{cm}^{\perp}$ in PIT-processed MgB_2 strands, attributing observed differences to microstructural properties of the superconducting core – porosity and agglomerations of superconducting crystals. The model presented here also includes these basic elements but is bolstered on one hand by critical state analysis and on the other by detailed SEM observations.

3.4 Limited Connectivity- the Cause of the Anisotropic Critical Current Density

For an MgB_2 wire the microstructure of the reacted PIT strand core is characterized by an array of ~20 x ~2.5 μm polycrystalline MgB_2 fibers and their associated elongated pores aligned along the wire direction, as mention earlier with regard to Figure 26. The presence of anisotropic critical current density was initially surprising, given that the MgB_2 is polycrystalline with fine randomly oriented grains, as evidenced by Figure 27. However, in light of the evolution of fibrous stringers of Mg during the wire drawing process, the following explanation is proposed for the observed electrical anisotropy in MgB_2 strands.

The microstructure of the as-drawn but unreacted strand is depicted in Figure 32a which shows the B as the dark phase and the Mg as the white phase. As the strand is drawn down to its final diameter of 0.83 mm, the Mg elongates and fractures, forming isolated, aspected stringers (the white regions in Figure 32). It is well-known that Mg readily oxidizes in air. Accordingly an MgO or $Mg(OH)_2$ film will surround every starting Mg particle. As the Mg elongates with drawing, the brittle film will fracture leaving a partially coated surface.

During drawing, the B powder will be forced to rearrange itself into veins lying continuously along the length of the strand. The Mg vapor that evolves during HT permeates the B and begins to convert it to fibers of MgB_2. As a result of the density difference between B and MgB_2 [5] these veins will swell during this conversion (resulting in a 1.2-fold increase in volume assuming an initial B density of 65%) and will stop growing when either all the B is converted to MgB_2 or until neighboring veins of MgB_2 impinge upon each other. Just as in the internal Mg diffusion (IMD) process used for producing MgB_2 bulks and strands [168], [169], [187], [188] (which can be taken as an extreme case), each reacting Mg stringer leaves behind a matching vacancy. As a result these elongated pores that separate the veins of MgB_2 have a deleterious effect on the transverse connectivity. Impurity phases such as MgO, originating from the starting Mg particles and as a product of oxidation by B_2O_3 during the HT [75], [189], also decorate the surface of the MgB_2 veins and again contribute to the anisotropic connectivity. This explanation is presented pictorially in Figure 32, for clarity in terms of the pre-reacted structure (cf. Figures 22 and 26): i) Figure 32(a) shows the locations of

the elongated B and Mg sites; ii) in Figure 32b long dashed lines emphasize the continuous nature of the longitudinal B (future MgB_2) veins; iii) in Figure 32c short dashed lines emphasize the transverse B connections showing them to be both discontinuous and circuitous, leading to poor transverse connectivity in the heat-treated strand, and hence the large difference between the longitudinal and transverse critical current densities, $J_{ct}(B)$and $J_2(B)$; iv) the MgB_2 surrounding each pore in a FIBed TEM foil show a small, secondary phases, likely to be MgO, which serve to inhibit transverse supercurrent flow.

In short, the MgB_2 wires made from the PIT process consist of a series of poorly connected MgB_2 fibers. These fibers, consisting of a dense array of randomly oriented, polycrystalline grains, have excellent connectivity along their lengths. Fiber-to-fiber connections, however, are poorly connected and serve to reduce the azimuthal J_c, J_c^{ϕ}, which accounts for the differences between magnetic and transport J_c.

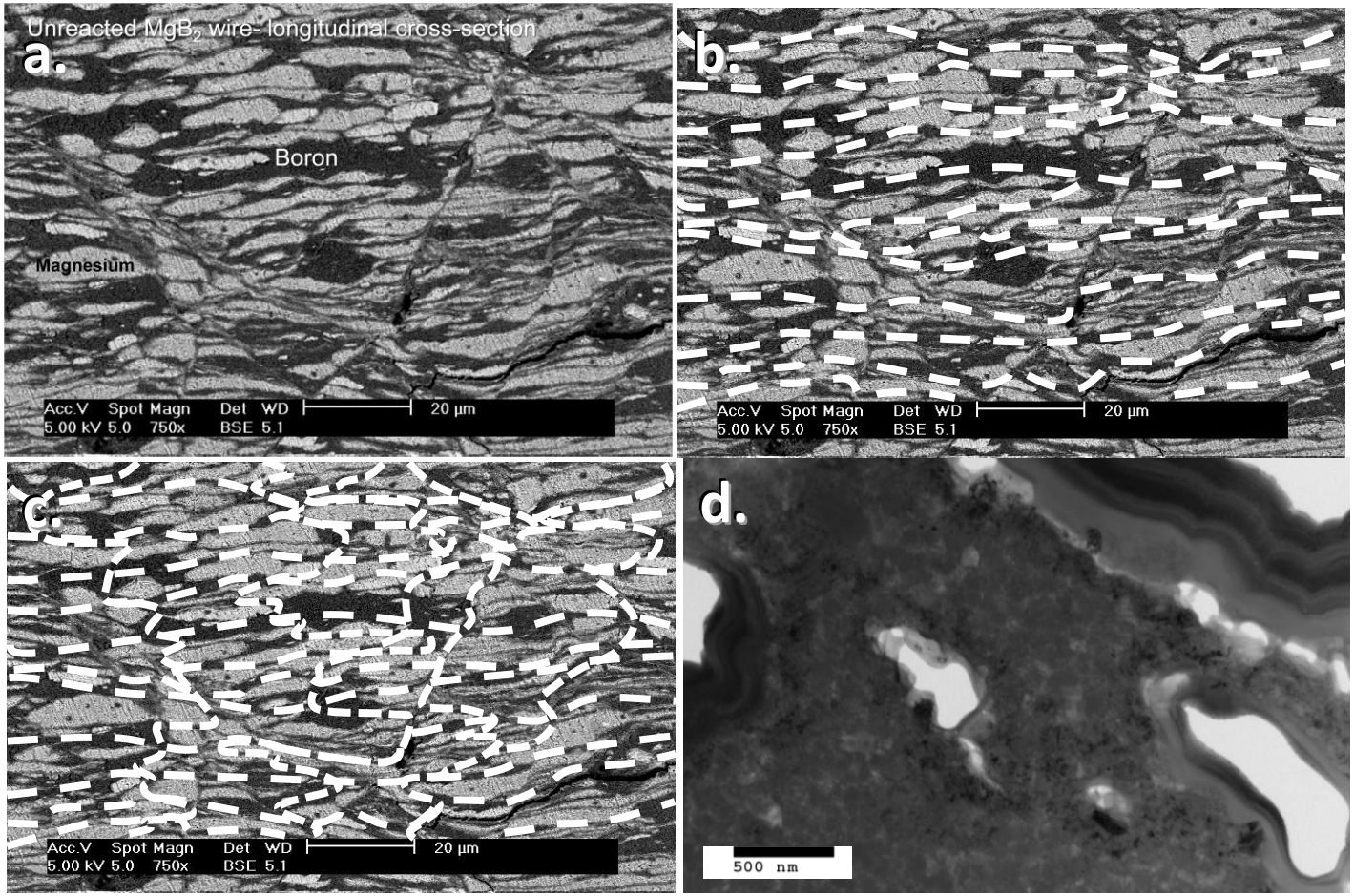

Figure 32. a) Unreacted Mg+B wire, longitudinal cross section; b) long dashed lines emphasizing the continuous nature of the longitudinal boron veins; c) short dashed lines showing the discontinuous and circuitous nature of the transversal boron connections; d) FIBed TEM foil of reacted MgB_2 showing likely oxide phases surrounding pores.

3.5 Limiting Case: IMD Wires

As previously mentioned, the internal Mg diffusion (IMD) process may be considered as a limiting case of the aforementioned PIT wire drawing process. Here, rather than several small agglomerations of Mg being drawn into aspected stringers, a single Mg rod is drawn together with the B powder. Additionally, the initial billet for these wires is assembled in an inert atmosphere, helping to limit the formation of oxide phases. For the sake of convenience, an image of an IMD wire is again presented in Figure 33 together with the microstructure after HT. It is evident that the microstructure of the IMD-route MgB_2 is drastically different than that of the PIT wire. Here the grains have a completely different morphology, being aspected and more lath-like in appearance. Additionally, the overall porosity of the MgB_2 phase is much reduced, having been transferred to the center of the wire.

Presumably with no possibility of an insulating oxide phase between large agglomerations of MgB_2 fibers (or indeed the existence of any fibers at all) the anisotropy of Jc in these samples would be much reduced. Accordingly, an IMD wire sample was prepared under similar conditions to the PIT wire mentioned earlier in this chapter[7]. Both $J_{cm}^{\perp}$ and J_{cm}^{ϕ} were measured on the IMD wire; these results are plotted in Figure 34.

[7] Specifically, the IMD sample was wire S1022-2281-675-30 HT at 675°C for 30 min.

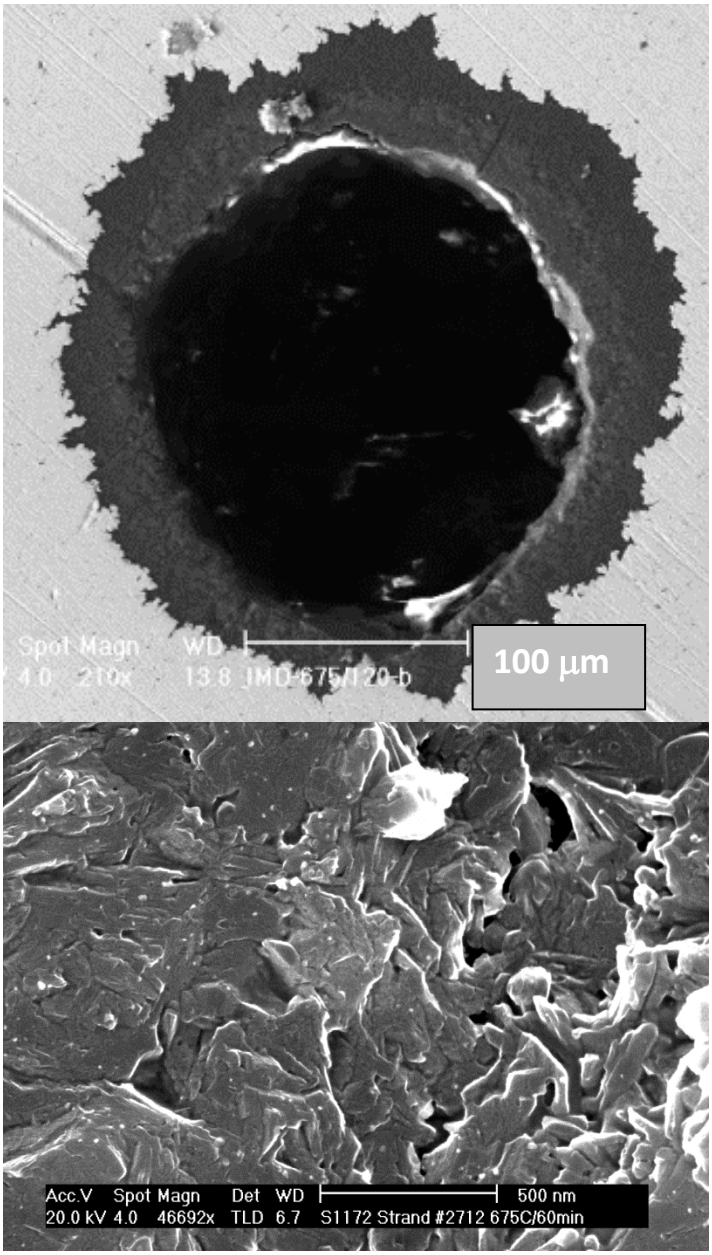

Figure 33. a.) Reacted monofilamentary Internal Mg Diffusion (IMD) MgB_2 wire showing dense MgB_2 reaction layer and large void where the Mg rod was located before heat-treatment and b.) Fracture-SEM microstructure of IMD wire showing dense arrangement of grains[8].

[8] These images were taken by Guangze Li

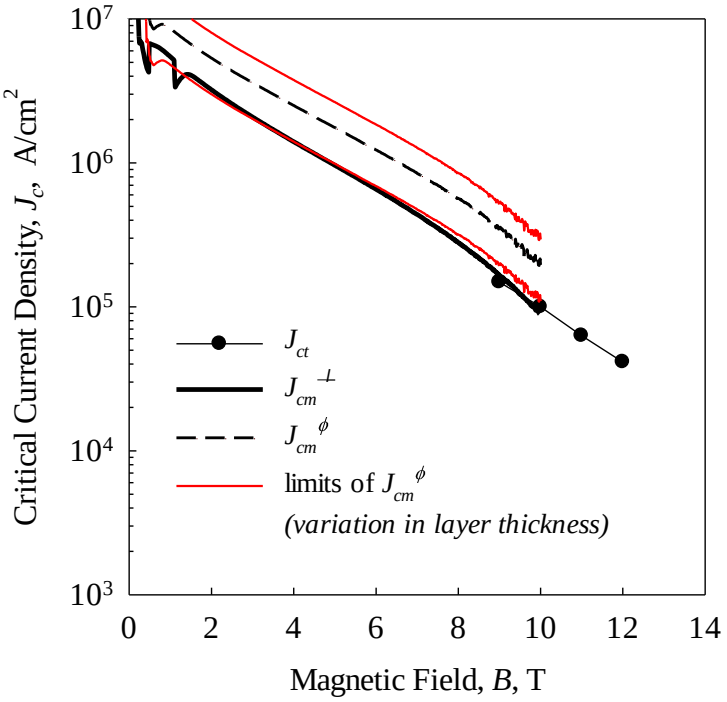

Figure 34. J_{ct}, J_{cm}^{ϕ} and $J_{cm}^{\perp}$ measurements performed on IMD wire.

Figure 34 shows a barely discernable bifurcation between J_{ct} and $J_{cm}^{\perp}$ occurring at a much higher magnetic field for the IMD-route wire than for the PIT-route MgB_2. Unfortunately, limitations in either the sensitivity of the magnetic measurements or the limits on the current source for the transport measurements prevent one from obtaining a more definitive comparison between the two types of measurements.

The most interesting aspect of Figure 34 is the comparison of the azimuthal CCD J_{cm}^{ϕ}, to the other values. From the previous sections it was stated that the J_{cm}^{ϕ} is dependent on the superconductive properties along the radial component of the strand.

The error in J_{cm}^{ϕ} is rather large due to the uneven thickness of the MgB_2 layer. An average layer thickness is used to determine the value of J_{cm}^{ϕ}; Figure 34 presents the limits of the value of J_{cm}^{ϕ} based on the minimum and maximum thicknesses of the MgB_2 layer (the red lines). Nevertheless, it is seen that for all observable variations in MgB_2 layer thickness the value of J_{cm}^{ϕ} is equal to or greater than the values of $J_{cm}^{\perp}$. These results imply that the radial connectivity is at least as good as the longitudinal connectivity, if not better.

3.6 Concluding Summary of Connectivity in MgB_2 Wires

After a complete analysis of a PIT-route MgB_2 wire important relationships were established between the drawing-induced unreacted precursor microstructure, the reacted microstructure, and the resultant superconductive properties in terms of J_c probing different types of current paths. It was found that the transverse or azimuthal current paths are poorly connected, likely due to insulating oxide phases. Additionally, the longitudinal current paths, consisting of a dense arrangement of randomly oriented polycrystalline grains, were seen to exhibit greater connectivity. Alternatively, the IMD-route MgB_2 wires are not restricted by limited azimuthal connectivity. Indeed, from the same techniques used to analyze the PIT-route MgB_2, it is seen that the azimuthal connectivity may be greater than the longitudinal connectivity, a phenomenon not

entirely understood but likely the result of defects along the longitudinal axis of the superconducting strand or the inhomogeneous MgB_2 layer thickness. It is evident then that the superconductive properties of MgB_2, besides being dependent on intrinsic properties such as grain orientation (which leads to percolation paths for supercurrent) and doping (which changes the electronic scattering and serves to reduce the anisotropy), extrinsic factors such as connectivity must be considered. These observations again re-enforce the need to deconvolute these topics.

Chapter 4: Synthesis and Microstructural and Electronic Characterization of Undoped c-axis Oriented MgB_2 Thin Films

C-axis oriented MgB_2 thin films were grown on 6H-SiC substrates using PLD. The PLD target was made from the high pressure and high temperature reaction of Mg and B to form large-grained (~1-50 μm) MgB_2. A Mg cap layer was applied, also through PLD, and the films were sintered *in-situ*. Microstructural analysis via electron microscopy found that the resulting grains of the film were ~19-30 nm, depending on the applied heat treatment schedule. XRD analysis showed the MgB_2 films to be c-axis oriented; the *a*-axis and *c*-axis lattice parameters were determined to be 3.073 ± 0.005 Å and 3.528 ± 0.010 Å, respectively.. The superconducting critical temperature, $T_{c,onset}$, increased monotonically as the annealing temperature was increased, varying from 25.2 K to 33.7 K. The superconducting critical current density as determined from magnetic measurements, J_{cm}, at 5 K, was 10^5 A/cm^2 at 7.8 T; at 20 K, 10^5 A/cm^2 was reached at 3.08 T. Additionally, examination of the pinning mechanism showed that the films follow the grain boundary, or surface pinning, mechanism quite well, in contrast to the behavior seen in MgB_2 wires in which deviations are seen at high b ($b = B/B_{c2}$).

4.1 Pulsed Laser Deposition of MgB_2 Thin Films: Approach

Since the discovery of superconductivity in MgB_2 in 2001 [2] much research has been done to improve and manipulate its properties for superconducting applications. Generally speaking, materials-science-based investigations have followed three main thrusts [5]: i) improving the J_c through increases in flux pinning, ii) increasing the B_{c2} of the material by impurity scattering, and iii) increasing the inter-grain connectivity of the material. However, separating these variables from each other is problematic in that MgB_2 has many unique characteristics that make synthesis of a well-connected, homogeneous sample rather difficult. These challenges include the presence of oxide layers on both the precursor Mg [96] and the precursor B [97] (in the forms of MgO and B_2O_3, respectively) and the high vapor pressure of Mg [85] which makes high-temperature reactions for improving homogeneity difficult without specialized high-pressure apparatus.

We have used superconducting thin films prepared by PLD to deconvolute these topics. Pulsed laser deposition is an ideal tool for systematically adding doping precursors or impurities for structure-property investigations of the MgB_2 system. The UHV chamber and proper filtering of the process gas used to control the plasma plume allows for the careful control of the impurities allowed into the system. Of course, all these precautions are unnecessary when the starting MgB_2 PLD target itself contains the

same impurities one is attempting to avoid. Targets for PLD have been made using i) compressed MgB_2 powder, either sintered or unsintered [190], ii) a specially reacted combination of Mg and B precursor powders [94], [191], [192], or iii) individual Mg and B precursor targets [193][92]. Figure 35 outlines the various methods used for MgB_2 PLD thin film synthesis. No matter the route employed, the main issue with traditional powder synthesis for targets is oxide contamination of the starting powders; due to the small grain sizes of the powders, the resultant increase in surface area allows for a greater chance of oxide passivation on these surfaces, which contaminates the target before deposition is even started. It is clear, then, that one of the simplest methods to reduce the oxide contamination of the target, and hence of the final film, would be to limit the initial surface area of the starting powder. However, this method has its own drawback- namely the shrinking-core MgB_2 reaction where Mg vapor or liquid contacts the surface of the B grain, first forming MgB_7, followed by MgB_4 and finally MgB_2 [65]. Unfortunately, the reaction kinetics for the shrinking core model are fairly slow and require, for a 100 μm diameter fiber, a reaction time of ~1 h. in liquid Mg at 1000^{o}C [64]. Clearly, even though thin film synthesis of MgB_2 can be used as an ideal mechanism for the investigation of fundamental MgB_2 properties, there is no escaping the need for high-pressure, high temperature synthesis of relatively pure MgB_2, at least initially for the synthesis of the target.

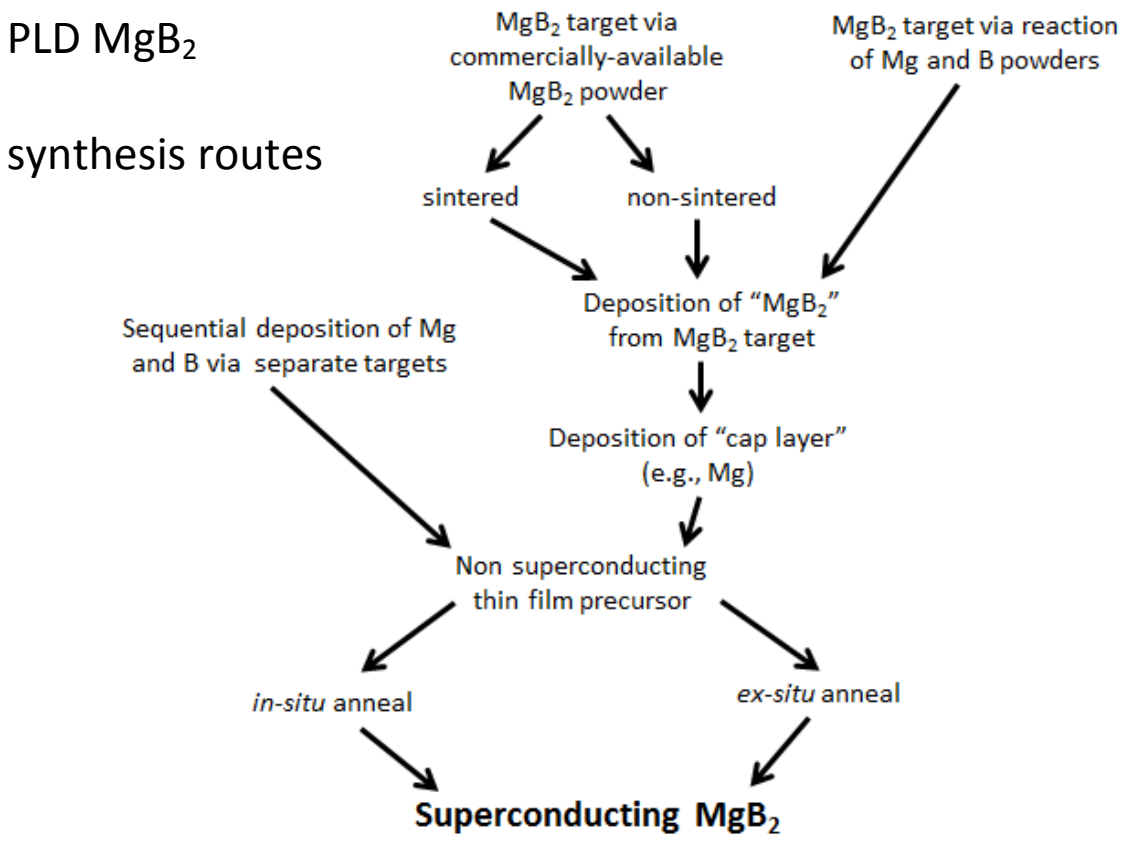

Figure 35. Various PLD synthesis routes of MgB_2 thin films.

4.2 PLD Procedure

To help synthesize homogeneous MgB_2 for use in PLD, it is necessary to first manufacture a high density, oxide-free (or as close as is practically possible) target. To this end we have synthesized coarse-grained MgB_2 from ~60 mesh B powder (Sigma Aldrich, 99% Lot# MKBG4568V) and Mg turnings, (Alfa Aesar, 99.98%) with a composition of $Mg_{35}B_{65}$. The elemental ingredients were RF-induction heated for 10

min at 1500^{o}C in 10 MPa of Ar in a specially instrumented autoclave; for further details please refer to [56]. The resulting ingot, consisting of homogeneous MgB_2 (~50 μm grain size) plus unreacted Mg, was ~2.0 cm in diameter. A section of the ingot was use for the PLD target. Similarly, Mg turnings were melted without B to provide for a Mg target. All MgB_2 ingots were carefully stored in a desiccator to prevent them from reacting with ambient moisture; ingots left out in the open were found to pest into powder in a period of days to weeks (dependent, of course, on the relative ambient humidity). This effect has been previously noted in MgB_2 thin films [194] and bulks [195]. Electron probe microanalysis (EPMA) performed on a sample of the ingot, revealed stoichiometric MgB_2, Mg, and 0.5 at% O [56] (most likely due to surface oxide contamination).

After careful cleaning and polishing, the MgB_2 and Mg targets were mounted on target posts in the PLD chamber with Ag paint such that the polished target surfaces were ~35 mm from the substrate (this distance represents the closest substrate-target distance practically achievable with our PLD configuration). The vacuum chamber was then pumped until the base pressure read ~1 x 10^{-8} to 5 x 10^{-7} torr on the attached cold cathode gauge. The heater was then set to 375^{o}C which, allowing for the thermal diffusivity of the Inconel 400 substrate holder, means that the substrate itself acquired a temperature of 300^{o}C, as verified by a run in which a Type-K thermocouple was welded directly to the surface of the substrate holder during the heating cycle. The set-point temperature and the actual substrate temperature were both recorded for calibration purposes. The substrate chosen was 6H-SiC ((0001)-oriented), as its "a" lattice parameter of 3.081Å closely matches that reported for MgB_2 (deviation -0.2%, resulting in compressive stress).

Additionally, SiC does not contain any oxygen, thus preventing the formation of the secondary oxide phases that are seen in MgB_2 thin films deposited on Al_2O_3 [196]. However, although SiC substrates have the potential to react with MgB_2 at elevated temperatures (forming Mg_2Si as a reaction product), Gu *et al.* [197] and He *et al*. [198] both note little second phase formation, even up to $T = 800^oC$ [198].

All depositions took place in high-purity Ar at 10 Pa. The Ar was nominally 99.998% pure and was further filtered via a Centorr Ti getter furnace (set to 800^oC) and a Microtorr MC1-902F in-line filter. The laser energy was set to 330-350 mJ and focused into a small spot. From analysis of the laser interaction with the burn paper, it was determined that the energy density across the laser spot was not uniform. The energies used were ~330-350 mJ. The energy densities, depending on how the laser spot size was measured, were likely in excess of 12-20 J/cm^2. Please refer to Chapter 2 on more details concerning this issue.

The MgB_2 was deposited for 20000 pulses at 10 Hz as slower pulse rates served to inhibit the deposition rate. 10000 pulses of Mg were subsequently deposited at 10 Hz. After deposition, Ar was introduced to the chamber to bring the pressure up to ~80 kPa to prevent Mg loss during the subsequent due to this element's high vapor pressure annealing steps, Table 2. The temperature was ramped at 20^oC/min. to the final annealing temperature ($550\text{-}750^oC$) and held for the annealing time (1-30 min), after which the heater switch was turned off and the substrate allowed to rapidly cool (typically ~30-50^oC/min.). After annealing, the effective growth rate was determined to be very slow, at 0.065 Å/pulse. Table 2 lists the annealing parameters used in the thin film experiments.

Table 2. Heat-Treatment Parameters and resulting T_c for PLD, *in-situ* HT, MgB_2 thin films.

t_{anneal}, min.	T_{anneal}, °C				
	550	*600*	*650*	*700*	*750*
0	MgB_2-079 T_c < 5 K				
1	MgB_2-071 T_c = 25.3 K	MgB_2-072 --	MgB_2-070 T_c = 29.5 K	MgB_2-069 T_c = 30.4 K	--
10	MgB_2-066 T_c = 25.2 K	MgB_2-104 T_c = 28.2 K	MgB_2-067 T_c = 30.1 K	MgB_2-068 T_c = 32.3 K	MgB_2-115 T_c = 33.7 K
30	MgB_2-076 T_c = 28.3 K	MgB_2-075 T_c = 29.1 K	MgB_2-074 T_c = 29.4 K	MgB_2-073 T_c = 33.4 K	--

4.3 MgB_2 Thin Film Microstructural Properties: X-ray Diffraction Studies

Due to the small MgB_2 volume of the 3 mm x 3 mm samples given in Table 2, a larger MgB_2 sample was made using the exact same deposition parameters as MgB_2 so as to obtain a larger interaction volume for XRD studied. Due to MgB_2 having a low X-ray scattering coefficient combined with the fact that the films were 100-200 nm thick, Grazing Incidence Diffraction (GID) was employed. The GID XRD plot of an MgB_2 thin film HT at 700°C for 10 min. after deposition[9], using an incident angle of 0.5°, is represented in Figure 36; Cu K_α (λ = 1.5406 Å) radiation was used for all experiments. Although limited in intensity, the only visible non-substrate peaks are for the (0 0 0 1) and (0 0 0 2) reflection of MgB_2, showing that the films are c-axis oriented. Since this is a GID measurement, the SiC substrate peak, e.g. the (0 0 0 6) and (0 0 0 12) reflections at 2θ = 35.63° and 71.26° respectively, are attenuated in this scan. Figure 37 shows the

[9] Specifically, sample MgB_2-182A with an area of 3 mm x 10 mm

rocking curve around the MgB_2 (0 0 0 2) reflection. The FWHM of this rocking curve is 770 Arcseconds (0.214^o), comparible to values found in the literature for PLD MgB_2 thin films [199].

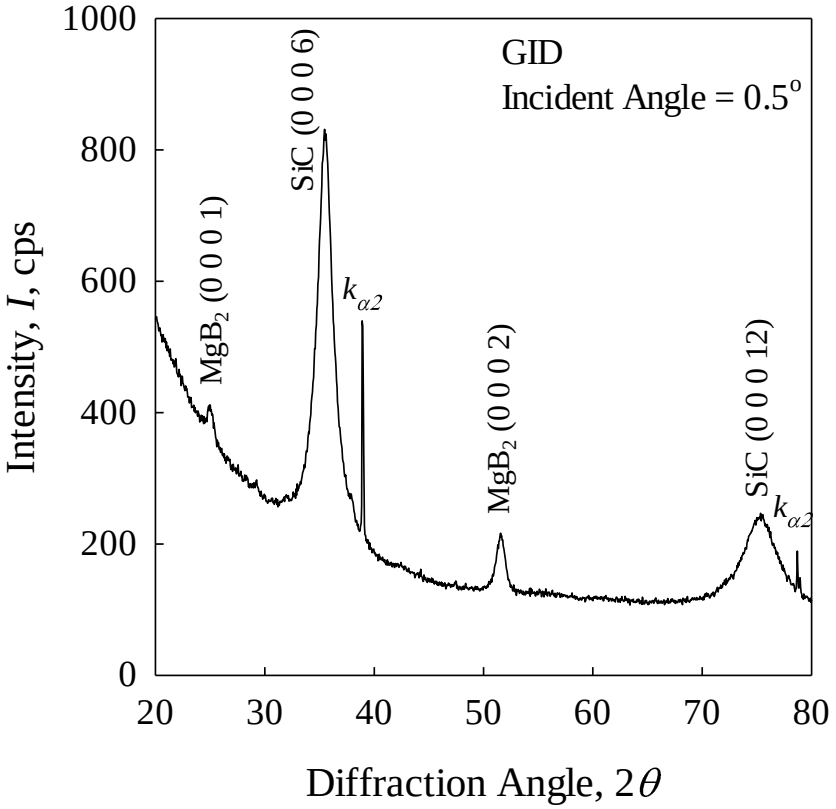

Figure 36. GID at 0.5^o XRD of MgB_2 HT at 700^{o}C for 10 min.

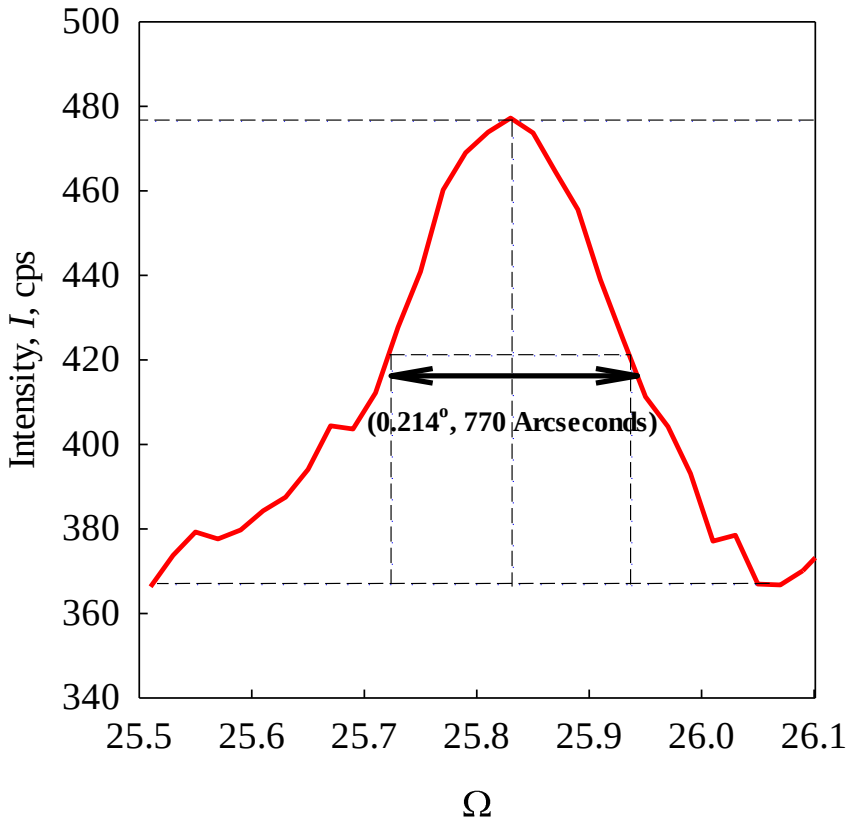

Figure 37. Rocking curve about MgB_2 (0 0 0 2) reflection.

Figure 38 sows the GID in-plane scan, taken at the same incident angle. Here only the in-plane MgB_2 $(10\bar{1}0), (11\bar{2}0)$, and $(20\bar{2}0)$ reflections are apparent. Also noticeable are reflections from Ag, resulting from the Ag paint used in the mounting of the sample. Some Ag paint likely caked onto the sides of the films. Finally, some reflections are visible that indicate the presence of unreacted Mg.

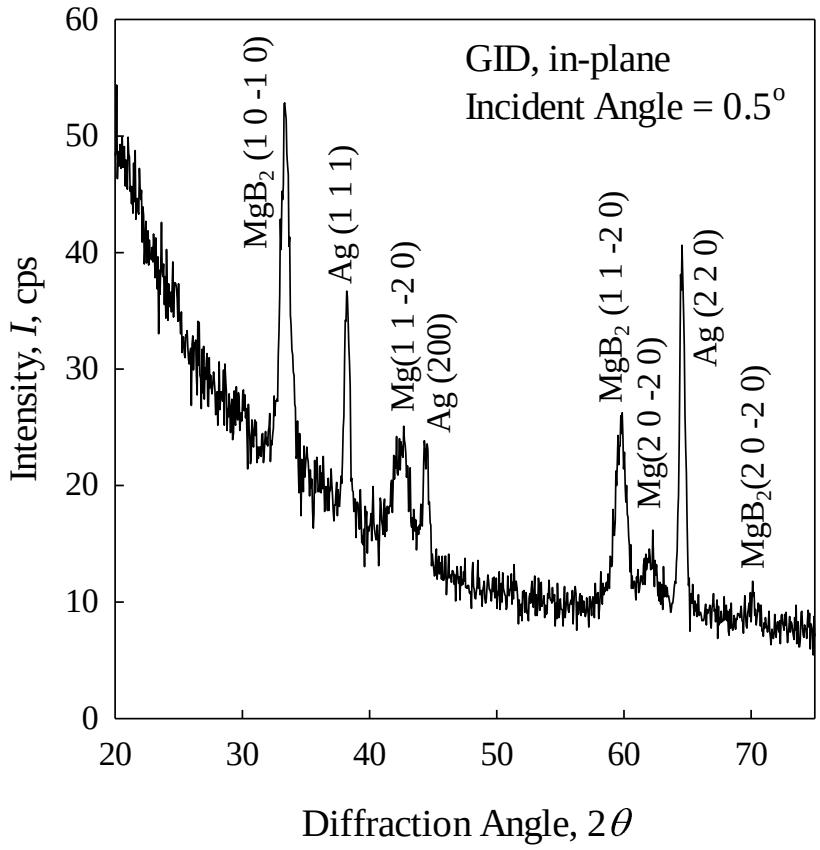

Figure 38. In-plane GID at 0.5° XRD of MgB_2 HT at 700°C for 10 min.

From the above data the "a" and "c" lattice parameters were determined to be 3.073 ± 0.005 and 3.528 ± 0.010 Å, respectively. These parameters were determined by careful peak-fitting of the highest order reflections. Error was determined by changing the criteria of the peak fit. The data in Figure 38 suggests that, though the films are c-axis oriented, the *a*-axis is randomly oriented in-plane.

Further analyses were done to establish the texturing, if any, of the MgB_2 films. Here the value of 2θ was fixed at 42.44°, corresponding to the $(10\bar{1}1)$ reflection, and α and β were rotated from 0-90° and 0-360°, respectively. These data are presented in the pole-figure of Figure 39 and shows the 6-fold symmetry of the MgB_2 film and SiC substrate, consistent with similar analyses performed by Pogrebnyakov *et al.* [200]. Here two spots are visible every 60°, one corresponding to the SiC $(10\bar{1}4)$ peak and another corresponding to the MgB_2 $(10\bar{1}1)$ peak. Based on the literature [200] this orientation relationship is not unexpected. However, as evidenced from the data in Figure 38, not every grain has this relationship. To truly establish the degree of texture in-plane, it is necessary to perform more pole-figure measurements around additional MgB_2 reflections.

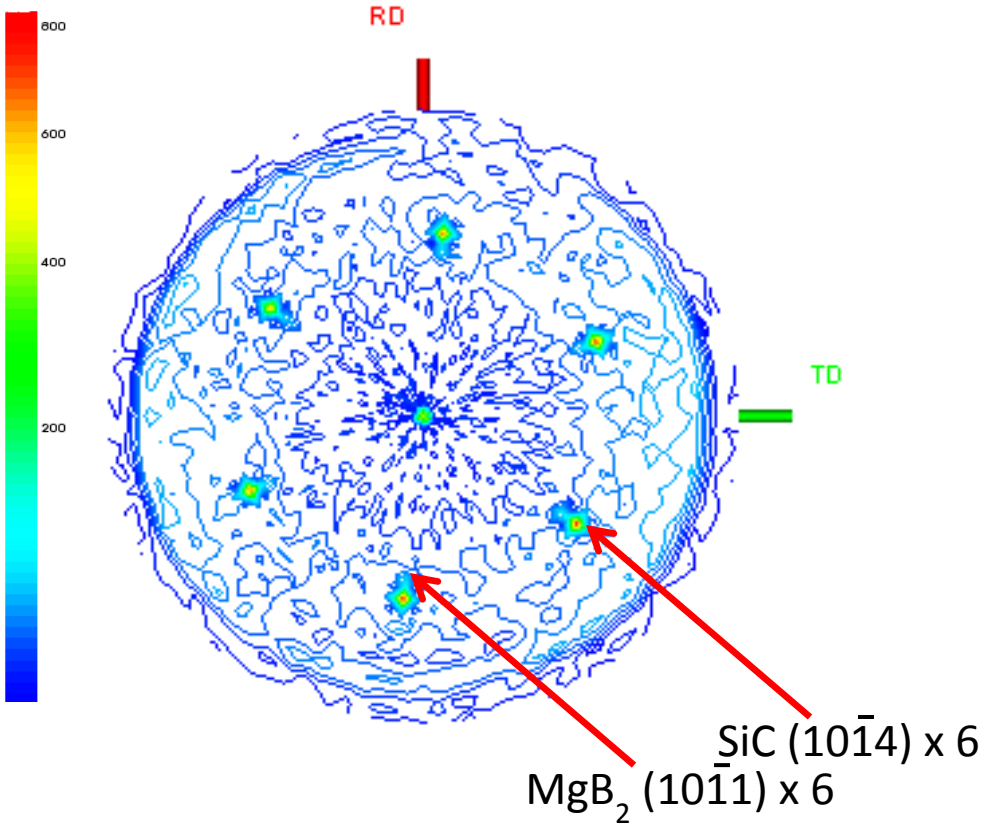

Figure 39. X-ray diffraction pole figure of undoped MgB_2 thin film.

4.4 MgB_2 Thin Film Microstructural Properties: Electron Microscopy Characterization

Further characterization of undoped MgB_2 thin films was performed via both SEM and TEM. Figure 40 shows the microstructure of sample MgB_2-068 (see Table 2). Here one can see that grains are small, exhibiting sizes, on average, of less than 30 nm. Further analysis of the microstructure of other HT temperatures for the same HT time (10 min.), presented in Figure 41, shows a possible increase in grain size for increased HT temperatures at a fixed time. During HT for 10 min. the average grain size increased

monotonically from 23.4 ± 4.7 nm at 550^{o}C to 27.3 ± 2.8 nm at 700^{o}C. However, these results must be interpreted with caution in that a large error is present in the measured averages. Further investigations of grain growth at longer HT times were impeded by the loss of Mg during these longer annealing times.

From analysis of the microstructure it is unclear what the precise growth mechanism is for these films. Figure 42 shows an intermediate magnification view of the film surface, showing large areas of unreacted Mg from the Mg cap layer deposited pre-annealing (dark areas) together with large colonies of MgB_2 grains. All told, the surfaces of the films are fairly rough. Figure 43 shows a low magnification BSE image of the film surface. Large agglomerations of Mg and dark areas representing splashing from the target are visible.

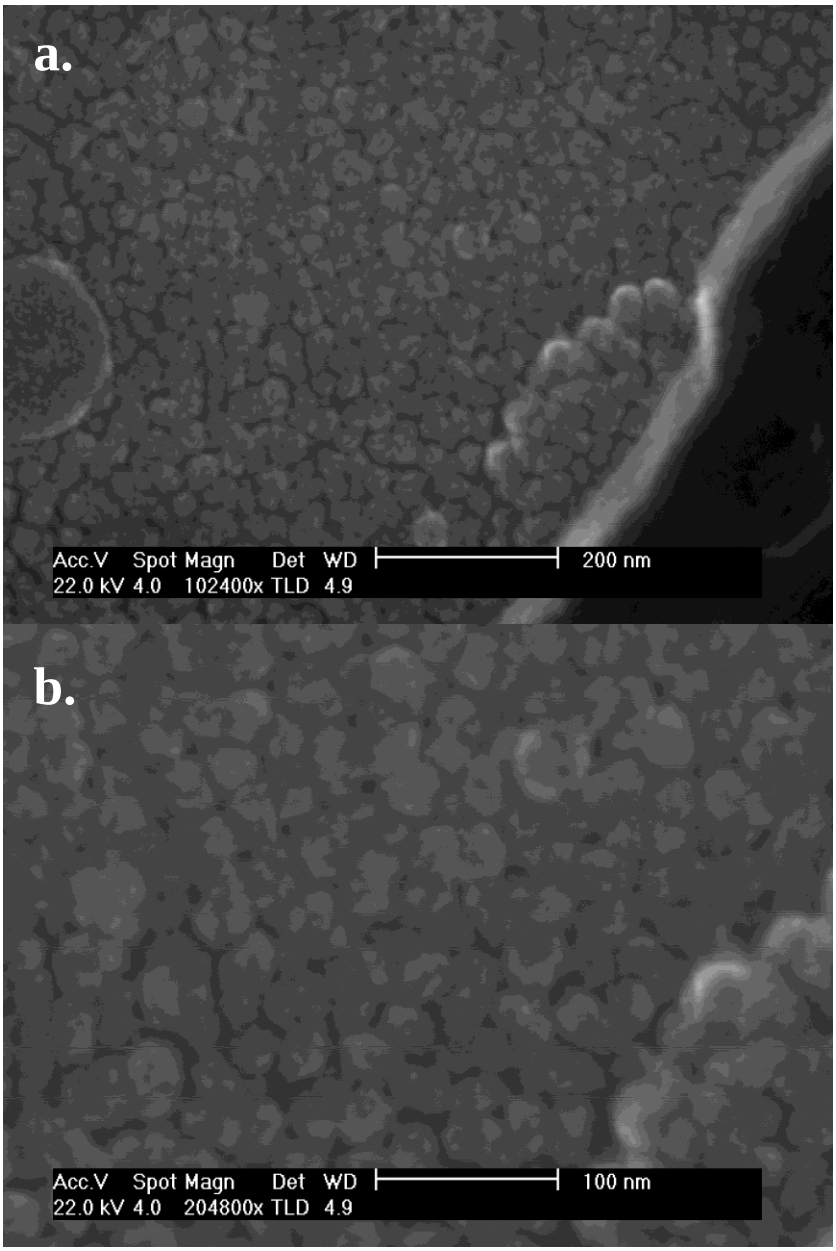

Figure 40. a). Grains of sample MgB_2-068 at ~100 kx magnification; b) Detail of the microstructure at ~200 kx magnification.

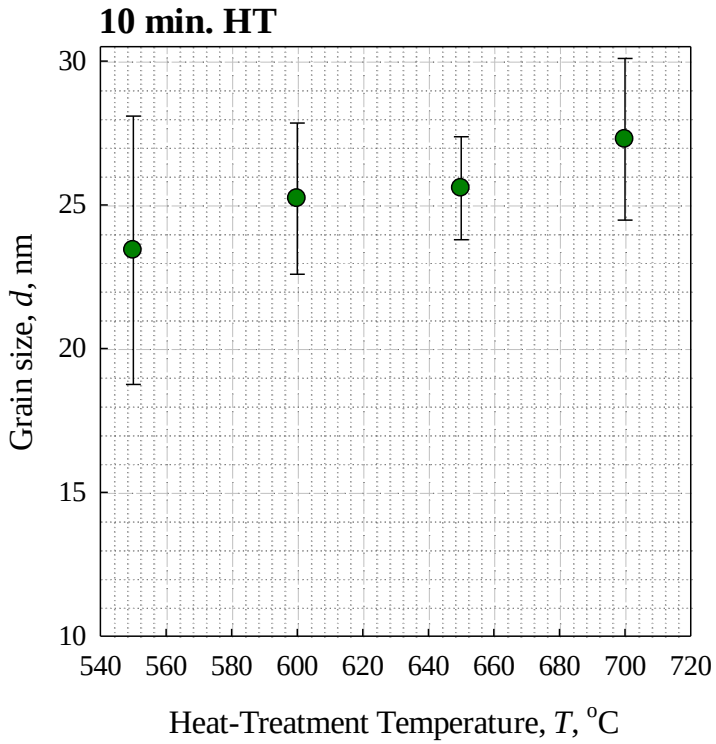

Figure 41. Relationship between average grain size and HT temperature for 10 min. HT time.

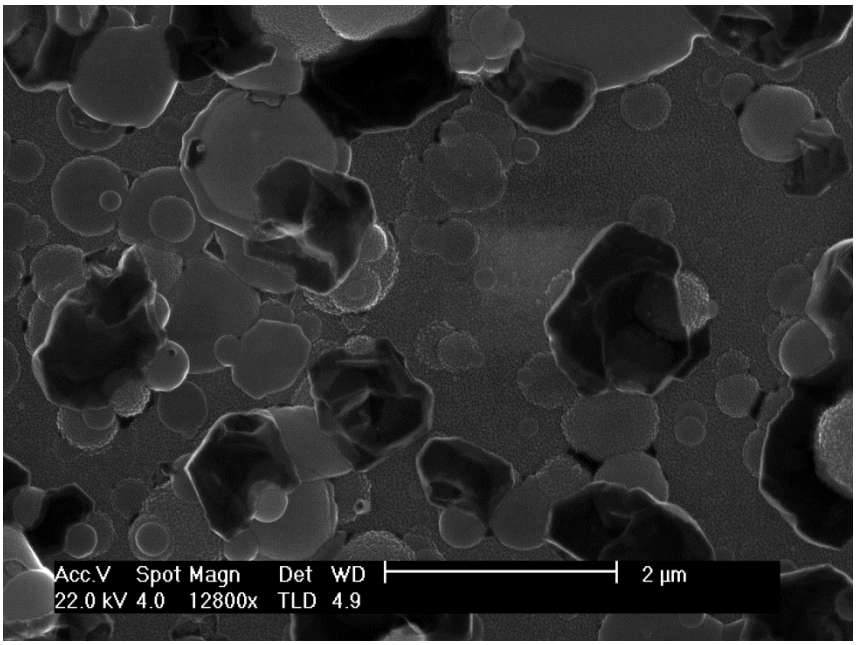

Figure 42. High resolution through the lens detector (TLD) image of undoped MgB_2 PLD sample MgB_2-068.

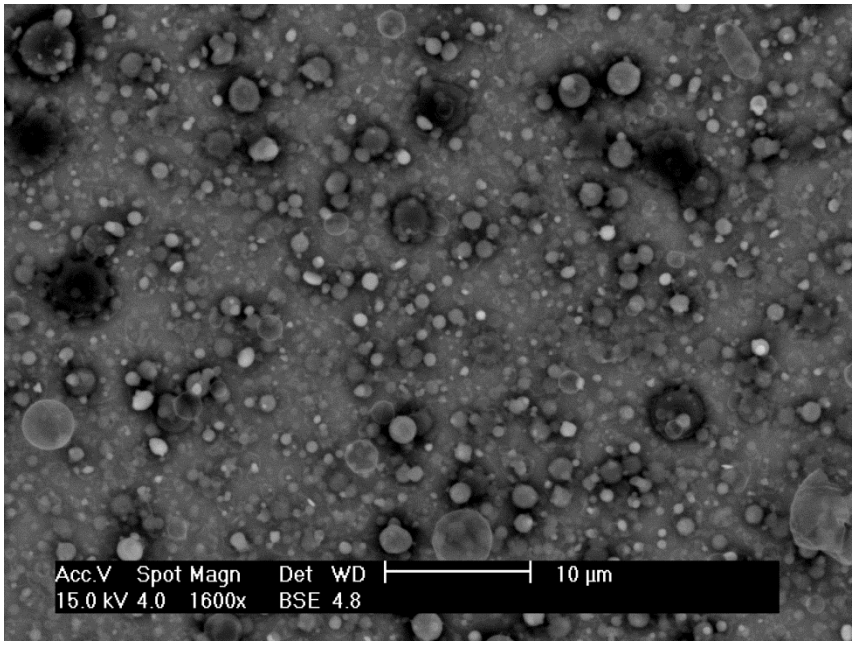

Figure 43. High resolution BSE image of undoped MgB_2 PLD sample MgB_2-068.

Further characterization of undoped MgB_2 samples was performed via TEM. TEM foils were prepared via FIB procedures outlined in Chapter 2 of this work. Figure 44 shows the cross-sections of the film and the substrate following the ion-beam milling for the creation of a TEM foil. The top layer is Pt which was deposited in the FIB to protect the MgB_2 from the ion milling procedure. Large agglomerates are noticeable in the micrograph, which are likely a result of splashing from the MgB_2 target caused by the high energy densities needed to ablate the MgB_2. These features, ~0.2-0.5 μm in diameter, are found dispersed throughout the film surface. Their presence is likely due to the fact that the MgB_2 and the Mg in the MgB_2 target ablate at different rates (with Mg ablating at a much faster rate, likely due to its high vapor pressure), leading to an effective "undercutting" of material in the target. Although techniques such as off-axis deposition can help increase the smoothness of the film surface, as reported in [201], the purpose of this work was to investigate the effect of using a highly dense target on the resulting superconducting properties and microstructure of the MgB_2 thin film.

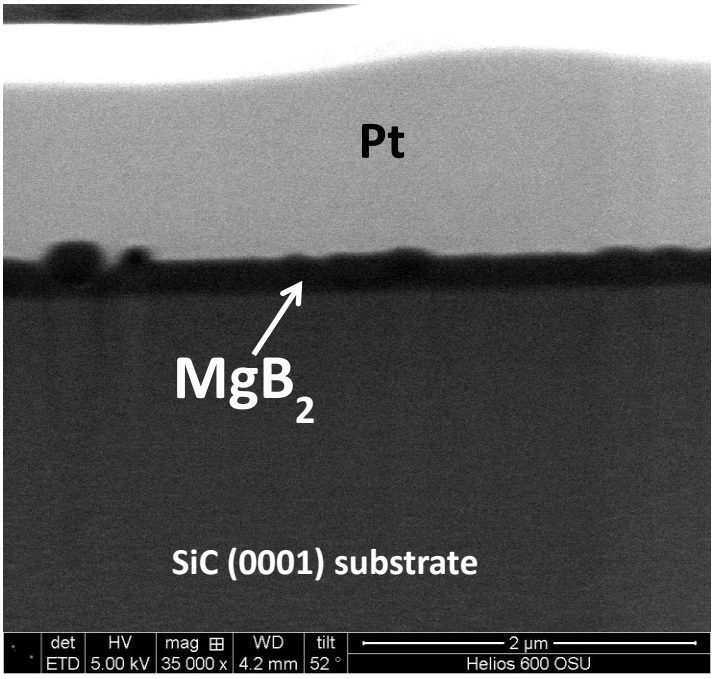

Figure 44. Cross-sectioned FIB-produced TEM foil showing large agglomerations of material that are likely the result of "splashing" from the target.

Figure 45 shows the bright-field TEM of the final thin film cross-section of MgB_2-068 looking down the $[20\bar{2}0]$ axis. The inset shows the selected area diffraction (SAD) pattern. The orientation relationship derived from the analysis of the SAD pattern for this grain showed that an orientation relationship of $(0001)[11\bar{2}0]_{MgB_2} \| (0001)[11\bar{2}0]_{6H-SiC}$. This particular film, MgB_2-068, also had a final average thickness of 230 nm, with the other films having similar thicknesses. This orientation relationship given above may not be representative of the entire sample, however, as only a small fraction of the MgB_2 film was investigated.

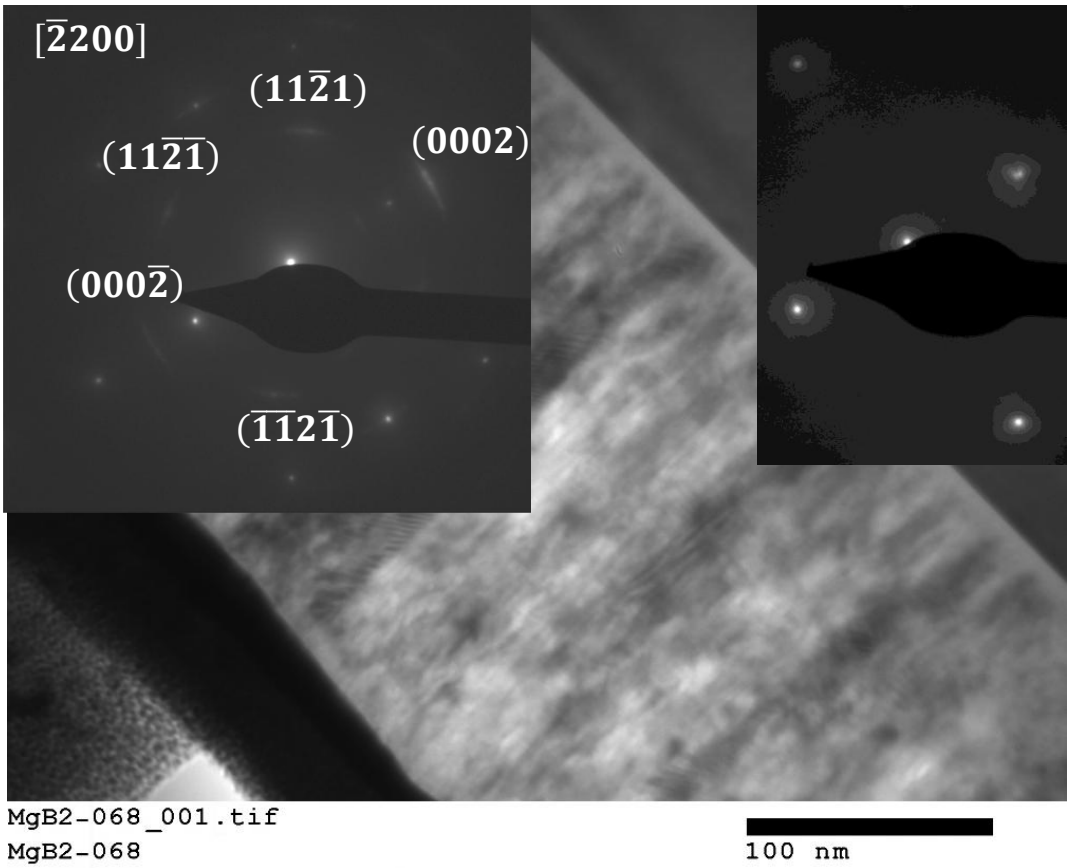

Figure 45. Bright-field TEM micrograph of MgB_2-068. The accompanying diffraction pattern (top-left) shows the expected hexagonal symmetry of the MgB_2 phase. The TEM diffraction in the top-right shows diffraction from only the SiC substrate.

Figure 46a shows the dark field image of the film, highlighting strain or a second phase at the substrate-film interface that appears to propagate through the MgB_2 layer to the film surface. These white regions roughly correspond to the distance between grain boundaries seen in the SEM characterization in Figure 40 (25-30 nm). SAD patterns were also obtained on the large agglomerates which were seen to be diffuse, indicating that these features are largely amorphous in nature (Figures 46b and 46c).

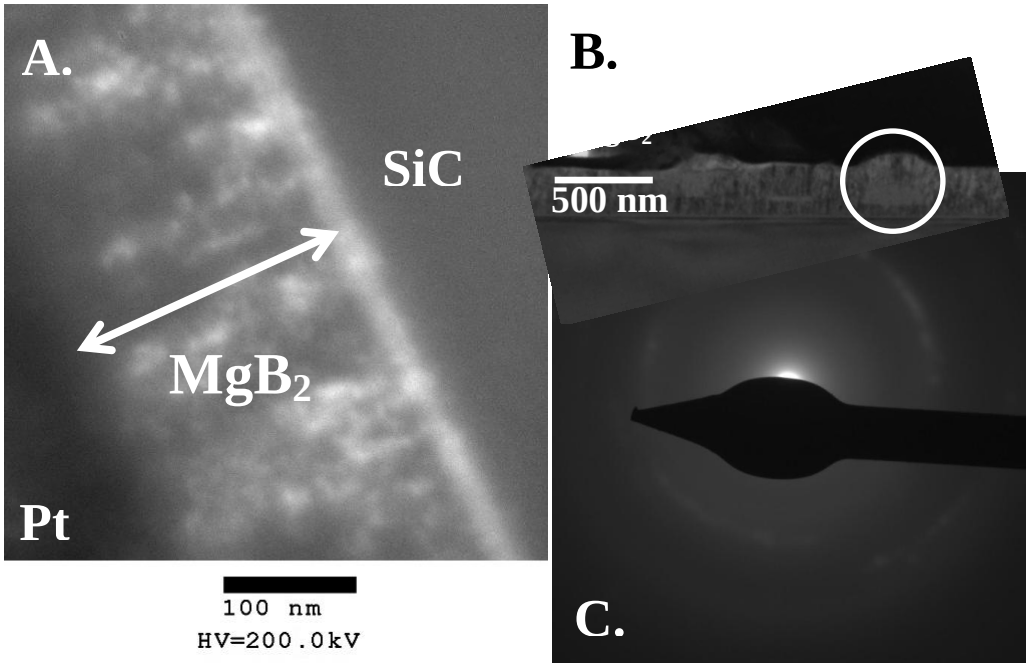

Figure 46 a) Dark-field TEM micrograph of MgB_2-068 showing strain at the interface which propagates toward the surface; b) Bright-field TEM image detailing typical agglomerates; and c) SA diffraction pattern of the agglomerate showing diffuse rings, indicating that these regions are largely amorphous.

4.5 Superconductive Properties of Undoped MgB_2 Thin Films

Superconducting properties such as *M* vs. *T* and *M* vs. *B* were measured using a Quantum Design Model 6000 PPMS. The superconducting critical temperature a, T_c, was determined as a function of *B* via the ac susceptibility option (ACMS), enabling the determination of the B_{c2} as a function of *T*. Susceptibility was measured at 10 Oe and 1000 Hz after a zero-field cool (ZFC) sequence was applied to the sample. Magnetization (*M-B)* loops were run using the DC extraction measurement on the ACMS option which

uses the ACMS accessory as a DC magnetometer. The magnetic field ramp rate was 130 Oe/s. Magnetic J_c was calculated from the height of the hysteresis loops using the formula $J_{cm}\left[A/m^2\right] = 2\Delta M\left[A/m\right]/\left\{b\left(1-b/3a\right)\right\}$ where *a* and *b* are the film dimensions in meters and $a > b$. Hysteresis loops were taken with the film surface perpendicular to the magnetic field.

The effect of heat-treatment temperature on the resultant onset T_c of the superconductor is plotted in Figure 47. These results represent annealing times of 10 minutes; longer HT times marginally increased $T_{c,onset}$ but served to increase the width of the transition. Increasing the HT temperature from 550^{o}C to 750 ^{o}C caused T_c to increase from 25.2 K to 33.7 K. Lower T_c values, at least in part, may be attributed to the lack of full reaction at the lower HT temperatures. During the PLD procedure, the "MgB_2" deposited on the substrate surface is highly disordered: lack of appropriate stoichiometry, the presence of defects, and lack of structure are all prevalent. It is hypothesized that lower HT temperatures do not provide enough activation energy for all of these issues to be overcome for "pure" MgB_2 to form. Although higher HT temperatures do provide this energy, the Mg volatility prevents MgB_2 from being stable during *in-situ* PLD annealing at $T > 750^oC$; the MgB_2 reflections were undetectable in the XRD, indicating Mg loss and decomposition of the MgB_2 phase. Consequently, the lack of coherence caused by the presence of disorder serves to reduce the T_c from the 39 K seen in pristine MgB_2 [2], [3].

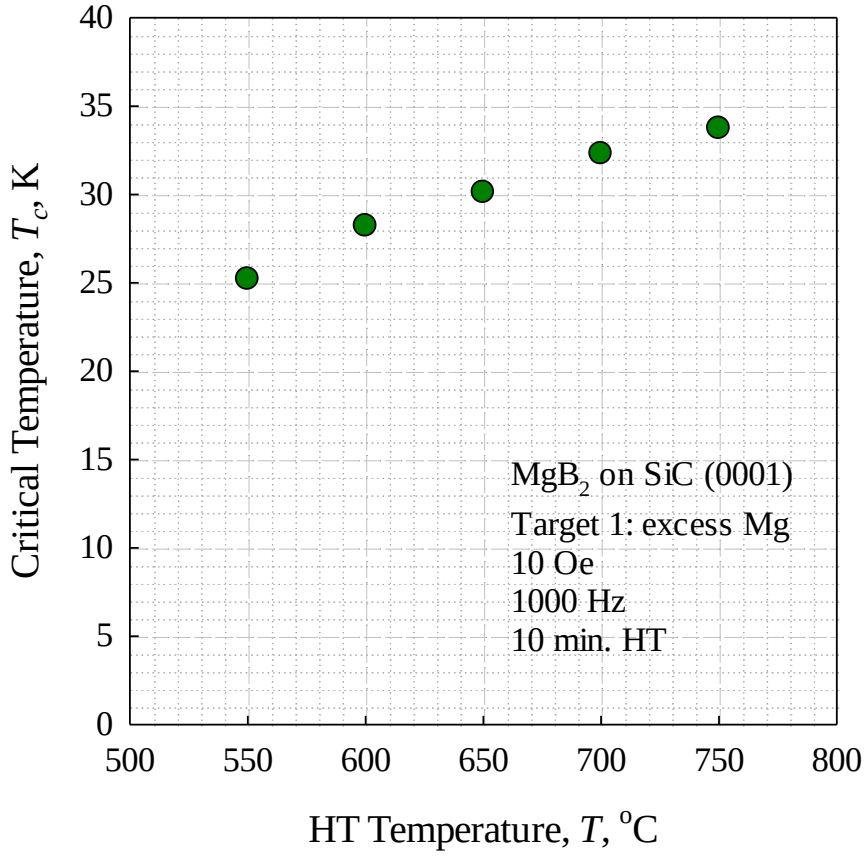

Figure 47. Evolution of onset T_c with heat-treatment temperature at 10 mins. heat treatment time; longer HT times marginally increased T_c but served to increase the width of the transition.

Figure 48 shows the relationship of the B_{c2} vs. T data on MgB_2 thin films annealed at different temperatures for 10 mins. Increasing the HT temperature serves to increase *both* B_{c2} and T_c (see also Figure 10) without changing the slope of the plot. The slope would of course change value if some degree of doping or impurity phase were present (usually with an increased value of B_{c2} at 0 K and a decreased value for the 0 T T_c); the lack of such a change suggests that increasing the HT temperature serves to

increase the quality of the MgB_2 phase without significantly altering its chemical composition, probably through the reduction of defects (e.g. Mg vacancies caused by the highly non-equilibrium PLD process) or the reduction of strain.

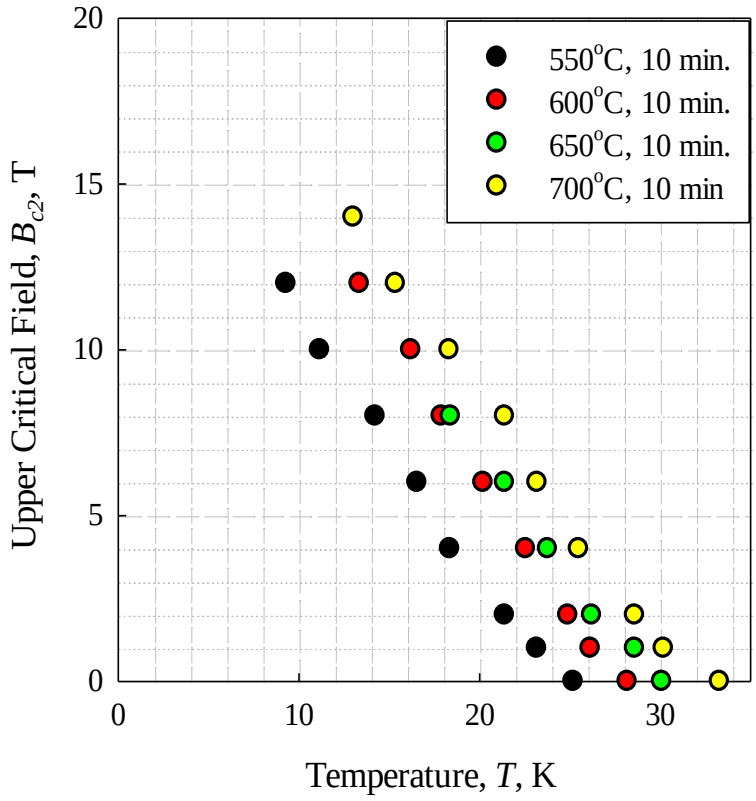

Figure 48. Evolution of B_{c2} vs. T with heat-treatment temperature at 10 mins. heat-treatment time.

Figure 49 plots the values of the magnetic J_{cm} vs. B for the thin film MgB_2-068 for the temperatures 5, 10, 15, 20, and 25 K. At 5 K, a J_{cm} of 10^5 A/cm^2 is achieved at 7.8 T. At 20 K, 10^5 A/cm^2 is reached at 3.08 T. Both of these values are among the highest seen

in the literature. It is worth additionally noting that J_{cm} extends out to high fields, unlike the results of magnetic measurements taken on wires. As pointed out in [103] and [177] the magnetic J_{cm} of powder-in-tube strand is restricted by the relatively low J_c perpendicular to the strand axis. This restriction does not exist for the film with its isotropic in-plane J_c.

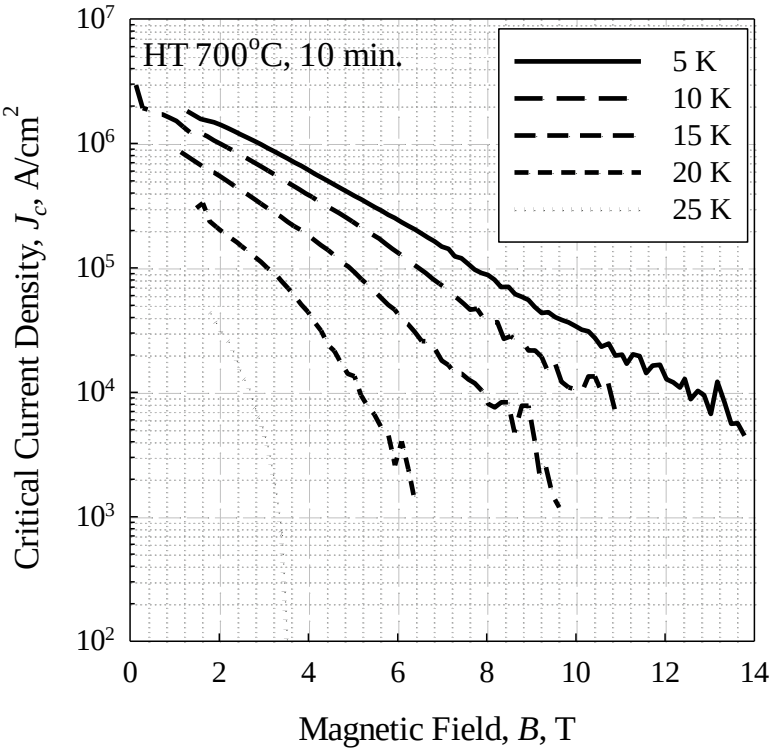

Figure 49. Magnetic critical current density, J_{cm} vs. B for thin film MgB_2-068 at various temperatures.

Figure 50 compares the J_{cm} vs. B of MgB_2-068 with transport and magnetic values for doped and undoped MgB_2 thin films and tapes seen in the literature [92], [202–207]. It is seen that the J_{cm} of this film compares well to most of these films, especially at high magnetic fields. A transport $J_c(B)$ curve for an undoped PIT wire is included for comparison[10].

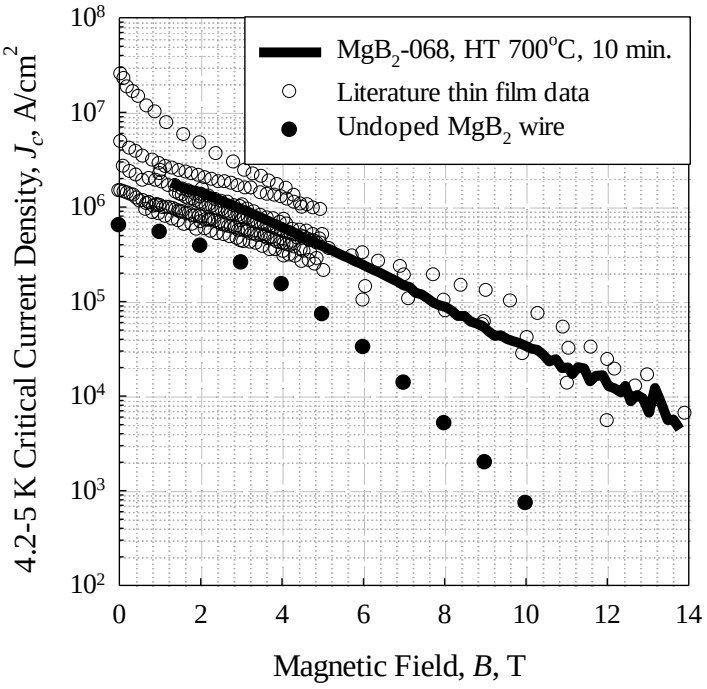

Figure 50. 5 K $J_{c,m}$ vs. B of thin film MgB_2-068 compared to 4.2-5 K data in the literature [92], [202–207], as well as the transport-measured J_c of measured undoped monofilamentary PIT wire.

[10] Strand S1033-1968B-700-20 HT at 700°C for 20 min.

In Figure 51, the data of Figure 50 has been transformed into the field dependence of bulk pinning force density $F_p = J_c \times B$, shows the 5 K F_p maximizing at 29.3 GN/m^3, a value much larger than those achieved in conventional powder-in-tube strands [5]. Figure 52a shows the differences between the F_p vs. B plots of an undoped MgB_2 thin films and an MgB_2 wire, highlighting the large difference in the pinning forces between the two classes MgB_2 superconductor. Both the film and the wire have a maximum at ~0.2 x B_{irr}, wholly consistent with a pinning force density that follows the grain boundary pinning (i.e. surface pinning) behavior where 2-D grain boundaries are the main pinning centers [78], [140], [144]. The wire exhibits a 4.2 K $F_{p,max}$ of 7.7 GN/m^3 while the film shows a 5 K $F_{p,max}$ of 29.3 GN/m^3. This difference may be attributed to a combination of three factors: i) the somewhat smaller grain size of the film (~24-30 nm) compared to that of the wire (typically > 50 nm), ii) a higher connectivity in the film, and iii) the c-axis oriented nature (and hence the lack of percolative current paths) of the film. These topics will be discussed further in the next chapter of this work.

Normalizing the ordinate and abscissa of Figure 52a such that a plot of $F_p/F_{p,max}$ vs. b is generated can be misleading for the case of MgB_2 (see Figure 12 in chapter 1) due to the difficulty in establishing correct values of B_{irr} and B_{c2}. In chapter 1 it was shown that MgB_2 is a grain boundary pinned material; therefore, it will therefore exhibit its maximum pinning force at $0.2*B_{c2}$. If the abscissa in Figure 52a in normalized as $B/B(F_{p,max})$ then a fairer comparison may be made between MgB_2 F_p curves without concern as to how the value of B_{c2} (or, more correctly, B_{irr} for MgB_2) was determined.

Figure 52b shows the plot of $F_p/F_{p,max}$ vs. $B/B(F_{p,max})$ for the data in Figure 52a in addition to the Kramer-Dew-Hughes surface pinning function. It is seen from Figure 52b that the thin film data follows the surface pinning function rather well, even at high fields. In contrast, the MgB_2 wire data shows a deviation from the surface pinning function at high fields, consistent with the observations of Larbalestier *et al.* [4]. Now that the magnitude of the F_p has been factored out with normalization, the differences between the thin film and wire data can be attributed to either: i) the lack of anisotropy in the MgB_2 due to its c-axis oriented nature or ii) the lack of porosity in the thin film as compared to the wire. Chapter 5 will deconvolute these effects.

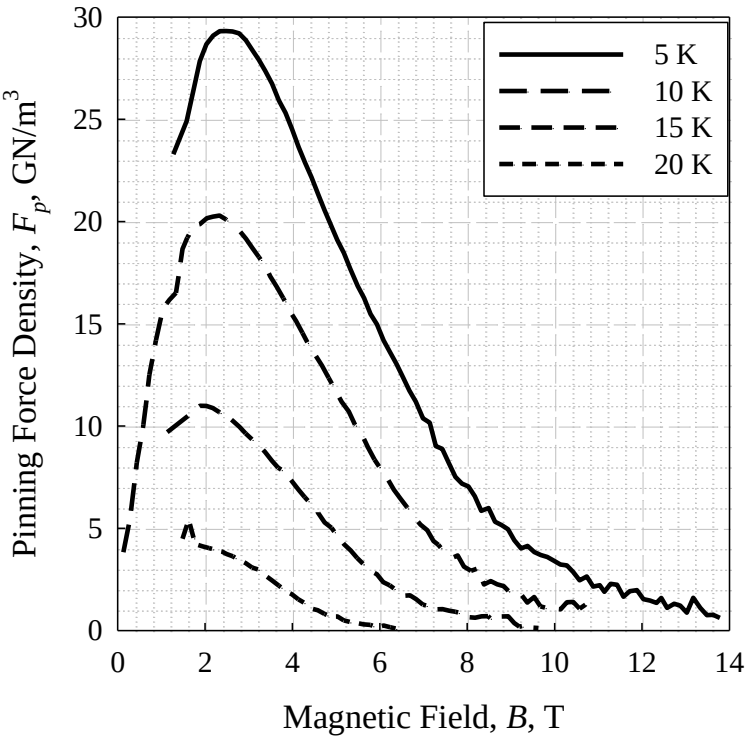

Figure 51. Magnetic bulk pinning force density, F_p, vs. B curves at different temperatures for MgB_2-068 derived from the relationship $F_p = J_{cm} \times B$.

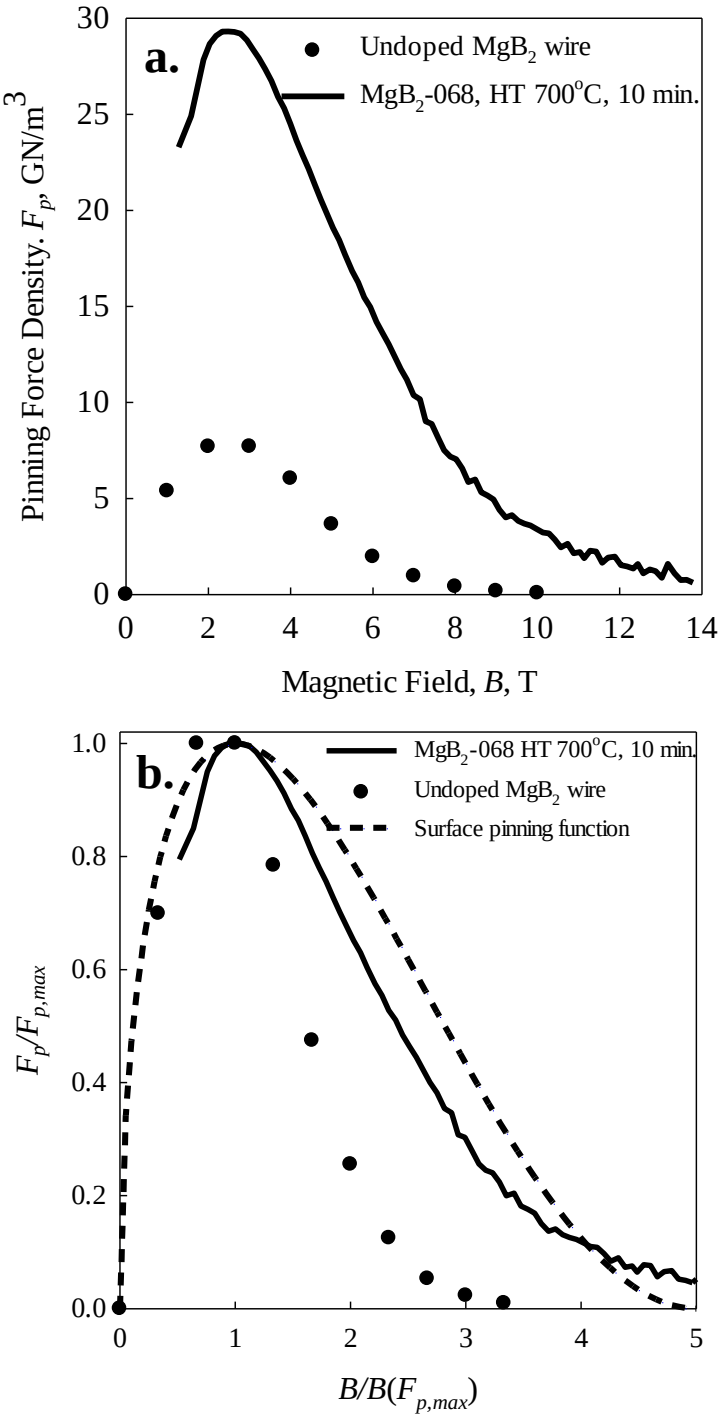

Figure 52. a) Bulk pinning force density, F_p, vs. B curves for MgB_2 thin film MgB_2-068 and MgB_2 wire [208] showing large difference between the properties of the two types of MgB_2; b) $F_p/F_{p,max}$ vs. $B/B(F_{p,max})$ highlighting the lack of high-field deviation in the thin film.

4.6 Undoped MgB_2 Thin Film Summary

C-axis oriented MgB_2 thin films were grown on 6H-SiC substrates using Pulsed Laser Deposition (PLD). The PLD target was made from the high pressure and high temperature reaction of Mg and B to form large-grained (~50 μm) MgB_2. Although the quality of the thin films produced via PLD is not as high as that seen in CVD or HPCVD produced MgB_2 thin films (at least in terms of T_c or surface smoothness), PLD offers a simple method of modifying the chemical composition and microstructure of the film. The MgB_2 films were found to be c-axis oriented through diffraction analysis. In-plane orientation was determined to be random, implying that, though the SiC offered a good lattice match with the MgB_2 film, its use as a substrate was probably unnecessary.

The superconducting critical temperature, $T_{c,onset}$, increased monotonically as the annealing temperature was increased, varying from 25.2 K to 33.7 K which was ascribed to a reduction of disorder. Finally, examination of the pinning mechanism showed that the films follow the grain boundary, or surface pinning, mechanism quite well, in contrast to the deviations at high fields exhibited by the wires. This difference can be ascribed to the c-axis oriented nature of the films and/or the poorer connectivity in the wires.

Chapter 5: Influence of Connectivity and Anisotropy on MgB_2 Supercurrent Transport

In this chapter two key questions concerning MgB_2 are addressed: the relative contributions of anisotropy and connectivity to the supercurrent transport. Here J_c is systematically investigated in terms of a percolation model. Different MgB_2 systems with differing properties in terms of orientation, anisotropy, and connectivity are compared so that the contributions from these variables may be quantified.

5.1 General Percolation Model for a Superconducting Material

A good starting point for the discussion of connectivity in MgB_2 is the work of Eisterer *et al.* [52] where a percolation model is developed for a superconductor from a modification of the normal-state model of Straley and Kenkel [209], [210]. This percolation model was previously used to investigate systems of two or more materials having different resistances. For example, systems with networks of conductors and insulators have been investigated by Abeles *et al.* [211], Clerc *et al.* [212], Lee *et al.* [213], and Last and Thouless [214]. Additionally, networks consisting of normal and superconducting materials have been investigated by Herrmann *et al.* [215] and Xiao *et al.* [216].

Straley and Kenkel [209],[210] present a model that uses a network of equal resistors, *R*, described by the power-law equations:

$$R = V / I^{\alpha}$$
$$I = \left(V / R\right)^{1/\alpha} \tag{20}$$
$$G = I / V^{1/\alpha}$$

where V is the voltage, I is the current, and α is a power-law exponent used to describe non-linear I-V characteristics. G=1/R and represents the conductance. Kenkel and Straley [209] showed that near the percolation limit the current-voltage relationship is

$$I_{eff} \propto (p - p_c)^t V^{1/\alpha} \tag{21}$$

where p is the probability that a component or region of the network is conducting [212] and p_c is the percolation threshold, defined as the minimum fraction of conducting regions necessary for a continuous current path. It is immediately obvious that as $p_c \rightarrow p$ the electrical conductance ($G = I/V^{1/\alpha}$) goes to 0. Furthermore from combining Equations 20 and 21 it is seen that the effective electrical conductance G_{eff},

$$G_{eff} = I_{eff} / V^{1/\alpha} \propto (p - p_c)^t \tag{22}$$

The exponent t is dependent on dimensionality and can be written as:

$$t = (d-1)\nu + \frac{(\zeta - \nu)}{\alpha} \tag{23}$$

where d is the number of dimensions in the system, ζ describes the exponential dependence of the distance between links [210], [217] and may be approximated as ~ 1 [209] and ν represents the correlation exponent or, more precisely, the critical exponent for the correlation length (see Essam [218] for a complete review on percolation theory), which is shown to be 0.88 for a 3D system [219].

For a normal conductor (defined as having linear *V-I* relationship), α = 1 (and thus *V=IR*). Deutscher and Rappaport [220] and Herrmann *et al*. [215] showed that, for a superconductor, α is infinite in value (which can be interpreted as a consequence of zero resistance), in which case Equation 23 simplifies to:

$$t = (d-1)\nu \tag{24}$$

which serves to free t from dependence on α. The value of t from Equation 24 then can be easily seen to be 1.76, which has also been proven by Deutscher *et al*. [220], [221].

For a granular superconducting material (where α is ∞ and thus $G_{eff}=I_{eff}$) and given a sample cross section A_0 such that $J_{eff}=I_{eff}/A_0$, Equation 22 simplifies to

$$J_{eff} \propto (p - p_c)^t \tag{25}$$

where J_{eff} is the effective current density. If i) the variable p represents the fraction of grains carrying supercurrent (i.e. $J<J_c$) and ii) the proportionality in Equation 25 is normalized such that at p = 1 (i.e. all grains are carrying supercurrent) $J_{eff} = J$:

$$J_{eff} = \left(\frac{p(J) - p_c}{1 - p_c} \right)^t J \tag{26}$$

The expression $\left(\frac{p(J) - p_c}{1 - p_c} \right)^t$ can be defined as A_p, the percolation area fraction and represents, for a given p, the cross section of existing current paths [52]. Therefore, $J_{eff} = A_p J$. If J is increased by ΔJ from the current density at which $J_{eff}=J$ then p becomes smaller than 1 and the value A_p decreases. At a large enough J, p will equal p_c and J_{eff} will thus be 0. Integrating Equation 26 over all possible J gives:

$$J_c(B) = \int_0^{J_{c,\max}(B)} A_p dJ = \int_0^{J_{c,\max}(B)} \left(\frac{p(J) - p_c}{1 - p_c} \right)^t dJ \qquad (27)$$

where $J_c(B)$ is the J_c at a given B, $J_{c,max}(B)$ is the maximum J_c for the material, and all other variables have the same meanings as previously described.

Of course, the model presented in Equation 27 assumes that the system wholly consists of the superconducting material in question (i.e., there is no porosity and the grains are assumed to be perfectly connected). The presence of porosity can be included in the description using a simple modification which involves including another parameter, generally referred to as p_s [222]. This parameter describes the fraction of the material that is MgB_2, with the remainder consisting of pores, wholly insulated grains, secondary phases, or other inclusions [222]. Any current blocking due to insulating layers at the grain boundaries would be included in this term. The value of p_s can be field dependent in the case of partially insulating grains but for the sake of simplicity (not to mention the risk of over-extending the model) it shall be considered as a constant for the present work. After replacing $p(J)$ by $p_s p(J)$, the modified model becomes:

$$J_c(B) = \int_0^{J_{c,\max}(B)} \left(\frac{p_s p(J) - p_c}{1 - p_c} \right)^t dJ \qquad (28)$$

A modified percolation threshold p_c* can be quantified and is defined as p_c/p_s [222]. Since the value of p_s is a constant, Equation 28 can be rearranged as:

$$J_c(B) = \int_0^{J_{c,\max}(B)} \left(\frac{p(J) - p_c^*}{1 - p_c^*} \right)^t \left(\frac{p_s - p_c}{1 - p_c} \right)^t dJ \qquad (29)$$

Conceptually, the first term within the integral may be thought of as the effective superconducting cross section, A_p (or, more precisely, area fraction) which changes as a function of the number of superconducting grains present for a given field. The second term represents the connectivity (or at least the fraction of connected material) of the MgB_2 and is field and temperature independent, A_{con}. Formally the expression may then be expressed as:

$$J_c(B) = \int_0^{J_{c,\max}(B)} A_p(p, p_c^*) A_{con} dJ \qquad (30)$$

5.2 Percolation Model for MgB_2

Application of the percolation model presented in Equation 26 to MgB_2 necessitates defining how J_c changes with orientation (i.e. the anisotropy). The anisotropy of B_{c2} in a superconductor can be quantified in terms of the Ginzburg-Landau theory:

$$B_{c2}(\theta) = \frac{B_{c2}\left(\frac{\pi}{2}\right)}{\sqrt{\gamma^2 \cos^2(\theta) + \sin^2(\theta)}} \tag{31}$$

Where $\pi/2$ is the angle (in radians) with respect to the c-axis (in this case) and γ is the anisotropy parameter [223]. Here $B_{c2}(\pi/2)$ is defined as the in-plane B_{c2} (i.e., the highest B_{c2}). The percolation here presented is only valid for a fixed B_{c2} and thus must be applied at a fixed T. Further extension of the model to higher T is possible insofar as the B_{c2} vs. T relationship is known.

As described in the introduction, the relationship between J_c and B is dependent on the type of flux pinning present in the material. It was established in the introduction that the literature overwhelmingly supports the Kramer-Dew-Hughes model of grain boundary pinning for MgB_2 [140], [78]:

$$J_c \propto \frac{B_{c2}^{3/2}(\theta)\left[1 - B/B_{c2}(\theta)\right]^2}{\kappa^2(\theta)\sqrt{B}} \tag{32}$$

where κ is the Ginzburg-Landau parameter (equal to the ratio of the penetration depth λ over the coherence length ξ). Equation 32 was developed for NbTi and Nb_3Sn superconductors where no real difference is exhibited between B_{irr} (the magnetic field at which J_c is 0) and B_{c2} (the magnetic field at which superconductivity is no longer present and the coherence length ξ goes to infinity). In MgB_2 there is a quantifiable difference between these two values [141]. As a result, it would be more correct to use B_{irr} in the normalization for B (B/B_{irr}) for the term inside the brackets of Equation 32. The field

term outside the parentheses is based on thermodynamic considerations from the original Dew-Hughes derivation [78] and thus should always be B_{c2}. However, measuring a value of B_{irr} that is not dependent on current percolation (which would serve to underestimate its value) is not a trivial task. Pradhan *et al.* [141] measured the values of B_{irr} and B_{c2} on an MgB_2 single crystal and found the $B_{irr} = \sim 0.9 x B_{c2}$ at 25 K. Lower temperature single crystal data (i.e. B_{irr} & $B_{c2} > 10$ T) were unfortunately unavailable in the work of Pradhan *et al.* or, for that matter, for any other single crystal MgB_2 studies. For the sake of simplicity, then, the B_{c2} in Equation 32 is assumed to be the magnetic field at which $J_c \rightarrow 0$.

Since κ can be shown to have the relation

$$\kappa = B_{c2} \Big/ (2^{1/2} B_c) \tag{33}$$

where B_c is the thermodynamic critical field (which is constant for a given T and can thus be removed from the proportionality), Equation 32 can be simplified to [52]:

$$J_c = J_0 \frac{\left[1 - B / B_{c2}(\theta)\right]^2}{\sqrt{B_{c2}(\theta) B}} \tag{34}$$

where J_0 is the 0 T J_c at a defined T. Generally speaking, as long as the pinning type is known for a superconducting material, a J_c-B relationship can be described by an equation similar to that given in Equation 34.

5.3 Theoretical Predictions of the Percolation Model

Application of the percolation model described by Equation 28 to MgB_2 then requires fitting 5 parameters: γ, B_{c2}, J_0, p_c, and p_s. Fortunately, J_0 and B_{c2} can be extracted from experimental data (J_c-B plots or resistivity vs. T measurements, respectively).

The value of the anisotropy parameter, γ, needs to be applied with care. The reported values of γ have been shown to vary widely, even for single crystal samples [46][224] where γ varies from 1.7-6. However, in the case of MgB_2 wires, γ has been shown to vary between 1.8-3.0, depending on C-doping level (where the anisotropy decreases with increasing C-doping) [125].

Before applying the percolation model to experimental data, it is first essential that a complete understanding of the limits of the percolation theory be established. For the following analyses, all given parameters are taken from the literature and represent reasonable, reported values for typical MgB_2 wires.

The percolation model is applied using 10^4 grains, each with a value of $\sin(\theta)$ randomly distributed between 0 and 1. The B_{c2} was then calculated according to Equation 31. From the B_{c2}, the J_c of each grain (out of 10^4 total) was calculated according to Equation 34. A plot of $n(J)$ vs. J is then generated and used in the integral given in Equation 28.

First, the effects of the anisotropy, γ, on J_c are quantified. Here for generality the values of γ are varied from unity (i.e., an isotropic superconducting material like Nb_3Sn) to 6. The last value represents the upper range of the anisotropy according to [46]. Figure

53 models the effect of increasing γ on transport J_c for an MgB_2 superconductor with a 4.2 K B_{c2} of 20 T and a 4.2 K J_0 (0T J_c) of 5 x 10^6 A/cm^2; the percolation threshold, p_c, is set to be 0.2. These values represent a high-performing undoped MgB_2 wire like those seen in [188].

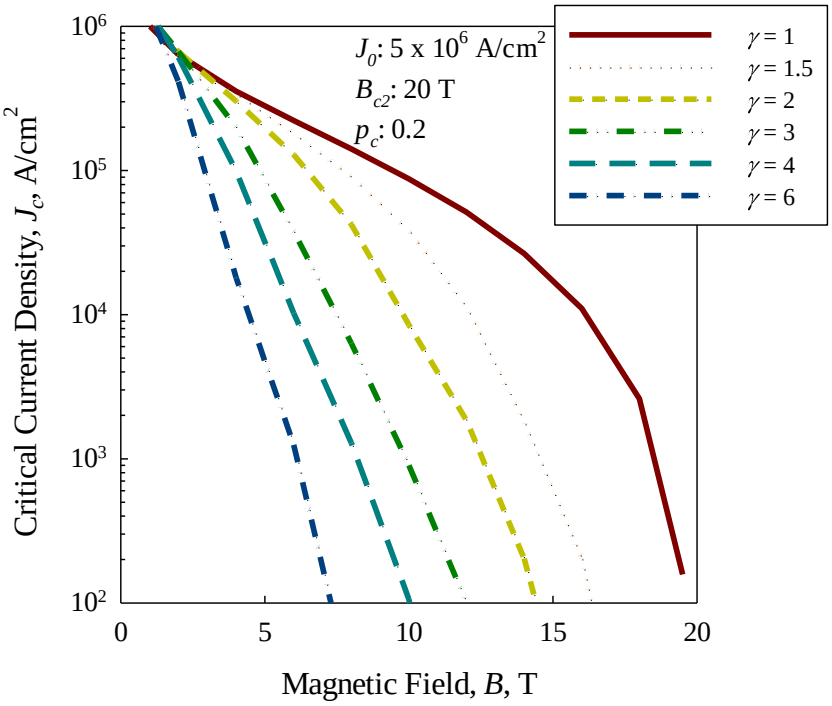

Figure 53. Modeled J_c vs. B plot of MgB_2 with variation in γ for a sample with a B_{c2} of 20 T.

The most striking feature in Figure 53 is the degradation in high-field (i.e. > 10 T) J_c. Keeping in mind that J_c vs. B data like that presented in Figure 53 is typically presented in a log-linear plot, the effects of anisotropy are even more striking. At 10 T,

for example, if γ is assumed to be 3 (a value typically cited for undoped MgB_2 [125], [225]), then the value of J_c falls by nearly two orders of magnitude from the grain-boundary pinned isotropic value of 88 x 10^3 to 1 x 10^3 A/cm^2. It is clear, then, that γ has a large effect on J_c vs. B plot. Eisterer *et al.* use γ as a semi-constrained fitting parameter in [52], with values listed as high as 4.4. A comparison is made to the variation in the transition width, ΔT_c, attributing it to the anisotropy, but any disorder in the system could contribute to an increase in ΔT_c.

Even though the above γ=4.4 is still less than the greatest literature value for pure single crystals [226], it is not typical of the values measured for carefully separated individual MgB_2 crystallites made from commercial B and Mg powders where γ is 1.7-2.8 [227]. MgB_2 wires are made from these same powders and it follows that the γ in wires should be within this range.

For an undoped MgB_2 sample with the values of J_0 and B_{c2} given in Figure 53 and γ=4, the 4.2 K, 10 T J_c is modeled to be ~100 A/cm^2. This means that the observed B_{irr} (using the 100 A/cm^2 criterion) is 10 T. In other words, for a sample with γ = 4, this means that B_{irr}~0.5xB_{c2}, which can potentially lead to severe underestimations of a given sample's true B_{irr} from a J_c vs. B plot. Also, this large difference between B_{irr}(100 A/cm^2) and B_{c2} (as measured resistively by a small sensing current or as measured magnetically) is simply not seen in the literature [103].

The use of an errantly high value of γ is even more deleterious when applying the model to a doped sample with a B_{c2} of 30 T (see [188], [125], [52], and [228]). At 4.2 K

and 10 T, the isotropic J_c for a grain-boundary pinned material with a J_0 of 5 x 10^6 A/cm^2 and a B_{c2} of 30 T is 128 x 10^3 A/cm^2, Figure 54. For doped MgB_2 (with the associated γ of 1.5-2.5), J_c would be between 97 x 10^3 and 32 x 10^3 A/cm^2. For a γ of 4.4, J_c would fall to 2 x 10^3 A/cm^2. It is clear that use of an artificially high value of γ for fitting Equation 26 to experimental data causes an underestimation of the high-field J_c.

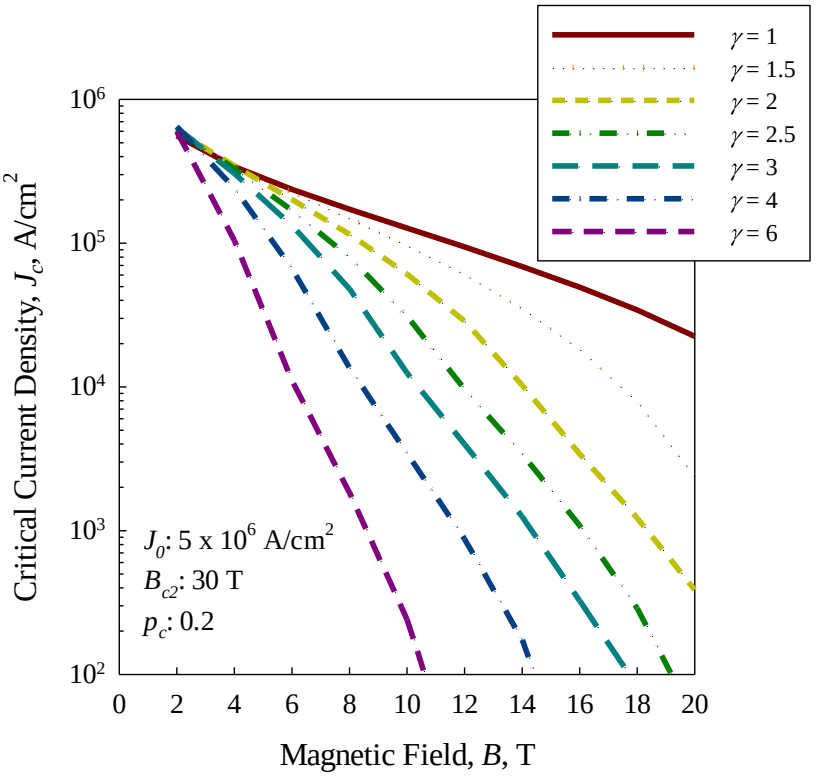

Figure 54. Modeled J_c vs. B plot of MgB_2 with variation in γ for a sample with a B_{c2} of 30 T.

The effects of a percolation threshold (p_c) in terms of variations on $J_c(B)$ are now addressed. Van der Marck [229] calculates the p_c in terms of various geometries for both

3D and 2D objects. For a close-packed 3D object (i.e. fcc or hcp stacking), the lowest value of p_c is 0.199. For a square lattice the value of p_c is 0.593. Figure 55 shows the effect of increasing p_c within these values on the J_c vs. B characteristics of an MgB_2 sample with 4.2 K γ of 2.5, J_0 of 5 x 10^6 A/cm^2 and B_{c2} of 20 T.

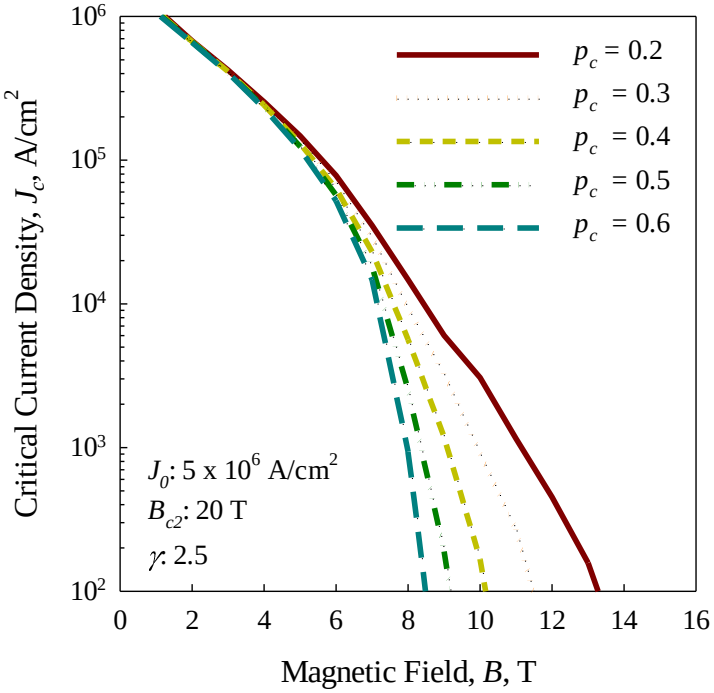

Figure 55. Modeled J_c vs. B plot of MgB_2 with variation in p_c for a sample with a B_{c2} of 20 T.

Figure 55 shows that increasing p_c, which may be interpreted as increasing the fraction of MgB_2 needed to carry a current at a given field, decreases the high-field J_c and thus, by extension, the measured value of B_{irr} (cf. Figure 54 which showed a similar effect in reference to increasing γ). Again, increasing the value of a fitting variable, in

this case p_c, causes the value of B_{irr} to markedly decrease (e.g. to a value of 10.1 T at p_c = 0.4). $J_c(B)$ is quite sensitive to the choice of p_c, which needs to be chosen carefully if the fit is to be believed.

Eisterer *et al.* [52] initially justified the use of a high γ by stating that varying p_c has virtually no effect on J_c at low B and thus variation of γ was needed to explain the observed $J_c(B)$ at low B. However, no mention was made of the effects of porosity or secondary, non-superconducting phases. Eisterer *et al.* [222] later add another term, here denoted p_s, to account for these effects.

Figure 56 displays the effect of varying p_s (i.e. the phase fraction of the superconductor) for an MgB_2 sample with a 4.2 K B_{c2} of 20 T, J_0 of 5 x 10^6 A/cm^2, and γ of 2.5; p_c was chosen to be 0.2, appropriate to a system whose groups of grains have a high degree of connectivity.

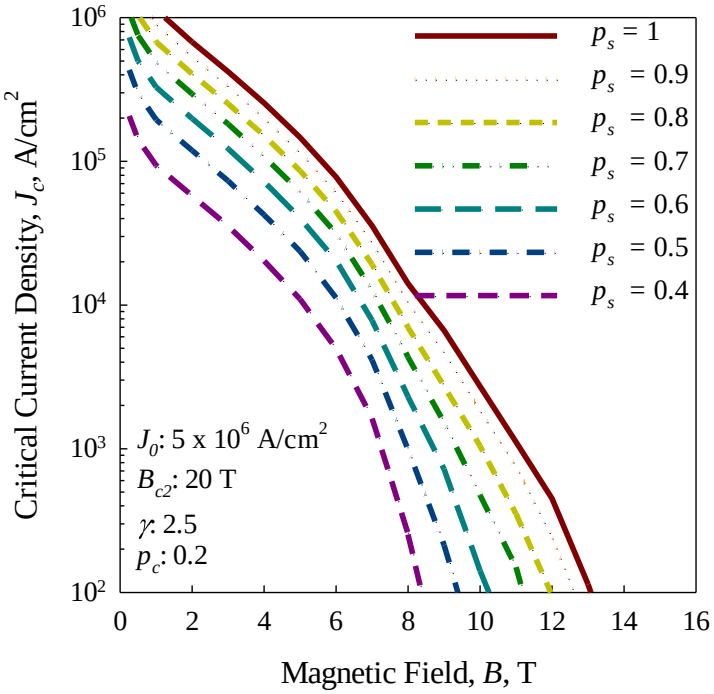

Figure 56. Modeled J_c vs. B plot of MgB_2 with variation in p_s for a sample with a B_{c2} of 20 T and p_c of 0.2.

The effect of decreasing p_s (which for an otherwise homogeneous system can be interpreted as an increase in porosity) causes a global decrease in $J_c(B)$. An interesting consequence of decreasing the value of p_s is seen in the Kramer plot of the J_c vs. B curve. The Kramer plot is simply a geometric re-interpretation of a $J_c(B)$ plot where the ordinate is modified to $J_c^{0.5}B^{0.25}$ so that linearity denotes perfect grain boundary pinning. Figure 57 is a re-interpretation of the data in Figure 56 using this technique.

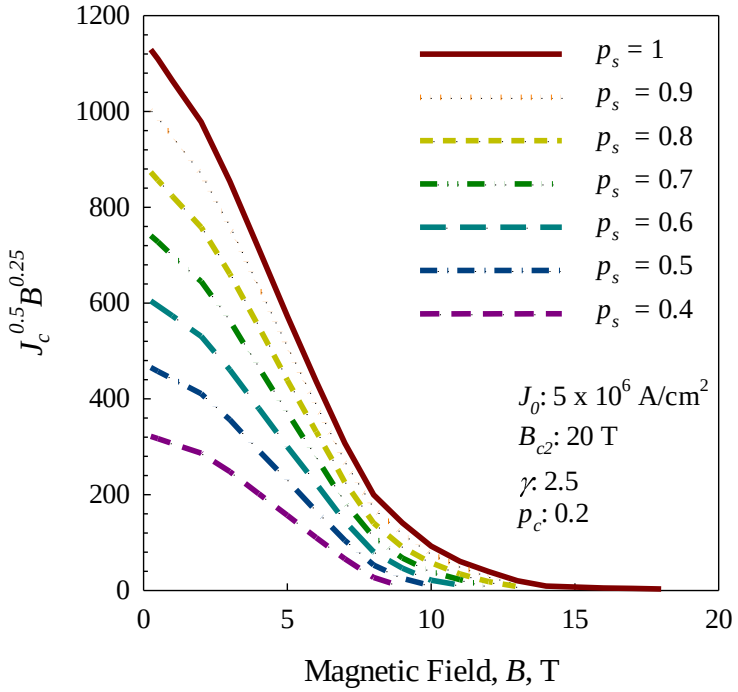

Figure 57. Modeled Kramer plots of MgB_2 with variation in p_s for a sample with a B_{c2} of 20 T and p_c of 0.2.

Not only does the Kramer plot have a "tail" at high fields as initially noticed by Larbalestier *et al.* [4] but also a deviation from linearity at low *B*.

Bhatia [148], followed by Susner *et al.* [230], used the *normal state* resistivity of MgB_2 together with Rowell's formulation [99] (with modifications) to estimate a connectivity of ~20 % in SiC-added MgB_2, an expected result considering that the ubiquitous porosity and presence of Mg_2Si and unreacted SiC[183] can all serve to inhibit current flow. The Kramer plot of a SiC-added wire with J_0 and B_{c2} values comparable to those modeled in Figure 57 is given in Figure 58. These experimental results clearly

show the “tail” at high fields due to the anisotropy and resultant percolation and the “hook” at low fields due to porosity and the presence of secondary phases.

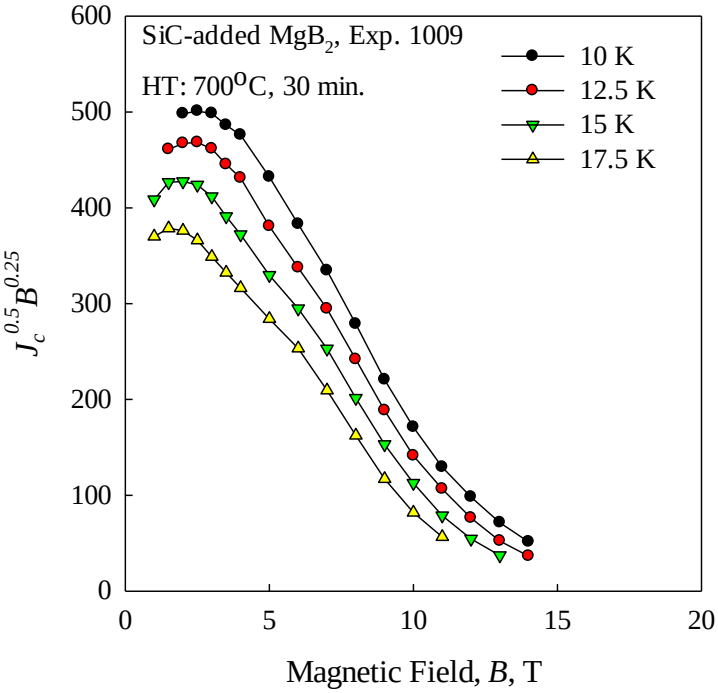

Figure 58. Kramer plots from J_c vs. B data collected for SiC-added MgB_2 sample.

Unfortunately, due to the multitude of unknown variables is not realistically possible to fit the data in Figure 58 to Equation 28. The experimental data in Figure 58 is from a wire comparable to that shown in Chapter 3, as the microstructures of the SiC-added sample has been shown to have the same properties with the same tell-tale differences between magnetic and transport J_c [103], [183]. Further detailed studies aimed at deconvoluting the joint effects of anisotropy, porosity, p_c, p_s, J_0, and B_{c2} would

demand the creation of an extensive set of new research samples. With this in mind, two new samples have already been made.

5.4 Application of the Percolation Model to Experimental Data

To quantify the individual effects of B_{c2}, p_c, p_s, and γ on the transport $J_c(B)$ of MgB_2 wires, two samples were manufactured by Hyper Tech Research, Inc (Table 3). The first sample, referred to as MgB_2-IMD[11] is a 6 filament strand utilizing the IMD manufacturing technique as described in the introduction. Amorphous B powder, made via RF plasma synthesis of BCl_3 gas reduced by H_2 [231], is C-doped by adding CH_4 to the gas stream at various flow rates. The concentration of C in the B powder was quantified by LECO using a LECO CS600 combustion analyzer. The amount of C substitution for B was measured by comparing lattice parameter shifts of the reacted MgB_2 with those of the single crystal data of Lee *et al.* [102]. Further information about this analysis may be obtained by referring to [125]. The second sample, hereafter referred to as MgB_2-PIT[12], was made via the PIT process using the exact same powder as the IMD wire. B_{c2} was determined by reconstructing ρ vs. T data measured at different values of B (Figures 59 and 60) in the form of B_{c2} (and B_{irr}) vs. T (Figure 61). Since the maximum available B for these measurements was 14 T, the measured values of B_{c2} were not obtained beyond ~18 K; 4.2 K values were obtained by extrapolation.

[11] Sample S1022-E2281, heat-treated at 675°C for 30 min.
[12] Sample S1131-E2285-B1, heat-treated at 675°C for 30 min.

Table 3. Sample parameters for MgB_2 wire specimens.

	B_{c2}*, T	dB_{c2}/dT, T/K
MgB2-IMD	31.8	-0.89
MgB_2-PIT	28.6	-0.93

**extrapolated to 4.2 K*

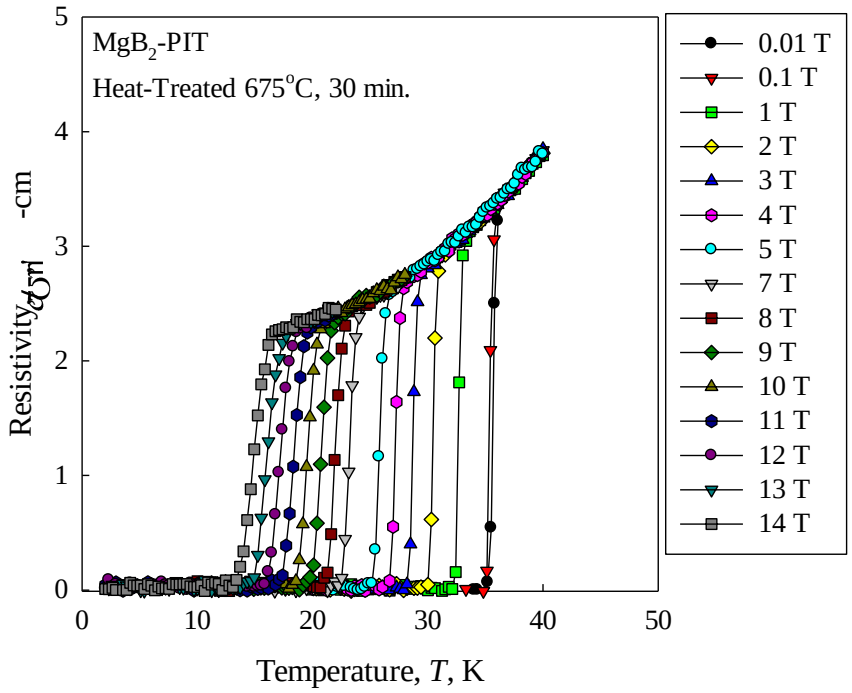

Figure 59. ρ vs. T data at different B for MgB_2-PIT.

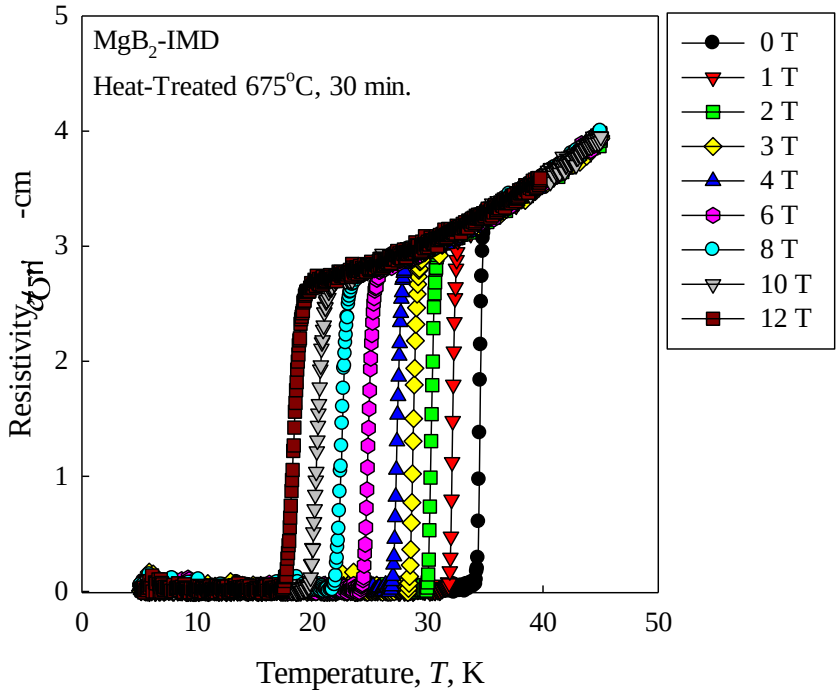

Figure 60. ρ vs. T data at different B for MgB_2-IMD.

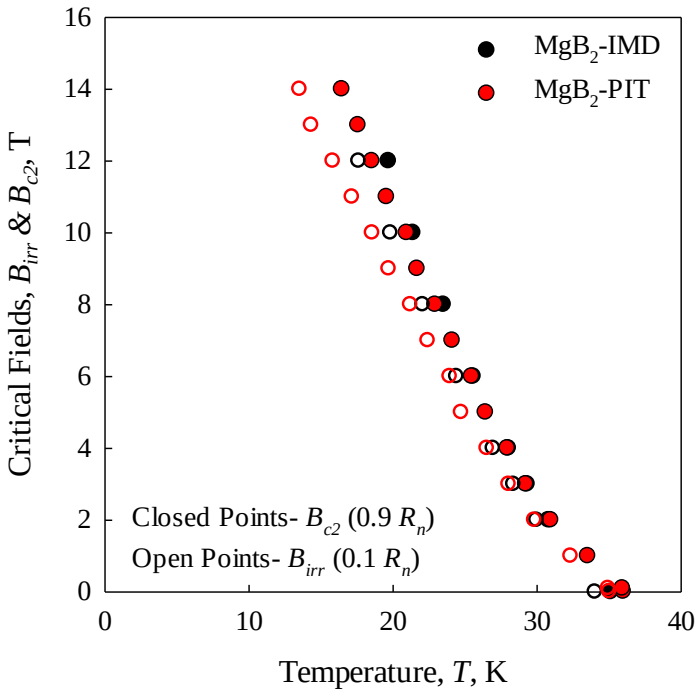

Figure 61. Critical fields vs. T for MgB_2-IMD and MgB_2-PIT

The values of B_{irr} and B_{c2} in Figure 61 were defined as the 10% and 90% of the resistive transitions, respectively (Figures 59 and 60). Because the wire samples consist of a collection of randomly oriented polycrystalline grains, it is difficult to ascertain the precise value of the anisotropy in terms of the ratios of the $B_{c2}{}^{ab}/B_{c2}{}^{c}$. The only method that can be used without isolating and characterizing individual crystallites as a function of orientation is to extract γ from Eisterer's equation [52]:

$$\Delta T_c = \frac{\sqrt{(\gamma^2 - 1)\, p_c^2 + 1} - 1}{-\partial B_{c2} / \partial T} B_0 \qquad (35a)$$

In which ΔT_c is the width of the superconducting transition, p_c is the percolation threshold, B_o is the magnetic field at which the value of ΔT_c was measured, and dB_{c2}/dT is the slope of the upper critical field with respect to temperature. The immediate difficulty in applying Equation 35 is that ΔT_c is dependent on two unknowns- γ *and* p_c. Nevertheless, for the dense MgB_2-IMD sample it might be assumed that the percolation threshold is close to 0.2; indeed, for similar bulk samples Eisterer found values of 0.21 [52]. Based on Equation 35. a plot of γ for three values of p_c for the MgB_2-IMD sample has been created, Figure 60. For p_c = 0.2, γ is estimated to be 3.06; for p_c = 0.3, γ is seen to be 2.2.

Implicit in the assumption behind Equation 35 is the fact that the transition broadening depends only on p_c and γ. Realistically, ΔT_c can be increased by material inhomogeneities [103],[232], thermal fluctuations [103],[232], or even grain size [141] resulting in a modification of Equation 35a in the form

$$\Delta T_c = \Delta T_0 + \frac{\sqrt{(\gamma^2 - 1)\, p_c^2 + 1} - 1}{-\partial B_{c2} / \partial T} B_0 \qquad (35b)$$

where ΔT_0 represents the transition width at 0 T. Given this fact, the value of γ estimated using Equation 35 represents an upper limit for γ.

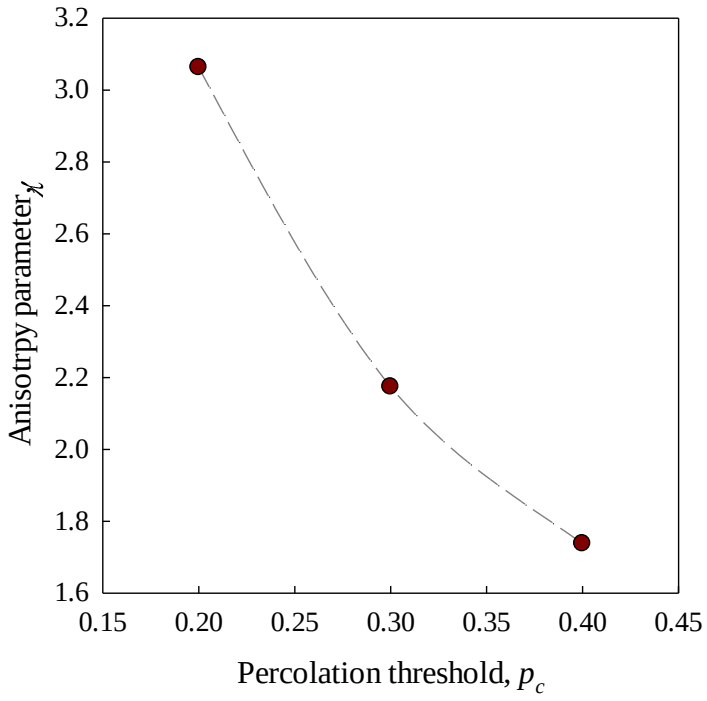

Figure 62. Anisotropy parameter, γ, vs. percolation threshold. p_c for MgB_2-IMD. The line serves as a guide to the eye.

Using the B_{c2} extrapolated from Figure 61, the γ extracted from Equation 35, and the J_0 from the J_c vs. B curve as initial fitting parameters, the $J_c(B)$ data of MgB_2-IMD was fitted to Equation 28. Since this strand was made via the IMD process and therefore contains the microstructural properties characteristic of IMD wires (see Figure 33), it can be assumed that porosity is negligible. Therefore, p_s was assumed to be equal to 1. Figure 63 gives the $J_c(B)$ curve, the fit to Equation 28 for p_s = 1, and the resulting fitting parameters for MgB_2-IMD.

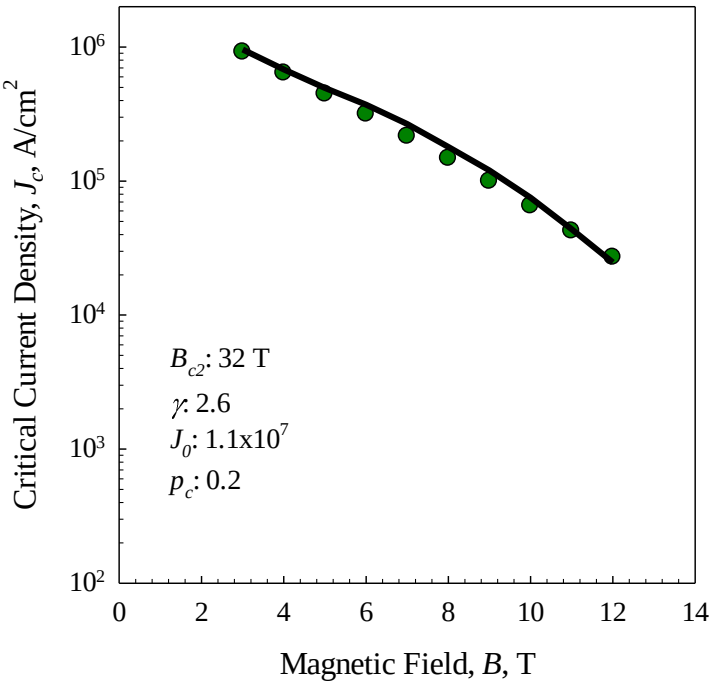

Figure 63. 4.2 K J_c vs. B for MgB_2-IMD together with percolation model fitting.

Figure 64 applies the same analysis used for MgB_2-IMD. It was assumed that the properties *within* an MgB_2 *fiber* in MgB_2-PIT would be similar to those seen in the MgB2-IMD reaction layer. Therefore, the fitting parameters γ, p_c, and B_{c2} remained invariant (or close to it since it was necessary to increase B_{c2} from 32 to 33 T for the MgB_2-PIT fit, an indication that the extrapolation implied in Figure 61 could have some error). The only fitting parameter from Equation 28 that needed to be substantially changed from MgB_2-IMD to fit MgB_2-PIT was p_s, the porosity term. The value of p_s yielding the best fit in the case of MgB_2-PIT was found to be 0.67, indicating 33% total

porosity. This value of p_s is wholly consistent with the microstructure seen in Chapter 3 (specifically Figure 26). Table 4 lists the fitting parameters used in the analyses of Figures 63 and 64; these will be referred to in the following section.

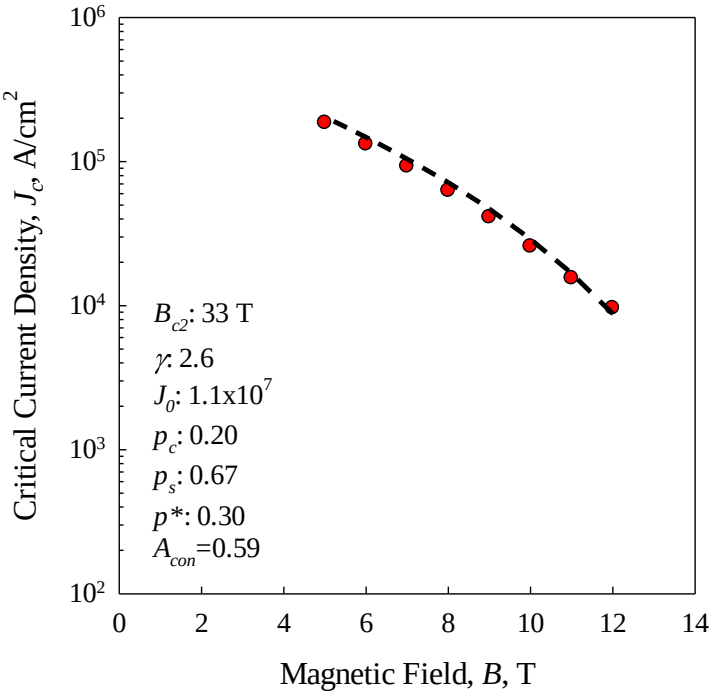

Figure 64. 4.2 K J_c vs. B for MgB_2-PIT together with percolation model fitting.

Table 4. Fitting parameters from the analyses in Figures 63 and 64.

	MgB_2-IMD	MgB_2-PIT
J_0	1.1 x 10^7 A/cm^2	1.1 x 10^7 A/cm^2
B_{c2}	32 T	33 T
γ	2.6	2.6
p_c	0.2	0.2
p_s	1	0.67
$p^* = p_c/p_s$	0.2	0.30
$A_{con} = [(p_s-p_c)/(1-p_c)]^{1.76}$	1	0.59

5.5 Implications of Connectivity in MgB_2 for High-Field Applications

The preceding analysis can be used to determine the limits imposed on supercurrent transport of MgB_2 from its intrinsic anisotropy. Figure 65 shows the J_c vs. B fittings for MgB_2-IMD, MgB_2-PIT, and a theoretical isotropic grain-boundary pinned superconductor with the same values of J_0 and B_{c2} as MgB_2-IMD*;* see Table 3 for the respective fitting parameters.

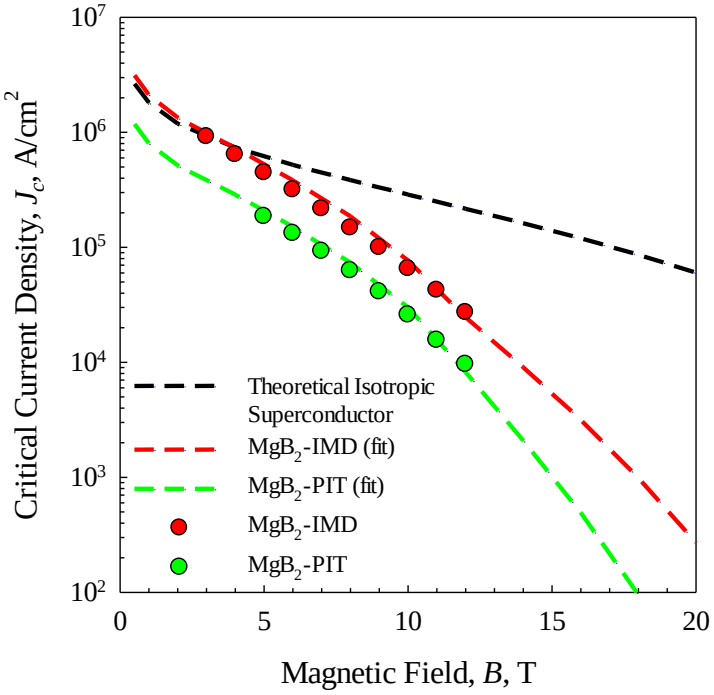

Figure 65. Percolation model fittings for samples MgB_2-IMD and MgB_2-PIT, together with plot of an isotropic grain-boundary pinned superconductor with the same J_0 and B_{c2}.

From Figure 65, it is seen that when comparing the isotropic grain-boundary pinned material to MgB_2-PIT, the 4.2 K J_c at 10 T drops by a factor of 9.6, from 289 kA/cm^2 to 30 kA/cm^2. However, when a similar comparison is made to an IMD-route wire, the 4.2 K J_c at 10 T drops only by a factor of 3.8, from an isotropic value of 289 kA/cm^2 to 77 kA/cm^2.

Generally speaking then, from this analysis it is clear that at 4.2 K, 10 T, ~59 % of the decrease in J_c from a theoretical isotropic superconductor to the values seen in PIT wires is due to the anisotropy of MgB_2 and ~41% results from the presence of porosity.

The deleterious effect of the anisotropy increases in magnitude as the magnetic field is increased. Consequently, even for IMD-route MgB_2 wires, applications where MgB_2 is useful are probably limited to those requiring less than 14 T, after which point J_c drops rapidly with increasing B.

5.6 Summary of Connectivity in MgB_2

A percolation model was applied to MgB_2 wires so that the effects of anisotropy and porosity could be deconvoluted. Anisotropy in B_{c2} and porosity were found to deleteriously affect J_c in PIT wires, especially at large B. Reducing the porosity by using the IMD route removed half of the problem. A true test of the strengths and weaknesses of the model requires a series of samples with a carefully controlled phase fractions of MgB_2 to determine validity of the p_s term. Additionally, a series of samples where p_c is increased for the MgB_2 phase (say by irradiating the sample to introduce more disorder) could be used to test the limits of p_c. Eisterer *et al.* [52], [222] used a set of rather elegant experiments such as these to test the percolation model for MgB_2 bulks. Wires, on the other hand, are a more complex system, as evidenced by Chapter 3 of this work. Given the drawing-induced microstructure of a typical PIT wire, it is essential that the anisotropic connectivity between fibers be addressed. This feat may be accomplished via modification of the percolation model for different connectivities or by re-evaluating the geometric assumptions in the model.

Working within the limits of the above model, however, one finds that 59% of the drop in 4.2 K, 10 T J_c from an isotropic grain boundary pinned material to a porous PIT wire is due to the anisotropy in MgB_2 and 41% is due to the presence of porosity, resulting in a 4.2 K, 10 T J_c of 30 kA/cm^2. Reducing the porosity (1-p_s) from ~30% to ~0% can increase the 4.2 K, 10 T J_c to 77 kA/cm^2. Next, increasing the C concentration has been shown to reduce γ [125],[233]. If γ can be reduced to 1.8-2.0, then the 4.2 K, 10 T J_c may be further increased to 98-116 kA/cm^2, values as high or higher than those exhibited by MgB_2 thin films [5].

Chapter 6: Doping of MgB_2 Thin Films, Wires, and Bulks

In this chapter, dopants are systematically added to MgB_2 thin films, bulks, or wires. Carbon, which substitutes for B and is the most ubiquitously investigated dopant, is introduced to MgB_2 via wires made from "pre-doping" of B by SMI, Inc. process, or through high temperature, high pressure synthesis of C-doped MgB_2 from B_4C + Mg. Additionally, Zr may be added to MgB_2 through ZrB_2 addition via the PLD of MgB_2.

Both sets of doped MgB_2 (C- & Zr- added) were investigated in terms of their superconductive properties. Materials characterization via XRD and TEM was employed to determine the nature of the doping; specifically, if these additions site-substituted.

6.1 Carbon Doping of MgB_2

Carbon (the only element that substitutes into the B sublattice [56], [234], [102], [235]) is, by a very large margin, the most widely studied dopant for MgB_2. The reasons for the popularity of C-doping are the large increases seen in B_{irr} and B_{c2}- effects whose ultimate utility is the increase in high field J_c [228],[236].

A variety of methods have been used to introduce C to into MgB_2. One of the earliest routes is SiC-addition [185]. In this approach SiC is mixed together with Mg and

B powders; upon heating the powder mixture to final temperatures of 625^{o}C [176] to 800^{o}C [237], SiC is reduced by Mg to form Mg_2Si and C near 524^{o}C [5]. This reaction provides free C for the MgB_2 reaction which starts at ~615^{o}C [60],[5]. The homogeneity of the C-doping is then dependent on the size and distribution of the initial SiC particles. For example, small, evenly dispersed SiC leads to short distances between SiC particles. This short diffusion distance in turn leads to a high probability that C will be available for incorporation into the B sublattice during MgB_2 formation. This type of C addition, whereby a C-containing precursor is added to the Mg and B powder mixture such that C produced during (or immediately preceding) the MgB_2 reaction is designated "indirect addition [125]." The main disadvantage of this technique is that the homogeneity of C substitution is directly tied to the size and distribution of the precursor C-containing compound (e.g. SiC or B_4C [238]). Additionally, at least in the case of SiC, Mg_2Si is left behind as a reaction product and serves to reduce the connectivity of the material (an effect exacerbated by the observation that Mg_2Si particles collect at the grain boundaries) [239].

Other C-doping methods employ use of organic precursors (e.g. malic acid) added together with an easily evaporable solvent such as toluene to the initial B powder [71]. The resulting slurry is subsequently heated such that only C and B remain [71], an amorphous C layer, 10-20 nm thick, having formed on the outside of the initial B agglomerates [240]. This B/C mixture is then mixed with Mg and heat-treated to form MgB_2. This approach is termed "direct addition" as C is effectively directly added to the Mg and B powder mixture. The limiting diffusion distance for C is then governed by the

the initial B agglomerate size rather than the spacing between C-containing compounds as in indirect addition. Since the initial particle size for B can be very small with values as low as ~50-200 nm for amorphous B [231], the homogeneity of doping can be much improved using the direct addition technique. LECO analysis of the C-content of the malic acid (MA) treated B revealed < 1.5 at% C [71], even after extended treatments. Therefore, the maximum level of C substitution using the MA treatment in $MgB_{2-x}C_x$ would be x = 0.0267, which is too small to raise B_{irr} and B_{c2} to values significantly higher than those exhibited by undoped MgB_2. For comparison, to achieve 4.2 K values of B_{irr}> 20 T, *x* needs to be 0.05-0.074 [183].

In a further improvement on the direct-addition approach a technique referred to as "pre-doping" was developed by Specialty Materials. Inc. Here, the partially amorphous [72] B powder is made by reducing BCl_3 gas with H_2 in an RF plasma plume [231]. The main products of this reaction are nano-scale B powder and HCl. Methane (CH_4) gas is introduced in controlled quantities to the H_2 gas stream to act as a vector for C addition. The exact quantity of C in the B powder may be quantified by LECO, Inc. using a LECO CS600 combustion analyzer.

A series of wires, each 0.83 mm in diameter, were made using these powders, Table 5. Also given in Table 5 are the initial C concentrations as well as the expected levels of C substitution assuming full reaction. Pellets (0.95 cm diameter) were made from the C-doped B powder mixed together with Mg (Hart Metals, 99.9%, 20-25 μm diameter) by pressing in a pellet die (44.4 kN). These pellets were used to elucidate the change in lattice parameter from doping via XRD analysis. A Scintag XDS 2000 with Cu

K_α radiation (0.9 kW) was used to determine the lattice parameters of the MgB_2. These lattice parameters were then compared to values seen for single crystal specimens with known C concentrations [102] to determine the amount of C substitution present. All wires and pellets were heat treated at 700°C for 20 minutes under Ar atmosphere. Susner *et al.* [125] have described the measurement details and results for these samples. Zero-field *R* vs. *T* measurements were used to determine the T_c of these samples, which was defined as the onset of the superconductivity from the normal state.

Table 5. Sample properties for C-doped MgB_2 wire specimens.

Sample Name	Tracking No.[a]	SC fraction[b]	at% C in B powder[c]	Expected *x* in $MgB_{2-x}C_x$[d]	Actual *x* in $MgB_{2-x}C_x$[e]	T_c (K)[f]
MgB_2-00	2134	0.252	0	0	0	38.3
MgB_2-01	1990	0.115	1.88 ± 0.05	0.038 ± 0.001	0.039 ± 0.001	36.3
MgB_2-02	1650	0.152	3.13 ± 0.03	0.063 ± 0.001	0.063 ± 0.001	36.3
MgB_2-03	1991	0.131	4.72 ± 0.23	0.095 ± 0.005	0.076 ± 0.009	33.9
MgB_2-04	1952	0.183	6.48 ± 0.10	0.130 ± 0.002	0.120 ± 0.003	32.1

[a] Internal tracking number for data traceability; [b] Area fraction of strand that is Mg + B powder mixture; [c] from LECO analysis of B powder; [d] Assuming full reaction; [e] Taken from extrapolation of single crystal data from [102]; [f] Defined as onset of SC transition from the normal state.

T_c was also measured as a function of *B* to determine the values of B_{irr} and B_{c2}. *R* vs. *T* curves were taken of all samples at differing values of *B*. The point marking 10% of the resistive transition from the SC state to the normal state was taken as the point at which the applied *B* was the B_{irr}; the point at which the transition was 90% complete marked the value of B_{c2} (see Chapter 2). Additionally, *R* vs. *B* curves were taken at the National High Magnetic Field Laboratory (NHMFL) at fixed values of *T* using a 35 T magnet. The same criteria applied to the transitions of the *R* vs. *T* curves were applied to

the R vs. B data. Figure 66 displays B_{irr} and B_{c2} as functions of T. Figure 67, which displays dB_{c2}/dT (in the range of 15-32 K) as a function of C concentration, shows the magnitude of the slope increasing with dopant concentration.

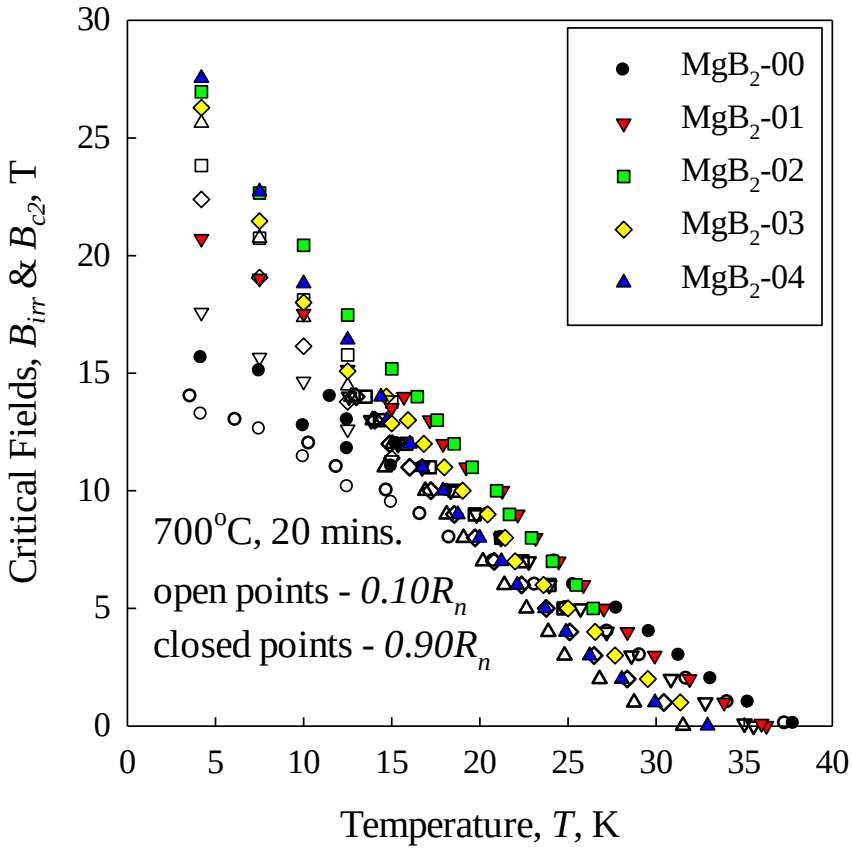

Figure 66. B_{irr} & B_{c2} vs. T for C-doped MgB_2 samples. Data above 14 T was collected at the NHMFL.

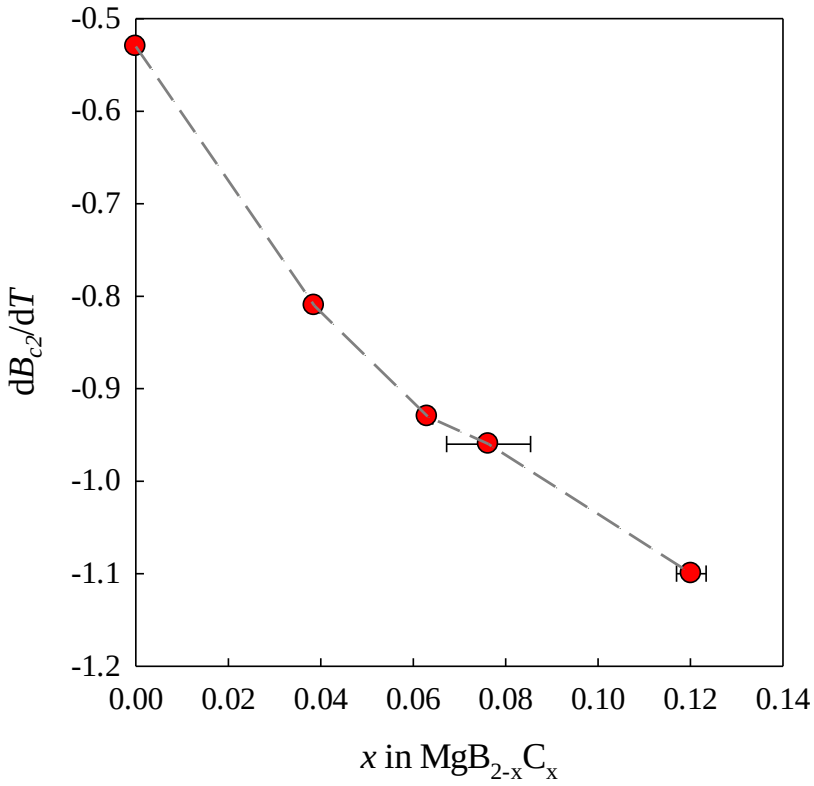

Figure 67. dB_{c2}/dT (in the range of 15-32 K) vs. C substitution for MgB_2 wire samples. The line serves as a guide to the eye.

6.2 "Efficiency" of C-doping in MgB_2

Figure 68 shows the 4.2 K B_{irr} (using the 100 A/cm^2 criterion as these are the only values available for *all* of the samples) for undoped MgB_2 and C-doped MgB_2 made via three different techniques- pre-doped B, MA-treatment, and SiC addition. The MA-treated sample data is from [71] while the SiC added (15 nm and 200 nm SiC particle

size) data are from [148][13]. The abscissa is in the "expected C concentration," i.e. x-values that assume full and homogeneous substitution of C for B for a given doping method (e.g. complete dissociation of SiC and uniform distribution of the resultant C). This comparison expresses the relative efficiencies of C doping by the various techniques in terms of their abilities to increase B_{irr} [125].

The MgB_2 made from pre-doped B yielded the highest values of B_{irr} at every nominal doping level. The MgB_2 made using MA-treated B is relatively close to the pre-doped C line, suggesting that the MA-treatment is nearly as efficient as pre-doping the B for introducing C to MgB_2. Again, the main limitation of this technique is that, even for extended treatments, the C level maximizes at ~ 1.5 at% C, preventing higher substitution levels (and thus higher values of B_{irr}) from being realized. The most telling points on the graph, however, are those of the SiC-added MgB_2. For the same quantity of SiC added, a ~5 T difference in B_{irr} is noted. The likeliest explanation of this phenomenon is that the size of the SiC particles is different between the two samples. Due to their larger average size, the 200 nm SiC particles have, by necessity, a greater separation than the 15 nm SiC, and making homogeneous distribution of C more difficult unless longer reaction times and higher reaction temperatures are used.

[13] Specifically, Exp. 1021 (15 nm) and Exp 1023 (200 nm); both HT at 675°C for 40 min.

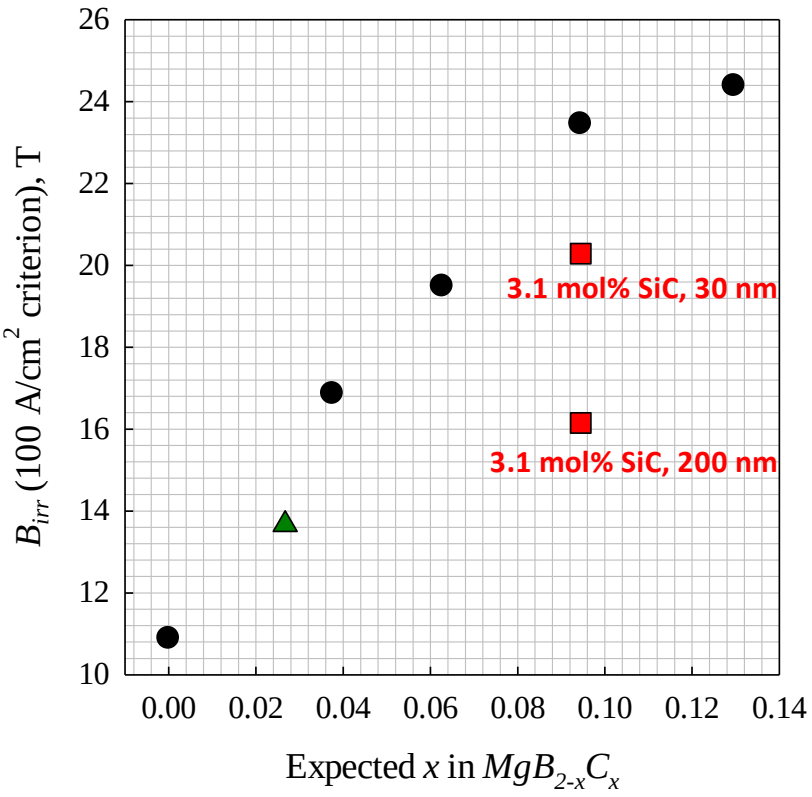

Figure 68. B_{irr} (100 A/cm^2 criterion) as a function of nominal C-doping for undoped MgB_2, pre-doped-B-based MgB_2, SiC-added MgB_2, and MA-treated MgB_2; ▲ "directly added" C (MA-treated), ● "pre-doped B" (SMI), and ■ "indirectly added" C (SiC-added).

From Table 5 it is seen that the expected level of C-substitution and the actual amount as determined from the change in lattice parameter are more or less equal except for sample MgB_2-04, which signals the start of significant deviation. Figure 69 also shows a departure from linearity, suggesting that the solubility limit for C in B is being approached.

Figures 69-72 show the longitudinal microstructure of undoped and C-doped MgB_2 made via different techniques. Figure 69 shows a BSE image of the microstructure of undoped MgB_2 (sample 2134). A fibrous microstructure, characteristic of all drawn polycrystalline materials, is seen. Figure 70 presents the longitudinal microstructure of MgB_2-04 made from pre-doped B containing 6.48 at% C. This sample was found to have a final composition of $MgB_{0.88}C_{0.12.}$ Large dark regions (corresponding to areas of lower atomic mass in a BSE image) are noted. Though quantitative EDS analysis on light elements such B is not possible without a windowless or ultra-thin window detector because of the low K-absorption edge of 0.188 keV [153], qualitative EDS detected significant quantities of both B and C in these regions with little Mg. These dark regions are likely the result of oversaturation of C in the MgB_2. This is in accord with the results of high temperature synthesis of C-substituted MgB_2 in which the greatest amount of C present was found to be ~5.9 at%, corresponding to a composition of ~$MgB_{0.80}C_{0.20}$ [56].

Figure 71 shows the longitudinal microstructure of an MgB_2 wire made from the MA-treated B[14]. Besides the fibrous microstructure, a presence of large areas of high B concentration is noticeable, features previously detailed in Chapter 3. Finally, Figure 72 shows the longitudinal microstructure (this time with the strand direction oriented along the length of the page) for a SiC-added MgB_2 strand[15]. This micrograph shows B-rich agglomerations embedded in the MgB_2 fibers.

[14] Sample 1391, HT at 700^{o}C for 2 hrs. (see Chapter 3)
[15] Exp. 1021, HT at 675^{o}C for 40 min.

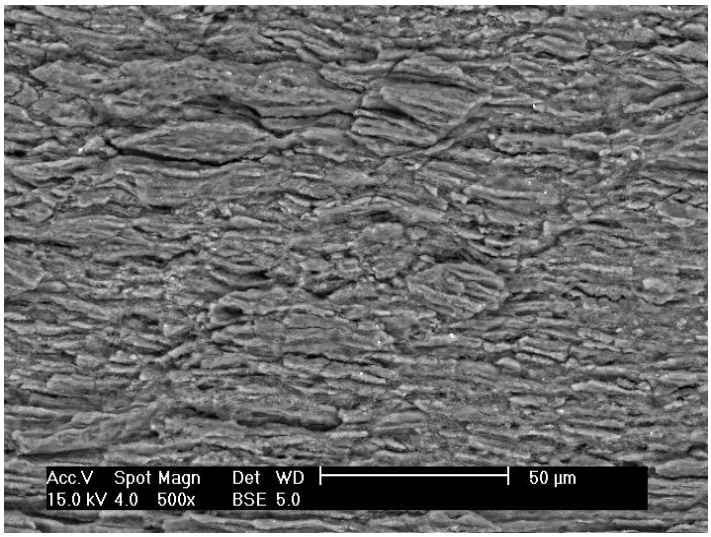

Figure 69. Longitudinal BSE micrograph of undoped MgB_2 wire MgB_2-00.

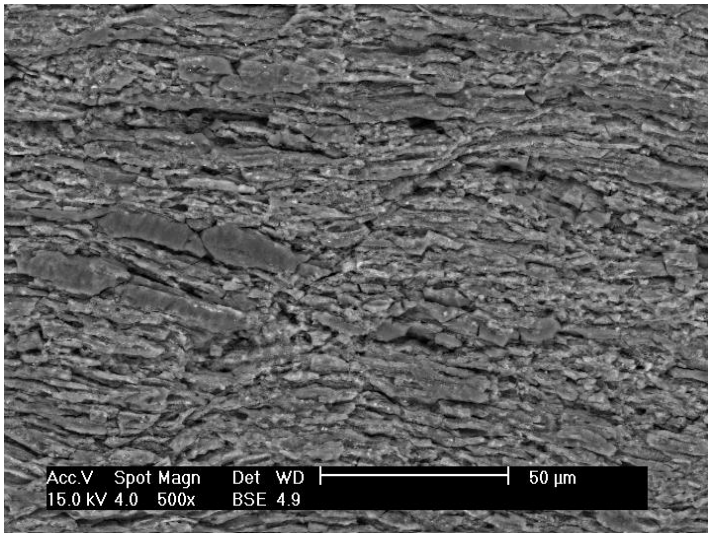

Figure 70. Longitudinal BSE micrograph of C-doped MgB_2 wire MgB_2-04.

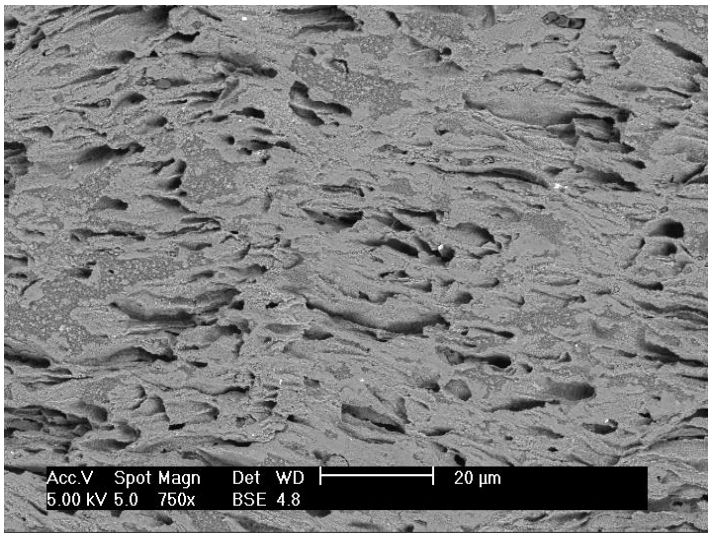

Figure 71. Longitudinal BSE micrograph of MA-treated MgB_2 wire.

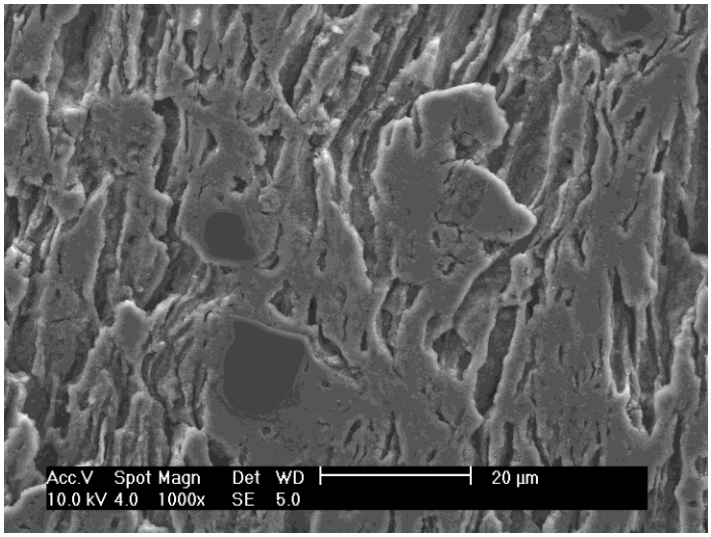

Figure 72. Longitudinal BSE micrograph of SiC-added (15 nm) MgB_2.

6.3 T_c Distribution of C-doping

Though the work of Bohnenstiehl [56] unequivocally shows that C substitutes for B in MgB_2, the question remains as to how homogeneous this C-doping can be. Using the high pressure, high temperature synthesis techniques of Bohnenstiehl [56], the ultimate practical homogeneity of C-doping may be deduced. From the results of the work, several important observations can be made concerning the results of C-doping by various techniques:

i) A high-pressure, high T synthesized C-doped MgB_2 specimen prepared by Bohnenstiehl [56] is by reacting B_4C with Mg under 10 MPa Ar at 1700^{o}C for 10 min. (henceforth referred to as C-MgB_2-HPHT) is investigated in terms of T_c distribution. The procedure used by Bohnenstiehl [56] followed the earlier work of Avdeev *et al.* [234], who used a similar procedure for synthesizing C-doped MgB_2.

ii) A SiC-added bulk MgB_2 sample made with 15 nm SiC particles at 3.1 mol% concentration HT at 675^{o}C for 40 min. This sample will be referred to as C-MgB_2-SiC

iii) An SMI C-doped bulk MgB_2 sample analog of MgB_2-03. The C concentration in the precursor B powder was 4.72 ± 0.23 at%. This sample will be referred to as C-MgB_2-SMI.

The method for elucidating the T_c distribution of a superconducting sample is discussed in Chapters 1 and 2 and can be summarized by applying the following equation (the derivation of which may be found in Appendix D):

$$\int_0^T f(T_c)dT_c = \frac{nS_e(T) - C_e(T)}{(n-1)\gamma_e T} \tag{36}$$

where the left-hand side of the equation denotes the distribution of T_c, T represents temperature, S_e represents the superconducting electronic entropy term, C_e represents the superconducting electronic specific heat, and γ_e is the electronic specific heat coefficient. The variable n is simply the exponent of the Gorter-Casimir two fluid model from which the expression is derived (and whose theoretical value is 3) but can be modified such that the integral of the T_c distribution equals 1 [119].

The heat capacities for the T_c distribution analysis were taken on the samples in both the superconducting and normal states using a Quantum Design Model 6000 PPMS. Because the magnetic field in this system is limited to 14 T, it was necessary to fit the normal-state data to the equation [118], [122], [124]:

$$\frac{C_{fit}}{T} = \gamma_e + \beta_3 T^2 + \beta_5 T^4 \tag{37}$$

where γ_e is the electronic specific heat coefficient and β_3 and β_5 are fitting constants.

The fitted data was used to extract the superconducting contribution to the electronic specific heat, C_{es}, through subtracting the normal state data from the 0 T data.

Using the well-known thermodynamic relation:

$$C = T\left(\frac{\partial S}{\partial T}\right) \tag{38}$$

it is possible to calculate the entropy of the sample. Using these data, Equation 36 may be applied to determine the T_c distribution of a sample. The same procedure is used to analyze the T_c distribution of Nb_3Sn samples of varying compositions in [225].

6.3.1 High-T synthesized C-doped MgB_2 from B_4C

Figure 73 shows the normal state and superconducting heat capacities for C-MgB_2-HTHP. Subtracting the former from the latter yields Figure 74, which plots both C_e and S_e for C-MgB_2-HTHP.

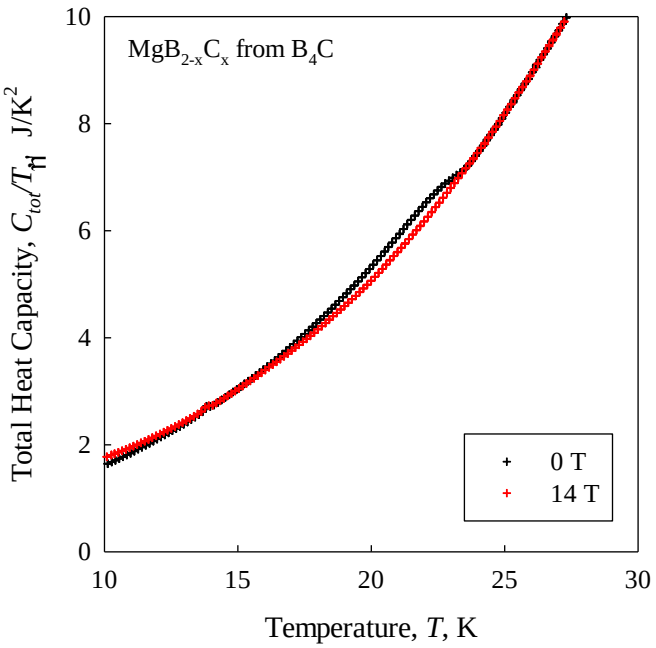

Figure 73. Heat Capacity vs. T for C-MgB_2-HTHP.

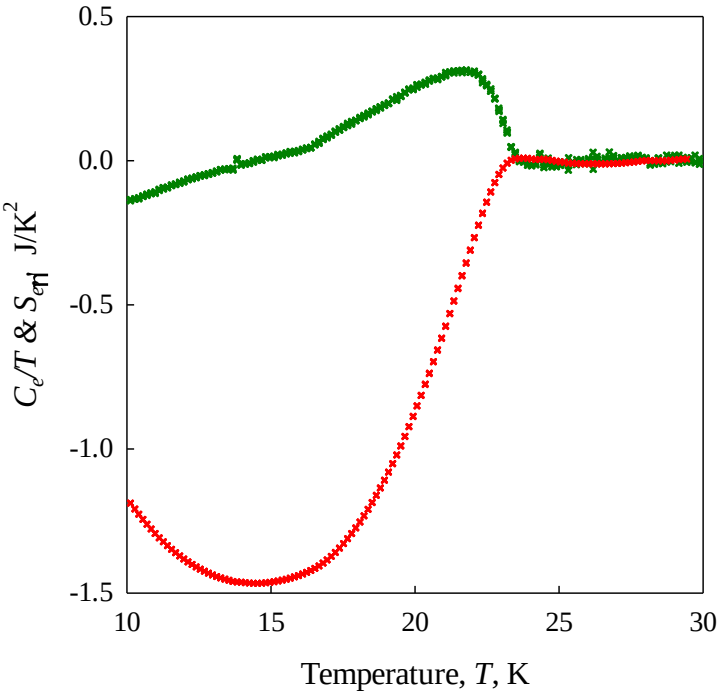

Figure 74. Superconducting electronic heat capacity for C-MgB_2-HTHP.

Figure 75 shows the T_c distribution of C-MgB_2-HTHP. Immediately noticeable are the fact that two peaks are present- one centered about T_c~ 22 K and another, smaller, peak centered about T_c ~ 13 K. Similar analysis on the T_c distribution of Nb_3Sn showed that a second peak occurred in the ternary Nb-Cu-Sn bulk sample [241] - a result proposed as being indicative of the presence of separate superconducting phases. However, for the C-doped MgB_2 made from Mg and B_4C and Mg, only three phases are present- Mg, C-doped MgB_2, and MgB_2C_2 [56]. Only one of these, C-doped MgB_2 was shown to be superconducting. Although some variation in C doping of MgB_2 was seen by the electron probe micro-analysis, this variation was relatively small (on the order of x =

0.20 ± 0.04 for $MgB_{2-x}C_x$ [56]) and would only to broaden the transition, not create a second one. The likeliest scenario, then, is that the second peak in the T_c distribution is the result of the second energy gap intrinsic to MgB_2. Indeed, Bouquet *et al.* [242] see a similar phenomenon in their heat capacity measurements of undoped MgB_2 samples, with the second peak appearing in a similar position. The T_c distribution of the high pressure, high T synthesized C-doped MgB_2 is seen to be quite sharp, with a 3-6 K variation of T_c for the main peak (some smearing is present at the lower T end) and a 1.4 K FWHM.

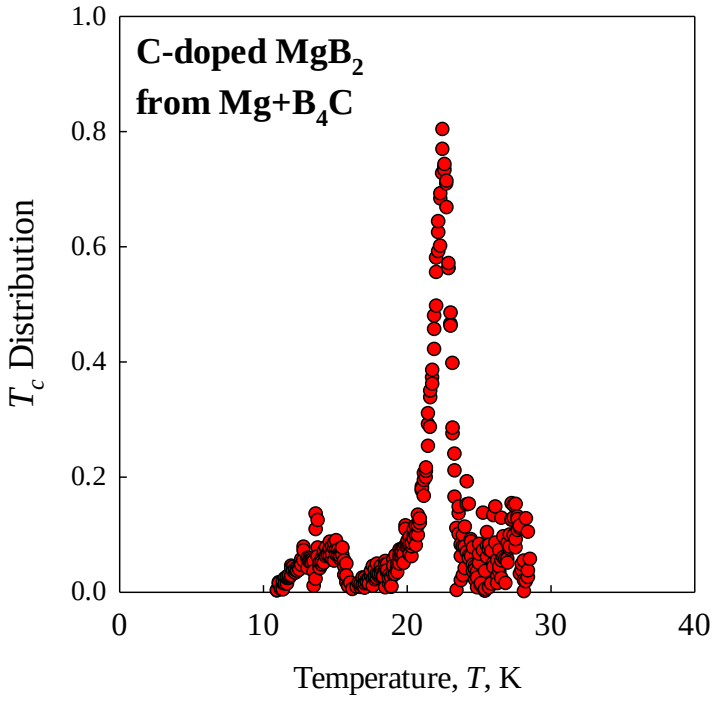

Figure 75. T_c distribution of C-MgB_2-HTHP. The second, lower T peak is likely the result of the second energy gap.

6.3.2 SiC-Added Bulk MgB_2 (15 nm SiC, 3.1 mol%)

The T_c distribution of C-MgB_2-SiC is presented in Figure 76. This reaction route represents the route initially heavily employed to dope MgB_2 with C [228]. In this case, the peak is wider, with a 10 K distribution in T_c and a FWHM of 5 K. Due to the lack of a sharp transition in this sample the low T peak representing the second energy gap is not able to be distinguished from the background.

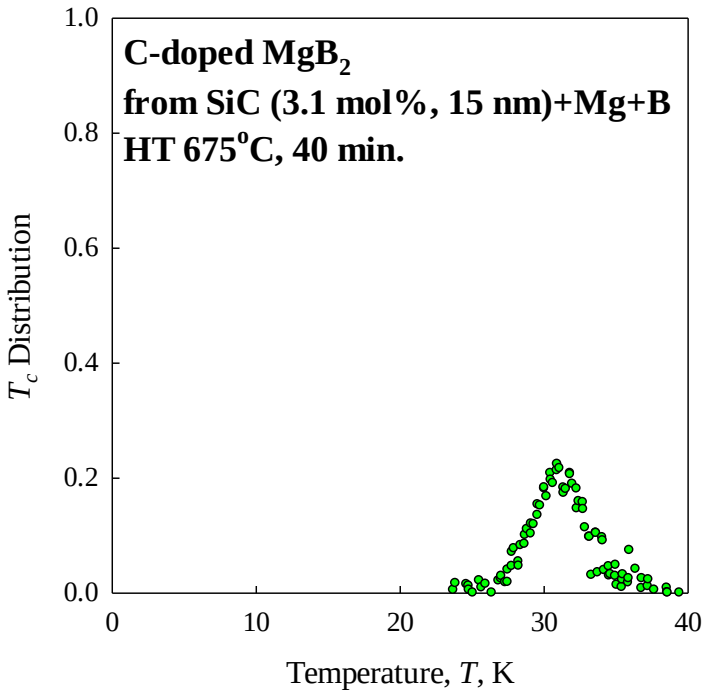

Figure 76. T_c distribution of C-doped MgB_2 made via SiC addition.

6.3.3 SMI C-Doped Bulk Version of C-MgB_2-SMI

Figure 77 shows the T_c distribution of C-MgB_2-SMI. The peak width is ~3.8 K; the FWHM has a value of 3 K. This sample has a much sharper distribution of T_c than that seen for the SiC-added MgB_2, leading to the conclusion that using pre-doped B in the synthesis of MgB_2 enables C to be more homogeneously substituted for B. Again, due to the lack of sharpness in the transition the lower T peak was unable to be distinguished from the noise.

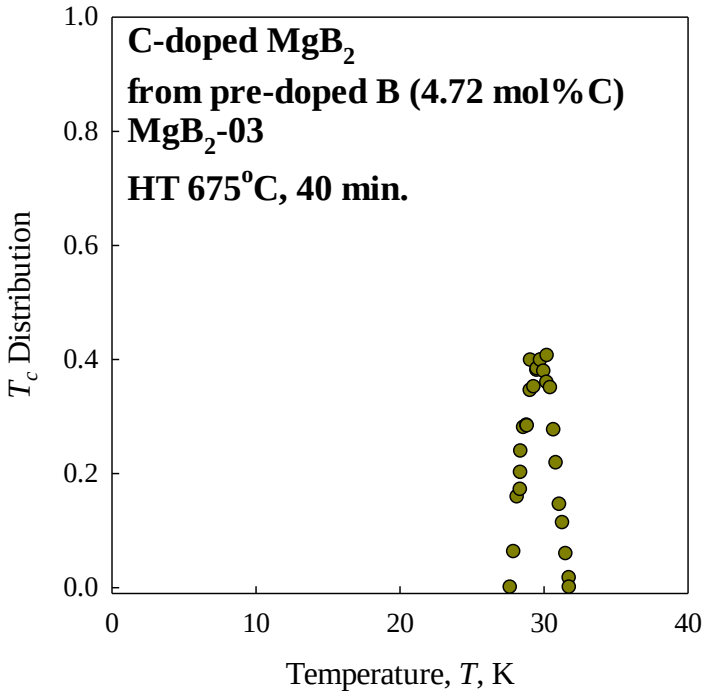

Figure 77. T_c distribution of C-MgB_2-SMI.

6.4 Zr Doping Via Pulsed Laser Deposition: Sample Preparation

Pulsed Laser Deposition (PLD) was employed to more efficiently and intimately add Zr to MgB_2 as either a pinning center or a possible substitutional atom for Mg. Here the vector for Zr addition was ZrB_2. Using a modified form of the procedure outlined in Chapter 4, a ZrB_2 target (1" diameter, 99.998% manufactured by Kurt Lesker, Inc.) was used in conjunction with the MgB_2 target used in Chapter 4. The targets were sequentially rastered such that the MgB_2 target was exposed to 200 laser pulses at 10 Hz and the ZrB_2 target was exposed to 0-70 pulses, also at 10 Hz, so as to study a variety of doping levels. This process was repeated 200 times, after which a Mg cap layer (40000 pulses) was applied and the film annealed for 10 min. at 700^{o}C, the optimum HT found in Chapter 4. Two sets of samples were created: smaller 3 mm x 3 mm samples (Table 6) for optimizing the deposition procedure and for performing magnetic measurements, and larger 3 mm x 10 mm samples (Table 7) for resistivity, TEM, and XRD measurements. The Zr/Mg ratio was established by using STEM-EDS analysis on the thin films. As stated previously, B and C are difficult to accurately measure using EDS. Mg and Zr, being heavier elements, are both easily detected. These two observations result in an EDS spectrum that does not display all elements that are present in the sample. Regardless, the *ratios* of these two elements (Mg and Zr) should remain invariant for a given sample (assuming a homogeneous composition of the $Mg_{1-x}Zr_xB_2$ phase), no matter what other elements are included in the compositional profile. Moreover, a truly quantitative EDS analysis should utilize a standard for comparison which was unavailable for this work.

Table 6. ZrB_2/MgB_2 ratios and resultant $T_{c,\,onset}$ for 3 mm x 3 mm PLD samples.

Sample Name	ZrB_2/MgB_2	Nominal %ZrB_2	$T_{c,onset}$, K (magnetic)
MgB_2-164	0	0	30.4
MgB_2-165	5/200	2.4	25.3
MgB_2-166	10/200	4.8	22.5
MgB_2-167	20/200	9.1	18.1
MgB_2-168	30/200	13.0	15.0
MgB_2-169	50/200	20.0	9.99
MgB_2-172	70/200	25.9	5.88

Table 7. ZrB_2/MgB_2 ratios, resistive $T_{c,\,onset}$, and B_{c2} (in-plane) data for 3 mm x 10 mm PLD samples.

Sample Name	ZrB_2/MgB_2	Nominal %ZrB_2	Zr:Mg ratio in film from STEM-EDS analysis	$T_{c,\,onset}$, K (resistively measured)	(4.2) K B_{c2} (in-plane), T (resistively measured)
MgB_2-182A	0	0	0	34.3	--
MgB_2-190	5/200	2.4	--	28.6	29.8
MgB_2-189	10/200	4.8	--	25.0	22.8
MgB_2-188	20/200	9.1	--	22.4	18.3
MgB_2-192	30/200	13.0	--	19.8	15.5
MgB_2-194	50/200	20.0	11.6:89.4	--	16.3

6.5 Zr Doping via Pulsed Laser Deposition: Magnetic Superconductive Properties

The property first measured on the Zr-doped thin films was the zero-field superconducting critical temperature, T_c, as a function of Zr-doping. Figure 78 charts the zero-field $T_{c,onset}$ as measured via AC susceptibility. The undoped sample has a T_c of 30.5 K, much lower than the 32.3 K seen for another film made under the same conditions in Chapter 4. This is likely due to the fact the entirety of the PLD apparatus was disassembled, exposed to air, and re-assembled due to a building renovation. This circumstance necessitated re-alignment of the laser optics and re-optimization of the deposition parameters.

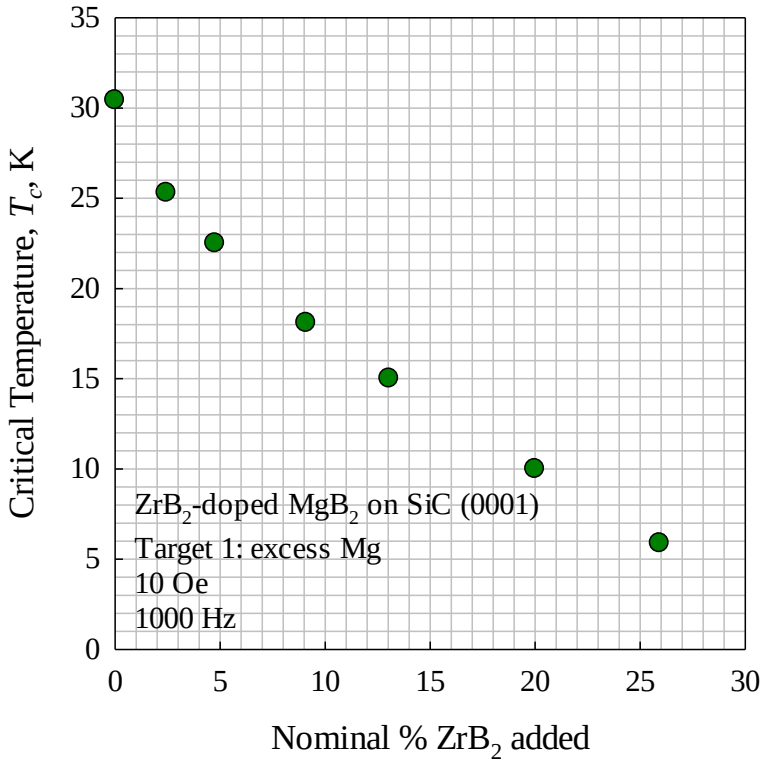

Figure 78. AC susceptibility-measured zero-field $T_{c,onset}$ of Zr-doped MgB_2 thin films. The T_c of ZrB_2 is 5.5 K [243].

From the data presented in Figure 78, it is clear that as the amount of ZrB_2 is increased, the T_c monotonically decreases such that at 20 nominal mol% ZrB_2, the T_c falls to 10.0 K. At 25.9 nominal mol% ZrB_2, the T_c is 5.88 K. It should be noted that the T_c of pure ZrB_2 is 5.5 K [243]. The fact that the T_c does not decrease more gradually is not surprising considering that similar non-linear behavior has been seen in NbTi alloys [244]; in this case the effect was claimed to be caused by variations in the microstructure where a martensitic phase formed at low Nb concentrations. Here there is no phase transformation as ZrB_2 and MgB_2 have the same space group and crystal structure. A

fairer comparison would be in the intermetallic Nb_3Sn-Nb_3Al pseudobinary phase diagram (in which complete solid solubility is exhibited) plotted in terms of T_c by Bachner *et al.* [218] where the T_c of the intermediate composition of $Nb_3Al_{0.5}Sn_{0.5}$ is lower (at a value of 15.3 K) than the pure Nb_3Al or Nb_3Sn phases (~17.2 K and 18.1 K, respectively). Bachner *et al.* offer no explanation for this phenomenon. Willens *et al.* [246] also noted similar variability in T_c in the TaC-WC and the MoC-WC pseudobinary systems. The former system (where TaC has a T_c of 10.1 K and WC has a T_c of 10.0 K) shows a maximum in T_c at ~$Ta_{0.5}W_{0.5}C$ (~10.2 K), has a decrease to a minimum T_c at $Ta_{0.2}W_{0.8}C$ (~8.8 K), and exhibits an increase again at WC. The latter system (where MoC has a T_c of 14.3 K) exhibits a local minimum in T_c (~11.7 K) at $Mo_{0.9}W_{0.1}C$, a local maximum in T_c (~12.0 K) at $Mo_{0.8}W_{0.2}C$, and a minimum in T_c at $Mo_{0.1}W_{0.9}C$ (~8.4 K). Willens *et al.* describe these changes in T_c as the result of an increase in the attractive phonon interactions caused by "improving" the stoichiometry. In reality, according to the McMillan formula describing the T_c of a superconductor [105], the interplay between density of states, electron-phonon coupling, and atomic mass is complex in that these terms are not entirely independent of each other. In this context, it is unsurprising that the T_c decreases rapidly when Zr is added to MgB_2; indeed, the T_c of a heavily Zr-doped MgB_2 sample might fall below that of a pure ZrB_2 specimen.

In Figure 79, plots of B_{c2} vs. T as measured via AC susceptibility for a selected range of compositions for the smaller set of samples listed in Table 6, show B_{c2} decreasing as the concentration of Zrb2 increases while $-(dB_{c2}/dT)$ increases, Figure 80. A closer look at Figure 79, specifically for samples MgB_2-164 and MgB_2-165, shows that

the more-steeply sloped MgB_2-165 (2.4 nominal mol% doping) has a B_{c2} that extrapolates to a higher value than that of the undoped sample. Unfortunately, 14 T was the limit of the susceptometer used to collect these data, so extrapolations to higher fields must be made with caution. Nevertheless, the data in Figures 79 and 80 suggest that for a moderate amount of ZrB_2 addition (e.g. 2.4 nominal mol%ZrB_2), there exists a regime of low temperature (e.g. < ~10 K) with which ZrB_2 additions to MgB_2 can be expected to increase B_{c2}.

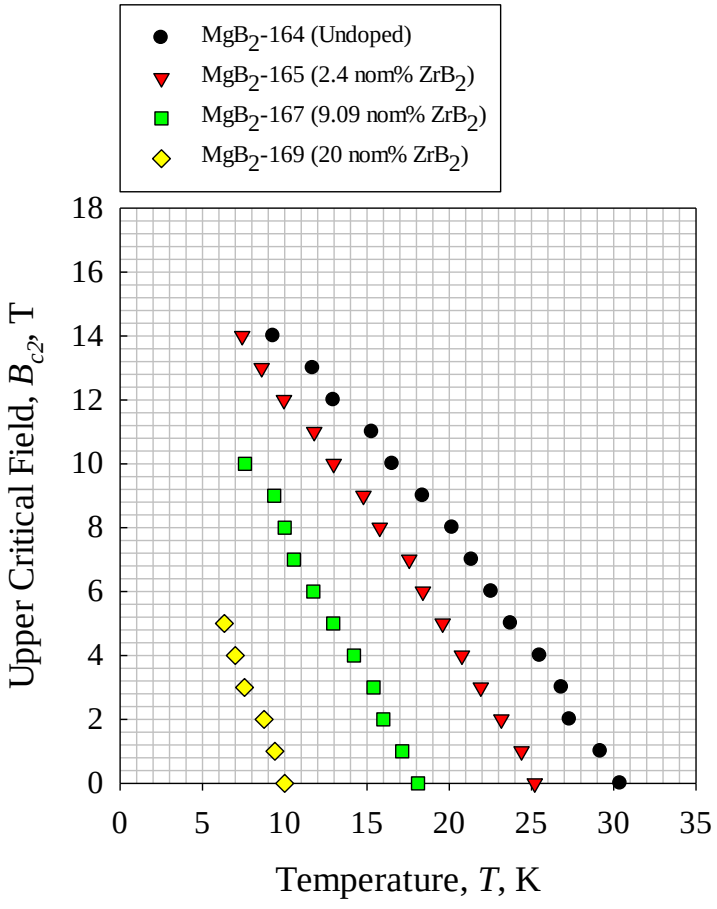

Figure 79. B_{c2} vs. T as measured via AC susceptibility for selected compositions.

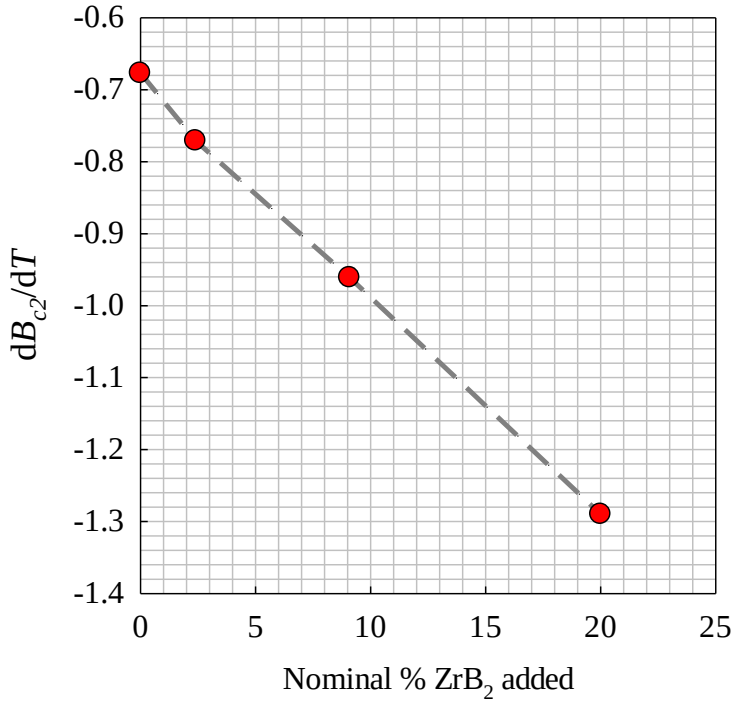

Figure 80. dB_{c2}/dT vs. nominal ZrB_2 addition, adapted from the data in Figure 70. The line serves as a guide to the eye.

6.6 Zr Doping Via Pulsed Laser Deposition: STEM- EDS Characterization

Due to time and equipment-scheduling constraints, only one film was analyzed via STEM-EDS: MgB_2-194 (the most heavily doped sample). Figure 81 shows the BF TEM image of the microstructure of the film at ~70 kx magnification. The most readily apparent feature is the presence of large "bubbles" of Mg. These bubbles were shown by electron diffraction to be amorphous in nature (Figure 82). Interestingly, the MgB_2 film

growth is not limited to the surface of the substrate, but also occurs on the surfaces of these bubbles, likely due to diffusion of MgB_2 to the surface of the Mg. The MgB_2 grains on the surface of the bubbles are also c-axis oriented with respect to the surface of the bubble, implying that the MgB_2 grains in thin films preferentially align with this orientation independently of the crystallographic characteristics of the substrate. This orientation phenomenon may be limited to PLD thin films where MgB_2 formation occurs during a high temperature anneal, as other thin film deposition techniques such as HPCVD (where MgB_2 is formed during deposition) show that the grain alignment of MgB_2 can be manipulating depending on the substrate used during deposition [247].

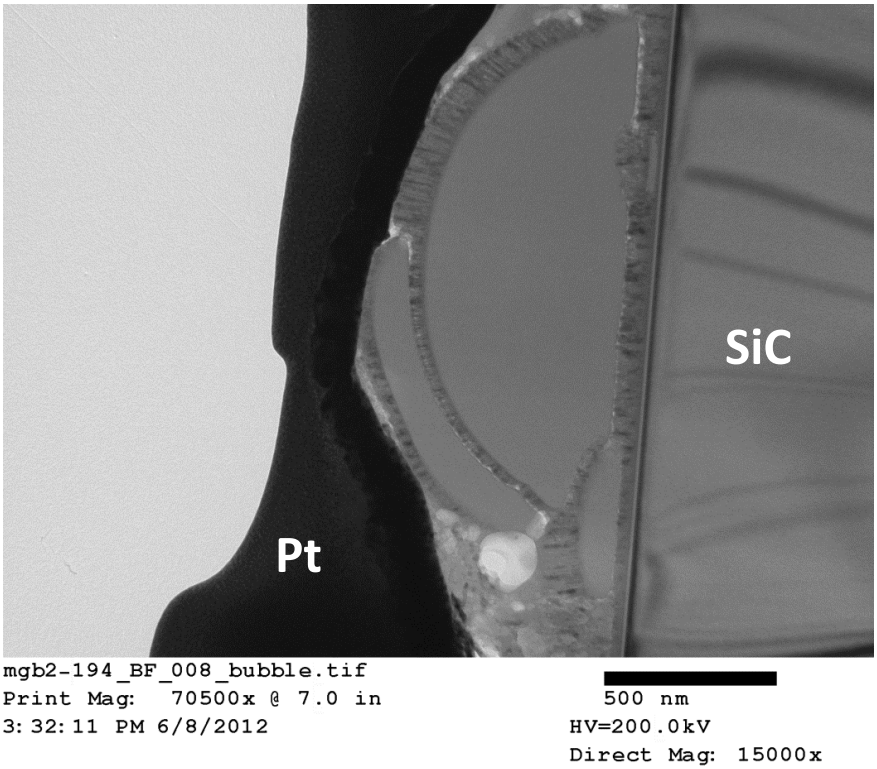

Figure 81. BF TEM image of the microstructure of MgB_2-094 showing MgB_2 growth on top of amorphous Mg "bubbles".

Figure 82. Electron diffraction pattern of Mg bubble showing diffuse rings.

The presence of the amorphous Mg bubbles and the c-axis oriented grains that grow on the surface of these bubbles have important implications with regard to the characterization of these films. For example, XRD measurements of the films using a standard Bragg-Brentano configuration will show all allowed MgB_2 reflections as the film growing on top of the bubbles provides the full spectrum of possible orientations. However, careful application of grazing incidence diffraction (GID- both in-plane and not) can be used to discern only the MgB_2 reflections from the "base" layer, provided a precise alignment in *z*(the height of the sample) is achieved.

H.O. Colijn applied STEM-EDS analysis to the film layer using an FEI Technai with a FEG electron using STEM mode. The EDS analysis was performed without a standard (due to its lack of availability) so atomic compositions can potentially vary by as much as 10% from the reported values. Nevertheless, EDS analysis of the heavily-doped MgB_2 was useful for discerning several important features of the ZrB_2 doped films.

Figure 83 shows the areas of the film that was investigated by STEM-EDS analysis (i.e. the line perpendicular to the film surface in the image). This particular region had a thickness of ~200 nm and no Mg bubble at its surface. The FEG source provides a higher resolution image than was possible with the LaB_6 source used to image Figure 81, permitting more detail to be resolved. Here it can be seen that two distinct regions are present: a fine grained columnar region close to the substrate surface and a coarser grained region close to the film surface. The reason for this is not clear

The STEM-EDS analysis was applied using 26 distinct points from the film surface through the film/substrate interface. The relative concentrations of Mg and Zr are compared and presented in Figure 84. The composition of the Zr (compared to the Mg) varies from 5-16 at%, with an average of 11.6 at % Zr. It can then be inferred that the MgB_2 deposits at twice the rate of the ZrB_2 since the composition given by the EDS analysis is ~50% of the nominal composition given in Tables 6 and 7. A slight increase in Zr concentration as one approaches the substrate from the film surface is also present. Additionally, Zr is absent from the interface layer which is Mg rich and likely to be Mg_2Si.

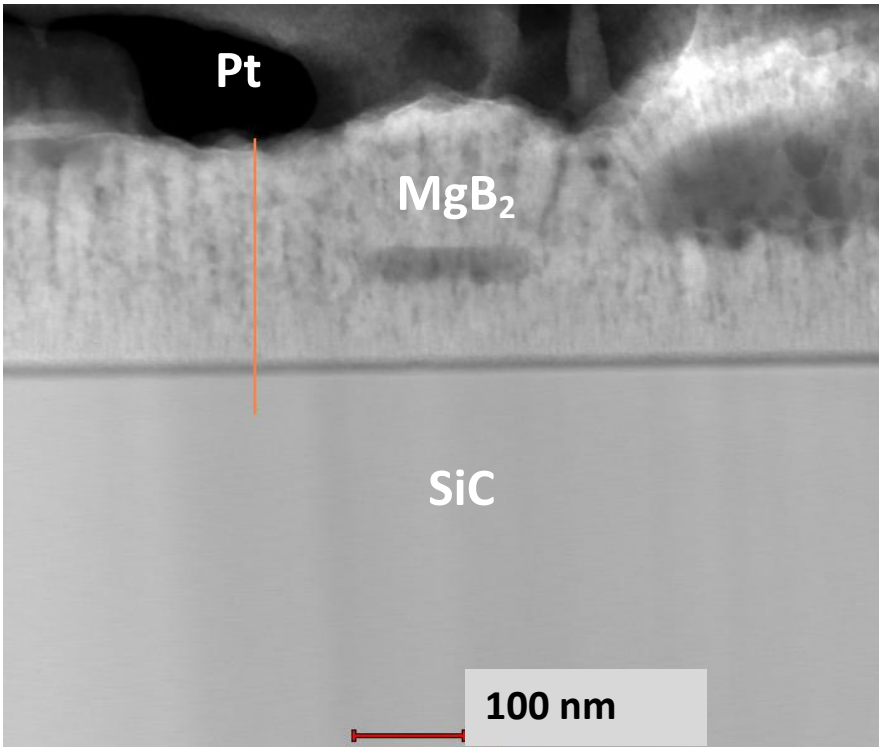

Figure 83. BF TEM image of MgB_2-094 showing first region scanned by STEM for EDS analysis.

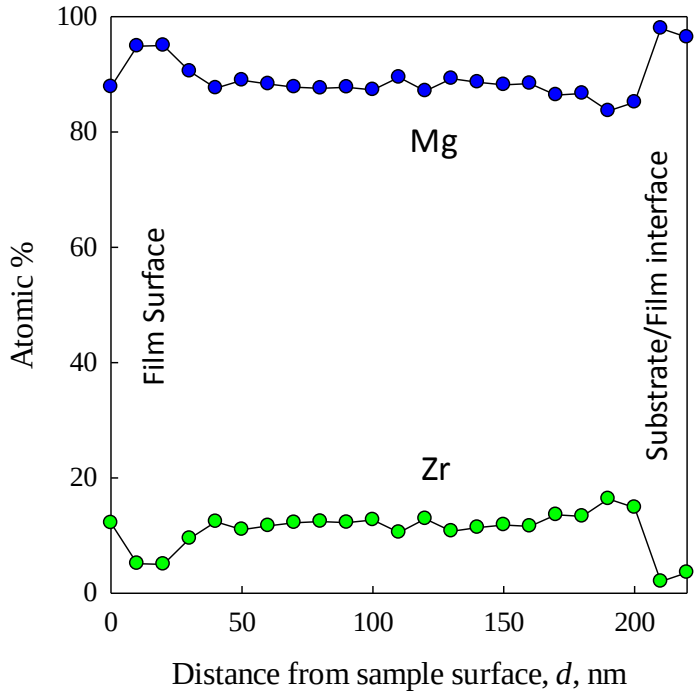

Figure 84. Mg/Zr EDS composition profile of ~200 nm region in Figure 83.

Figure 85 shows the second and third regions to be investigated by EDS. This image presents these regions upon which STEM-EDS analysis revealed an interesting effect: an apparent density gradient in the film. Near the film surface the electron beam drills through the film, leaving behind a dark hole. Approaching the substrate, these holes close and hence become lighter in color- a result of C deposition (C being present in significant quantities in the Pt layer as the Pt forms from an organo-metallic compound). The transition from the e-beam drilled hole through the film to where the e-beam causes C takes place exactly where the microstructure transitions from fine columns to coarse columns. Given that the TEM foil thickness is relatively constant, this transition shows

that a change in density is present. This result can be explained by one of the following: i) a compositional change as a result of the higher concentration of Zr close to the substrate; ii) decreased porosity in the finer grain region; iii) some combination of i) and ii). Figure 86 shows the composition profile of the Zr in the thinner region (compared to the Mg), which varies from 5-18 at%, with an average of 11.5 at % Zr, similar to the concentration profile in the thicker region of the film.

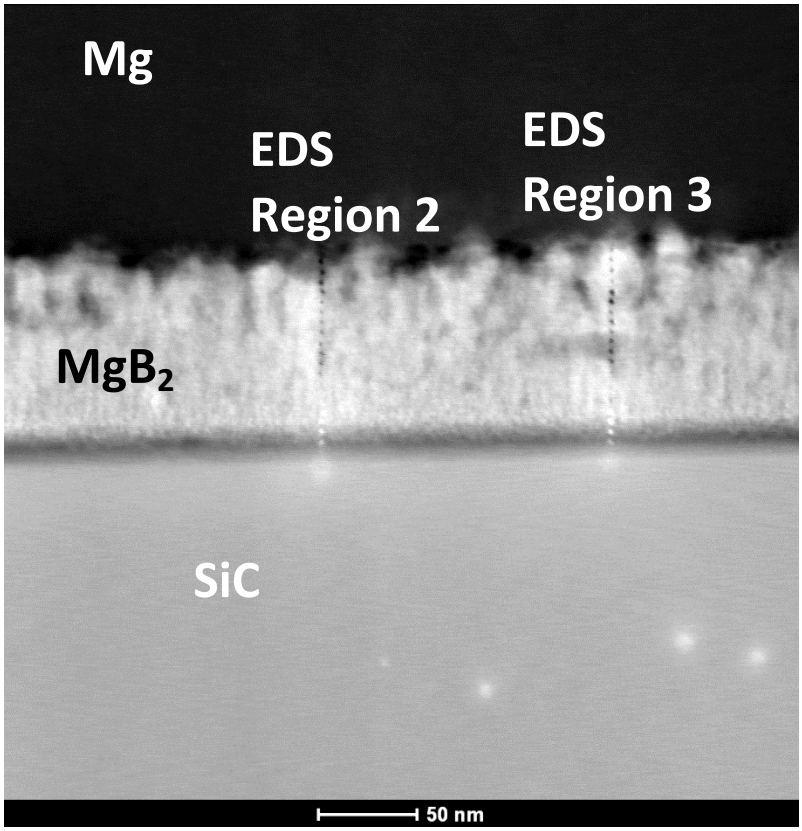

Figure 85. BF TEM image of MgB_2-094 showing second and third regions (thinner part of film) scanned by STEM for EDS analysis.

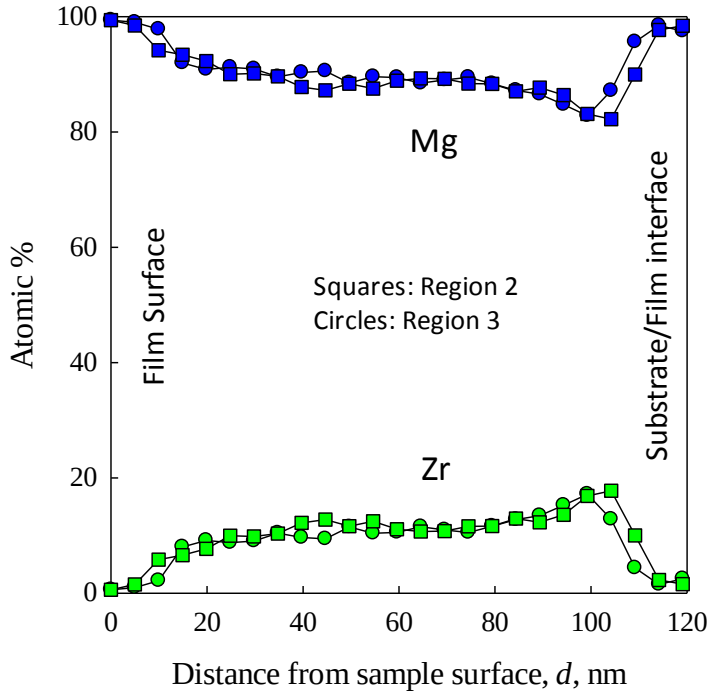

Figure 86. Mg/Zr EDS composition profile of ~200 nm region in Figure 85.

6.7 Zr Doping Via Pulsed Laser Deposition: XRD analysis

From the BF TEM images, it is seen that the columnar grains in the thin film are quite small, <<10 nm in cross section. As a result, there remains a possibility that the STEM-EDS probed a cluster of grains, leaving open the question of whether or not the Zr is located at the Mg sites and/or grain boundaries. To determine if substitution was indeed present, GID XRD was used to determine the structure of the thin film via analysis of both the in-plane and out of plane lattice parameters on a selection of films

from Table 7. The height of the film was carefully adjusted such that diffraction from the "base film" (i.e. the film under the Mg bubbles) was the only major contribution to the observed diffraction peaks. The out of plane GID data for the MgB_2 (0 0 0 2) reflections for the films in Table 7 presented in Figure 87 show little variation in the 2θ position of this peak with ZrB_2 content. Figure 88, which displays the GID in-plane data, shows a systematic peak shift with increasing Zr content. The "a" lattice parameter varies from 3.073 ± 0.005 Å for the undoped film (MgB_2-182A) to a value of 3.105 ± 0.001 Å for the most heavily doped film (MgB_2-194). Again, as in Chapter 4, lattice parameters were determined by peak fittings of the highest-order reflections. Error was determined by variations in the peak fitting.

Also seen in Figure 88 are peaks resulting from the Ag paste used to secure the substrate to the heater, as previously discussed in Chapter 4. Interestingly, the Mg $(11\bar{2}0)$ reflection is also seen, indicating that some of the Mg is crystalline, contradicting the TEM data presented earlier. It is likely that the TEM foil did not represent the entirety of the sample and that larger areas of crystalline Mg await discovery.

Figure 89 shows the resultant "*a*" and "*c*" lattice parameters with increasing Zr addition. The abscissa was scaled according to the STEM-EDS data performed on MgB_2-094 and assumes that a linear relationship exists between the observed EDS concentration of Zr and the number of deposition pulses. This assumption is not necessarily true and requires additional STEM analyses on the remainder of the thin film samples to verify. Nevertheless, the plot is useful in showing the changes in the evolution of the lattice

parameter with increasing Zr content. It should be noted that the lattice parameters of pure ZrB_2 are a = 3.170 Å and c = 3.532 Å [243]. According to Vegard's law the "*a*" lattice parameter should increase linearly going from MgB_2 to ZrB_2. Figure 89 shows significant deviations from this rule, likely a result of concentration gradients in the samples or errors in the assumptions on the actual concentration of Zr present. Nevertheless, the systematic shift in "a" lattice parameter with increasing Zr concentration is suggestive but not necessarily conclusive that the Zr is indeed substituting for the Mg site in MgB_2.

It is likely that changes in B_{c2} caused by increased Zr doping are caused by this modification of lattice parameter. Changing the structure of the unit cell will change the electronic properties (and hence the electron scattering).

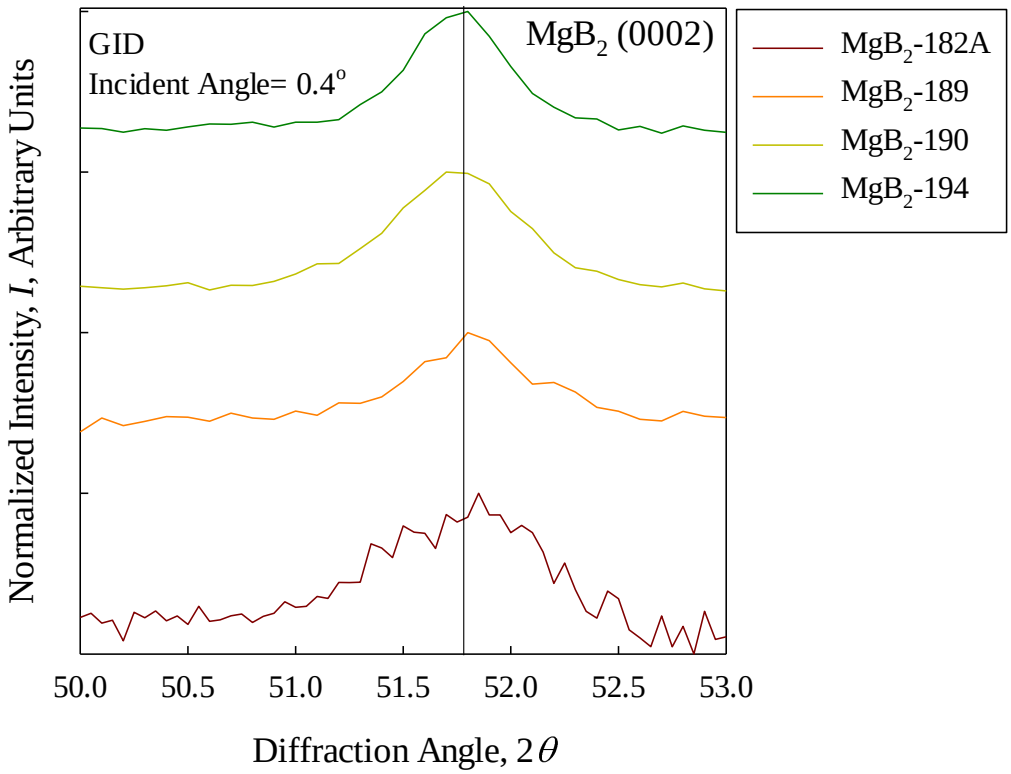

Figure 87. GID out of plane diffraction showing little change in location of *c*-axis reflections with increasing Zr concentration.

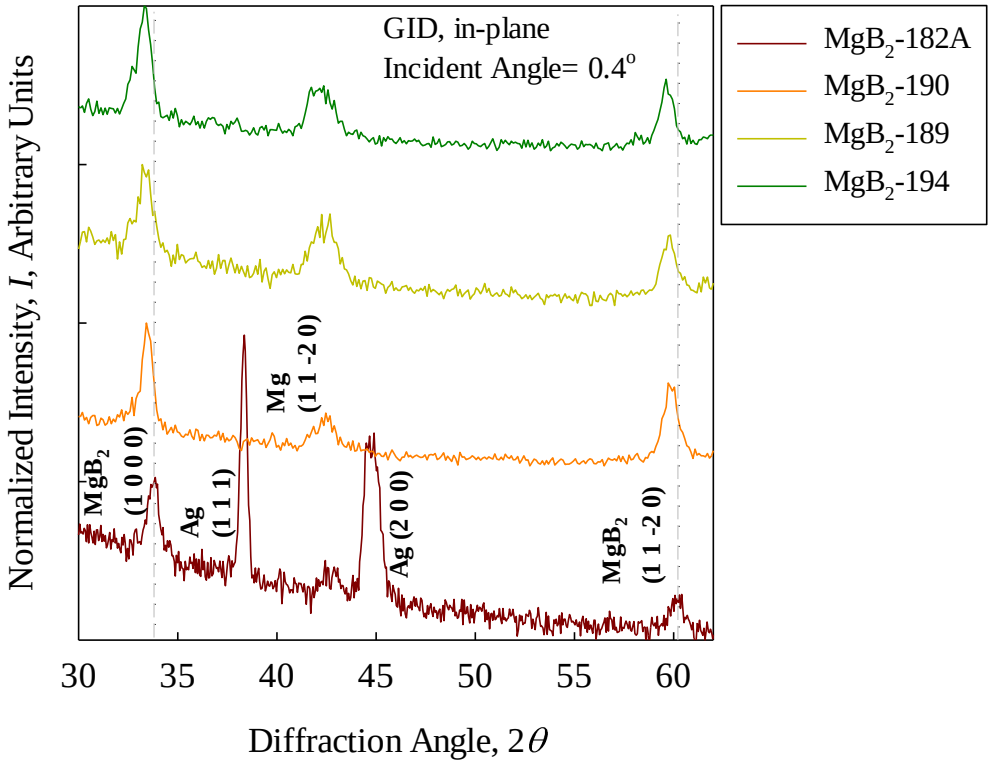

Figure 88. GID in plane diffraction showing increasing peak shift in *a*-axis reflections with Zr concentration.

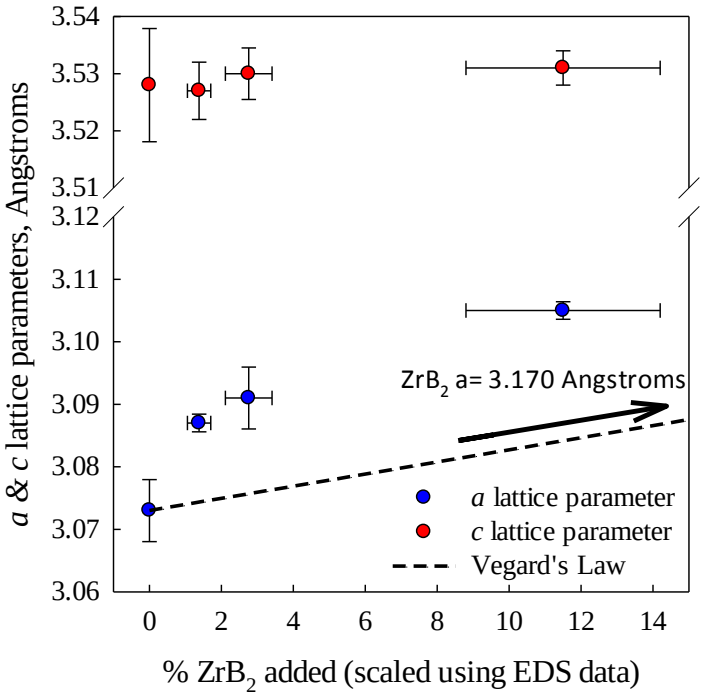

Figure 89. Lattice parameters from GID and GID in-plane diffraction showing peak shift in *a*-axis reflections with increasing Zr concentration.

6.9 Zr Doping Via Pulsed Laser Deposition: Resistively Measured Critical Fields

Both in-plane and out-of-plane (with respect to the thin film) *R* vs. *T* as a function of *B* or *R* vs. *B* as a function of *T* measurements were performed on the films listed in Table 7. These data were collected via 4 point measurements either for the latter case, at the National High Magnetic Field Laboratory (NHMFL) using a 35 T magnet or, for the former case, using the 14 T Model 6000 PPMS at the CSMM. The results were analyzed (as described in Chapter 6, pp. 159-160) for presentation in the format B_{c2} vs. *T*, Figure 90.

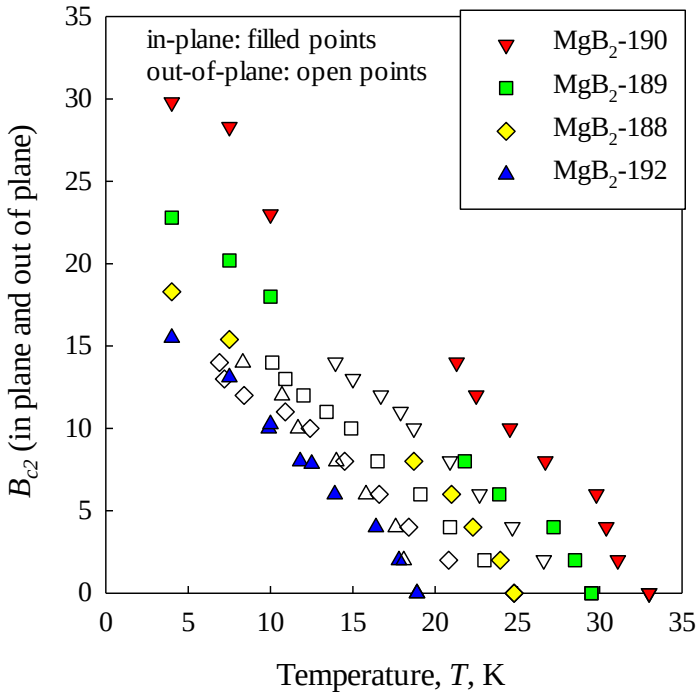

Figure 90. In-plane (filled ponts) and out-of-plane (open points) B_{c2} vs. T. Data above 14 T was collected at the NHMFL.

The control sample (MgB_2-182a) became degraded due to moisture before it could be properly characterized at the NHMFL preventing data from being displayed in Figure 90. As a result, it is difficult to ascertain whether doping with Zr has a positive effect of the value of B_{c2} at low temperatures (say $T < 10$ K), in contrast to the magnetic data presented in Figure 79. Interestingly, magnitude of the slope, dB_{c2}/dT, actually remains constant or *decreases* for increased doping concentration, again in contrast to the magnetic data shown in Figure 79. The reason for this discrepancy is as of yet unclear but may be due to the doping inhomogeneity exhibited by the larger samples. Also it can be seen that the data in Figure 90 sometimes vary quite a bit from linearity. This

phenomenon could cause a misinterpretation of the value of dB_{c2}/dT due to the lack of available data points for the resistivity measurements as compared to the magnetic measurements.

6.10 Doping Summary

Chemical substitution on the B and Mg sites for the MgB_2 superconductor was investigated. With respect to C, it was seen that use of "pre-doped" B nanopowder greatly enhanced the value of B_{irr}. Additionally, the use of pre-doped B powder enables a greater homogeneity of T_c (and hence doping) than the use of SiC.

Zr addition was also investigated via PLD synthesized thin films made by sequential deposition of MgB_2 and ZrB_2. Both resistive and magnetic measurements showed T_c decreases monotonically with Zr addition, as did B_{c2}. GID in-plane XRD showed a systematic increase in the *a*-lattice parameter with increased Zr addition implying Zr substitution for Mg; no change was seen in *c*-lattice parameter. STEM-EDS mapping showed large concentration gradients in the most heavily doped sample.

Chapter 7: Summary and Conclusions

Magnesium diboride, with its superconducting transition temperature of 39 K, is a material that has engendered much interest in the decade since its discovery in 2001. The central research thrusts since then have included i) increasing in the critical fields through chemical substitutions on the B or Mg lattice and ii) improvements in critical current density through decreasing porosity. However, complete deconvolution of the effects of flux pinning, crystalline anisotropy, porosity, electrical connectivity, doping, and doping homogeneity has been problematic, resulting in misleading interpretations of experimental data.

7.1 Electrical Connectivity in MgB_2

To deconvolute the effects of porosity and anisotropy on supercurrent transport in MgB_2, a series of MgB_2 specimens was created using several experimental procedures. These included i) porous, randomly oriented MgB_2 wires made by the powder-in-tube method; ii) dense, randomly oriented MgB_2 wires made with the internal Mg diffusion technique, and iii) dense, c-axis oriented MgB_2 thin films made by pulsed laser deposition. Through comparison of these different sample types the effects of crystalline anisotropy and porosity on the supercurrent transport properties of MgB_2 were isolated,

allowing for a detailed explanation of the degradation of supercurrent in MgB_2 wires at high fields as compared to an ideal (i.e. dense and isotropic) material.

Through the application of a percolation model to dense MgB_2-IMD wires and porous MgB_2-PIT wires it was found that at 4.2 K and 10T, ~60% of the degradation in current transport of a standard powder-in-tube MgB_2 wire compared to that of an ideal (isotropic , well-connected, and dense) material was due to MgB_2's intrinsic crystalline anisotropy. The remaining 40% could be eliminated by reducing the porosity.

The applied percolation model was additionally able to use the influences of anisotropy and porosity on the $J_c(B)$ characteristics of MgB_2 to explain deviations in the flux pinning force density that have been ubiquitously observed in MgB_2 bulks and wires [4], [148], [183], [236].

7.2 Doping in MgB_2 Via Chemical Substitution

Chemical substitution was explored for both the Mg and B sites in MgB_2 in terms of effects on structure and superconducting properties. Carbon (which has been conclusively proven to substitute for B [56]) is the most widely studied dopant for MgB_2 and yields large increases in the values of B_{irr} and B_{c2} with relatively small amounts of chemical substitution (x ~ 0.04-0.14 in $MgB_{2-x}C_x$). In the literature C is introduced to MgB_2 using what may be grouped as: i) *indirect addition* where a C-containing precursor is added to the Mg and B powder mixture such that C produced during (or immediately preceding) the MgB_2 reaction and ii) *direct addition* where C is effectively directly added

to the Mg and B powder mixture. It is important to determine which of these yields the most nearly homogeneous distribution of C (as gauged by the measured T_c distribution, the C-concentration being directly linked to the T_c [102]).

The homogeneity of C-distribution was quantified in terms of the width of the superconducting specific heat transition. Specific heat measurements were performed on a series of C-doped MgB_2 samples made with differing doping techniques. The first sample, where C-doped MgB_2 is synthesized via high temperature (1700^{o}C), high pressure (10 MPa) reaction of B_4C and Mg (x= 0.20 in $MgB_{2-x}C_x$), yielded a 3-6 K distribution of T_c with a FWHM of 1.4 K. This sample, made under extreme conditions, probably represents the ultimate vale that the homogeneity of C doping may reach. Using SiC as a vector for C addition (such that x = 0.07 in $MgB_{2-x}C_x$), however, produces a sample with a broader T_c transition width of 10 K and a FWHM of 5 K. The same specific heat analysis performed on C-doped MgB_2 made with pre-doped B (x = 0.076 in $Mg_{2-x}C_x$) showed a much tighter T_c distribution, with a T_c transition width of ~3.8 K and a FWHM of ~3 K. Using pre-doped powder thus provides for a much higher degree of homogeneity in MgB_2.

Although substitution of various metals for the Mg site has been previously accomplished using high pressure, high temperature synthesis [248], [249], conclusive proof of Mg site substitution had yet to be offered for MgB_2 wires and thin films.

Zr addition was investigated by examining samples prepared by pulsed laser deposition (PLD). Changes in magnetic, resistive, chemical, and structural properties were investigated over a wide range of Zr composition. The value of the magnetically

measured T_c monotonically decreased with increasing ZrB_2 concentration; the magnitude of the magnetically measured dB_{c2}/dT monotonically increased with ZrB_2 addition. Resistive measurements also showed a clear change in B_{c2} with increasing ZrB_2 addition. XRD analysis showed a gradual shift in *a* lattice parameter with increasing ZrB_2. STEM-EDS showed a concentration gradient of Zr in the thin films, with a higher concentration exhibited closer to the substrate surface. Taken together these results provided, for the first time, clear evidence of Zr substitution on the Mg site.

7.3 Implications of This Work and Future Considerations

7.3.1 Porosity, Electrical Connectivity, and Anisotropy

Previous applications of a percolation model to MgB_2 [52], [222], [250], [251] have resulted in the conclusion that MgB_2, because of its anisotropy, is not suited for high-field applications (here defined as $B > 8$ T). However, through careful synthesis of wires with reduced anisotropy and porosity, it is seen that MgB_2 can achieve a current density nearly 10^5 A/cm^2 at 4.2 K, 10 T and 10^4 A/cm^2 at 4.2 K, 15 T.

In a further extension of percolation theory, reduction of the anisotropy parameter γ through chemical substitution (e.g. C for B [125], [233], [252]) may allow for even greater high-field increases in J_c. However, care must be taken to enact these substitutions as homogeneously as possible such that no deleterious second phases are formed that could inhibit supercurrent flow.

7.3.2 Porosity, Electrical Connectivity, and Anisotropy

The PLD procedure for MgB_2 thin films was optimized in terms of T_c. However, further efforts need to be made to optimize compositional homogeneity and surface smoothness.

Having developed a relatively simple procedure to allow for chemical substitution of Zr onto the Mg site, it is now possible to explore the structure-property relationships of other Mg-site substituted films using other metals or metal diborides. The addition of pinning centers which do not substitute for either B or Mg should also be investigated.

Appendix A: List of Acronyms

Acronym	Definition
ACMS	Alternating current magnetic susceptibility
BCS	Bardeen-Cooper-Schrieffer
BF	Bright field
BSE	Back scattered electrons
CCD	Charge-coupled device
CCD	Critical current density
CRT	Cathode ray tube
CSMM	Center for Superconducting & Magnetic Materials
CTFF	Continuous forming and filling
CVD	Chemical vapor deposition
DF	Dark field
EDS	Energy-dispersive X-ray spectroscopy
EELS	Electron energy loss spectroscopy
ESI	Energy-loss spectroscopy imaging
FC	Field cool
FEI	FEI Company, formerly Philips
FIB (DB-FIB)	Focused ion beam
FWHM	Full width at half-maximum
GID	Grazing incidence diffraction
HPCVD	Hybrid physical chemical vapor deposition
HT	Heat treat, heat treatment, heat treated
HTR	Hyper Tech Research, Inc.
HTS	High temperature superconductor
IMD	Internal Mg diffusion
LCD	Liquid crystal display
MRI	Magnetic resonance imaging
NHMFL	National high magnetic field laboratory
NIST	National institute of standards and technology
PIT	Powder in tube
PLD	Pulsed laser deposition
RRR	Residual resistivity ratio
SC	Superconductivity, superconducting
SEM	Scanning electron microscopy
STEM	Scanning transmission electron microscopy
TEM	Transmission electron microscopy
TLD	Through the lens detector
UHV	Ultra-high vacuum
VSM	Vibrating sample magnetometer
XRD	X-ray diffraction
YBCO	Yttrium barium copper oxide ($YBa_2Cu_3O_7$)
ZFC	Zero field cool

Appendix B: List of Latin Symbols

Symbol	Definition
A_0	Sample cross-section
A_{con}	Connectivity area fraction from percolation model
A_p	Percolation area fraction (effective cross section)
B	Magnetic flux density; on a macroscopic scale referred to as" magnetic field"
B_a	Applied magnetic field
B_c	Critical field
B_{c1}	Lower critical field
B_{c2}	Upper critical field
B_{irr}	Irreversibility field
B_K	Kramer-defined irreversibility field
b	Reduced B (B/B_{c2})
C_e	Electronic specific heat; heat capacity
C_{en}	Normal-state electronic specific heat; heat capacity
C_{es}	Superconducting electronic specific heat; heat capacity
C_p	Specific heat; heat capacity
D	Charge carrier diffusivity
d	Diameter
d	Number of dimensions
d	Flux lattice spacing, d(nm) = $1.072 \times 10^9 (\phi_0/B)^{½}$.
F^{-1}	Normalized connectivity parameter
F_p	Flux pinning force density
f	Fraction
f	Frequency
G	Electrical conductance
G_{eff}	Effective electrical conductance
H	Magnetic field
$\hbar$	Angular Planck's constant ($h/2\pi$)
I	Current
I_{eff}	Effective current
J	Current density
J_0	0 T, 4.2 K J_c
J_c	Critical current density (see Table 1 for more details)
J_{eff}	Effective current density
k_B	Boltzmann constant (1.380649×10^{-23} J/K)
K_w	Thermal conductance
M	Magnetization
m	Magnetic moment
m	Mass

(continued on the next page)

Symbol	Definition
	(continued from previous page)
$N(E_F)$	Density of itinerant electron states
n	Number (integer)
n	Gorter-Casimer exponent (canonically" 3" [119])
P	Power
p	Fraction of network with a given electrical conductivity
p_c	Percolation threshold
p_c*	modified percolation threshold p_c* ; defined as p_c/p_s
p_s	Superconductor area fraction
R	Resistance
S	Entropy
S_e	Electronic entropy
S_{es}	Superconducting electronic entropy
T	Temperature
T_c	Superconducting critical transition temperature
$T_{c,onset}$	Superconducting critical transition temperature as measured by the onset of superconductivity from the normal state
t	Time
t	Dimensionality constant for percolation model
V	Phonon mediated electron-electron interaction potential
V	Voltage
x	Cartesian axis, orthogonal to y and z
y	Cartesian axis, orthogonal to x and z
Z	Atomic number
z	Cartesian axis, orthogonal to y and z

Appendix C: List of Greek Symbols

Symbol	Definition
α	Power law exponent for percolation theory
α_d	Demagnetization factor
β_3, β_5	Specific heat fitting constants for phononic component
γ	Anisotropy parameter
γ_e	Electronic specific heat coefficient
ε	Electric current
ζ	Exponential dependence on distance between links for percolation model
θ	Angle
κ	Ginzburg-Landau parameter
λ	Penetration depth
λ	Wavelength
λ_{ep}	Intraband electron-phonon coupling parameter
μ_0	Permeability of free space (4π x 10^{-7} V-s/A-m)
ν	Correlation exponent for percolation model
ξ	Superconducting coherence length
π	Ratio of the circumference to the diameter in a circle
ρ	Resistivity
ρ_0	Residual resistivity (impurity scattering)
ρ_i	Intrinsic (phononic) resistivity
ρ_m	Measured resistivity
σ_{eff}	Effective electrical conductivity
ϕ	Magnetic flux
ϕ_0	Magnetic flux quantum (2.067833758 x 10^{-15} Wb)
χ_{AC}	AC susceptibility
χ_{DC}	DC susceptibility
ω_D	Debye frequency

Appendix D: Derivation of T_c Distribution Formula

At a given $T < T_c$ the electronic specific heat (and similarly, the entropy) of a superconducting material may be divided into two parts [253] : i) a superconducting component and ii) a normal state component. This is shown mathematically in Equations A1 and A2

$$C_e = \int_{T}^{T_{c,\max}} f(T_c) C_{es}(T, T_c) dT_c + \int_{0}^{T} f(T_c) C_{en}(T, T_c) dT_c \qquad \text{(A1)}$$

$$S_e = \int_{T}^{T_{c,\max}} f(T_c) S_{es}(T, T_c) dT_c + \int_{0}^{T} f(T_c) S_{en}(T, T_c) dT_c \qquad \text{(A2)}$$

where C_e and S_e are the total electronic specific heat and entropy (respectively), C_{es} and S_{es} are the superconducting electronic specific heat and entropy, and C_{en} and S_{en} are the normal state electronic specific heat and entropy. The fraction of the material with a given superconducting critical temperature, T_c, is given as $f(T_c)$. The normal state electronic specific (which depends on only the normal state properties and is thus independent of T_c) heat may be described as :

$$C_{en}(T, T_c) = C_{en}(T) = \gamma_e T \qquad \text{(A3)}$$

Where γ_e is the Sommerfeld constant, or normal state electronic specific heat coefficient [120]. The superconducting electronic specific heat may be described by the Gorter-Casimer two fluid model [119].

$$C_{es}(T,T_c) = \frac{3\gamma_e T^3}{T_c^2} \tag{A4}$$

If one wishes to vary the exponent in the numerator to compensate for scaling effects in the final distribution, then Equation A4 transforms to:

$$C_{es}(T,T_c) = C_{es}(T) = n\gamma_e T_c \left(\frac{T}{T_c}\right)^n \tag{A5}$$

in which the T_c may be considered a constant. Integrating Equations A3 and A5 according to the relation:

$$C = T\left(\frac{\partial S}{\partial T}\right) \tag{A6}$$

yields the following relations for the normal state and superconducting entropies:

$$S_{en}(T,T_c) = \int \frac{C_{en}(T)}{T} dT = \int \frac{\gamma_e T}{T} dT = \gamma_e T \tag{A7}$$

$$\begin{aligned} S_{es}(T,T_c) &= \int \frac{n\gamma_e T_c \left(T/T_c\right)^n}{T} = \int \frac{n\gamma_e T^{n-1}}{T_c^{n-1}} \\ &= \frac{n\gamma_e T^n}{(n-1)T_c^{n-1}} = \frac{n\gamma_e T_c}{(n-1)}\left(\frac{T}{T_c}\right)^n \end{aligned} \tag{A8}$$

Substituting Equations A3, A5, A7, and A8 into the appropriate places in Equations A1 and A2 then yields (after some rearranging):

$$\int_{T}^{T_{c,\max}} f(T_c) n\gamma_e T_c \left(\frac{T}{T_c}\right)^n = C_e(T) - \int_0^T f\left(T_c\right)\gamma_e T dT_c \qquad \text{(A9)}$$

$$\int_{T}^{T_{c,\max}} f(T_c) \frac{n\gamma_e T_c}{n-1} \left(\frac{T}{T_c}\right)^n = S_e(T) - \int_0^T f\left(T_c\right)\gamma_e T dT_c \qquad \text{(A10)}$$

Rearranging Equations A9 and A10 such that the left hand sides of the equations share the same form gives:

$$\int_{T}^{T_{c,\max}} f(T_c) T_c \left(\frac{T}{T_c}\right)^n = \frac{1}{n\gamma_e}\left[C_e(T) - \int_0^T f\left(T_c\right)\gamma_e T dT_c \right] \qquad \text{(A11)}$$

$$\int_{T}^{T_{c,\max}} f(T_c) T_c \left(\frac{T}{T_c}\right)^n = \frac{n-1}{n\gamma_e}\left[S_e(T) - \int_0^T f\left(T_c\right)\gamma_e T dT_c \right] \qquad \text{(A12)}$$

Now the right-hand sides of Equations A11 and A12 may be set equal to each other, yielding:

$$\frac{1}{n\gamma_e}\left[C_e(T) - \int_0^T f(T_c)\gamma_e T dT_c \right] = \frac{n-1}{n\gamma_e}\left[S_e(T) - \int_0^T f\left(T_c\right)\gamma_e T dT_c \right] \qquad \text{(A13)}$$

After simplification Equation A13 then becomes:

$$\int_0^T f(T_c) dT_c = \frac{nS_e(T) - C_e(T)}{\left(n-1\right)\gamma_e T} \qquad \text{(A14)}$$

which can be used to find the T_c distribution of a superconducting material from analysis of the normal state and superconducting specific heat data [118], [122–124].

List of References

[1] V. Russell, R. Hirst, F. A. Kanda, and A. J. King, "An X-ray study of the magnesium borides," *Acta Crystallographica*, vol. 6, no. 11–12, p. 870, 1953.

[2] J. Nagamatsu, N. Nakagawa, T. Muranaka, Y. Zenitani, and J. Akimitsu, "Superconductivity at 39 K in magnesium diboride," *Nature*, vol. 410, no. 6824, pp. 63–4, 2001.

[3] S. L. Bud'ko, G. Lapertot, C. Petrovic, C. E. Cunningham, N. Anderson, and P. C. Canfield, "Boron Isotope Effect in Superconducting MgB_2," *Phys. Rev. Lett.*, vol. 86, no. 9, pp. 1877–1880, 2001.

[4] D. C. Larbalestier, L. D. Cooley, M. O. Rikel, A. A. Polyanskii, J. Jiang, S. Patnaik, X. Y. Cai, D. M. Feldmann, A. Gurevich, A. A. Squitieri, M. T. Naus, C. B. Eom, E. E. Hellstrom, R. J. Cava, K. A. Regan, N. Rogado, M. A. Hayward, T. He, J. S. Slusky, P. Khalifah, K. Inumaru, and M. Haas, "Strongly linked current flow in polycrystalline forms of the superconductor MgB_2," *Nature*, vol. 410, no. 6825, pp. 186–189, 2001.

[5] E. W. Collings, M. D. Sumption, M. Bhatia, M. A. Susner, and S. D. Bohnenstiehl, "Prospects for improving the intrinsic and extrinsic properties of magnesium diboride superconducting strands.," *Supercond. Sci. Technol.*, vol. 21, no. 10, pp. 103001/1–103001/14, 2008.

[6] F. Jones and R. L. Taylor, "On boron hydride.," *J. Chem. Soc., Trans.*, vol. 39, pp. 213–219, 1881.

[7] H. Moissan, "Preparation of amorphous boron.," *Compt. rend.*, vol. 114, pp. 392–7, 1892.

[8] R. C. Ray, "Magnesium boride and amorphous boron.," *J. Chem. Soc., Trans.*, vol. 105, pp. 2162–8, 1914.

[9] M. E. Jones and R. E. Marsh, "Preparation and structure of magnesium boride, MgB_2.," *J. Am. Chem. Soc.*, vol. 76, pp. 1434–6, 1954.

[10] R. Naslain, A. Guette, and M. Barret, "Magnesium diborides and tetraborides. Crystallochemical considerations of the tetraborides.," *J. Solid State Chem.*, vol. 8, no. 1, pp. 68–85, 1973.

[11] A. Guette, M. Barret, R. Naslain, P. Hagenmuller, L. E. Tergenius, and T. Lundstroem, "Crystal structure of magnesium heptaboride Mg_2B_{14}.," *J. Less-Common Met.*, vol. 82, pp. 325–34, 1981.

[12] R. M. Swift and D. White, "Low Temperature Heat Capacities of Magnesium Diboride (MgB_2) and Magnesium Tetraboride (MgB_4)," *Journal of the American Chemical Society*, vol. 79, no. 14, pp. 3641–3644, 1957.

[13] B. T. Matthias, T. H. Geballe, S. Geller, and E. Corenzwit, "Superconductivity of Nb3Sn.," *Phys. Rev.*, vol. 95, p. 1435, 1954.

[14] A. A. Popovich and V. E. Ustinov, “Mechanochemical reduction of boron oxide by magnesium.,” in *Mekhanokhim. Sint., Dokl. Vses. Nauchno-Tekh. Konf.*, 1990, pp. 83–8.

[15] T. I. Serebryakova, V. A. Ponomarenko, A. I. Karasev, V. I. Shemanin, and E. V. Marek, “Magnesium diboride and its use in reactions for cubic boron nitride synthesis.,” *Poroshk. Metall. (Kiev)*, no. 11, pp. 77–9, 1980.

[16] “Diaphragm for honeycomb-structure speaker.,” U.S. Patent JP56141694A05-Nov-1981.

[17] A. S. Cooper, E. Corenzwit, L. D. Longinotti, B. T. Matthias, and W. H. Zachariasen, “Superconductivity: the transition temperature peak below four electrons per atom,” *Proc Natl Acad Sci U S A*, vol. 67, no. 1, pp. 313–9, 1970.

[18] L. Leyarovska and E. Leyarovski, “A search for superconductivity below 1 K in transition metal borides.,” *J. Less-Common Met.*, vol. 67, no. 1, pp. 249–55, 1979.

[19] P. C. Canfield and G. W. Crabtree, “Magnesium diboride: better late than never.,” *Phys. Today*, vol. 56, no. 3, pp. 34–40, 2003.

[20] J. Bardeen, L. N. Cooper, and J. R. Schrieffer, “Theory of Superconductivity,” *Phys. Rev.*, vol. 108, no. 5, pp. 1175–1204, Dec. 1957.

[21] M. K. Wu, J. R. Ashburn, C. J. Torng, P. H. Hor, R. L. Meng, L. Gao, Z. J. Huang, Y. Q. Wang, and C. W. Chu, “Superconductivity at 93 K in a new mixed-phase Y-Ba-Cu-O compound system at ambient pressure,” *Phys. Rev. Lett.*, vol. 58, no. 9, pp. 908–910, Mar. 1987.

[22] M. A. Subramanian, C. C. Torardi, J. C. Calabrese, J. Gopalakrishnan, K. J. Morrissey, T. R. Askew, R. B. Flippen, U. Chowdhry, and A. W. Sleight, “A New High-Temperature Superconductor: $Bi_2Sr_{3-x}Ca_xCu_2O_{8+y}$,” *Science*, vol. 239, no. 4843, pp. 1015 –1017, Feb. 1988.

[23] S. A. Sunshine, T. Siegrist, L. F. Schneemeyer, D. W. Murphy, R. J. Cava, B. Batlogg, R. B. van Dover, R. M. Fleming, S. H. Glarum, S. Nakahara, R. Farrow, J. J. Krajewski, S. M. Zahurak, J. V. Waszczak, J. H. Marshall, P. Marsh, L. W. Rupp, and W. F. Peck, “Structure and physical properties of single crystals of the 84-K superconductor $Bi_{2.2}Sr_2Ca_{0.8}Cu_2O_{8+\delta}$,” *Phys. Rev. B*, vol. 38, no. 1, pp. 893–896, Jul. 1988.

[24] K Vinod and R G Abhilash Kumar and U Syamaprasad, “Prospects for MgB_2 superconductors for magnet application,” *Superconductor Science and Technology*, vol. 20, no. 1, p. R1, 2007.

[25] “World helium reserves are running out, Nobel laureate claims - Telegraph.” [Online]. Available: http://www.telegraph.co.uk/science/science-news/7959624/World-helium-reserves-are-running-out-Nobel-laureate-claims.html. [Accessed: 01-Feb-2012].

[26] M. Modica, S. Angius, L. Bertora, D. Damiani, M. Marabotto, D. Nardelli, M. Perrella, M. Razeti, and M. Tassisto, “Design, Construction and Tests of MgB2 Coils for the Development of a Cryogen Free Magnet,” *IEEE Trans. Appl. Supercond.*, vol. 17, no. 2, pp. 2196–2199, 2007.

[27] S. D. Bohnenstiehl, M. D. Sumption, M. Majoros, M. Tomsic, M. Rindfleisch, J. Phillips, J. Yue, and E. W. Collings, "Wind and React MgB_2 Rotor Coils," *AIP Conf. Proc.*, vol. 986, no. 1, pp. 382–387, 2008.

[28] M. D. Sumption, M. Bhatia, F. Buta, S. Bohnenstiehl, M. Tomsic, M. Rindfleisch, J. Yue, J. Phillips, S. Kawabata, and E. W. Collings, "Solenoidal coils made from monofilamentary and multifilamentary MgB_2 strands.," *Los Alamos Natl. Lab., Prepr. Arch., Condens. Matter*, pp. 1–22, arXiv:cond–mat/0503755, 2005.

[29] W. W. Schultz, A. P. van, I. Sabelis, and E. Mooyaart, "Magnetic resonance imaging of male and female genitals during coitus and female sexual arousal," *BMJ*, vol. 319, no. 7225, pp. 1596–600, 1999.

[30] M V Berry and A K Geim, "Of flying frogs and levitrons," *European Journal of Physics*, vol. 18, no. 4, p. 307, 1997.

[31] H. Weeren van, "Magnesium diboride superconductors for magnet applications," Enschede, 2007.

[32] W. Hofmann and W. Janiche, "The structural type of aluminum boride (AlB_2)," *Naturwissenschaften*, vol. 23, p. 851, 1935.

[33] J. Kortus, I. I. Mazin, K. D. Belashchenko, V. P. Antropov, and L. L. Boyer, "Superconductivity of Metallic Boron in MgB_2.," *Phys. Rev. Lett.*, vol. 86, no. 20, pp. 4656–4659, 2001.

[34] A. L. Ivanovskii, "Band Structure and Properties of Superconducting MgB_2 and Related Compounds (A Review).," *Phys. Solid State*, vol. 45, no. 10, pp. 1829–1859, 2003.

[35] K. D. Belashchenko, M. Schilfgaarde, and V. P. Antropov, "Coexistence of covalent and metallic bonding in the boron intercalation superconductor MgB_2," *Phys. Rev. B*, vol. 64, no. 9, p. 092503, 2001.

[36] V. P. Antropov, K. D. Belashchenko, S. van, and S. N. Rashkeev, "Electronic structure, bonding and optical spectrum of MgB_2.," *Stud. High Temp. Supercond.*, vol. 38, no. Superconducting Magnesium Diboride, pp. 91–116, 2002.

[37] J. Bardeen, L. N. Cooper, and J. R. Schrieffer, "Microscopic theory of superconductivity.," *Phys. Rev.*, vol. 106, pp. 162–4, 1957.

[38] D. G. Hinks, H. Claus, and J. D. Jorgensen, "The complex nature of superconductivity in MgB_2 as revealed by the reduced total isotope effect.," *Nature (London, U. K.)*, vol. 411, no. 6836, pp. 457–460, 2001.

[39] J. P. Carbotte, "Properties of boson-exchange superconductors.," *Rev. Mod. Phys.*, vol. 62, no. 4, pp. 1027–157, 1990.

[40] P. Brotto, M. Tropeano, C. Ferdeghini, P. Manfrinetti, A. Palenzona, d'Agliano Galleani, and M. Putti, "Experimental confirmation of the low B isotope coefficient of MgB_2.," *Phys. Rev. B: Condens. Matter Mater. Phys.*, vol. 78, no. 9, pp. 092502/1–092502/4, 2008.

[41] H. J. Choi, M. L. Cohen, and S. G. Louie, "Anisotropic Eliashberg theory of MgB2: Tc, isotope effects, superconducting energy gaps, quasiparticles, and specific heat.," *Physica C (Amsterdam, Neth.)*, vol. 385, no. 1–2, pp. 66–74, 2003.

[42] T. Schneider and C. Di, “Pressure and isotope effect on the anisotropy of MgB2.,” *Phys. Rev. B: Condens. Matter Mater. Phys.*, vol. 72, no. 5, pp. 054501/1–054501/4, 2005.
[43] M. Wang, Z.-J. Xu, and X.-Y. Su, “Isotope effect of MgB_2 superconductor.,” *Diwen Wuli Xuebao*, vol. 25, no. 2, pp. 147–150, 2003.
[44] A. Bharathi, Y. Hariharan, J. Balaselvi, and C. S. Sundar, “Superconductivity in MgB_2: Phonon modes and influence of carbon doping.,” *Sadhana*, vol. 28, no. 1 & 2, pp. 263–272, 2003.
[45] H. Martinho, C. Rettori, P. G. Pagliuso, A. A. Martin, N. O. Moreno, and J. L. Sarrao, “Role of the E_{2g} phonon in the superconductivity of MgB_2: a Raman scattering study,” *Solid State Communications*, vol. 125, no. 9, pp. 499–502, Mar. 2003.
[46] C. Buzea and T. Yamashita, “Review of the superconducting properties of MgB_2,” *Superconductor Science and Technology*, vol. 14, no. 11, pp. R115–R146, 2001.
[47] S. Souma, Y. Machida, T. Sato, T. Takahashi, H. Matsui, S.-C. Wang, H. Ding, A. Kaminski, J. C. Campuzano, S. Sasaki, and K. Kadowaki, “The origin of multiple superconducting gaps in MgB_2.,” *Nature (London, U. K.)*, vol. 423, no. 6935, pp. 65–67, 2003.
[48] F. Manzano, A. Carrington, N. E. Hussey, S. Lee, A. Yamamoto, and S. Tajima, “Exponential Temperature Dependence of the Penetration Depth in Single Crystal MgB_2,” *Phys. Rev. Lett.*, vol. 88, no. 4, p. 047002, Jan. 2002.
[49] X. X. Xi, A. V. Pogrebnyakov, S. Y. Xu, K. Chen, Y. Cui, E. C. Maertz, C. G. Zhuang, Q. Li, D. R. Lamborn, J. M. Redwing, Z. K. Liu, A. Soukiassian, D. G. Schlom, X. J. Weng, E. C. Dickey, Y. B. Chen, W. Tian, X. Q. Pan, S. A. Cybart, and R. C. Dynes, “MgB_2 thin films by hybrid physical–chemical vapor deposition,” *Physica C: Superconductivity*, vol. 456, no. 1–2, pp. 22–37, Jun. 2007.
[50] R. Cubitt, M. R. Eskildsen, C. D. Dewhurst, J. Jun, S. M. Kazakov, and J. Karpinski, “Effects of Two-Band Superconductivity on the Flux-Line Lattice in Magnesium Diboride.,” *Phys. Rev. Lett.*, vol. 91, no. 4, pp. 047002/1–047002/4, 2003.
[51] J. D. Fletcher, A. Carrington, O. J. Taylor, S. M. Kazakov, and J. Karpinski, “Temperature-Dependent Anisotropy of the Penetration Depth and Coherence Length of MgB_2,” *Phys. Rev. Lett.*, vol. 95, no. 9, p. 097005, 2005.
[52] M. Eisterer, M. Zehetmayer, and H. W. Weber, “Current Percolation and Anisotropy in Polycrystalline MgB_2,” *Phys. Rev. Lett.*, vol. 90, no. 24, p. 247002, Jun. 2003.
[53] S. Kim, D. S. Stone, J. Cho, C. Jeong, C. Kang, and J. Bae, “Phase stability determination of the Mg–B binary system using the CALPHAD method and ab initio calculations,” *Journal of Alloys and Compounds*, vol. 470, no. 1–2, pp. 85–89, 2009.
[54] “CompuTherm LLC.” [Online]. Available: http://www.computherm.com/. [Accessed: 15-Feb-2012].

[55] P.J. Spencer, “A brief history of CALPHAD,” *Calphad*, vol. 32, no. 1, pp. 1–8, Mar. 2008.
[56] S. Bohnenstiehl, “Thermal analysis, phase equilibria, and superconducting properties in MgB_2 and carbon-doped MgB_2,” Doctor of Philosophy, The Ohio State University, Columbus, OH, 2012.
[57] V. Adasch, K. Hess, T. Ludwig, N. Vojteer, and H. Hillebrecht, “Synthesis and crystal structure of MgB_{12},” *Journal of Solid State Chemistry*, vol. 179, no. 9, pp. 2916–2926, 2006.
[58] V. Adasch, K.-U. Hess, T. Ludwig, N. Vojteer, and H. Hillebrecht, “Synthesis, crystal growth and structure of Mg containing β-rhombohedral boron: $MgB_{17.4}$,” *Journal of Solid State Chemistry*, vol. 179, no. 9, pp. 2900–2907, Sep. 2006.
[59] S. Brutti, M. Colapietro, G. Balducci, L. Barba, P. Manfrinetti, and A. Palenzona, “Synchrotron powder diffraction Rietveld refinement of MgB_{20} crystal structure,” *Intermetallics*, vol. 10, no. 8, pp. 811–817, 2002.
[60] S. Bohnenstiehl, S. A. Dregia, M. D. Sumption, and E. W. Collings, “Thermal analysis of MgB_2 formation.,” *IEEE Trans. Appl. Supercond.*, vol. 17, no. 2, Pt. 3, pp. 2754–2756, 2007.
[61] G. Balducci, S. Brutti, A. Ciccioli, G. Gigli, P. Manfrinetti, A. Palenzona, M. F. Butman, and L. Kudin, “Thermodynamics of the intermediate phases in the Mg–B system,” *Journal of Physics and Chemistry of Solids*, vol. 66, no. 2–4, pp. 292–297, 2005.
[62] L. P. Cook, R. Klein, W. Wong-Ng, Q. Huang, R. A. Ribeiro, and P. C. Canfield, “Thermodynamics of MgB_2 by calorimetry and Knudsen thermogravimetry,” *IEEE Transactions on Applied Superconductivity*, vol. 15, no. 2, pp. 3227–3229, 2005.
[63] S. Lee, “Crystal growth of MgB_2,” *Physica C*, vol. 385, no. 1–2, pp. 31–41, 2003.
[64] J. D. DeFouw and D. C. Dunand, “Effect of processing variables on the reaction kinetics of MgB_2 fibers,” *Physica C: Superconductivity*, vol. 470, no. 15–16, pp. 648–653, Aug. 2010.
[65] J. D. DeFouw and D. C. Dunand, “Mechanisms and kinetics of MgB_2 synthesis from boron fibers,” *Acta Materialia*, vol. 56, no. 19, pp. 5751–5763, Nov. 2008.
[66] A. Serquis, Y. T. Zhu, E. J. Peterson, J. Y. Coulter, D. E. Peterson, and F. M. Mueller, “Effect of lattice strain and defects on the superconductivity of MgB_2,” *Appl. Phys. Lett.*, vol. 79, no. 26, pp. 4399–4401, Dec. 2001.
[67] R. A. Ribeiro, S. L. Bud’ko, C. Petrovic, and P. C. Canfield, “Effects of boron purity, Mg stoichiometry and carbon substitution on properties of polycrystalline MgB_2,” *Physica C*, vol. 385, no. 1–2, pp. 16–23, 2003.
[68] D. G. Hinks, J. D. Jorgensen, H. Zheng, and S. Short, “Synthesis and stoichiometry of MgB_2,” *Physica C*, vol. 382, no. 2–3, pp. 166–176, 2002.
[69] “Oops! Make That Four Forms of Pure Boron - NYTimes.com.” [Online]. Available: http://tierneylab.blogs.nytimes.com/2009/02/09/oops-make-that-four-forms-of-pure-boron/?hp. [Accessed: 12-Mar-2012].
[70] A. R. Oganov, J. Chen, C. Gatti, Y. Ma, Y. Ma, C. W. Glass, Z. Liu, T. Yu, O. O. Kurakevych, and V. L. Solozhenko, “Ionic high-pressure form of elemental boron.,” *Nature (London, U. K.)*, vol. 457, no. 7231, pp. 863–867, 2009.

[71] S. D. Bohnenstiehl, M. A. Susner, Y. Yang, E. W. Collings, M. D. Sumption, M. A. Rindfleisch, and R. Boone, "Carbon doping of MgB_2 by toluene and malic-acid-in-toluene," *Physica C: Superconductivity*, vol. 471, no. 3–4, pp. 108–111, Feb. 2011.

[72] J. H. Kim, Y.-U. Heo, A. Matsumoto, H. Kumakura, M. Rindfleisch, M. Tomsic, and S. X. Dou, "Comparative study of mono- and multi-filament MgB_2 wires with different boron powders and malic acid addition," *Superconductor Science and Technology*, vol. 23, no. 7, p. 075014, 2010.

[73] S. K. Chen, K. A. Yates, M. G. Blamire, and J. L. MacManus-Driscoll, "Strong influence of boron precursor powder on the critical current density of MgB_2," *Superconductor Science and Technology*, vol. 18, no. 11, p. 1473, 2005.

[74] X. Xu, M. J. Qin, K. Konstantinov, D. Santos, W. K. Yeoh, J. H. Kim, and S. X. Dou, "Effect of boron powder purity on superconducting properties of MgB_2," *Superconductor Science and Technology*, vol. 19, no. 6, p. 466, 2006.

[75] J. Jiang, B. J. Senkowicz, D. C. Larbalestier, and E. E. Hellstrom, "Influence of boron powder purification on the connectivity of bulk MgB_2," *Superconductor Science and Technology*, vol. 19, no. 8, p. L33, 2006.

[76] Y. Zhang, X. Xu, Y. Zhao, J. H. Kim, C. Lu, S. H. Zhou, and S. X. Dou, "Significant improvement of J_c in MgB_2 bulk superconductor using ball-milled high-purity crystalline boron.," *Supercond. Sci. Technol.*, vol. 21, no. 11, pp. 115004/1–115004/6, 2008.

[77] M. A. A. Mahmud, M. A. Susner, M. D. Sumption, M. A. Rindfleisch, M. J. Tomsic, J. Yue, and E. W. Collings, "Comparison of critical current density in MgB_2 with different boron sources and nano-particle dopant additions.," *IEEE Trans. Appl. Supercond.*, vol. 19, no. 3, Pt. 3, pp. 2756–2759, 2009.

[78] D. Dew-Hughes, "Flux pinning mechanisms in type II superconductors.," *Philos. Mag.*, vol. 30, no. 2, pp. 293–305, 1974.

[79] J. M. Rowell, "The widely variable resistivity of MgB2 samples," *Superconductor Science and Technology*, vol. 16, no. 6, p. R17, 2003.

[80] H. Fujii, K. Togano, and H. Kumakura, "Enhancement of critical current densities of powder-in-tube processed MgB_2 tapes by using MgH_2 as a precursor powder.," *Supercond. Sci. Technol.*, vol. 15, no. 11, pp. 1571–1576, 2002.

[81] C. E. J. Dancer, P. Mikheenko, A. Bevan, J. S. Abell, R. I. Todd, and C. R. M. Grovenor, "A study of the sintering behaviour of magnesium diboride," *Journal of the European Ceramic Society*, vol. 29, no. 9, pp. 1817–1824, 2009.

[82] M. A. Rindfleisch, "Experiment 1391." 2008.

[83] C R M Grovenor and L Goodsir and C J Salter and P Kovac and I Husek, "Interfacial reactions and oxygen distribution in MgB_2 wires in Fe, stainless steel and Nb sheaths," *Superconductor Science and Technology*, vol. 17, no. 3, p. 479, 2004.

[84] M. D. Sumption, S. Bohnenstiehl, F. Buta, M. Majoros, S. Kawabata, M. Tomsic, M. Rindfleisch, J. Phillips, J. Yue, and E. W. Collings, "Wind and react and react and wind MgB_2 solenoid, racetrack and pancake coils.," *IEEE Trans. Appl. Supercond.*, vol. 17, no. 2, Pt. 2, pp. 2286–2290, 2007.

[85] A. Nesmeyanov, *Vapor pressure of the Chemical Elements*. New York: Elsevier, 1963.

[86] X. X. Xi, X. H. Zeng, A. Soukiassian, J. Jones, J. Hotchkiss, Y. Zhong, C. O. Brubaker, Z.-K. Liu, J. Lettieri, D. G. Schlom, Y. F. Hu, E. Wertz, Q. Li, W. Tian, H. P. Sun, and X. Q. Pan, "Thermodynamics and thin film deposition of MgB_2 superconductors," *Superconductor Science and Technology*, vol. 15, no. 3, pp. 451–457, 2002.

[87] X. X. Xi, X. H. Zeng, A. V. Pogrebnyakov, S. Y. Xu, Qi Li, Yu Zhong, C. O. Brubaker, Zi-Kui Liu, E. M. Lysczek, J. M. Redwing, J. Lettieri, D. G. Schlom, W. Tian, and X. Q. Pan, "In situ growth of MgB_2 thin films by hybrid physical-chemical vapor deposition," *Applied Superconductivity, IEEE Transactions on DOI - 10.1109/TASC.2003.812209*, vol. 13, no. 2, pp. 3233–3237, 2003.

[88] X. X. Xi, A. V. Pogrebnyakov, X. H. Zeng, J. M. Redwing, S. Y. Xu, Q. Li, Z.-K. Liu, J. Lettieri, V. Vaithyanathan, D. G. Schlom, H. M. Christen, H. Y. Zhai, and A. Goyal, "Progress in the deposition of MgB_2 thin films.," *Inst. Phys. Conf. Ser.*, vol. 181, no. Applied Superconductivity 2003, pp. 37–44, 2004.

[89] B. H. Moeckly and W. S. Ruby, "Growth of high-quality large-area MgB2 thin films by reactive evaporation.," *Supercond. Sci. Technol.*, vol. 19, no. 6, pp. L21–L24, 2006.

[90] Eun Kyu Park and J H Lee and Sang Young Lee and Brian H Moeckly and John H Claassen, "Effects of proton irradiation on the microwave properties of polycrystalline MgB_2 films in the Meissner state," *Superconductor Science and Technology*, vol. 21, no. 7, p. 075005, 2008.

[91] T. Haugan, P. N. Barnes, R. Wheeler, F. Meisenkothen, and M. Sumption, "Addition of nanoparticle dispersions to enhance flux pinning of the $YBa_2Cu_3O_{7-x}$ superconductor," *Nature*, vol. 430, no. 7002, pp. 867–870, print 2004.

[92] W. N. Kang, H.-J. Kim, E.-M. Choi, C. U. Jung, and S.-I. Lee, "MgB_2 superconducting thin films with a transition temperature of 39 Kelvin.," *Science (Washington, DC, U. S.)*, vol. 292, no. 5521, pp. 1521–1523, 2001.

[93] Y. Zhao, M. Ionescu, J. Horvat, and S. X. Dou, "Off-axis MgB_2 films using an in situ annealing pulsed laser deposition method.," *Supercond. Sci. Technol.*, vol. 18, no. 4, pp. 395–399, 2005.

[94] A. Brinkman, D. Mijatovic, H. Hilgenkamp, G. Rijnders, I. Oomen, D. Veldhuis, F. Roesthuis, H. Rogalla, and D. H. A. Blank, "The road to magnesium diboride thin films, Josephson junctions and SQUIDs.," *Supercond. Sci. Technol.*, vol. 16, no. 2, pp. 246–253, 2003.

[95] Yue Zhao and Mihail Ionescu and Josip Horvat and Shi Xue Dou, "Comparative study of in situ and ex situ MgB_2 films prepared by pulsed laser deposition," *Superconductor Science and Technology*, vol. 17, no. 9, p. S482, 2004.

[96] R. F. Klie, J. C. Idrobo, N. D. Browning, K. A. Regan, N. S. Rogado, and R. J. Cava, "Direct observation of nanometer-scale Mg- and B-oxide phases at grain boundaries in MgB_2.," *Appl. Phys. Lett.*, vol. 79, no. 12, pp. 1837–1839, 2001.

[97] B. Birajdar, N. Peranio, and O. Eibl, "Quantitative electron microscopy and spectroscopy of MgB_2 wires and tapes.," *Supercond. Sci. Technol.*, vol. 21, no. 7, pp. 073001/1–073001/20, 2008.
[98] K. A. Yates, Z. Lockman, A. Kursumovic, G. Burnell, N. A. Stelmashenko, J. L. M. Driscoll, and M. G. Blamire, "The effect of oxygenation on the superconducting properties of MgB_2 thin films," *Appl. Phys. Lett.*, vol. 86, no. 2, pp. 022502–3, Jan. 2005.
[99] J. M. Rowell, S. Y. Xu, X. H. Zeng, A. V. Pogrebnyakov, Q. Li, X. X. Xi, J. M. Redwing, W. Tian, and X. Pan, "Critical current density and resistivity of MgB_2 films," *Applied Physics Letters*, vol. 83, no. 1, pp. 102–104, 2003.
[100] Y. Eltsev, "Resistive behavior and magnetic phase diagram of MgB_2 single crystals," *Physica C*, vol. 385, no. 1–2, pp. 162–168, 2003.
[101] T. Matsushita, M. Kiuchi, A. Yamamoto, J. Shimoyama, and K. Kishio, "Critical current density and flux pinning in superconducting MgB2," *Physica C: Superconductivity*, vol. 468, no. 15–20, pp. 1833–1835, Sep. 2008.
[102] S. Lee, T. Masui, A. Yamamoto, H. Uchiyama, and S. Tajima, "Carbon-substituted MgB_2 single crystals," *Physica C: Superconductivity*, vol. 397, no. 1–2, pp. 7–13, Oct. 2003.
[103] Z. X. Shi, M. A. Susner, M. Majoros, M. D. Sumption, X. Peng, M. Rindfleisch, M. J. Tomsic, and E. W. Collings, "Anisotropic connectivity and its influence on critical current densities, irreversibility fields, and flux creep in in situ processed MgB_2 strands," *Superconductor Science and Technology*, vol. 23, no. 4, p. 045018, 2010.
[104] E. W. Collings, in *Applied Superconductivity, Metallurgy, and Physics of Titanium Alloys: Volume 1- Fundamentals*, 1st ed., New York: Plenum Press, 1986, pp. 499–517.
[105] E. W. Collings, in *Applied Superconductivity, Metallurgy, and Physics of Titanium Alloys: Volume 1- Fundamentals*, 1st ed., New York: Plenum Press, 1986, pp. 205–215.
[106] A. Gurevich, "Limits of the upper critical field in dirty two-gap superconductors.," *Phys. C (Amsterdam, Neth.)*, vol. 456, no. 1–2, pp. 160–169, 2007.
[107] W. K. Yeoh and S. X. Dou, "Enhancement of H_{c2} and J_c by carbon-based chemical doping.," *Phys. C (Amsterdam, Neth.)*, vol. 456, no. 1–2, pp. 170–179, 2007.
[108] A. Agostino, M. Panetta, P. Volpe, M. Truccato, S. Cagliero, L. Gozzelino, R. Gerbaldo, G. Ghigo, F. Laviano, G. Lopardo, and B. Minetti, "Na substitution effects on MgB_2 synthesized with a microwave-assisted technique.," *IEEE Trans. Appl. Supercond.*, vol. 17, no. 2, Pt. 3, pp. 2774–2777, 2007.
[109] M. Bhatia, M. D. Sumption, E. W. Collings, and S. Dregia, "Increases in the irreversibility field and the upper critical field of bulk MgB_2 by ZrB_2 addition.," *Appl. Phys. Lett.*, vol. 87, no. 4, pp. 042505/1–042505/3, 2005.
[110] X. Zhang, Z. Gao, D. Wang, Z. Yu, Y. Ma, S. Awaji, and K. Watanabe, "Improved critical current densities in MgB_2 tapes with ZrB_2 doping," *Appl. Phys. Lett.*, vol. 89, no. 13, pp. 132510–3, 2006.

[111] J. S. Slusky, N. Rogado, K. A. Regan, M. A. Hayward, P. Khalifah, T. He, K. Inumaru, S. M. Loureiro, M. K. Haas, H. W. Zandbergen, and R. J. Cava, "Loss of superconductivity with the addition of Al to MgB_2 and a structural transition in $Mg_{1-x}Al_xB_2$.," *Nature (London, U. K.)*, vol. 410, no. 6826, pp. 343–345, 2001.
[112] Y. Sun, D. Yu, Z. Liu, J. He, X. Zhang, Y. Tian, J. Xiang, and D. Zheng, "Decrease of Tc and persistent two gaps upon enhancement of the Ca doping in MgB_2 superconductor.," *Appl. Phys. Lett.*, vol. 90, no. 5, pp. 052507/1–052507/3, 2007.
[113] N. Suemitsu, T. Masui, S. Lee, and S. Tajima, "Mn substitution effect on superconducting properties of MgB_2 single crystals.," *Phys. C (Amsterdam, Neth.)*, vol. 445–448, pp. 39–41, 2006.
[114] K. M. Elsabawy and E. E. Kandyel, "Lead substitutions for promoted critical current density J_c and mechanical properties of $Mg_{1-x}Pb_xB_2$ regime.," *Mater. Res. Bull.*, vol. 42, no. 6, pp. 1051–1060, 2007.
[115] N. W. Ashcroft and N. D. Mermin, in *Solid State Physics*, 1st ed., New York: Harcourt College Press, 1976, p. 43.
[116] C. H. Poole, H. A. Farach, R. J. Creswick, and R. Prozorov, in *Superconductivity*, London: Elsevier, 1976, p. 84.
[117] E. Bucher, F. Heiniger, J. Mueller, and J. L. Olsen, "Experimental relations for electron interactions in transition metals, determined from superconductivity data.," *Low Temp. Phys., Proc. Int. Conf., 9th*, vol. 1964, no. Pt. A, pp. 616–20, 1965.
[118] A. Junod, T. Jarlborg, and J. Muller, "Heat-capacity analysis of a large number of A15-type compounds.," *Phys. Rev. B: Condens. Matter*, vol. 27, no. 3, pp. 1568–85, 1983.
[119] G. Rickayzen, "Theory of Superconductivity," New York: John Wiley & Sons, 1965, pp. 204–207.
[120] A. C. Rose-Innes and E. H. Rhoderick, "Introduction to Superconductivity," 1st ed., London: Pergamon Press, Ltd., 1969, pp. 61–63.
[121] E. W. Collings, in *Applied Superconductivity, Metallurgy, and Physics of Titanium Alloys: Volume 1- Fundamentals*, 1st ed., New York: Plenum Press, 1986, pp. 453–460.
[122] C. Senatore, P. Lezza, R. Lortz, O. Shcherbakova, W. K. Yeoh, S. X. Dou, and R. Flukiger, "Specific heat and magnetic relaxation analysis of MgB_2 bulk samples with and without additives.," *IEEE Trans. Appl. Supercond.*, vol. 17, no. 2, Pt. 3, pp. 2941–2944, 2007.
[123] Y. Wang, C. Senatore, V. Abacherli, D. Uglietti, and R. Flukiger, "Specific heat of Nb_3Sn wires.," *Supercond. Sci. Technol.*, vol. 19, no. 4, pp. 263–266, 2006.
[124] C. Senatore, D. Uglietti, V. Abacherli, A. Junod, and R. Flukiger, "Specific heat, a method to determine the Tc distribution in industrial Nb3Sn wires prepared by various techniques.," *IEEE Trans. Appl. Supercond.*, vol. 17, no. 2, Pt. 3, pp. 2611–2614, 2007.
[125] M. A. Susner, Y. Yang, M. D. Sumption, E. W. Collings, M. A. Rindfleisch, M. J. Tomsic, and J. V. Marzik, "Enhanced critical fields and superconducting properties

of pre-doped B powder-type MgB_2 strands," *Superconductor Science and Technology*, vol. 24, no. 1, p. 012001, 2011.
[126] R. Fluekiger, "Presentation 4MB02," Chicago, IL, 2008.
[127] A. C. Rose-Innes and E. H. Rhoderick, "Introduction to Superconductivity," 1st ed., London: Pergamon Press, Ltd., 1969, pp. 79–81.
[128] J. Bardeen and M. J. Stephen, "Theory of the Motion of Vortices in Superconductors," *Phys. Rev.*, vol. 140, no. 4A, pp. A1197–A1207, Nov. 1965.
[129] K. Fossheim and A. Sudbo, "Superconductivity: Physics and Applications," Chiciester, England: John Wiley & Sons, 2004, p. 89.
[130] P. Lee, Ed., "Engineering Superconductivity," New York: Wiley-Interscience, 2001, p. 99.
[131] E. W. Collings, in *Applied Superconductivity, Metallurgy, and Physics of Titanium Alloys: Volume 1- Fundamentals*, 1st ed., New York: Plenum Press, 1986, pp. 473–492.
[132] D. Dew-Hughes, "Hard superconductors.," *Mater. Sci. Eng. (Amsterdam)*, vol. 1, no. 1, pp. 2–29, 1966.
[133] M. J. Witcomb and D. Dew-Hughes, "Superconductivity of heat-treated niobium-65 at. % titanium alloy.," *J. Mater. Sci.*, vol. 8, no. 10, pp. 1383–400, 1973.
[134] M. Tinkham, "Introduction to Superconductivity," New York: Dover Publications, Inc., 1996, p. 23.
[135] A. M. Campbell and J. E. Evetts, "Flux vortices and transport currents in type II superconductors.," *Advan. Phys.*, vol. 21, no. 90, pp. 199–428, 1972.
[136] R. Labusch, "Calculation of the Critical Field Gradient in Type II Superconductors," *Cryst. Latt. Def.*, vol. 1, pp. 1–16, 1969.
[137] T. Matsushita, "Flux Pinning in Superconductors," New York: Springer, 2007, pp. 271–272.
[138] P. Lee, Ed., "Engineering Superconductivity," New York: Wiley-Interscience, 2001, p. 100.
[139] W. A. Fietz and W. W. Webb, "Hysteresis in superconducting alloys--temperature and field dependence of dislocation pinning in niobium alloys.," *Phys. Rev.*, vol. 178, no. 2, pp. 657–67, 1969.
[140] E. J. Kramer, "Scaling laws for flux pinning in hard superconductors.," *J. Appl. Phys.*, vol. 44, no. 3, pp. 1360–70, 1973.
[141] A. K. Pradhan, Z. X. Shi, M. Tokunaga, T. Tamegai, Y. Takano, K. Togano, H. Kito, and H. Ihara, "Electrical transport and anisotropic superconducting properties in single crystalline and dense polycrystalline MgB_2," *Phys. Rev. B*, vol. 64, no. 21, p. 212509, Nov. 2001.
[142] W. Buckel and R. Kleiner, "Superconductivity: Fundamentals and Applications," 2nd ed., Weinheim, Federal Republic of Germany: Wiley-VCH Verlag GmbH & Co. KGaA, 2004, p. 12.
[143] E. H. Brandt, "On the shear modulus of the flux line lattice.," *Phys. Status Solidi B*, vol. 77, no. 2, pp. 551–60, 1976.
[144] D. Dew-Hughes, "The role of grain boundaries in determining J_c in high-field high-current superconductors.," *Philos. Mag. B*, vol. 55, no. 4, pp. 459–79, 1987.

[145] A. A. Godeke, “Performance boundaries in niobium tin superconductors.,” 2005.
[146] S. Oh and K. Kim, “consistent description of scaling law for flux pinning in Nb_3Sn strands based on the Kramer model.,” *IEEE Trans. Appl. Supercond.*, vol. 16, no. 2, pp. 1216–1219, 2006.
[147] X. Peng, X. Wu, M. D. Sumption, M. Tomsic, E. Gregory, and E. W. Collings, “Characterization of Ti and Ta influence on grain shape and size, as well as transport properties of conductors fabricated by the internal-Sn process.,” *AIP Conf. Proc.*, vol. 824, no. Advances in Cryogenic Engineering, Volume 52B, pp. 489–496, 2006.
[148] M. Bhatia, “Magnesium boride superconductors: Processing, characterization and enhancement of critical fields.,” 2007.
[149] S. De, X. Xu, W. X. Li, Y. Zhang, M. Rindfleisch, and M. Tomsic, “Improving superconducting properties of MgB2 by graphene doping.,” *IEEE Trans. Appl. Supercond.*, vol. 21, no. 3, Pt. 3, pp. 2686–2689, 2011.
[150] B. D. Cullity, “Elements of X-Ray Diffraction,” 2nd ed., Reading, Massachusetts: Addison-Wesley Publishing Co., Inc., 1978, p. 84.
[151] D. A. Skoog, J. H. Holler, and T. A. Nieman, “Principles of Instrumental Analysis,” 5th ed., New York: Brooks Cole, 1998, pp. 550–554.
[152] J Byrne and N Howarth, “The K-shell fluorescence yield and atomic shell structure effects,” *Journal of Physics B: Atomic and Molecular Physics*, vol. 3, no. 2, p. 280, 1970.
[153] J. Goldstein, D. E. Newbury, D. C. Joy, C. E. Lyman, P. Echlin, E. Lifshin, L. Sawyer, and J. R. Michael, “Scanning Electron Microscopy and X-Ray Microanalysis,” 3rd ed., New York: Springer, 2003, pp. 503–505.
[154] “TEM_ray_diag.basic.de.png (PNG Image, 359 × 329 pixels).” [Online]. Available: http://upload.wikimedia.org/wikipedia/commons/0/03/TEM_ray_diag.basic.de.png. [Accessed: 09-May-2012].
[155] J. F. Schenck, “The role of magnetic susceptibility in magnetic resonance imaging: MRI magnetic compatibility of the first and second kinds,” *Med Phys*, vol. 23, no. 6, pp. 815–50, 1996.
[156] C. P. Bean, “Magnetization of Hard Superconductors,” *Phys. Rev. Lett.*, vol. 8, no. 6, pp. 250–253, Mar. 1962.
[157] C. P. BEAN, “Magnetization of High-Field Superconductors,” *Rev. Mod. Phys.*, vol. 36, no. 1, pp. 31–39, Jan. 1964.
[158] H.-L. Ji, X. Jin, and H.-C. Fan, “Bean Model and Critical Current Density in Samples with Different Geometries,” *Chinese Journal of Low Temperature Physics*, vol. 14, no. 1, pp. 12–16, 1992.
[159] J. Ekin, “Experimental Techniques for Low-Temperature Measurements,” 1st ed., New York: Oxford University Press, 2006, pp. 274–276.
[160] J. S. Hwang, K. J. Lin, and C. Tien, “Measurement of heat capacity by fitting the whole temperature response of a heat-pulse calorimeter.,” *Rev. Sci. Instrum.*, vol. 68, no. 1, Pt. 1, pp. 94–101, 1997.

[161] G. R. Stewart, “Measurement of low-temperature specific heat.,” *Rev. Sci. Instrum.*, vol. 54, no. 1, pp. 1–11, 1983.
[162] Quantum Design, Inc., “Physical Property Measurement System Heat Capacity Option User’s Manual.” Jan-2004.
[163] R. Eason, Ed., “Pulsed Laser Deposition of Thin Films,” 1st ed., Hoboken, New Jersey: John Wiley & Sons, 2007, pp. 3–6.
[164] Y. Zhao, “Fabrication and Characterization of Superconducting PLD MgB_2 Thin Films,” PhD Dissertation, University of Wollongong, Wollongong, New South Wales, Commonwealth of Australia, 2005.
[165] X. Zeng, A. V. Pogrebnyakov, A. Kotcharov, J. E. Jones, X. X. Xi, E. M. Lysczek, J. M. Redwing, S. Xu, Q. Li, J. Lettieri, D. G. Schlom, W. Tian, X. Pan, and Z.-K. Liu, “In situ epitaxial MgB2 thin films for superconducting electronics,” *Nat Mater*, vol. 1, no. 1, pp. 35–38, print 2002.
[166] R. N. Bhattacharya and M. P. Paranthaman, Eds., “High Temperature Superconductors,” Wiley-VCH Verlag GmbH & Co. KGaA, 2010, pp. 34–45.
[167] Y. Yang, M. A. Susner, M. D. Sumption, M. Rindfleisch, M. Tomsic, and E. W. Collings, “Influence of Strand Design, Boron Type, and Carbon Doping Method on the Transport Properties of Powder-in-Tube $MgB_{2-x}C_x$ strands,” *Applied Superconductivity, IEEE Transactions on*, vol. 22, no. 2, p. 6200110, 2012.
[168] G. Giunchi, S. Ceresara, G. Ripamonti, Z. Di, S. Rossi, S. Chiarelli, M. Spadoni, R. Wesche, and P. L. Bruzzone, “High performance new MgB_2 superconducting hollow wires.,” *Supercond. Sci. Technol.*, vol. 16, no. 2, pp. 285–291, 2003.
[169] G. Giunchi, G. Ripamonti, E. Perini, T. Cavallin, and E. Bassani, “Advancements in the reactive liquid Mg infiltration technique to produce long superconducting MgB_2 tubular wires.,” *IEEE Trans. Appl. Supercond.*, vol. 17, no. 2, Pt. 3, pp. 2761–2765, 2007.
[170] J. M. Hur, K. Togano, A. Matsumoto, H. Kumakura, H. Wada, and K. Kimura, “Fabrication of high-performance MgB_2 wires by an internal Mg diffusion process.,” *Supercond. Sci. Technol.*, vol. 21, no. 3, pp. 032001/1–032001/4, 2008.
[171] D. Uchiyama, K. Mizuno, T. Akao, M. Maeda, T. Kawakami, H. Kobayashi, Y. Kubota, and K. Yasohama, “Fibrous structure and critical current density of MgB_2 superconducting wire.,” *Cryogenics*, vol. 47, no. 5–6, pp. 282–286, 2007.
[172] S. J. Gregg and W. B. Jepson, “The high-temperature oxidation of magnesium in dry and in moist oxygen.,” *J. Inst. Met.*, vol. 87, pp. 187–203, 1959.
[173] M. D. Sumption, M. A. Susner, M. Bhatia, M. A. Rindfleisch, M. J. Tomsic, K. J. McFadden, and E. W. Collings, “High critical current density multifilamentary MgB_2 strands.,” *IEEE Trans. Appl. Supercond.*, vol. 17, no. 2, Pt. 3, pp. 2838–2841, 2007.
[174] M. Tomsic, M. Rindfleisch, J. Yue, K. McFadden, D. Doll, J. Phillips, M. D. Sumption, M. Bhatia, S. Bohnenstiehl, and E. W. Collings, “Development of magnesium diboride (MgB_2) wires and magnets using *in situ* strand fabrication method.,” *Phys. C (Amsterdam, Neth.)*, vol. 456, no. 1–2, pp. 203–208, 2007.

[175] M. D. Sumption, M. Bhatia, M. Rindfleisch, M. Tomsic, and E. W. Collings, "Transport and magnetic J_c of MgB_2 strands and small helical coils.," *Appl. Phys. Lett.*, vol. 86, no. 10, pp. 102501/1–102501/3, 2005.
[176] M. Bhatia, M. D. Sumption, S. Bohnenstiehl, S. A. Dregia, E. W. Collings, M. Tomsic, and M. Rindfleisch, "Superconducting Properties of SiC Doped MgB_2 Formed Below and Above Mg's Melting Point," *Applied Superconductivity, IEEE Transactions on DOI - 10.1109/TASC.2007.899396*, vol. 17, no. 2, pp. 2750–2753, 2007.
[177] M A Susner and T W Daniels and M D Sumption and M A Rindfleisch and C J Thong and E W Collings, "Drawing induced texture and the evolution of superconductive properties with heat treatment time in powder-in-tube in situ processed MgB_2 strands," *Superconductor Science and Technology*, vol. 25, no. 6, p. 065002, 2012.
[178] M. Vignolo, G. Romano, A. Malagoli, V. Braccini, M. Tropeano, E. Bellingeri, C. Fanciulli, C. Bernini, V. Honkimaki, M. Putti, and C. Ferdeghini, "Role of the Grain Oxidation in Improving the In-Field Behavior of MgB_2 Ex-Situ Tapes," *Applied Superconductivity, IEEE Transactions on*, vol. 19, no. 3, pp. 2718–2721, 2009.
[179] J. Horvat, W. K. Yeoh, J. H. Kim, and S. X. Dou, "Transport and magnetic critical current in superconducting MgB_2 wires.," *Supercond. Sci. Technol.*, vol. 21, no. 6, pp. 065003/1–065003/6, 2008.
[180] E. Bartolome, F. Goemoery, X. Granados, T. Puig, and X. Obradors, "Transport versus magnetization technique for determination of critical current densities in superconducting tapes with macroscopic defects.," *Supercond. Sci. Technol.*, vol. 18, no. 4, pp. 388–394, 2005.
[181] A. Ghosh, K. Robins, and W. Sampson, "Magnetization measurements on multifilamentary Nb_3Sn and NbTi conductors," *Magnetics, IEEE Transactions on*, vol. 21, no. 2, pp. 328– 331, 1985.
[182] M. D. Sumption, "Calculation of the magnetization of anisotropic superconductors with cylindrical geometry in transverse fields.," *Appl. Supercond.*, vol. 2, no. 1, pp. 41–6, 1994.
[183] Z. X. Shi, M. A. Susner, M. D. Sumption, E. W. Collings, X. Peng, M. Rindfleisch, and M. J. Tomsic, "Doping effect and flux pinning mechanism of nano-SiC additions in MgB_2 strands," *Superconductor Science and Technology*, vol. 24, no. 6, p. 065015, 2011.
[184] M. J. Qin, S. Keshavarzi, S. Soltanian, X. L. Wang, H. K. Liu, and S. X. Dou, "Sample-size dependence of the magnetic critical current density in MgB_2 superconductors.," *Phys. Rev. B: Condens. Matter Mater. Phys.*, vol. 69, no. 1, pp. 012507/1–012507/4, 2004.
[185] S. Soltanian, M. J. Qin, S. Keshavarzi, X. L. Wang, and S. X. Dou, "Effect of sample size on the magnetic critical current density in nano-SiC doped MgB_2 superconductors.," *Phys. Rev. B: Condens. Matter Mater. Phys.*, vol. 68, no. 13, pp. 134509/1–134509/4, 2003.

[186] J. Horvat, S. Soltanian, X. L. Wang, and S. X. Dou, "Effect of sample size on magnetic J_c for MgB_2 superconductor.," *Appl. Phys. Lett.*, vol. 84, no. 16, pp. 3109–3111, 2004.
[187] G. Giunchi, "The Superconducting Properties of High Density Bulk MgB2 Obtained by Reactive Liquid Mg Infiltration," *AIP Conf. Proc.*, vol. 824, no. 1, pp. 813–819, 2006.
[188] G. Z. Li, Y. Yang, M. A. Susner, M. D. Sumption, and E. W. Collings, "Critical current densities and n-values of MgB_2 strands over a wide range of temperatures and fields.," *Supercond. Sci. Technol.*, vol. 25, no. 2, pp. 025001/1–025001/10, 2012.
[189] X. Song, V. Braccini, and D. C. Larbalestier, "Inter- and intragranular nanostructure and possible spinodal decomposition in low-resistivity bulk MgB_2 with varying critical fields," *Journal of Materials Research*, vol. 19, no. 8, pp. 2245–2255, 2004.
[190] A. Berenov, Z. Lockman, X. Qi, J. L. MacManus-Driscoll, Y. Bugoslavsky, L. F. Cohen, M.-H. Jo, N. A. Stelmashenko, V. N. Tsaneva, M. Kambara, B. Hari, D. A. Cardwell, and M. G. Blamire, "Growth of strongly biaxially aligned MgB_2 thin films on sapphire by post-annealing of amorphous precursors.," *Appl. Phys. Lett.*, vol. 79, no. 24, pp. 4001–4003, 2001.
[191] D. Mijatovic, A. Brinkman, H. Hilgenkamp, H. Rogalla, G. Rijnders, and D. H. A. Blank, "Pulsed-laser deposition of MgB_2 and B thin films.," *Appl. Phys. A: Mater. Sci. Process.*, vol. 79, no. 4–6, pp. 1243–1246, 2004.
[192] M. Ionescu, J. McKinnon, C. Cai, A. Li, K. Konstantinov, A. V. Pan, and S. X. Dou, "Growths of MgB_2 thin films by pulsed laser deposition.," *Cryst. Eng.*, vol. 5, no. 3–4, pp. 391–400, 2002.
[193] K. Chen, P. Ma, R. J. Nie, T. Yang, F. X. Xie, L. Y. Liu, S. Z. Wang, Y. D. Dai, and F. Wang, "Growth and superconductivity characteristics of MgB_2 thin films.," *Supercond. Sci. Technol.*, vol. 15, no. 12, pp. 1721–1724, 2002.
[194] Y. Cui, J. E. Jones, A. Beckley, R. Donovan, D. Lishego, E. Maertz, A. V. Pogrebnyakov, P. Orgiani, J. M. Redwing, and X. X. Xi, "Degradation of MgB_2 thin films in water.," *IEEE Trans. Appl. Supercond.*, vol. 15, no. 2, Pt. 1, pp. 224–227, 2005.
[195] M. Annabi, A. M'Chirgui, A. Ben, M. Zouaoui, and S. Ben, "Corrosion process of MgB_2 superconductor in a moisture atmosphere.," *Phys. Status Solidi C*, vol. 1, no. 7, pp. 1916–1919, 2004.
[196] S. D. Bu, D. M. Kim, J. H. Choi, J. Giencke, E. E. Hellstrom, D. C. Larbalestier, S. Patnaik, L. Cooley, C. B. Eom, J. Lettieri, D. G. Schlom, W. Tian, and X. Q. Pan, "Synthesis and properties of c-axis oriented epitaxial MgB_2 thin films.," *Appl. Phys. Lett.*, vol. 81, no. 10, pp. 1851–1853, 2002.
[197] L. Gu, B. H. Moeckly, and D. J. Smith, "Electron microscopy studies of epitaxial MgB_2 superconducting thin films grown by in situ reactive evaporation.," *J. Cryst. Growth*, vol. 280, no. 3–4, pp. 602–611, 2005.
[198] T. He, R. J. Cava, and J. M. Rowell, "Reactivity of MgB_2 with common substrate and electronic materials.," *Appl. Phys. Lett.*, vol. 80, no. 2, pp. 291–293, 2002.

[199] V Ferrando and S Amoruso and E Bellingeri and R Bruzzese and P Manfrinetti and D Marrè and R Velotta and X Wang and C Ferdeghini, "Growth methods of c -axis oriented MgB_2 thin films by pulsed laser deposition," *Superconductor Science and Technology*, vol. 16, no. 2, p. 241, 2003.

[200] A. V. Pogrebnyakov, J. M. Redwing, J. E. Giencke, C. B. Eom, V. Vaithyanathan, D. G. Schlom, A. Soukiassian, S. B. Mi, C. L. Jia, J. Chen, Y. F. Hu, Y. Cui, Q. Li, and X. X. Xi, "Carbon-doped MgB_2 thin films grown by hybrid physical-chemical vapor deposition.," *IEEE Trans. Appl. Supercond.*, vol. 15, no. 2, Pt. 3, pp. 3321–3324, 2005.

[201] Y. S. Wu, Y. Zhao, D. Wexler, J. H. Kim, and S. X. Dou, "Optimization of in situ annealing conditions for off-axis PLD MgB_2 films.," *Phys. C (Amsterdam, Neth.)*, vol. 468, no. 3, pp. 218–222, 2008.

[202] C. B. Eom, M. K. Lee, J. H. Chol, L. J. Belenky, X. Song, L. D. Cooley, M. T. Naus, S. Patnaik, J. Jiang, M. Rikel, A. Polyanskil, A. Gurevich, X. Y. Cai, S. D. Bu, S. E. Babcock, E. E. Hellstrom, D. C. Larbalestler, N. Rogado, K. A. Regan, M. A. Hayward, T. He, J. S. Slusky, K. Inumaru, M. K. Haas, and R. J. Cava, "High critical current density and enhanced irreversibility field in superconducting MgB_2 thin films.," *Nature (London, U. K.)*, vol. 411, no. 6837, pp. 558–560, 2001.

[203] W. N. Kang, E.-M. Choi, H.-J. Kim, H.-J. Kim, and S.-I. Lee, "Growth of superconducting MgB2 thin films via postannealing techniques.," *Physica C (Amsterdam, Neth.)*, vol. 385, no. 1–2, pp. 24–30, 2003.

[204] K. Komori, K. Kawagishi, Y. Takano, H. Fujii, S. Arisawa, H. Kumakura, M. Fukutomi, and K. Togano, "Approach for the fabrication of MgB_2 superconducting tape with large in-field transport critical current density.," *Appl. Phys. Lett.*, vol. 81, no. 6, pp. 1047–1049, 2002.

[205] Y. Zhao, M. Ionescu, M. Roussel, A. V. Pan, J. Horvat, and S. X. Dou, "Superconducting and microstructural properties of two types of MgB_2 films prepared by pulsed laser deposition.," *IEEE Trans. Appl. Supercond.*, vol. 15, no. 2, Pt. 3, pp. 3261–3264, 2005.

[206] H. Kitaguchi and T. Doi, "High-temperature and high-field performance of MgB_2 films with J_c of 10^6 A cm^{-2} (4.2 K, 4 T).," *Supercond. Sci. Technol.*, vol. 18, no. 4, pp. 489–493, 2005.

[207] H. Kitaguchi, T. Doi, Y. Kobayashi, A. Matsumoto, H. Sosiati, S. Hata, M. Fukutomi, and H. Kumakura, "Properties of MgB2 films with very high transport critical current densities.," *IEEE Trans. Appl. Supercond.*, vol. 15, no. 2, Pt. 3, pp. 3313–3316, 2005.

[208] M A Rindfleisch and Hyper-Tech Research, Inc., *Strand S1033-1968B-700-20*. 2009.

[209] S. W. Kenkel and J. P. Straley, "Percolation Theory of Nonlinear Circuit Elements," *Phys. Rev. Lett.*, vol. 49, no. 11, pp. 767–770, 1982.

[210] J. P. Straley and S. W. Kenkel, "Percolation theory for nonlinear conductors," *Phys. Rev. B*, vol. 29, no. 11, pp. 6299–6305, Jun. 1984.

[211] B. Abeles, H. L. Pinch, and J. I. Gittleman, "Percolation conductivity in tungsten-aluminum oxide granular metal films.," *Phys. Rev. Lett.*, vol. 35, no. 4, pp. 247–50, 1975.
[212] J. P. Clerc, G. Giraud, S. Alexander, and E. Guyon, "Conductivity of a mixture of conducting and insulating grains: dimensionality effects.," *Phys. Rev. B: Condens. Matter*, vol. 22, no. 5, pp. 2489–94, 1980.
[213] S. I. Lee, Y. Song, T. W. Noh, X. D. Chen, and J. R. Gaines, "Experimental observation of nonuniversal behavior of the conductivity exponent for three-dimensional continuum percolation systems.," *Phys. Rev. B: Condens. Matter*, vol. 34, no. 10, pp. 6719–24, 1986.
[214] B. J. Last and D. J. Thouless, "Percolation theory and electrical conductivity.," *Phys. Rev. Lett.*, vol. 27, no. 25, pp. 1719–21, 1971.
[215] H. J. Herrmann, B. Derrida, and J. Vannimenus, "Superconductivity exponents in two- and three-dimensional percolation," *Phys. Rev. B*, vol. 30, no. 7, pp. 4080–4082, Oct. 1984.
[216] G. Xiao, F. H. Streitz, M. Z. Cieplak, A. Bakhshai, A. Gavrin, and C. L. Chien, "Electrical transport and superconductivity in a gold-yttrium barium copper oxide (YBa2Cu3O7) percolation system.," *Phys. Rev. B: Condens. Matter*, vol. 38, no. 1, pp. 776–9, 1988.
[217] Y. Gefen, A. Aharony, B. B. Mandelbrot, and S. Kirkpatrick, "Solvable Fractal Family, and Its Possible Relation to the Backbone at Percolation," *Phys. Rev. Lett.*, vol. 47, no. 25, pp. 1771–1774, Dec. 1981.
[218] J W Essam, "Percolation theory," *Reports on Progress in Physics*, vol. 43, no. 7, p. 833, 1980.
[219] D S Gaunt and M F Sykes, "Series study of random percolation in three dimensions," *Journal of Physics A: Mathematical and General*, vol. 16, no. 4, p. 783, 1983.
[220] G. Deutscher and M. L. Rappaport, "Critical currents of superconducting aluminum-germanium and lead-germanium thin film alloys near the metal-insulator transition.," *J. Phys., Lett. (Orsay, Fr.)*, vol. 40, no. 10, pp. 219–21, 1979.
[221] G. Deutscher, A. Kapitulnik, and M. Rappaport, "Percolation in metal-insulator systems.," *Ann. Isr. Phys. Soc.*, vol. 5, no. Percolation Struct. Processes, pp. 207–28, 1983.
[222] M Eisterer and J Emhofer and S Sorta and M Zehetmayer and H W Weber, "Connectivity and critical currents in polycrystalline MgB_2," *Superconductor Science and Technology*, vol. 22, no. 3, p. 034016, 2009.
[223] D R Tilley, "The Ginsburg-Landau equations for anisotropic alloys," *Proceedings of the Physical Society*, vol. 86, no. 2, p. 289, 1965.
[224] V. G. Kogan and S. L. Bud'ko, "Anisotropy parameters of superconducting MgB_2," *Physica C: Superconductivity*, vol. 385, no. 1–2, pp. 131–142, Mar. 2003.
[225] Y. Eltsev, S. Lee, K. Nakao, N. Chikumoto, S. Tajima, N. Koshizuka, and M. Murakami, "Anisotropic superconducting properties of MgB_2 single crystals probed by in-plane electrical transport measurements," *Phys. Rev. B*, vol. 65, no. 14, p. 140501, Mar. 2002.

[226] L. Lyard, P. Samuely, P. Szabo, T. Klein, C. Marcenat, L. Paulius, K. H. P. Kim, C. U. Jung, H.-S. Lee, B. Kang, S. Choi, S.-I. Lee, J. Marcus, S. Blanchard, A. G. M. Jansen, U. Welp, G. Karapetrov, and W. K. Kwok, "Anisotropy of the upper critical field and critical current in single crystal MgB_2," *Phys. Rev. B*, vol. 66, no. 18, p. 180502, 2002.

[227] O. F. de Lima and C. A. Cardoso, "Anisotropy in MgB_2," *Brazilian Journal of Physics*, vol. 33, pp. 709–712, 2003.

[228] M. D. Sumption, M. Bhatia, M. Rindfleisch, M. Tomsic, S. Soltanian, S. X. Dou, and E. W. Collings, "Large upper critical field and irreversibility field in MgB_2 wires with SiC additions.," *Appl. Phys. Lett.*, vol. 86, no. 9, pp. 092507/1–092507/3, 2005.

[229] S. C. van der Marck, "Percolation thresholds and universal formulas," *Phys. Rev. E*, vol. 55, no. 2, pp. 1514–1517, Feb. 1997.

[230] M. A. Susner, M. Bhatia, M. D. Sumption, and E. W. Collings, "Electrical resistivity, Debye temperature, and connectivity in heavily doped bulk MgB2 superconductors.," *J. Appl. Phys.*, vol. 105, no. 10, pp. 103916/1–103916/7, 2009.

[231] J. V. Marzik, R. J. Suplinskas, R. H. T. Wilke, P. C. Canfield, D. K. Finnemore, M. Rindfleisch, J. Margolies, and S. T. Hannahs, "Plasma synthesized doped B powders for MgB_2 superconductors," *Physica C*, vol. 423, no. 3–4, pp. 83–88, 2005.

[232] L Gozzelino and R Gerbaldo and G Ghigo and F Laviano and G Lopardo and E Mezzetti and G A Ummarino and G Giunchi and E Perini and L Saglietti and E Bassani and B Minetti, "Influence of nanoparticle doping on electronic properties of MgB_2 bulk samples," *Journal of Physics: Conference Series*, vol. 234, no. 1, p. 012014, 2010.

[233] M. Angst, S. L. Bud'ko, R. H. T. Wilke, and P. C. Canfield, "Difference between Al and C doping in anisotropic upper critical field development in MgB_2," *Phys. Rev. B*, vol. 71, no. 14, p. 144512, Apr. 2005.

[234] M. Avdeev, J. D. Jorgensen, R. A. Ribeiro, S. L. Bud'ko, and P. C. Canfield, "Crystal chemistry of carbon-substituted MgB_2," *Physica C*, vol. 387, no. 3–4, pp. 301–306, 2003.

[235] R. J. Cava, H. W. Zandbergen, and K. Inumaru, "The substitutional chemistry of MgB_2," *Physica C*, vol. 385, no. 1–2, pp. 8–15, 2003.

[236] M. A. Susner, M. D. Sumption, M. Bhatia, X. Peng, M. J. Tomsic, M. A. Rindfleisch, and E. W. Collings, "Influence of Mg/B ratio and SiC doping on microstructure and high field transport Jc in MgB_2 strands," *Physica C: Superconductivity*, vol. 456, no. 1–2, pp. 180–187, Jun. 2007.

[237] D. C. K. Wong, Wai Kong Yeoh, Rong Kun Zheng, S. P. Ringer, Wen Xian Li, Xun Xu, and Shi Xou Dou, "Magnetoelectric properties of MgB_2 superconductor by SiC doping," in *Applied Superconductivity and Electromagnetic Devices (ASEMD), 2011 International Conference on*, 2011, pp. 65–68.

[238] Akiyasu Yamamoto and Jun-ichi Shimoyama and Shinya Ueda and Isao Iwayama and Shigeru Horii and Kohji Kishio, "Effects of B 4 C doping on critical current

properties of MgB_2 superconductor," *Superconductor Science and Technology*, vol. 18, no. 10, p. 1323, 2005.
[239] A Matsumoto and H Kitaguchi and H Kumakura, "Superconducting properties of MgB_2 /Fe tape heavily doped with nanosized SiC," *Superconductor Science and Technology*, vol. 21, no. 6, p. 065007, 2008.
[240] O. V. Shcherbakova, A. V. Pan, S. X. Dou, R. Nigam, and D. Wexler, "Nanocoating of particles for optimal doping and universal enhancement of current-carrying ability in ``organic'' $MgB_{2-x}C_x$ superconductors," *J. Appl. Phys.*, vol. 107, no. 9, pp. 09E147–3, May 2010.
[241] M. G. T. Mentink, A. Anders, M. M. J. Dhalle, D. R. Dietderich, A. Godeke, W. Goldacker, F. Hellman, K. ten, D. Putnam, J. L. Slack, M. D. Sumption, and M. A. Susner, "Analysis of bulk and thin film model samples intended for investigating the strain sensitivity of niobium-tin.," *IEEE Trans. Appl. Supercond.*, vol. 21, no. 3, Pt. 3, pp. 2550–2553, 2011.
[242] F. Bouquet, R. A. Fisher, N. E. Phillips, D. G. Hinks, and J. D. Jorgensen, "Specific Heat of $Mg_{11}B_2$: Evidence for a Second Energy Gap.," *Phys. Rev. Lett.*, vol. 87, no. 4, pp. 047001/1–047001/4, 2001.
[243] V. Gasparov, N. Sidorov, I. Zver'kova, and M. Kulakov, "Electron transport in diborides: Observation of superconductivity in ZrB_2," *JETP Letters*, vol. 73, no. 10, pp. 532–535, May 2001.
[244] E. W. Collings, "A Sourcebook of Titanium Alloy Superconductivity," Plenum Press, 1983, pp. 215–218.
[245] F. J. Bachner, J. B. Goodenough, and H. C. Gatos, "Superconducting transition temperature and electronic structure in the pseudobinaries Nb_3Al-Nb_3Sn and Nb3Sn-Nb3Sb," *Journal of Physics and Chemistry of Solids*, vol. 28, no. 5, pp. 889–895, May 1967.
[246] R. H. Willens, E. Buehler, and B. T. Matthias, "Superconductivity of the Transition-Metal Carbides," *Phys. Rev.*, vol. 159, no. 2, pp. 327–330, Jul. 1967.
[247] Chenggang Zhuang and Teng Tan and Yazhou Wang and Shanshan Bai and Xiaobai Ma and Huan Yang and Guohua Zhang and Yusheng He and Haihu Wen and X X Xi and Qingrong Feng and Zizhao Gan, "Clean MgB_2 thin films on different types of single-crystal substrate fabricated by hybrid physical–chemical vapor deposition," *Superconductor Science and Technology*, vol. 22, no. 2, p. 025002, 2009.
[248] J. Karpinski, N. D. Zhigadlo, S. Katrych, K. Rogacki, B. Batlogg, M. Tortello, and R. Puzniak, "MgB_2 single crystals substituted with Li and with Li-C: Structural and superconducting properties," *Phys. Rev. B*, vol. 77, no. 21, p. 214507, 2008.
[249] J. Karpinski, N. D. Zhigadlo, S. Katrych, R. Puzniak, K. Rogacki, and R. Gonnelli, "Single crystals of MgB_2: Synthesis, substitutions and properties," *Physica C*, vol. 456, no. 1–2, pp. 3–13, 2007.
[250] M. Eisterer, "Magnetic properties and critical currents of MgB_2," *Superconductor Science and Technology*, vol. 20, no. 12, pp. R47–R73, 2007.

[251] M. Eisterer and H. W. Weber, “Consequences of the peculiar intrinsic properties of MgB_2 on its macroscopic current flow.,” *Phys. C (Amsterdam, Neth.)*, vol. 470, no. Suppl. 1, pp. S651–S652, 2010.
[252] M. Angst, R. Puzniak, A. Wisniewski, J. Jun, S. M. Kazakov, J. Karpinski, J. Roos, and H. Keller, “Temperature and Field Dependence of the Anisotropy of MgB_2.,” *Phys. Rev. Lett.*, vol. 88, no. 16, pp. 167004/1–167004/4, 2002.
[253] E. W. Collings, in *Applied Superconductivity, Metallurgy, and Physics of Titanium Alloys: Volume 1- Fundamentals*, 1st ed., New York: Plenum Press, 1986, pp. 383–411.